Dissertation

# Generation and detection of photo-thermal and photo-acoustic waves in solids for advanced near-field IR imaging

A thesis submitted for the degree of

Doctor of Technical Sciences (Dr. techn.)

at

Technische Universität Wien
Faculty of Technical Chemistry
Institute of Chemical Technologies and Analytics

under supervision of

Univ.Prof. Dr. Bernhard Lendl
Dr. William-Curtin (Liam O'Faolain)
Assistant Prof. Dr. Georg Ramer

defended by

**Yide Zhang, MSc**
Mat. Nr. 12128310

Vienna

*To people who I love.*

# Abstract

Atomic force microscopy-infrared (AFM-IR) spectroscopy has become an essential tool for nanoscale chemical imaging, offering spatial resolution beyond the diffraction limit of conventional infrared spectroscopy. A typical AFM-IR setup directs a pulsed IR laser onto the sample, precisely at the tip of an AFM cantilever, detecting local absorption indirectly as photothermal expansion via the tip. This combination of AFM's high spatial resolution and infrared spectroscopy's chemical specificity enables detailed studies of a wide range of materials, from polymers and biological tissues to nanomaterials. However, the factors influencing AFM-IR signal generation and spatial resolution-especially in complex and inhomogeneous samples-remain challenging to fully understand and predict.

While AFM-IR is a well-established technique for chemical imaging across various fields, existing theoretical models often rely on simplified geometries that do not fully capture the complexities of real-world samples. Early models, such as those by Dazzi et al. [1, 2], describe thermal expansion in homogeneous materials but overlook spatial resolution. Later refinements [3, 4] account for interfaces between distinct materials, yet they assume idealized boundary conditions that rarely apply to heterogeneous systems. Many practical samples, including biological structures, thin films, and composite materials, consist of absorbers embedded within a larger matrix, leading to complex signal transduction mechanisms. These limitations highlight the need for a more comprehensive model that accurately accounts for sample heterogeneity, spatial resolution, and realistic thermal interactions-key challenges our study seeks to address.

This thesis addresses these challenges by introducing several advancements in AFM-IR theory and application. First, an analytical point spread function (PSF) model that accounts for key factors such as absorber size, position, surrounding matrix properties, and laser parameters is developed. By using Green's functions, this model offers a computationally efficient and accurate description of the signal generation process, outperforming conventional finite element method (FEM) simulations. FEM verification and experimental validation confirm the model's accuracy, revealing how variables like laser pulse width, repetition rate, and interfacial thermal resistance affect AFM-IR's signal amplitude and spatial resolution. This PSF model provides deeper insights into the AFM-IR response and serves as a versatile tool for optimizing experimental setups, opening the door to advanced

AFM-IR techniques.

Beyond theoretical advancements, this thesis investigates the impact of sample's size, geometry, and surface topography on AFM-IR signal generation. Advanced nano-fabrication techniques are employed to create samples with controlled absorber sizes and complex surface features. The findings highlight the significant role of surface topography, particularly in complex three-dimensional structures, in shaping the detected signal. These insights are crucial for accurate interpretation of AFM-IR data, especially in applications related to nanoelectronics, energy materials, and biological systems, where complex geometries are common.

Advancements in optomechanical AFM probes are also introduced, integrating optical micro-ring resonators with suspended cantilevers. These optomechanical AFM probes achieve unprecedented displacement and force sensitivities, enabling piconewton-scale force detection and sub-femtometer displacement measurements. Experimental validation confirms the superior performance of these probes compared to conventional AFM cantilevers. The experimental validation of the micro-ring resonator design demonstrates its enhanced performance, with applications extending to material characterization and biological studies. The integration of optical and mechanical systems represents a significant advancement in nanoscale sensing.

Further improvements in AFM sensing capabilities are introduced by integrating photonic crystal cavities with suspended cantilevers, leveraging the high-quality factor and resonance characteristics of photonic crystal cavities. Additionally, designs incorporating Bragg gratings on micro-cantilevers fabricated on silicon-on-insulator (SOI) wafers are explored through Multiphysics simulations, integrating mechanical bending-induced refractive index changes into electromagnetic wave simulations. These sensors enable highly accurate and quantitative measurements of force and displacement, improving sensitivity and broadening the dynamic range. The implementation of this novel photonic transducer expands the scope of AFM applications, particularly in environments requiring precise measurements.

By bridging gaps in both theoretical and experimental aspects of AFM-IR and optomechanical AFM probes, this thesis advances high-resolution nanoscale imaging and sensing. The integration of novel theoretical models, advanced fabrication techniques, and optomechanical AFM probes expands the capabilities of AFM, offering new opportunities for research and applications in nanotechnology, materials science, and biomedical research.

# Kurzfassung

Die Kombination von Infrarotspektroskopie mit Rasterkraftmikroskopie (AFM-IR) hat sich als unverzichtbares Werkzeug für die chemische Bildgebung im Nanometerbereich etabliert und bietet eine Ortsauflösung, die weit unter das Beugungslimit konventioneller Infrarotspektroskopie hinausgeht. In einem typischen AFM-IR-Aufbau wird ein gepulster IR-Laser gezielt auf die Probenoberfläche im Bereich der Spitze eines AFM-Kantilevers fokussiert und die lokale Absorption mittels der AFM Spitze indirekt über photothermische Expansion detektiert. Diese Kombination aus der hohen lateralen Auflösung der AFM und der chemischen Spezifität der IR-Spektroskopie ermöglicht detaillierte Untersuchungen einer Vielzahl von Materialien – von Polymeren und biologischen Geweben bis hin zu Nanomaterialien. Dennoch sind die Mechanismen der Signalerzeugung und die erzielte Ortsauflösung, insbesondere bei komplexen und inhomogenen Proben, nach wie vor nicht vollständig verstanden und schwer vorhersagbar.

Obwohl AFM-IR mittlerweile eine etablierte Methode zur chemischen Bildgebung in unterschiedlichen Anwendungsfeldern darstellt, beruhen viele theoretische Modelle auf stark vereinfachten Geometrien, die die Komplexität realer Probenstrukturen nur unzureichend erfassen. Frühere Modelle, beispielsweise von Dazzi et al. [1, 2], beschreiben die thermische Ausdehnung homogener Materialien, berücksichtigen jedoch nicht die laterale Auflösung. Spätere Erweiterungen [3, 4] integrieren Materialgrenzflächen, basieren jedoch auf idealisierten Randbedingungen, die in heterogenen Systemen selten erfüllt sind. Viele praktische Proben – etwa biologische Strukturen, Dünnschichten oder Verbundmaterialien – bestehen aus absorbierenden Domänen, die in eine größere Matrix eingebettet sind, was zu komplexen Signaltransduktionsmechanismen führt. Diese Einschränkungen verdeutlichen den Bedarf nach umfassenderen Modellen, die Probeninhomogenität, laterale Auflösung und realistische thermische Wechselwirkungen adäquat berücksichtigen – zentrale Herausforderungen, denen sich diese Arbeit widmet.

Im Rahmen dieser Dissertation werden mehrere Fortschritte in Theorie und Anwendung der AFM-IR vorgestellt. Zunächst wird ein analytisches Modell der Punktverteilungsfunktion (Point Spread Function, PSF) entwickelt, das wesentliche Einflussfaktoren wie Größe und Position des Absorbers, Eigenschaften der umgebenden Matrix sowie Parameter des Laserpulses berücksichtigt. Durch die Verwendung von Green'schen Funktionen

ermöglicht dieses Modell eine recheneffiziente und zugleich genaue Beschreibung der Signalentstehung und übertrifft dabei herkömmliche Finite-Elemente-Simulationen (FEM) in Bezug auf Rechenzeit und Interpretierbarkeit. FEM-Simulationen und experimentelle Validierungen bestätigen die Genauigkeit des Modells und zeigen auf, wie Parameter wie Pulsdauer, Repetitionsrate und interfacialer thermischer Widerstand die Signalintensität und Ortsauflösung beeinflussen. Das PSF-Modell liefert damit ein vertieftes Verständnis der AFM-IR-Antwort und dient als vielseitiges Werkzeug zur Optimierung experimenteller Konfigurationen.

Über die theoretischen Fortschritte hinaus untersucht diese Arbeit den Einfluss von Probengröße, -geometrie und Oberflächentopographie auf die AFM-IR-Signalerzeugung. Mithilfe moderner Nanofabrikation werden Proben mit definierten Absorberdimensionen und komplexen topographischen Strukturen hergestellt. Die Ergebnisse zeigen, dass insbesondere die Oberflächentopographie – vor allem bei dreidimensionalen Strukturen – das gemessene Signal maßgeblich beeinflusst. Diese Erkenntnisse sind entscheidend für die präzise Interpretation von AFM-IR-Daten, insbesondere in Anwendungsbereichen wie Nanoelektronik, Energiematerialien und biologischen Systemen, in denen komplexe Geometrien typisch sind.

Darüber hinaus werden neuartige optomechanische AFM-Sensoren vorgestellt, die optische Mikroringresonatoren mit freitragenden Cantilevern integrieren. Diese Sensoren erreichen eine bisher unerreichte Empfindlichkeit hinsichtlich Auslenkung und Kraft, mit Nachweisgrenzen im Sub-Femtometer- bzw. Pikonewton-Bereich. Die experimentelle Validierung bestätigt die überlegene Leistungsfähigkeit dieser Sensoren im Vergleich zu konventionellen AFM-Kantilevern. Die verbesserte Mikroringstruktur eröffnet vielfältige Anwendungen in der Materialcharakterisierung und in biologischen Studien. Die Kopplung optischer und mechanischer Komponenten stellt einen bedeutenden Fortschritt in der hochpräzisen Nanosensorik dar.

Weitere Verbesserungen der AFM-Sensortechnologie werden durch die Integration von Photonischen Kristallkavitäten mit freitragenden Cantilevern erreicht. Aufgrund ihrer hohen Qualitätsfaktoren und Resonanzeigenschaften ermöglichen diese Strukturen äußerst empfindliche Messungen von Kräften und Verschiebungen. Zusätzlich werden Designs mit Bragg-Gittern auf Mikrocantilevern untersucht, die auf Silicon-on-Insulator (SOI)-Substraten gefertigt und mithilfe von Multiphysik-Simulationen charakterisiert werden. Diese Simulationen koppeln mechanisch induzierte Brechungsindexänderungen mit elektromagnetischen Wellenmoden und ermöglichen hochpräzise, quantitative Messungen mit erweitertem Dynamikbereich. Die Umsetzung dieses neuartigen photonischen Transduktors erweitert den Anwendungshorizont der AFM-Technik insbesondere in Umgebungen,

in denen höchste Präzision erforderlich ist.

Indem diese Arbeit bestehende Lücken in der theoretischen Modellierung wie auch in der experimentellen Umsetzung von AFM-IR und optomechanischen Sonden adressiert, leistet sie einen bedeutenden Beitrag zur Weiterentwicklung der hochauflösenden Nano-Bildgebung und Sensorik. Die Integration neuartiger Modelle, innovativer Fertigungstechniken und optomechanischer AFM-Sonden eröffnet neue Möglichkeiten für die Forschung und Anwendung in der Nanotechnologie, Materialwissenschaft und Biomedizin.

# Acknowledgments

It is always difficult to fully express my gratitude to everyone who has helped and supported me during my PhD—there are so many, and I deeply worry I may forget someone. If that happens, please forgive me — and come find me, I'll buy you a beer.

First and foremost, I would like to express my deepest gratitude to my supervisors: **Georg Ramer**, **William Whelan Curtin**, and **Bernhard Lendl**.

At the start of my PhD, Georg was already someone I deeply admired—I told myself that my goal was to complete this journey having learned even 30% of what Georg knows. He guided me with complete openness, and his rigorous scientific attitude inspired me not only to become a better researcher but also to take full responsibility for my work. I am especially grateful for his thoughtful and thorough revisions of my papers and thesis.

I thank William for his kind support, care, and supervision from the very beginning to the end. Even when my ideas were not yet fully developed, he always encouraged me, and that encouragement gave me confidence and motivation.

My sincere thanks also go to Bernhard, who always understood and supported my research, enthusiastically sharing it with others and opening the door to many prestigious opportunities—conferences, summer school, secondment, and even post-PhD funding applications. It has been an honour to be mentored by three supervisors with different styles, all of whom believed in my work. It has been a great pleasure to work with them.

I would also like to thank **Pily**, who takes care of the group and is always ready to help—not just with administrative matters, but with genuine care for our well-being.

Special thanks go to my colleague **Margaux**, whose generous help during the thesis correction process made a real difference. Your careful reading, feedback, and support were invaluable, and all of your comments were thoughtful and made perfect sense.

I'm also deeply grateful to **Artem** and **Ufuk**, with whom I had the pleasure of conducting collaborative research. They helped me prepare and fabricate samples, perform experiments, and publish articles. Without their support, I could not have handled the combined workload of theory, experiments, and fabrication. Beyond being collaborators, they are also two of my closest friends—people I constantly turn to for help, and who never hesitate to offer their support.

To those who were not only colleagues but also close friends—who shared both happiness

and difficult times with me—**Alicja and Jesus**—thank you for your trust, your generous care, and for bringing light and laughter into my life. Thanks to **Nikolaus, Sebi** for the unforgettable memories from our trip to Budapest, and for your constant care and support.

I'm also grateful to all the members of the **CAVS** group (**Lena, Elisabeth, Lisa, Shilpa, Conny, Giovanna, Felix, Dominik, Daniel, Leo, Iskander, Daniela, Alex, Paul, Harald, Kathi, Nelson, Gustavo and his family**) and the **CAPPA** group (**Giulia, Savda, Cian, Samira, Tay, David, Maria, Hadi, Gautham, Gabriele, Davide, Jack, Jenita, Diego, Chinna, Vamsi**), including those I haven't mentioned by name. Your discussions, input, and camaraderie were constant sources of motivation and inspiration throughout this journey.

To my dear friends **Maria, Steven, Ran, Francesco, Katya, Alba, Rokas**, and **Hong**—thank you for standing by me during the most challenging times. I will never forget the times we spent chatting, playing games, having parties and hanging out, sharing countless moments of fun and laughter. Your support and understanding helped me stay focused and persevere.

I would also like to take a moment to remember my cousin, **ShiChun Liu**, who accompanied me throughout my childhood and cared for me like an elder brother. His presence shaped many parts of my life, and his support meant more than words can express. Sadly, he passed away on January 13, 2024, and is not here to share in this joyful milestone. I miss him deeply and hope he is now in a place free from pain.

I also wish to remember my college colleagues, **Anton Walsh** and **Marco Grande**, whose lives and spirits touched those around them. Though they are no longer with us, their memory remains a part of this journey.

Finally, my deepest gratitude goes to my **mum**, my **father** , and my **grandma**. Although they never had the opportunity to attend college themselves, their unwavering love, patience, and belief in me have been the foundation of everything I've achieved. They devoted their lives to giving me the opportunity to study abroad and pursue my dreams. This work would not have been possible without their constant support.

# List of publications

**Journals**

- "An Analytical Model of Label-Free Nanoscale Chemical Imaging Reveals Avenues towards Improved Spatial Resolution and Sensitivity", Zhang, Y.; Yilmaz, U.; Lukasievicz, G. V. B.; O'Faolain, L.; Lendl, B.; Ramer, G. *Proceedings of the National Academy of Sciences*, 122, e2403079122. (2025)
- "Experimental and Theoretical Insights into Nanoscale AFM-IR Imaging of Complex Heterogeneous Structures", Zhang, Y.; Yilmaz, U.; Vorobev, A.; Iadanza, S.; O'Faolain, L.; Lendl, B.; Ramer, G. submitted to *Analytical Chemistry*. (2025)
- "Single-Mode Ring Resonator-Based Optomechanical Transducers for Advanced Atomic Force Sensing", Zhang, Y.; Vorobev, A; Sam, S.; Badri, S. H; David, M.; Lendl, B.; Ramer, G.; O'Faolain, L., submitted to *ACS Photonics*. (2025)
- "Silicon Nitride Photonic Crystal-Cantilever Sensor for Quantitative Force and Displacement Measurements"
- "Novel insights into nanoscale surface displacement detection in polystyrene thin films using photothermal mirror- and atomic force microscopy-mid-IR spectroscopy", Yilmaz, U.; Lukasievicz, G. V. B.; Sehn, E.; Zhang, Y.; Astrath, N. G. C.; Ramer, G.; Lendl, B., *RSC Adv.* 2025,15, 9243-9253. (2025)

**Conference Proceedings**

- "Development of silicon nitride phase shifted Bragg grating cantilever for AFM-IR", Sam, S.; Zhang, Y.; Vorobev, A.; Foglini, D.; Kotlyar, M.; Iadanza, S.; Devarapu, G.C.R.; Ramer, G.; Lendl, B.; O'Faolain, *Conference: Integrated Optics: Devices, Materials, and Technologies XXIX*, DOI: 10.1117/12.3058169. (2025)
- "Design and Simulation of Cantilever Beam with a Bragg Grating based Optomechanical Senor for Atomic Force Microscopy in COMSOL", Zhang, Y.; O'Faolain., L; Ramer, G., *COMSOL Technical Papers and Presentations* https://www.comsol.com/paper/design-and-simulation-of-bragg-grating-based-optomechanical-sensor-for-atomic-force-microscopy-122231. (2023)

- "Image processing as basis for chemometrics in photothermal atomic force microscopy infrared imaging", Ramer, G.; Santos, A. C. V. D.; Zhang, Y.; Yilmaz, U.; Lendl, B., *Conference: Advanced Chemical Microscopy for Life Science and Translational Medicine 2023*, DOI: 10.1117/12.2651424. (2023)

**Conference Presentations**

- "Modelling thermal expansion as a point spread function for nanoscale chemical imaging", oral presentation, Young Analytical Chemists Forum 2022, Tulln(2022)
- "Towards a point spread function for nanoscale chemical imaging", oral presentation, EFNS 2022: 5th European Forum on Nanoscale IR Spectroscopy, Vienna(2022)
- "Towards a point spread function for nanoscale chemical imaging", poster presentation, 21st International Conference on Photoacoustic and Photothermal Phenomena, Bled(2022)
- "Controlling Spatial Resolution and Sensitivity in Nanoscale Chemical Imaging by Photothermal-Induced Resonance Spectroscopy", poster presentation, ANAKON 2023, Vienna(2023)
- "Design and Simulation of Cantilever Beam with a Bragg Grating based Optomechanical Senor for Atomic Force Microscopy in COMSOL", oral presentation, COMSOL Conference 2023, Munich(2023)
- "Controlling Spatial Resolution and Sensitivity in Nanoscale Chemical Imaging by Photothermal-Induced Resonance Spectroscopy", oral presentation, C-Pass-CONFERENCE ON PHOTONICS FOR ADVANCED SPECTROSCOPY AND SENSING, Castellaneta Marina(2023)
- "Ring resonator based optomechanical transducers for atomic force sensing", poster presentation, 8th ePIXfab Silicon Photonics Summer School, Ghent(2023)
- "3D simulation of AFM-IR Nanoscale Chemical imaging", poster presentation, The Infrared and Raman Discussion Group (IRDG) Meeting 2023, London(2023)
- "3D Nanoscale Chemical Imaging and Simulation in AFM-IR", oral presentation, 1st European Meeting on InfraRed Nanospectro-Imaging, Paris(2024)
- "Advancing nanoscale chemical imaging for subsurface complex structures via AFM-IR", oral presentation, 22nd International Conference on Photoacoustic and Photothermal Phenomena, Coimbra(2024)
- "Advancing AFM-IR with Ultra-High Frequency Probes and Optomechanical Photonic Crystal Nanobeam Cavity Sensors", poster presentation, 19th International Workshop on Nanomechanical Sensing (NMC), Vienna(2024)

# Abbreviations

| | |
|---|---|
| **AFM** | atomic force microscopy |
| **AFM-IR** | atomic force microscopy-infrared spectroscopy |
| **HS-AFM** | High-speed atomic force microscopy |
| **FEM** | finite element method |
| **FDTD** | Finite-Difference Time-Domain method |
| **FFT** | fat Fourier transform |
| **FTIR** | Fourier transform infrared |
| **FWHM** | full width at half maximum |
| **IR** | Infrared |
| **NIR** | Near-infrared |
| **MIR** | Mid-infrared |
| **FIR** | Far-infrared |
| **PMMA** | poly(methyl methacrylate) |
| **QCLs** | quantum cascade lasers |
| **SNOM** | Scanning near-field optical microscopy |
| **PTIR** | Photothermal induced resonance |
| **PTS** | Photothermal spectroscopy |
| **PAS** | Photoacoustic spectroscopy |
| **PTM** | photothermal mirror |
| **SEM** | scanning electron microscope |

| | |
|---|---|
| **O-PTIR** | optical photothermal infrared |
| $Si_3N_4$ | silicon nitride |
| **SOI** | silicon-on-oxide |
| **Si** | silicon |
| **CVD** | chemical vapor deposition |
| **SNR** | signal-to-noise ratio |
| **EC-QCL** | external cavity-quantum cascade laser |
| **CW** | continuous wave |
| **ATR** | attenuated total reflection |
| **PID** | proportional-integral-derivative |
| **DMT model** | Derjaguin-Müller-Toporov model |
| **OPO** | optical parametric oscillator |
| **PLL** | phase locked loop |
| **PSBGs** | phase-shifted Bragg gratings |
| **CMT** | coupled mode theory |
| **PhCs** | Photonic crystals |
| **FSR** | free spectral range |
| **PBGs** | photonic bandgaps |
| **TIR** | total internal reflection |
| **PSF** | point spread function |
| **ODE** | ordinary differential equation |
| **PDEs** | partial differential equations |

# Symbols

| | |
|---|---|
| $A$ | absorbance |
| $d$ | path length |
| $\epsilon$ | molar extinction coefficient |
| $\alpha$ | absorption coefficient |
| $\alpha_z$ | thermal expansion coefficient |
| $P$ | laser power |
| $\rho$ | density |
| $C_p$ | heat capacity |
| $V$ | volume of interaction |
| $f_{IR}$ | laser modulation frequency |
| $f$ | focal length of a lens |
| $Q$ | quality factor |
| $Q_O$ | optical quality factor |
| $Q_M$ | mechanical quality factor |
| $\lambda$ | wavelength |
| $h$ | Plank's constant |
| $c$ | speed of light |
| $\nu$ | Poisson ratio |
| $E$ | Young's modulus |
| $E_{eff}$ | effective Young's modulus |
| $W$ | waveguide width |
| $\Delta W$ | grating width |
| $n_{eff}$ | effective refractive index |
| $n_g$ | group index |
| $I$ | moment of inertia of the beam cross-section |
| $\omega_n$ | angular frequency of the cantilever |
| $\omega_{IR}$ | excitation frequency of the IR laser |
| $\zeta$ | damping ratio |
| $\eta$ | damping coefficient |

# Contents

# 1. Introduction of the thesis

This thesis is part of the **OPTAPHI** project, funded by the European Union's Horizon 2020 research and innovation programme under the Marie Skłodowska-Curie grant agreement No.860808. Within the framework of Project 1.5, the aim is to combine integrated photonics and infrared spectroscopy to enable the next generation of nanoscale molecular imaging techniques.

This project has two main goals:

1. **Designing a novel nanophotonics-enhanced transducer for near-field IR imaging**
   The design leverages integrated photonics to measure photothermal expansion with an atomic force microscope (AFM) coupled to a pulsed, tunable mid-IR laser. The newly developed transducer, which achieves high sensitivity through integrated photonic detection, is pivotal for enabling spectroscopy at the monolayer or even single-molecule level. However, ensuring the transducer's robustness, dynamic range, and material compatibility with AFM-IR imaging poses a significant engineering challenge. The devices are fabricated using the cleanroom facilities at MTU and the Tyndall National Institute, and subsequently characterized at TU Wien.

2. **Gaining a deeper understanding of photothermal and photoacoustic signal generation**
   This objective focuses on studying the emergence and propagation of photothermal and photoacoustic waves following IR absorption in materials, with the goal of optimizing sensor performance. Surprisingly, the detailed processes by which these waves are generated and propagate are not yet fully understood in the literature. Developing a comprehensive understanding is crucial for advancing this technique. As part of this project, detailed mathematical studies on the generation and propagation of signal waves are conducted at TU Wien.

To achieve the project's goals, this thesis addresses two main perspectives.

1. **The first involves designing and fabricating novel nanophotonic AFM transducers, for which three different types of optomechanical AFM probes have been developed**:
   a) Ring-resonator-based AFM probes on a silicon-on-insulator (SOI) platform.

b) Photonic-cavity-based AFM probes on a silicon nitride (SiN) platform.

c) Integrated Bragg gratings on microcantilevers on both SOI and SiN platform.

These works are conducted in collaboration with OPTAPHI members Artem S. Vorobev, Gautham Paikkath and Savda Sam, all from the MTU research group.

2. **The second involves developing one- or three- dimentional photothermal and thermalelastic models in cylindrical and cartesian coordinates, by using Green's function method**.

   a) In the cylindrical coordinates, a point spread function (PSF) model has been developed for AFM-IR, which is verified with finite element method (FEM) simulations and validated with AFM-IR experiments. This model accounts for sample properties, sample geometries, absorber size, position, and laser parameters.

   b) Based on the PSF model, this thesis further investigates the impact of sample size, geometry, and surface topography on AFM-IR signal generation. Advanced nano-fabrication techniques are employed to create samples with controlled absorber sizes and complex surface features to experimentally confirm theoretical models.

   c) This thesis develops one-dimensional models to enhance the understanding of signal generation and detection in photothermal-based techniques.

This thesis is organized as:

- **Chapter 1** provides a comprehensive theoretical overview, beginning with the fundamental principles of Infrared (IR) spectroscopy and atomic force microscopy (AFM). It then introduces atomic force microscopy-infrared spectroscopy (AFM-IR), describing how AFM can be combined with infrared spectroscopy to enable nanoscale chemical characterization and imaging. Additionally, the chapter offers a conceptual explanation of photonic resonators.

- **Chapter 2** presents detailed theoretical derivations and analytical models relevant to the thesis. It begins with comprehensive derivations of analytical solutions for photothermal, thermoelastic and photoacoustic phenomena, which describes signal generation in photothermal-based AFM-IR techniques.

- **Chapter 3** summarizes the key publications resulting from this thesis work. Each publication is introduced with context, highlighting its main contributions, the motivation behind the study, and its relevance within the broader scope of the thesis.

# 2. Theory and Background

## 2.1. Infrared Spectroscopy and Imaging

### 2.1.1. Principles

This section is informed by the works of Barbara H. Stuart [5], John M. Chalmers and Peter R. Griffiths [6], James M. Thompson [7], and Thomas Mayerhöfer [8]. Readers seeking a more in-depth treatment of vibrational and infrared spectroscopy, as well as wave optics in these contexts, are encouraged to consult these references.

IR spectroscopy examines the interaction between electromagnetic waves and matter in the wavelength range of 0.8 µm to 300 µm.This interaction occurs through the absorption of IR light, which excites molecular vibrations, rotations, and lattice modes. The IR spectrum is typically divided into three regions, classified by wavelength and their corresponding wavenumbers, as follows:

- Near infrared (0.8 µm to 2.5 µm), 14 000 $\mathrm{cm}^{-1}$ to 4000 $\mathrm{cm}^{-1}$
- Mid infrared (2.5 µm to 25 µm), 4000 $\mathrm{cm}^{-1}$ to 400 $\mathrm{cm}^{-1}$
- Far infrared (25 µm to 300 µm), 400 $\mathrm{cm}^{-1}$ to 10 $\mathrm{cm}^{-1}$

The energy of light is inversely proportional to its wavelength, therefore, shorter wavelengths correspond to higher energy. This relationship is described by the equation:

$$E = hc/\lambda \tag{2.1}$$

where $E$ is the energy of light, $h$ is the Planck's constant, $c$ is the speed of light, and $\lambda$ is the wavelength.

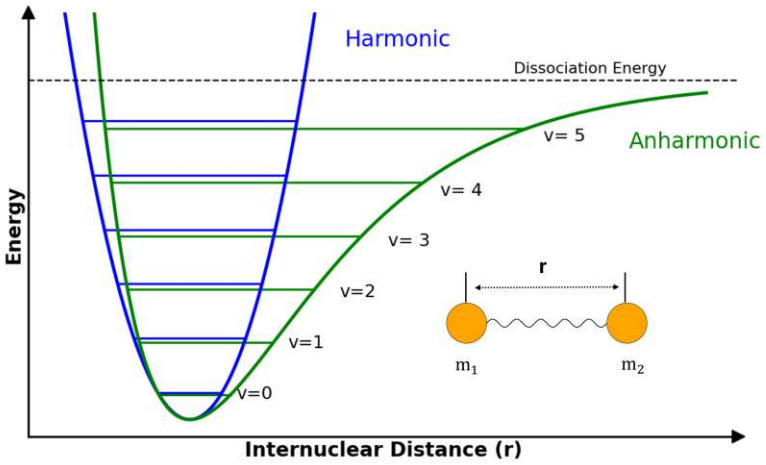


**Figure 2.1.:** A potential energy diagram displaying the harmonic oscillator approximation (blue parabola) superimposed with the anharmonic Morse potential (green curve).

In the IR range, the photon energy excites molecular vibrations, allowing the analysis of vibrational modes that reflect the underlying molecular structures. However, this energy is insufficient to break chemical bonds or induce electronic transitions.

Basic properties of molecular vibrations can be explained using the simple diatomic oscillator model, where two atoms are treated as point masses connected by a spring. The fundamental vibrational frequency ($\nu$) of this oscillator can be calculated as:

$$\nu = \frac{1}{2\pi}\sqrt{\frac{k}{\mu}} \tag{2.2}$$

Here, $k$ is the force constant of the bond, representing the stiffness of the "spring" (bond strength). $\mu$ is the reduced mass, calculated as $\mu = \frac{m_1 m_2}{m_1+m_2}$, where $m_1$ and $m_2$ are the masses of the two atoms. This model describes vibrational modes such as stretching (changing the bond length) or bending (changing the bond angle).

Higher-order vibrational energy $E_v$ of a simple harmonic oscillator can be described as [9]:

$$E_v = h\nu(v + \frac{1}{2}) \tag{2.3}$$

where $v = 0, 1, 2...$ is the vibrational quantum number, representing the mode number. In this equation, the term $\frac{1}{2}$ accounts for the zero-point energy, which is the minimum energy of the oscillator even in its ground state ($v = 0$).

The harmonic approximation, depicted as blue curves in Fig. 2.1, models the potential energy of the oscillator as a symmetric parabolic shape. In this model, only transitions with $\Delta v = \pm 1$ are allowed [9], and transitions between the vibrational ground state and the first excited state ($v = 1$) are referred to as fundamental transitions.

Mid-infrared (MIR) spectroscopy detects fundamental vibrational transitions of functional groups within a sample. The energy differences between these vibrational states determine the specific frequencies of light absorbed. These absorption frequencies correspond to the characteristic vibrational modes of various bond types [5], such as $CH_2$ rocking vibrations of alkanes at 730 $cm^{-1}$ or C-C stretching at 1400 $cm^{-1}$. This makes MIR spectroscopy an essential tool for identifying and analyzing molecular groups/functions/composition in a sample.

In contrast, the Near-infrared (NIR) region enables the study of overtones and harmonic or combination vibrations. Overtones occur when a molecule transitions from the ground state to an excitation level above the first state ($v > 1$), producing a series of integer multiples of the fundamental frequency 2.2 [10]. These actual transitions can be described using an anharmonic (Morse-type) potential function, which accounts for deviations from the ideal harmonic oscillator model at higher energy states. This anharmonic behavior is

illustrated in Fig. 2.1 as green curves, where the potential energy is approximated by the following equation [9]:

$$E_v = h\nu(v + \frac{1}{2}) + h\nu\hat{x}(v + \frac{1}{2})^2 \tag{2.4}$$

where $\hat{x}$ is the anharmonic constant. Non-fundamental vibrations typically produce weaker absorption bands, resulting in lower peak intensities in the NIR range compared to the MIR range.

On the other hand, the Far-infrared (FIR) region is commonly used to study lattice vibrations and other collective low-energy excitations in solid materials [11]. These modes are typically not accessible in the NIR and MIR regions, making FIR spectroscopy particularly valuable for investigating solid-state dynamics and crystal structure.

The position of IR absorption bands in the spectrum, typically expressed in wavenumbers ($\mathrm{cm}^{-1}$), is determined by the the atoms involved, the nature of their bonds and molecular structure. The wavenumber ($\tilde{\nu}$) of the molecular vibration band is related to the vibrational frequency ($v$) of the molecular given by the following expression:

$$\tilde{\nu} = \frac{v}{c_0} \tag{2.5}$$

where $c_0$ is the speed of light in the vacuum.

According to Eq. 2.2 and 2.5, the expression for the wavenumber of the band can be rewritten as:

$$\tilde{\nu} = \frac{1}{2\pi c_0}\sqrt{\frac{k}{\mu}} \tag{2.6}$$

From Eq. 2.6, we observe that the position of the vibrational band is influenced by three key variables:

- The wavenumber increases with greater bond strength, represented by the force constant $k$. Stronger bonds vibrate at higher frequencies.

- The wavenumber is inversely related to the reduced mass $\mu$ of the vibrating atomic pair. A smaller reduced mass results in a higher vibrational frequency.

### 2.1.2. Fourier Transform Infrared Spectroscopy

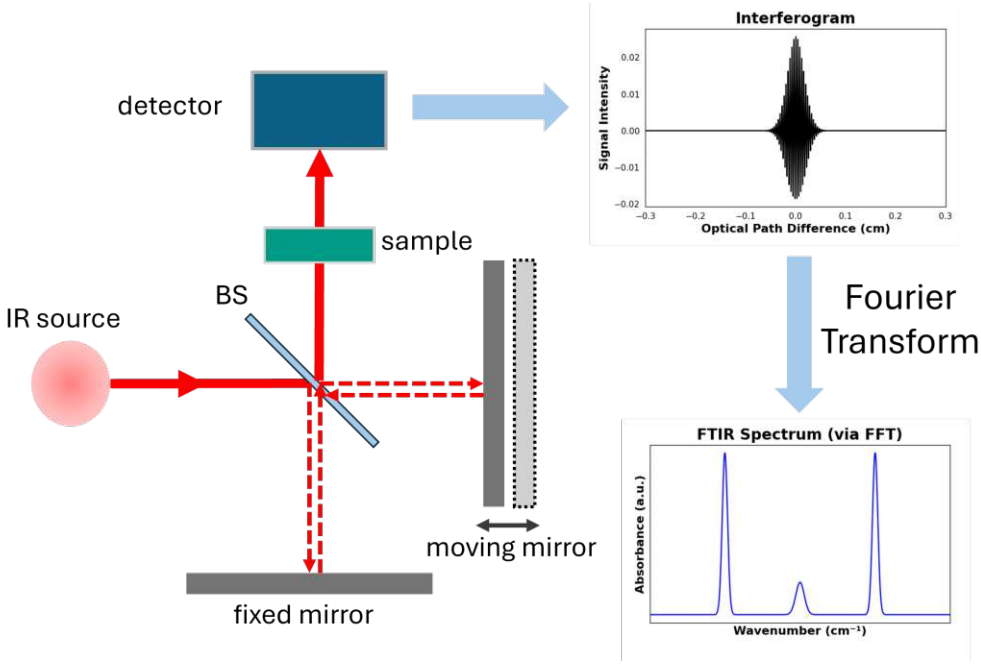


**Figure 2.2.:** schematic of FTIR spectrometer

Fourier transform infrared (FTIR) spectrometer is currently the predominant instrument used for MIR absorption spectroscopy. FTIR spectroscopy [9] employs an interferometer to simultaneously collect data over a wide range of wavelengths. The basic principle of this interferometer is illustrated in Fig. 2.2. A broad-spectrum IR light source emits radiation that is directed through a beam splitter. Half of the beam is sent to a fixed mirror, while the other half is directed to a mirror that moves at a constant velocity. These two beams are reflected and recombined, creating a path length difference ($\delta$) that generates an interference pattern due to constructive and destructive interference. At wavenumber ($\tilde{\nu}$), the intensity ad the detector is given by [9]:

$$I'(\delta) = 0.5I(\tilde{\nu})(1 + \cos 2\pi\tilde{\nu}\delta) \tag{2.7}$$

where $I'(\delta)$ is the intensity of the beam at the detector, $\delta$ represents the optical path difference. It can be seen that $I'(\delta)$ is composed of a constant (DC) component equal to $0.5I(\tilde{\nu})$ and a modulated (AC) component equal to $0.5I(\tilde{\nu})\cos 2\pi\tilde{\nu}\delta$. Only the AC component is important in spectrometric measurements, as it contains the spectral information. This modulated component is generally referred to as the interferogram, $I(\delta)$, is given by:

$$I(\delta) = 0.5I(\tilde{\nu})\cos 2\pi\tilde{\nu}\delta \tag{2.8}$$

The resulting data is processed using a Fourier transform, which produces an absorption spectrum that shows the absorption intensity across different wavenumbers.

There are several other ways to obtain IR spectra, which are generally categorized into two main approaches: direct and indirect techniques. Direct techniques measure changes in light intensity, phase shifts [12, 13] or changes in the polarization [14, 15, 16] after the incident IR light interacts with the sample. Indirect techniques, on the other hand, measure effects that occur in the sample or the surrounding medium as a result of IR absorption. Each of these techniques has its own strengths and weaknesses, which will be discussed in the following sections.

### 2.1.3. Direct Techniques

In direct IR measurements, the signal arises from intrinsic changes in the IR light due to its interaction with the sample—without the need for external transducers or probes. These techniques can be broadly categorized based on the nature of the detected optical signal: intensity change, phase shift, or polarization change. This classification offers insight into the underlying detection mechanisms and helps guide the selection of suitable methods for different material systems and experimental objectives.

To measure intensity changes, techniques such as transmission IR spectroscopy, reflection–absorption IR spectroscopy, and attenuated total reflection (ATR) spectroscopy are commonly employed. These methods generally fall under the umbrella of absorption spectroscopy, where IR light is attenuated due to vibrational transitions within the sample.

To detect phase shifts, techniques such as phase-resolved Fourier transform infrared (FTIR) spectroscopy and infrared dispersion spectroscopy are used. These approaches exploit interferometric or dispersive methods to resolve time- or frequency-dependent changes in the phase of IR light.

#### Absorption spectroscopy

Absorption spectroscopy, a type of direct measurement technique, measures changes in light intensity and is the most commonly used method in MIR spectroscopy. It quantifies the amount of light absorbed by a sample across a range of wavelengths following the interaction of light with the sample. In transmission-based measurements, the sample is positioned between the IR light source and the detector.

According to the Beer-Lambert law, the absorbance ($A$) is directly proportional to the concentration of the analyte ($c$), the pathlength ($d$) and the molar extinction coefficient

($\epsilon$) of the sample [17]:

$$A(\tilde{\nu}) = -\log_{10}\left(\frac{I(\tilde{\nu})}{I_0(\tilde{\nu})}\right) = \epsilon(\tilde{\nu}) \cdot d \cdot c \tag{2.9}$$

where $I_0(\tilde{\nu})$ and $I(\tilde{\nu})$ are the intensity of light before and after the sample, respectively. This relationship enables the determination of the concentration of analytes in a sample by analyzing the absorbance at specific wavelengths.

The Beer-Lambert law is an empirical and widely accepted principle for quantitative analysis; however, it tends to break down at very high concentrations [8]. At these levels, the relationship between absorbance and concentration becomes nonlinear due to molecular interactions [18], as well as changes in the solution's refractive index.

While direct IR spectroscopy is widely used for its simplicity and ability to provide direct vibrational information, it suffers from several limitations. One key drawback is its susceptibility to scattering effects, particularly in heterogeneous, rough, or particulate samples. Scattering can distort the baseline, reduce spectral contrast, and complicate quantitative analysis. In addition, strong absorption or optically thick samples can lead to signal saturation, while very thin films may produce signals below the detection limit [9, 19, 20]. Furthermore, direct techniques are fundamentally limited by the diffraction limit of IR light, restricting spatial resolution to several micrometers and making them unsuitable for nanoscale or localized measurements. These challenges have motivated the development of indirect techniques that circumvent many of these limitations by detecting secondary effects instead of relying on direct IR transmission or reflection.

### 2.1.4. Indirect Techniques

Indirect IR techniques offer several key advantages over conventional direct methods. Most notably, they enable nanoscale spatial resolution, far beyond the diffraction limit of mid-infrared light, making them ideal for studying heterogeneous materials, nanostructures, and ultra-thin films. Additionally, these methods can be applied to optically opaque or strongly scattering samples, which are often inaccessible to traditional transmission or reflection-based IR spectroscopy. Indirect techniques also support localized measurements, such as probing a single point on a surface, and can be integrated with complementary modalities—such as atomic force microscopy—to provide correlated topographical and chemical information [21, 22, 23, 24].

In indirect IR techniques, the signal intensity does not arise from the direct detection of absorbed IR light, but rather from a secondary physical response—such as thermal expansion, photothermal deflection, or scattered near-field radiation—induced by IR absorption. Consequently, the signal strength depends not only on the absorption cross-section of the sample but also on its thermal conductivity, mechanical properties, probe sensitivity, and local field enhancement. While this can introduce complexity in quantitative interpretation, it also enables high sensitivity to localized vibrational features, even in samples where direct detection would be limited by weak absorption or optical diffraction.

In this work, we primarily focus on three representative indirect techniques: photothermal spectroscopy and photoacoustic spectroscopy. Each of these methods leverages a distinct physical mechanism to convert IR absorption into a measurable signal, offering versatile platforms for probing chemical and structural information in challenging or nanoscale systems.

#### Photothermal Spectroscopy

Photothermal spectroscopy (PTS) is a form of absorption spectroscopy that detects density changes in a sample resulting from the conversion of absorbed optical energy into heat. Unlike direct techniques for IR absorption, where scattering and reflection can cause losses, these effects do not generate photothermal signals. Consequently, PTS provides precise measurements of optical absorption in scattering solutions and at interfaces [25]. This accuracy makes it particularly valuable for surface and solid absorption studies, as well as research in scattering media [26].

PTS typically involves two key components: an excitation laser (most commonly used mid-IR pulsed tunable QCLs), which induces a temperature change in the sample, and a probe, which detects either the corresponding changes in the refractive index or the surface deformation caused by thermal expansion at certain IR wavelength. The photothermal sig-

nals are influenced by the sample's thermodynamic and energy transfer properties, making this technique useful for analyzing the thermal structure of materials.

The photothermal signal is generally proportional to the temperature change ($\Delta T$) in the sample. This temperature change, in turn, is directly proportional to factors such as the laser power ($P$), sample's absorption coefficient ($\alpha$) and the optical pathlength ($d$). Conversely, it is inversely proportional to the sample's density ($\rho$), heat capacity ($C_p$), laser modulation frequency ($f_{laser}$) and volume of interaction ($V$), as illustrated in the following equation [27]:

$$\text{Photothermal Signal } \propto \Delta T \propto \frac{P(\tilde{\nu}) \cdot \alpha(\tilde{\nu}) \cdot d}{\rho \cdot C_p \cdot V \cdot f_{laser}} \tag{2.10}$$

Therefore, the higher the power or energy, the stronger the resulting signal. For this reason, the external cavity-quantum cascade laser (EC-QCL) [28], with its high power (up to the watt range), narrow linewidth and a broad tuning range, is an ideal source for MIR spectroscopy. Recent studies have demonstrated the versatility and precision of the EC-QCL in photothermal spectroscopy (PTS) for IR measurements, successfully applying it to both liquid [29] and solid [30] phases.

In PTS, the probe used to detect signals can be either light-based optical probe or atomic force microscopy (AFM)-based mechanical probe, each designed for specific principles and applications. Light-based probes, typically visible laser focus on the sample surface, detect changes induced by optical heating, which alters the medium's optical properties, such as refractive index or optical path length. The change of real part of refractive index ($\Delta n$) due to temperature change is given by:

$$\Delta n = \frac{\partial n}{\partial T} \cdot \Delta T \tag{2.11}$$

where $\frac{\partial n}{\partial T}$ represents the rate of change of the refractive index with respect to temperature. These alterations can cause variations in the laser beam's focus or deflection. Conversely, cantilever-based probes quantify mechanical responses, including thermal expansion, providing complementary insights into the sample's properties.

For the AFM-based methods, which will be elaborated upon in Section 2.3 focusing on atomic force microscopy-infrared spectroscopy (AFM-IR), provides the key advantage of achieving nanoscale spatial resolution in chemical imaging, an accomplishment unattainable with light-based probes. For related methods, such as photo-induced force microscopy, readers are encouraged to consult the review paper by Sifat et al. [31].

### Photoacoustic Spectroscopy

Photoacoustic spectroscopy (PAS) [25] detects pressure waves generated in a sample following the absorption of light and resulting phtothermal expansion. Although both pho-

toacoustic and photothermal spectroscopies arise from the same underlying photothermal effects, they are traditionally regarded as distinct methods. PTS focuses on monitoring temperature-induced changes in the refractive index, often employing a probe laser. In contrast, PAS detects pressure variations caused by modulated continuous wave (CW) [32] or pulsed laser [33] heating of the sample. Light absorption in a localized area generates heat waves, which subsequently induce pressure waves as the thermal energy causes localized expansion and contraction in the sample. These pressure waves propagate through the sample at frequencies corresponding to the light source modulation. Typically, a microphone or another pressure transducer is used to detect the resulting acoustic waves. Pulsed excitation is generally preferred over CW excitation due to its higher photoacoustic signal-to-noise ratio (SNR), even though CW lasers are more cost-effective than EC-QCL lasers [32].

Thus far, we have explored the principles of IR spectroscopy. Beyond this, IR microscopy has gained widespread application by combining the chemical specificity of IR spectroscopy with spatial resolution. This powerful combination enables the detailed analysis of complex samples, offering spatially resolved chemical insights across a wide range of fields. However, like other optical microscopes, it relies on far-field imaging through optical systems that are fundamentally constrained by optical diffraction. The limitations of IR microscopy techniques spatial resolution will be discussed in the following section.

### 2.1.5. Spatial Resolution of IR Microscopy

In far-field optical imaging, light is assumed to propagate as a plane wave, with a sufficiently long distance from the radiating source to the aperture. Additionally, the aperture size is considered much larger than the wavelength of light. Due to the wave nature of light, diffraction occurs at the aperture, producing a symmetric pattern at the center of the detector. This phenomenon is well described by Fraunhofer diffraction theory [34].

The Fraunhofer diffraction pattern arises when a beam of light is focused through a lens of focal length $f$ and passes through a circular aperture with a diameter $D$ (Fig. 2.3). The resulting pattern of the focused spot is [35]:

$$I(x,y) = I_0 \left[ \frac{2J_1(\pi D\rho/\lambda f)}{\pi D\rho/\lambda f} \right], \quad with \quad \rho = \sqrt{x^2+y^2} \tag{2.12}$$

where $x$ and $y$ are spatial coordinate, $\rho$ is the radius of the spot. $I_0$ is the peak intensity power of the input light, $J_1(\pi D\rho/\lambda D)$ is the Bessel function of order one, and $\lambda$ represents the wavelength of the light. The first minimum of the intensity distribution occurs at the position of the first zero of the Bessel function $J_1(\pi D\rho/\lambda f)$, which can be numerically calculated as approximately 3.8317. The first zero of the intensity distribution-corresponding

to the first dark ring in the Airy pattern [35]-is often used to define the resolution-limiting radius of the system:

$$\rho_s = \frac{3.8317}{\pi}\lambda\frac{f}{D} \approx 1.22\lambda\frac{f}{D} \tag{2.13}$$

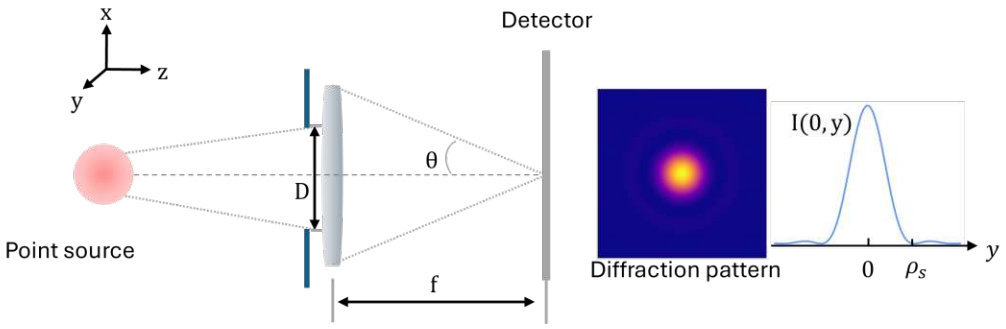


**Figure 2.3.:** Schematic of a diffraction pattern produced by a point light source in an optical microscope. A point source is considered, and its light is diffracted by the optical components of the microscope objective, resulting in a circularly symmetric intensity distribution at the detector. This pattern, known as an Airy disk, defines the fundamental limit of resolution in far-field optical systems due to diffraction.

The number of photons collected by the objective depends on the size of the objective aperture angle ($\theta$) and the refractive index ($n$) of the surrounding medium. As shown in the diagram in Fig. 2.3, the numerical aperture (NA) of the objective is defined as:

$$\mathrm{NA} = \mathrm{n}\sin\theta = \mathrm{n}\sin\left(\arctan\left(\frac{D}{2fn}\right)\right) \approx \frac{D}{2f} \tag{2.14}$$

The numerical aperture specifies the maximum acceptance angle of the objective. Substituting Eq. 2.14 into Eq. 2.13, we can rederive the expression for the focused spot radius. This is commonly known as the Rayleigh criterion [34], which describes the minimum distance ($\Delta x$) between two point sources that is required to resolve them as two distinct points in an optical system. This concept is illustrated in Fig. 2.4. According to this criterion, two sources are considered resolvable when the central maximum of one Airy disk [35] coincides with the first minimum of the other. The minimum distance is given by:

$$\Delta x = 0.61\frac{\lambda}{\mathrm{NA}} \tag{2.15}$$

From Eq. 2.15, a fundamental limitation of mid-IR microscopy becomes evident: the mid-IR wavelength range-typically between 2.5 µm and 25 µm are too large to resolve nanoscale features. For a commonly used numerical aperture of 0.6 [36], the diffraction-limited spatial resolution directly proportional to the wavelength.

The spatial resolution can be improved by increasing the acceptance angle of the objective through the use of a wider lens and a shorter working distance. Recently, PIKE Technologies released new reflective objectives with enhanced optical designs and numerical apertures ranging from 0.7 to 0.8 [37]. These high-NA objectives deliver significantly improved spatial resolution, reaching values below 3 µm for the 40x objective—surpassing the performance of commonly used lower-NA objectives and approaching the theoretical diffraction limit. In addition to enhanced resolution, they also provide superior signal-to-noise ratios (SNR) compared to standard objectives of similar magnification in conventional FTIR microscopes. As a result, these objectives offer substantial performance advantages in both transmission and transflection geometries, even when used with standard thermal IR sources [37].

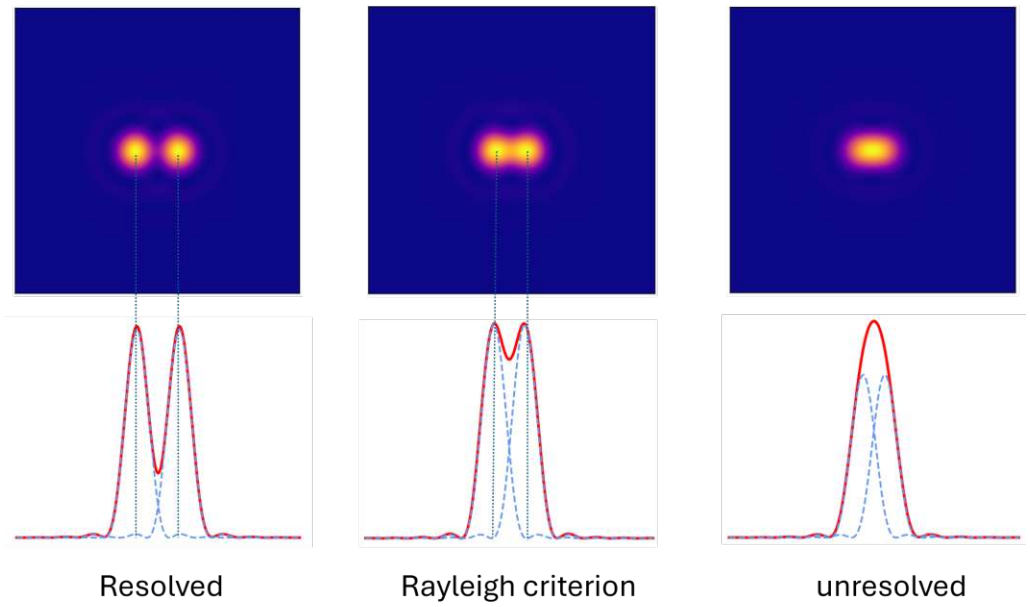


**Figure 2.4.:** Images of two point sources positioned at various distances demonstrate whether they are resolvable, meet the Rayleigh criterion, or remain unresolvable. The point spread functions of the two independent sources are shown in blue, while their combined intensity profile is represented in red.

Despite these advancements, the resolution of IR microscopy remains constrained by both wavelength and numerical aperture. A promising approach to further enhancing spatial resolution is increasing the refractive index of the internal reflection element, as utilized in attenuated total reflection (ATR) microscopy [38]. This technique involves placing a high-refractive-index material in direct contact with the sample surface. Germanium ($Ge$), with a refractive index of approximately $n \approx 4$, is the highest-refractive-index

IR-transparent material available. Incorporating germanium can improve lateral resolution by a factor of four [39]. However, even with this enhancement, the achievable resolution remains limited to the micrometer scale, falling short of the nanoscale resolution required for many emerging applications. Consequently, the diffraction limit imposed by mid-IR wavelengths continues to restrict spatial resolution in conventional far-field spectroscopy.

Recent studies [40, 41] have introduced advanced experimental setups that use a visible laser as a probe to detect refractive index changes and photothermal expansion induced by infrared absorption-a technique known as optical photothermal infrared (O-PTIR) (Optical Photothermal Infrared) spectroscopy. This approach enables sub-micrometer spatial resolution, which is notably independent of the IR excitation wavelength, thereby overcoming the diffraction limit inherent to conventional mid-IR optics. For a comprehensive review of this method, readers are referred to the work by Prater et al. [42].

High spatial resolution chemical imaging with IR spectroscopy is non-destructive and label-free, making it a powerful tool for advancing research in materials science, nanotechnology, and biology. AFM-based IR spectroscopy and microscopy techniques, such as Photothermal induced resonance (PTIR) or AFM-IR, have been developed to achieve nanoscale spatial resolution, allowing in-depth analysis of molecular and structural properties that traditional methods cannot capture. In the following sections, we will explore the fundamentals of AFM and AFM-IR, highlighting their potential and applications.

## 2.2. Atomic Force Microscopy

AFM is a scanning probe technique used for high-resolution imaging of surface morphology, as well as for mechanical characterization at the nanoscale. It is capable of achieving spatial resolutions down to the atomic level. This technique was first introduced by Binnig, Quate, and Gerber in 1986 [43]. Unlike conventional optical and electron microscopes, scanning probe microscopes measure the sample's surface with a probe (typically sharp tip) that physically moves across it, rather than relying on the focusing of photons or electrons to gather information.

Specifically, AFM measures the interaction forces between the probe tip and the sample surface, such as van der Waals forces [44, 45], thermal expansion [22, 46], electrical forces [47], magnetic force interactions [48], single molecule [49, 50] and more. AFM does not necessarily require a vacuum and can be operated in air, liquid, or controlled atmospheres [48, 51].

This non-destructive technique is capable of analyzing a wide range of materials, from soft biological tissues and polymers to hard crystalline structures. Its versatility has established AFM as an indispensable tool in nanotechnology [52], materials science [53, 46], and biology [11, 54, 55, 50]. It has become indispensable for high-resolution and rapid morphological imaging, and excels in nanoscale characterization of properties such as thermal [56], electrical [57], mechanical [58], and chemical properties [59].

### 2.2.1. Instrumentation

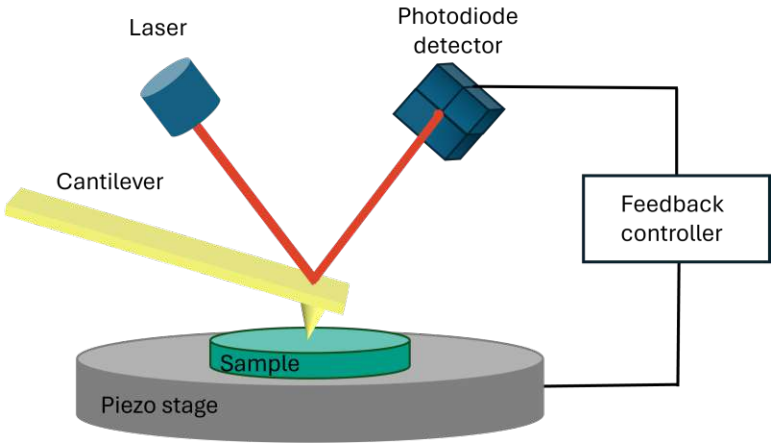


**Figure 2.5.:** Simplified schematic of the main components of an AFM setup.

A typical AFM setup is illustrated in Fig. 2.5, highlighting its key components: the cantilever, deflection laser, four-quadrant photodetector, piezoelectric stage, and feedback

controller. The cantilever is mounted on a fixed support at one end, with a sharp tip located at its free end. This tip interacts with the sample surface, which is typically positioned on a piezo stage capable of precise movement in the x, y, and z directions.

A core aspect of AFM is force transduction, which in conventional cantilever-based AFM probes is typically achieved using the beam-deflection method. This widely used approach involves focusing a diode laser onto the reflective backside of the cantilever, with the reflected beam directed onto a position-sensitive photodetector to monitor cantilever deflection in response to tip–sample interactions. The laser beam reflects off the cantilever and is directed toward the center of a four-quadrant photodiode detector, which tracks the position of the laser spot. As the AFM tip scans across the sample surface, variations in surface height cause the cantilever to bend upward or downward, depending on the local topography. This bending results in a change in the slope of the cantilever at the point where the laser is focused, which in turn deflects the reflected beam. This deflection is detected by the difference in voltages between the upper and lower parts of the photodetector. As the distance between the cantilever and photodetector is large, a small movement of the cantilever causes a large change in the laser spot position at the detector. This geometric amplification makes the beam-deflection method highly sensitive to subtle height variations at the sample surface. As a result, AFM instruments typically achieve vertical (axial) resolution down to the nanometer scale [51], enabling precise surface profiling and nanoscale imaging.

Another key component of the AFM system is the feedback controller, which is responsible for maintaining a constant interaction force between the probe and the sample surface. When the probe registers an increase in force—typically due to the cantilever encountering a raised feature on the sample—the feedback system instructs the piezoelectric actuator to retract the probe slightly. Conversely, if the force decreases, the probe is brought closer to the surface. This real-time adjustment ensures that the force between the tip and the sample remains constant throughout the measurement.

During scanning, the z-axis movements of the piezoelectric stage required to maintain this constant force are recorded at each (x, y) position. These recorded height values are then used to reconstruct the surface topography of the sample, providing a high-resolution three-dimensional image of the surface.

The feedback controller, primarily a proportional-integral-derivative (PID) controller, is widely used to regulate the scanner and maintain the optimal force between the sample and the probe by continuously adjusting their relative distance [60, 61]. It combines proportional (P) control for immediate error correction, integral (I) control to address cumulative errors, and derivative (D) control to predict and mitigate overshoot, thereby enhancing sta-

bility, precision, and automation while reducing reliance on manual adjustments. However, the D term is rarely used due to its sensitivity to noise, which can destabilize the system. As a result, most AFMs rely on PI control, though the term "PID" is still commonly used for convenience. The PID is governed by equation [62]:

$$Z_v = P \times Z_{err} + I \times \int Z_{err} dt + D \times \frac{dZ_{err}}{dt} \tag{2.16}$$

where $dt$ represents the time difference, $Z_{err}$ denotes the error signal, defined as the difference between the setpoint and the measured input signal. In contact mode, the input is typically the cantilever deflection (measured as a voltage difference) [63, 64], while in tapping mode, it corresponds to the oscillation amplitude (also in volts) [65]. The controller output $Z_v$ represents the output signal from the controller, typically measured in volts. The combined PID output-based on $Z_{err}$-is applied to the z-axis piezoelectric actuator, which adjusts the vertical position of the sample or probe to restore the interaction force to its target value. For effective tracking performance, the PID parameters (I and P gains) must be properly tuned for each experiment [66], due to variations in cantilever properties, sample type, and imaging conditions. As a result, parameter optimization process becomes a critical aspect of AFM operation [67].

### 2.2.2. AFM Cantilevers

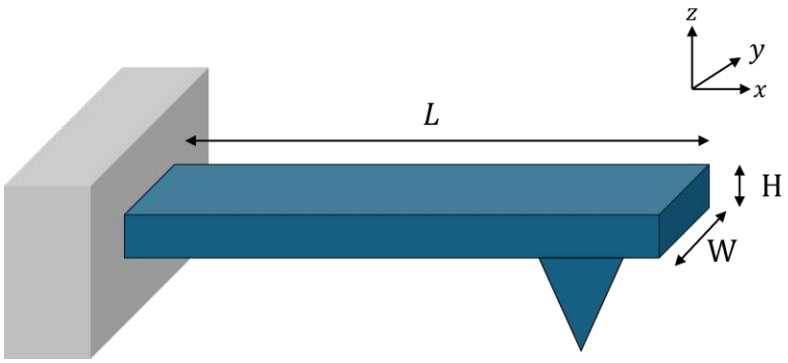


**Figure 2.6.:** Sketch of a beam-shape cantilever.

The key component of AFM setup is the cantilever, whose length, width and material directly influence its mechanical frequencies and spring constant. These parameters, in turn, determine the cantilever's force sensitivity, response time, and suitability for different imaging modes. The most commonly used cantilever shape is beam-shaped. A sketch of the cantilever is shown in Figure 2.6. The cantilever can be modeled using the Euler-Bernoulli

beam theory [68]:

$$EI\frac{\partial^4 z(x,t)}{\partial x^4} + \eta\rho A\frac{\partial z(x,t)}{\partial t} + \rho A\frac{\partial^2 z(x,t)}{\partial t^2} = 0 \tag{2.17}$$

where $z(x,t)$ is the transverse displacement of the cantilever along the beam axis x over time, $E$ is the Young's modulus of the beam material, $I = W \cdot H^3/12$ is the moment of inertia of the beam cross-section, $\eta$ is a damping coefficient, $\rho$ is the density, and $A = W \cdot H$ is the cross-sectional area of the beam.

For a damped cantilever, the damping factor $\eta$ is not negligible and is mainly caused by two factors: (1) structural damping, which depends on the geometry and internal friction of the cantilever, and (2) environmental damping, caused by interaction with the surrounding medium, such as air or liquid [69].

$z(x)$ is the deflection from the rest position of the length element at $x$. $\partial z/\partial x$ is the beam slope and $EI\frac{\partial^3 z}{\partial x^3}$ is the shear force at position $x$. To solve the equation, we assume a modal solution of the form:

$$z(x,t) = \phi(x)q_n(t) \tag{2.18}$$

where $\phi(x)$ represents the mode shapes of the beam, corresponding to the deformation profiles of the cantilever during its various vibrational modes. These mode shapes are determined by the boundary conditions, and $q_n(t)$ the time-dependent amplitude of each mode. Substituting the Eq. 2.18 into Eq. 2.17 yields:

$$EI\frac{\partial^4 \phi(x)}{\partial x^4}q_n(t) + \eta\rho A\phi(x)\frac{\partial q_n(t)}{\partial t} + \rho A\phi(x)\frac{\partial^2 q_n(t)}{\partial t^2} = 0 \tag{2.19}$$

Dividing by $\phi(x)q_n(t)$:

$$\frac{EI}{\rho A}\frac{\partial^4 \phi(x)}{\partial x^4}\frac{1}{\phi(x)} = -\frac{1}{q_n(t)}(\eta\frac{\partial q_n(t)}{\partial t} + \frac{\partial^2 q_n(t)}{\partial t^2}) = \omega^2 \tag{2.20}$$

where $\omega^2$ is a separation constant that emerges from the method of separation of variables.

Thus, the spatial equation becomes:

$$\frac{\partial^4 \phi(x)}{\partial x^4} = \frac{\rho A\omega^2}{EI}\phi(x) = k^4\phi(x) \tag{2.21}$$

where $k$ is a characteristic wavenumber, which defines the spatial frequency of the mode shape and is related to the beam's mechanical and geometrical properties. The general solution for $\phi(x)$ is [70]:

$$\phi(x) = C_1\cosh(kx) + C_2\sinh(kx) + C_3\cos(kx) + C_4\sin(kx) \tag{2.22}$$

where $C_1, C_2, C_3, C_4$ are constants determined by boundary conditions. $\cosh(kx)$ and $\sin(kx)$ represent exponentially growing and decaying terms, while $\cos(kx)$ and $\sin(kx)$ represent oscillatory motion.

In the case where one side of the beam is clamped and the other side is free without contact (typical configuration of the cantilever in an AFM), the boundary conditions are:

$$\begin{aligned} BC1: &\quad \phi(0) = 0 &&\text{(no displacement at fixed end x =0)} \\ BC2: &\quad \left.\frac{d\phi}{dx}\right|_{x=0} = 0 &&\text{(no slope at x =0)} \\ BC3: &\quad \left.\frac{d^2\phi}{dx^2}\right|_{x=L} = 0 &&\text{(no moment at free end x =L)} \\ BC4: &\quad \left.\frac{d^3\phi}{dx^3}\right|_{x=L} = 0 &&\text{(no shear force at x =L)} \end{aligned} \tag{2.23}$$

Applying BC1 and BC2, we get: $C_1 = -C_3$ and $C_2 = -C_4$. Then applying BC3 and BC4, we get:

$$\begin{aligned} C_1(\cosh(kL) + \cos(kL)) + C_2(\sinh(kL) + \sin(kL)) = 0 \\ C_1(\sinh(kL) - \sin(kL)) + C_2(\cosh(kL) + \cos(kL)) = 0 \end{aligned} \tag{2.24}$$

These two conditions form a characteristic equation that determines the eigenvalue $k_n$:

$$\cos(k_n L)\cosh(k_n L) + 1 = 0 \tag{2.25}$$

The first five roots of this transcendental equation are approximately $k_n L = 1.875, 4.694, 7.855, 10.996, 14.137$. These values define the eigenmodes of the system and can be used to plot the corresponding mode shapes of the beam.

The deflection $\phi(x)$ of each mode can be described by equation:

$$\phi(x) = C_1 \left[ (\cosh(k_n x) - \cos(k_n x)) - \frac{\cosh(k_n L) + \cos(k_n L)}{\sinh(k_n L) + \sin(k_n L)} (\sinh(k_n x) - \sin(k_n x)) \right] \tag{2.26}$$

where $C_1$ is the vibrational amplitude. The first five mode shapes derived from Eq.2.26 are shown in Fig.2.7.

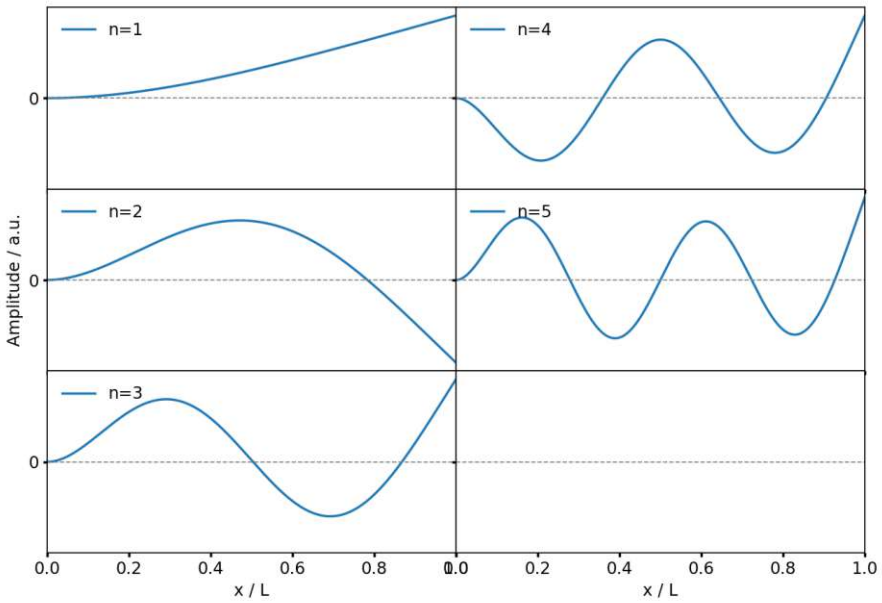


**Figure 2.7.:** Simulated first five mode shapes based on Eq. 2.26.

While the mode shapes of the AFM cantilever can be determined analytically using Eq.2.26, they can also be obtained numerically using finite element method (FEM) simulations. The first five vibrational modes computed via FEM are shown in Fig.2.8, providing both validation and a more flexible framework for modeling non-ideal geometries or boundary conditions.

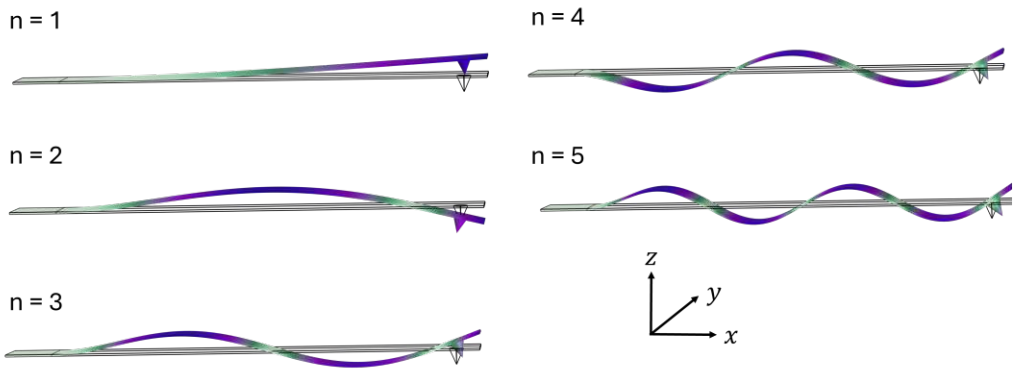


**Figure 2.8.:** FEM simulations were conducted to analyze the first five resonance modes of the cantilever, providing insights into its vibrational characteristics and dynamic behavior.

The time-dependent equation of motion can be derived from Eq. 2.20:

$$\frac{\partial^2 q_n(t)}{\partial t^2} + \eta \frac{\partial q_n(t)}{\partial t} + \omega_n^2 q_n(t) = 0 \tag{2.27}$$

where $\omega_n$ denotes the angular frequency of the $n$th vibrational mode. Assuming a solution of the form $q_n(t) = Ae^{\lambda t}$, which we substitute into Eq. 2.27:

$$\lambda^2 + \eta\lambda + \omega_n^2 = 0 \tag{2.28}$$

For the damped case, we have solution for $\lambda$:

$$\lambda = \frac{-\eta \pm \sqrt{\eta^2 - 4\omega_n^2}}{2} \tag{2.29}$$

If we replace the damping coefficient with the damping ratio $\eta = 2\zeta\omega_n$, Eq. 2.29 can be rewritten as:

$$\lambda = -\zeta\omega_n \pm \sqrt{1-\zeta^2}\omega_n \tag{2.30}$$

Finally, the time-dependent solution for the damped harmonic oscillation of the beam displacement-corresponding to its oscillatory motion (i.e., vibrating up and down), is given by:

$$q_n(t) = Ae^{-\zeta\omega_n t}\cos(w_d t + \varphi) \tag{2.31}$$

where $w_d = \sqrt{1-\zeta^2}\omega_n$ [71] is the damped natural frequency, $\varphi$ is the initial phase angle of the oscillation.

The spring constant ($k_c$) of the beam-shape cantilever can be calculated from the static deflection when a force acts at $x = L$,

$$k_c = \frac{EI}{3L^3} \tag{2.32}$$

Quantifying the damping factor of a cantilever can be challenging, so a common and practical approach is to determine it indirectly by measuring the quality factor (Q) of the cantilever. For a harmonic oscillator, the Q factor is defined as the ratio of the resonance frequency ($\omega$) to the full width at half maximum (FWHM) of the resonance peak ($\Delta\omega$), expressed as $Q = \omega/\Delta\omega$. Alternatively, the quality factor can be related to the damping ratio $\zeta$, with the relation $Q = 1/2\zeta$ for systems with slight damping ($\zeta \ll 1$) [71]. A high Q factor indicates that the cantilever dissipates energy slowly, enabling it to sustain oscillations over a longer duration in a steady-state regime. Conversely, a low Q factor implies rapid energy dissipation, resulting in quickly damped oscillations.

In this section, the theoretical modeling of the cantilever was discussed, with a focus on its mechanical behavior, vibrational modes, and the governing equations that describe

its dynamic response. While these models provide critical insights into the cantilever's performance, the actual behavior of the system also strongly depends on the material properties of the cantilever itself. Parameters such as Young's modulus, density, internal damping, and thermal conductivity directly influence its resonance frequency, stiffness, and sensitivity. Additionally, fabrication techniques—including lithography, etching, and material deposition—play a crucial role in defining the cantilever's geometry, surface quality, and mechanical stability. The following section introduces commonly used cantilever materials and outlines important fabrication considerations that inform the design of high-performance AFM probes.

### 2.2.3. AFM Cantilever Materials

The most commonly used materials for AFM cantilevers are silicon (Si) and silicon nitride ($Si_3N_4$). These materials are typically fabricated using silicon-on-oxide (SOI) wafers [72] or $Si_3N_4$ deposited on silicon wafers [73] by lithography. Low-stress $Si_3N_4$ is particularly advantageous for cantilever fabrication, as its thickness can be precisely controlled through chemical vapor deposition (CVD) [74, 75]. Additionally, $Si_3N_4$ is resistant to etching in common etchants, further enhancing its suitability for cantilever manufacturing [73]. $Si_3N_4$ tips can be fabricated integrally with $Si_3N_4$ cantilevers, or alternatively, carbon tips can be deposited onto $Si_3N_4$ cantilevers using electron beam deposition [76].

Despite its advantages, $Si_3N_4$ is less suitable for precise tip manufacturing, resulting in AFM tips that are typically less sharp and accurate compared to those made from Si. To address this limitation, hybrid AFM probes have been introduced, featuring a silicon tip integrated onto a $Si_3N_4$ cantilever [77]. These hybrid designs leverage the flexibility and low stiffness of $Si_3N_4$ cantilevers while retaining the sharpness and precision of silicon tips, offering a balanced solution for high-performance applications.

### 2.2.4. AFM Operating Mode

AFM can be operated in various modes depending on the environment and the specific application. These modes are designed to adapt to different sample properties and measurement goals, and can be implemented in vacuum, air, or liquid environments. A comprehensive overview of AFM operating modes and their physical principles can be found in the review by Garcia and Pérez [65].

In the scope of this work, only the two most commonly used modes in ambient (air) conditions are relevant: Contact Mode and Tapping Mode. These modes differ in how the tip interacts with the sample surface and how the forces are measured and controlled. Each offers unique advantages and trade-offs in terms of resolution, sample compatibility,

and mechanical interaction.

### Contact Mode AFM

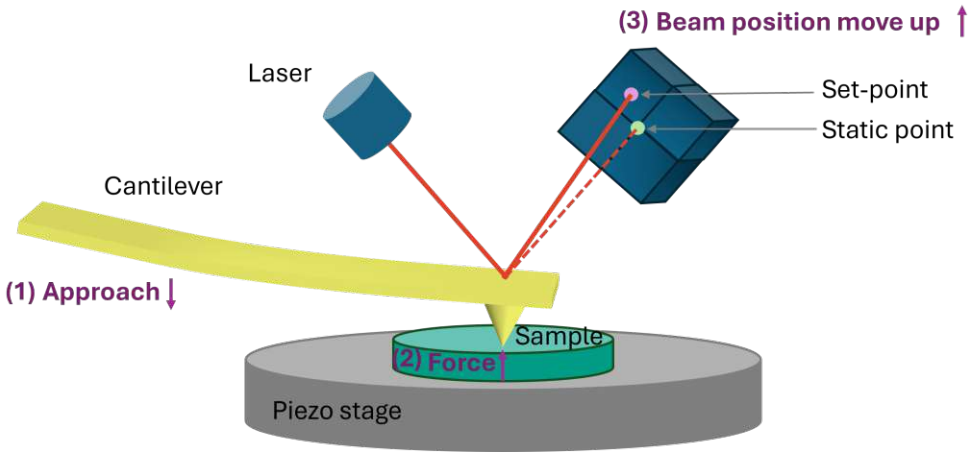


**Figure 2.9.:** Cantilever bending occurs as a result of repulsive forces between the tip and the sample in the contact mode.

Contact mode is the simplest and most intuitive method for operating an AFM. In this mode, the probe maintains continuous contact (force) with the sample while raster scanning the surface. Feedback is achieved by monitoring the cantilever deflection. In air, contact mode requires cantilever, with low spring constant (typically ranges from 0.01 to 1 N m [78]) to reduce the risk of damaging soft or delicate samples.

In contact mode, a PID controller continuously adjusts the height of the sample's piezo stage to maintain a constant set-point. This ensures stable interaction between the AFM tip and the sample surface. Repulsive forces arising from the tip–sample contact bend the cantilever. As the tip scans across the surface, these forces vary with changes in surface height. By tracking the cantilever's deflection during raster scanning, the system reconstructs the sample's topography, as illustrated in Fig. 2.9.

A commonly used model to describe the tip-sample interaction between the cantilever and the surface is the Derjaguin-Müller-Toporov model (DMT model) [79]. In the DMT model, the tip can, to some extent, indent into the sample, as presented in the formulation found in [80]:

$$F_{ts} = \begin{cases} -\frac{HR_{tip}}{6a_0^2} + \frac{4}{3}E_f\sqrt{R_{tip}}(a_0 - z)^{3/2} & \text{if z} < a_0 \\ -\frac{HR_{tip}}{6z^2} & \text{if z} \geq a_0 \end{cases} \tag{2.33}$$

where $H$ is the Hamaker's constant, $a_0$ is the effective interatomic distance, $R_{tip}$ is the radius of the cantilever tip, and $E_f$ is the effective Young's modulus. The effective Young's

modulus depends on both the sample's and tip's Poisson's ratio and Young's modulus according to the following formula:

$$\frac{1}{E_f} = \frac{1-\nu^2}{E} + \frac{1-\nu_s^2}{E_s} \tag{2.34}$$

where $\nu$ and $\nu_s$ are Poisson's ratios for tip and sample, respectively, and $E$ and $E_s$ are Young's moduli for tip and sample, respectively.

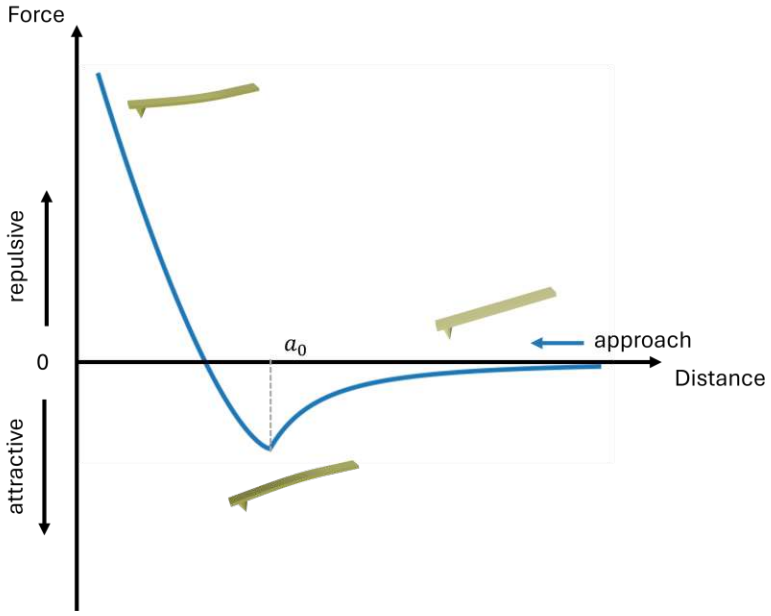


**Figure 2.10.:** Force-distance curve for contact mode in AFM.

The interaction between the tip and sample is characterized by the force-distance curve described by Eq. 2.33 (Fig. 2.10), which illustrates the variation of the force between the tip and the surface with cantilever-sample distance. As the tip approaches the sample, weak attractive forces (negative) initially dominate. However, when the interatomic distance ($a_0$) becomes sufficiently small, Pauli repulsion between the electron clouds of the tip and sample starts to increase. This repulsion counterbalances the attraction, reaching an equilibrium at an interatomic distance, roughly equivalent to the length of a chemical bond [81].

As illustrated in Fig. 2.9, the contact-mode imaging process begins as the cantilever tip approaches the sample surface [step (1)]. Once the tip comes within a distance shorter than the typical interatomic spacing, repulsive forces rapidly overcome the attractive van der Waals forces, marking the transition into the repulsive interaction regime [step (2)]. At this point, the total interatomic force becomes positive, indicating direct atomic contact. This interaction bends the cantilever upward, causing the reflected laser beam to shift

position on the photodetector [step (3)]. This beam deflection is continuously tracked to reconstruct the sample's topography.

Since the tip remains in continuous contact with the surface, it operates within the repulsive regime of the force–distance curve. This constant contact leads to significant lateral forces and friction, which can cause damage to the sample—particularly in the case of soft or fragile materials [82]. To avoid such damage, tapping mode was introduced as an alternative imaging technique. In this technique, the cantilever oscillates near its resonance frequency, making intermittent contact with the surface. This reduces both normal and lateral forces, making it ideal for imaging soft or fragile samples with high resolution. This mode will be introduced in the following section.

### Tapping Mode AFM

In tapping mode AFM, the cantilever is driven ,e.g. by a piezoelectric actuator, to oscillate near its resonance frequency, causing the sharp probe tip to move up and down in a sinusoidal motion. Unlike in contact mode, the tip only intermittently touches the sample surface during each oscillation cycle – hence the name tapping mode. This intermittent contact significantly reduces both normal and lateral forces, minimizing friction and sample deformation. As a result, tapping mode is particularly advantageous for imaging soft, fragile, or loosely bound samples, while still maintaining high spatial resolution. The operating principle is illustrated in Figure 2.11

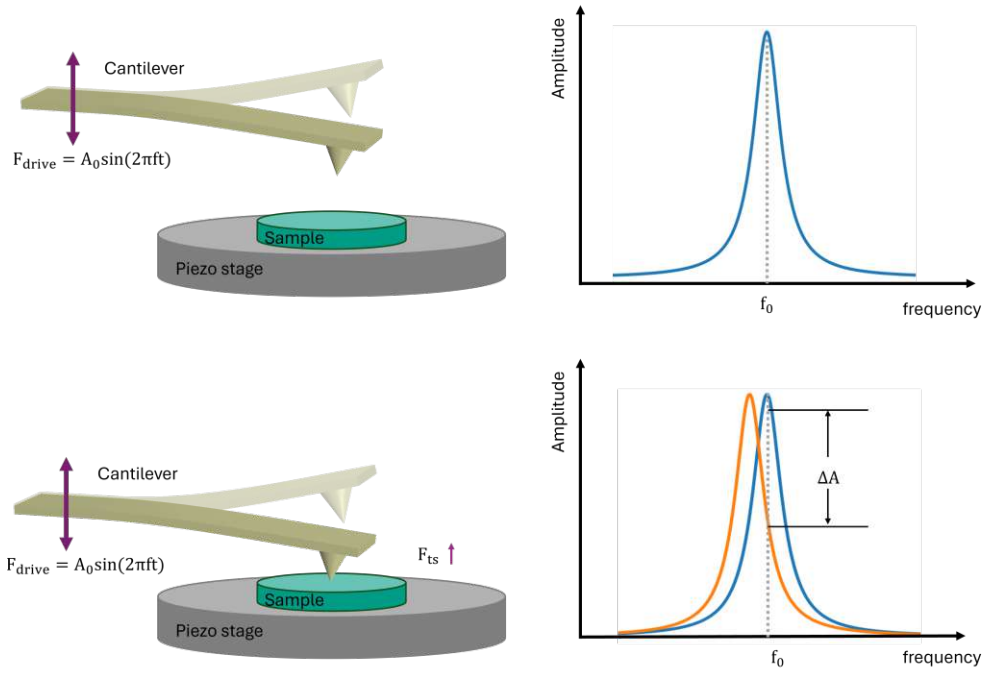


**Figure 2.11.:** Simplified schematic of tapping mode AFM. When the cantilever oscillates at the frequency $f_{drive}$ above the sample surface, its resonance peak is centered at $f_0$ (blue curve). As the tip approaches the sample, repulsive tip–sample interactions shift the resonance to lower frequencies (orange curve), reducing the oscillation amplitude by ($\Delta A$). This amplitude change reflects the nonlinear force regime the tip experiences as it transitions from long-range attractive to short-range repulsive forces.

The dynamics of a tapping-mode AFM cantilever can be modeled using the Euler-Bernoulli beam equation [83], assuming that one end is fixed while external forces act

on its free end (e.g. the tip). Thus, Eq. 2.17 is modified as:

$$EI\frac{\partial^4 z}{\partial x^4} + \eta\rho A\frac{\partial z}{\partial t} + \rho A\frac{\partial^2 z}{\partial t^2} - \delta(x-L)[F_{ts}(z) + F_{drive}(t)] = 0 \tag{2.35}$$

where $\delta(x-L)$ is the Dirac delta function, representing a force applied exclusively at the free end of the cantilever. $F_{ts}(z)$ denotes the tip-sample interaction force, which can be modeled using the DMT-model, as described in Eq. 2.33. On the other hand, $F_{drive}(t)$ corresponds to the external driving force acting on the fixed end of the cantilever, and is usually modeled as a harmonic function, $F_{drive}(t) = A_0 \sin 2\pi f_{drive} t$, where $A_0$ represents the driving amplitude, and $f_{drive}$ denotes the driving frequency, which usually close to the free resonance frequency ($f_0$) of the cantilever. In Eq. 2.35, other forms of damping—such as internal and hydrodynamic damping—are not considered. However, these effects are crucial for accurately modeling cantilever dynamics, particularly in determining the quality factor, and have been analyzed in detail in [80].

In tapping mode, the cantilever oscillates close to its resonant frequency ($f_0$) at a constant predefined amplitude. As the tip approaches the sample and begins interacting with it, the resonance frequency shifts towards higher or lower frequencies within each oscillation cycle, depending on whether the interactions are in the attractive or repulsive force regime, respectively [81]. These frequency shifts generate positive and negative changes in oscillation amplitude ($\Delta A$) of the cantilever as the tip moves through the attractive and repulsive force regions.

In tapping mode, the cantilever oscillation amplitude ($\Delta A$) is used as a feedback signal for the PID, which adjusts the z scanner. This adjustment compensates for variations in amplitude, which correspond to changes in the distance between the tip and the sample[62].

The main advantage of tapping mode is that the tip only makes brief contact with the surface, which significantly reduces the lateral forces that could potentially damage the sample [84, 85]. However, a key limitation of tapping mode is that it does not directly measure tip–sample interaction forces. As a result, it cannot directly quantify mechanical properties such as stiffness, elastic modulus, or viscoelastic coefficients [86], and it makes reconstructing the full force curve from standard tapping-mode data challenging [87]. Instead, it relies on oscillation amplitude, which is detected by a lock-in amplifier that provides an averaged response.

## 2.3. Atomic Force Microscopy–Infrared Spectroscopy

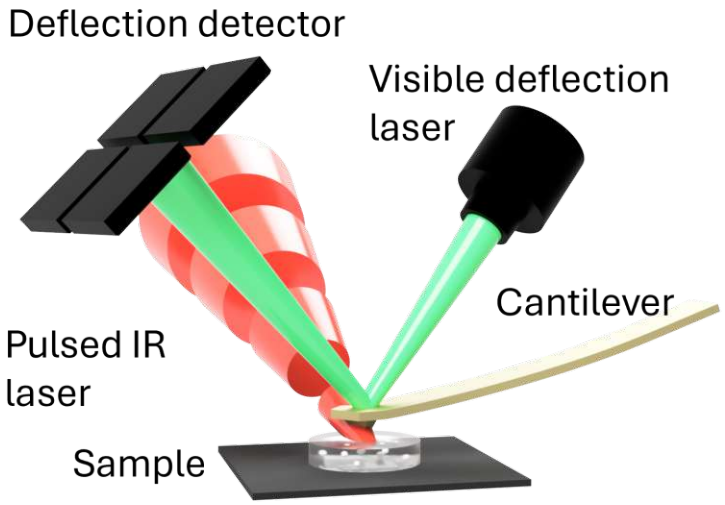


**Figure 2.12.:** Sketch illustrating a top-down illumination configuration AFM-IR setup. The sample is placed on a piece of silicon (gray) and illuminated from the top with a pulsed, tunable, infrared beam (red).

AFM-IR, also commonly referred to as PTIR, is a near-field technique combining an AFM and IR spectroscopy. This technique enables nanoscale spatial resolution chemical imaging, spatial resolution independent of the IR wavelength [46, 22, 88], allowing for chemical analysis at resolutions several orders of magnitude below the diffraction limit [89, 90, 50, 91, 92]. First introduced by Dazzi et al. in 2005 [93], AFM-IR has since gained recognition as a powerful tool for nanoscale chemical characterization [46, 94, 22, 21, 23, 24].

A typical AFM-IR setup consists of a pulsed and tunable IR laser focused on the sample's surface at the location of the AFM cantilever tip (see Figure 2.12). The technique operates by detecting the thermal expansion of the sample region beneath the tip following the absorption of pulsed IR radiation [22, 23]. When the sample absorbs the laser energy, it undergoes periodic temperature variations, leading to photothermal and photoacoustic effects [21]. This thermal expansion is rapide (give timescale) and induces localized surface displacement, which in turn excites the AFM cantilever in a oscillatory motion. The resulting cantilever motion is monitored and the oscillation amplitude is directly, with its amplitude directly correlating to the sample's wavelength-dependent absorption coefficient and thermal expansion properties [89]. This mechanical detection mechanism enables

AFM-IR to achieve high-resolution chemical imaging of local infrared absorption down to 10 nm [95].

The fundamental principles of AFM-IR are widely recognized, and its effectiveness in chemical imaging is well established. This technique has been applied across various fields, including materials science [96, 97], biological systems [54, 50, 98], as well as photonics, perovskite materials [99], and semiconductor research [22, 100].

### 2.3.1. AFM-IR Signal

The initial theoretical framework for AFM-IR signal generation and transduction was developed by Dazzi et al. [1]. The model assumed a homogeneous sample illuminated by a single laser pulse, without considering the sample geometry. The cantilever was modeled as a damped Euler-Bernoulli beam, and the amplitude of the measured AFM-IR signal was found to be proportional to the local IR absorption, described as the imaginary part of the refractive index at a given wavelength ($Im[n(\lambda)]$). Four proportionality constants define this relationship, as expressed by the equation:

$$\tilde{S_n}(\omega_n, \lambda) = H_m H_{AFM} H_{oopt} H_{th} \frac{Im[n(\lambda)]}{\lambda} \tag{2.36}$$

With:

- **The mechanical contribution** $H_M$ is proportional to the spring constant $k_z$, the thermal expansion coefficient $\alpha_{sph}$, and the radius of the spherical-shape sample $a$, as expressed by the following equation:

$$H_m = k_z \alpha_{sph} a \tag{2.37}$$

- **The cantilever contribution** $H_{AFM}$ depends on the properties of the AFM cantilever.

$$H_{AFM} = \frac{1}{\eta \omega_n} \left[\cos(\alpha)\delta x + \sin(\alpha) H\right] \frac{D}{\rho A L} \left[\frac{\partial g_n(x)}{\partial x}\Big|_{x=L}\right]^2 \tag{2.38}$$

  In the equation, $\omega_n$ represents the angular resonance frequency of the $n$-th mode, $\alpha$ is the cantilever angle, $[\cos(\alpha)\delta x + \sin(\alpha) H]$ describes the influence of the cantilever's angle on the signal, $H$ is the tip height and $\delta x$ is the distance from the tip to the end of the cantilever. The length of the cantilever illuminated by the laser spot is denoted by $D$, and $g_n(x)$ represents the spatial distribution of the mode, while the term $\frac{\partial g_n(x)}{\partial x}\Big|_{x=L}$ corresponds to the slope of the cantilever at its tip.

- **The optical contribution** $H_{\text{opt}}$ accounts for the incident optical power of the IR laser, represented by the squared electric field amplitude ($|E_{\text{inc}}|^2$), and the real part of the

sample's refractive index, Re($n$). Under the assumption of weak sample absorption and within the electric dipole approximation - valid when the absorber's size is much smaller than the wavelength - the optical contribution is given by:

$$H_{opt} = \frac{Re(n)}{(Re(n)^2 + 2)^2} c\epsilon_0 |E_{inc}|^2 \tag{2.39}$$

where $c$ is the speed of light and $\epsilon_0$ is the permittivity of free space.

- **The thermal contribution** $H_{\text{th}}$ depends on the thermal properties of the sample and is characterized by two distinct expressions, depending on the relationship between the laser pulse duration ($t_p$) and the thermal relaxation time ($\tau_{\text{relax}}$):

$$H_{th} = \begin{cases} \frac{6\pi}{\rho_{sph} C_{sph}} t_p (\frac{t_p}{2} + \tau_{relax}) & for \quad t_p \ll \tau_{relax} \\ \\ \frac{4\pi a^2}{\kappa} \left[ \frac{\sin(\frac{\omega_n t_p}{2})}{\omega_n} \right] & for \quad \tau_{relax} \ll t_p \end{cases} \tag{2.40}$$

where $\rho_{sph}$ is the density of the sample, $\kappa$, is the effective heat conductivity and $C_{sph}$ its thermal capacity. In the case of a shorter single pulse laser ($t_p \ll \tau_{relax}$), the sample does not have enough time to reach to the equilibrium state during the pulse. Instead, the energy is deposited rapidly, causing a transient temperature rise in the sample. Once the pulse ends, the system gradually returns to its initial temperature, following an exponential decay determined by $\tau_{relax} = (\rho_{sph} C_{sph} a^2 / 3\kappa)$ [1]. Conversely, when the pulse duration is much longer than the thermal relaxation time of the sample ($\tau_{relax} \ll t_p$), the system has sufficient time to reach thermal equilibrium during the pulse. As a result, the temperature increase and reach a plateau at which it remains stable while the pulse is on. Once the pulse is turned off, the temperature drops rapidly, producing a nearly rectangular thermal response [1].

To detect the photothermal signal, AFM-IR employs detection schemes similar to those used in conventional AFM. In contact-mode AFM-IR (either ringdown [93] or resonance-enhanced detection [101]), the probe maintains continuous contact with the sample at a fixed deflection setpoint. Alternatively, tapping-mode AFM-IR [95] utilizes an heterodyne detection scheme, where the cantilever's resonant excitation is modulated by the nonlinear interaction between its oscillation and the sample's photothermal expansion. This approach effectively suppresses background signals and enhances spatial resolution. The specific mechanisms of each detection scheme will be discussed in the following sections.

### 2.3.2. Contact Mode AFM-IR

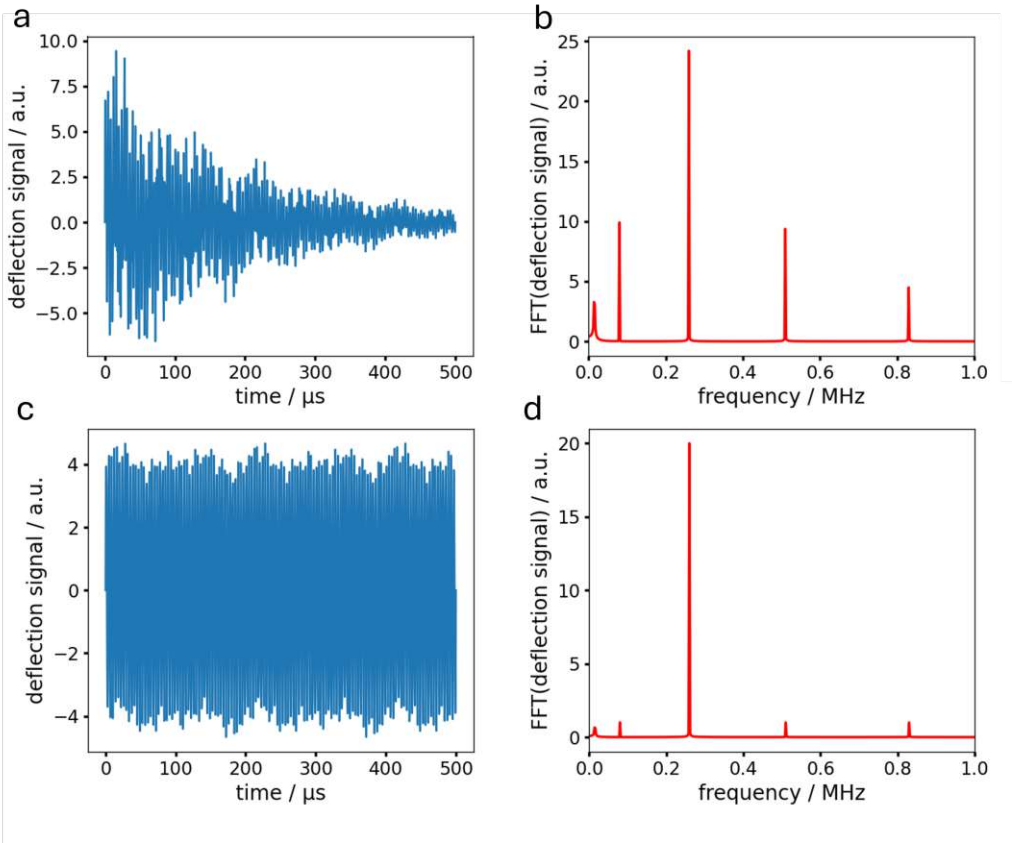


**Figure 2.13.:** (a) A typical time-domain cantilever ringdown response following the absorption of a single laser pulse by the sample. (b) The Fourier transform (FFT) of the ringdown signal, revealing the first four contact-resonance modes of the cantilever. (c) A typical time-domain signal measured when the laser is pulsed at a frequency resonant with one of the cantilever's contact-resonance modes (here at 260 kHz), referred to as resonance-enhanced mode. (d) The FFT of the resonance-enhanced signal, showing that the cantilever response is predominantly composed of the resonant contact-mode oscillation.

In contact mode AFM-IR, two primary detection schemes are commonly employed: ringdown and resonance-enhanced mode.

The cantilever oscillations decay (ring down) over a timescale of approximately 500 µs (see Fig. 2.13a), which is significantly longer than the sample thermalization time, typically on the nanosecond scale [91, 102, 103]. In the **ringdown detection** scheme, AFM-IR uses a soft contact-mode cantilever and relies on short laser pulses—typically on the order of 10 ns or shorter—to induce rapid thermal expansion in the sample. However, a wide range of

pulse durations has been demonstrated, including ultrashort pulses of approximately 0.1 ns using difference frequency generation sources [104], and longer pulses up to 500 ns with quantum cascade lasers (QCLs) [105]. The laser repetition rate is generally low (around 1 kHz), provided it remains below the cantilever's mechanical relaxation time [106]. Upon light absorption, the sample undergoes rapid photothermal expansion, exciting multiple cantilever modes.

The rapid photothermal expansion can be simply modeled as an excitation impulse force ($I_{imp}\delta(t)$) on the cantilever/tip. $I_{imp}$ is the impulse (with unites of momentum: $\mathrm{N}\cdot\mathrm{s}$), proportional to the optical absorption coefficient and thermal expansion coefficient [1]. Therefore, the equation of motion for a cantilever subjected to an impulse is:

$$\frac{\partial^2 q_n(t)}{\partial t^2} + 2\zeta\omega_n \frac{\partial q_n(t)}{\partial t} + \omega_n^2 q_n(t) = \frac{I_{imp}}{m}\delta(t) \tag{2.41}$$

The solution to Eq. 2.41 consists of two parts: a particular solution due to the impulse, which determines the initial displacement and velocity of the cantilever motion, and a homogeneous solution representing the free oscillations (ringdown) after the force is removed. The latter takes the form of Eq. 2.31. The impulse force (e.g. fast photothermal expansion of the sample) provides the initial velocity with $\frac{\partial q_n(t)}{\partial t}|_{t=0} = \frac{I_{imp}}{m}$ and zero displacement at $t = 0$. With these initial conditions, the solution of Eq. 2.41 after a short impulsive force, is given by:

$$q_n(t) = \frac{I_{imp}}{m\omega_d} e^{-\zeta\omega_n t}\sin(\omega_d t) \tag{2.42}$$

where $\omega_d = \omega_n\sqrt{1-\zeta^2}$ denotes the damped angular frequency [71].

As these oscillations ($\sin(\omega_d t)$) gradually decay over time with an exponential envelope $e^{-\zeta\omega_n t}$, the process is referred to as 'ringdown' (Fig. 2.13a). The cantilever is excited off-resonance by a short infrared pulse, and its oscillation amplitude (at $t = 0$) is directly proportional to the sample's absorption coefficient and thermal expansion coefficient, while inversely proportional to the cantilever frequencies [94]. Fourier transformation of the ringdown signal reveals the contact resonance frequencies of the cantilever that are excited (Fig. 2.13b).

As indicated in Eq. 2.39, the AFM-IR signal is directly proportional to the laser intensity, meaning that higher laser power theoretically results in a stronger signal. However, simply increasing the laser power could elevate the sample temperature to its melting point, potentially causing damage. An alternative approach to enhance the signal is to illuminate the sample with a series of weaker pulses, rather than a single strong pulse in the ringdown measurements [101].

In this scenario, the cantilever is excited by a train of impulsive forces rather than one single impulse excitation—an approach known as **resonance-enhanced** AFM-IR.

The periodic train of impulses is defined as:

$$F(t) = I_{imp} \sum_{n=0}^{\infty} \delta(t - nT) \tag{2.43}$$

where $T = \frac{2\pi}{\omega_{IR}}$ is the repetition period of the pulse train and $\omega_{IR}$ is the angular repetition frequency of the IR laser. So its Fourier series in real form is:

$$F(t) = \frac{I_{imp}}{T}[1 + 2\sum_{l=1}^{\infty} \cos(l\omega_{IR}t)] \tag{2.44}$$

where $l$ is the harmonic number. We approximate the periodic impulse train by keeping just the DC (zero frequency) term and first harmonic in the impulse train:

$$F(t) = \frac{I_{imp}}{T}[1 + 2\cos(\omega_{IR}t)] \tag{2.45}$$

We assume the cantilever starts from rest at $t = 0$, with no pre-displacement. Since no constant force is acting, any average (DC) displacement due to the Fourier expansion is excluded from the physical solution.

The cantilever motion in this regime can be described by the following damped driven harmonic oscillator equation:

$$\frac{\partial^2 q_n(t)}{\partial t^2} + 2\zeta\omega_n \frac{\partial q_n(t)}{\partial t} + \omega_n^2 q_n(t) = \frac{F_0}{m}\cos(\omega_{IR}t) \tag{2.46}$$

where, $\omega_{IR}$ is the excitation frequency, corresponding to the IR absorption frequency of the sample, and $F_0 = \frac{2I_{imp}}{T}$ is the dynamic force amplitude, proportional to the amount of IR absorption.

A common solution to the harmonic response equation takes the form:

$$q_n(t) = A_{osc}\cos(\omega_{IR}t - \varphi) \tag{2.47}$$

where, $A_{osc}$ is the amplitude of oscillation at frequency $\omega_{IR}$ and $\varphi$ is the phase shift between force and cantilever displacement. Substituting Eq. 2.47 into Eq. 2.46, we obtain:

$$(\omega_n^2 - \omega_{IR}^2)A_{osc}\cos(\omega_{IR}t - \varphi) - 2\zeta\omega_n\omega_{IR}A_{IR}\sin(\omega_{IR}t - \varphi) = \frac{F_0}{m}\cos(\omega_{IR}t) \tag{2.48}$$

Reformulating the above equation:

$$\begin{aligned}&(\omega_n^2 - \omega_{IR}^2)A_{osc}[\cos(\omega_{IR}t)\cos(\varphi) + \sin(\omega_{IR}t)\sin(\varphi))] \\ &- 2\zeta\omega_n\omega_{IR}A_{osc}[\sin(\omega_{IR}t)\cos(\varphi) - \cos(\omega_{IR}t)\sin(\varphi)] = \frac{F_0}{m}\cos(\omega_{IR}t)\end{aligned} \tag{2.49}$$

The above equation, must hold for all $t$, meaning that the coefficients of $\cos(\omega_{IR}t)$ and $\sin(\omega_{IR}t)$ must be equal. Therefore:

$$A_{osc}\left[(\omega_n^2-\omega_{IR}^2)\cos(\varphi)+2\zeta\omega_n\omega_{IR}\sin(\varphi)\right]\cos(\omega_{IR}t)=\frac{F_0}{m}\cos(\omega_{IR}t) \tag{2.50}$$

$$A_{osc}\left[(\omega_n^2-\omega_{IR}^2)\sin(\varphi)-2\zeta\omega_n\omega_{IR}\cos(\varphi)\right]\sin(\omega_{IR}t)=0 \tag{2.51}$$

In the following, we apply a standard trigonometric identity to reformulate the expression in Eq. 2.50 into a more compact amplitude–phase form:

$$A\cos(\theta)+B\sin(\theta)=Rcos(\theta-\phi) \tag{2.52}$$

where:

$$R=\sqrt{A^2+B^2},\quad \tan(\phi)=\frac{B}{A} \tag{2.53}$$

By comparing Eq. 2.50 with Eq. 2.52, we define:

$$A=\omega_n^2-\omega_{IR}^2,\quad B=2\zeta\omega_n\omega_{IR} \tag{2.54}$$

Thus:

$$R=\sqrt{(\omega_n^2-\omega_{IR}^2)^2+(2\zeta\omega_n\omega_{IR})^2},\qquad \tan(\phi)=\frac{2\zeta\omega_n\omega_{IR}}{\omega_n^2-\omega_{IR}^2} \tag{2.55}$$

Since $\phi=\varphi$ represents the phase shift between the excitation force and the cantilever displacement, we can solve the Eq. 2.48 for the amplitude of oscillation:

$$A_{osc}=\frac{F_0/m}{\sqrt{(\omega_n^2-\omega_{IR}^2)^2+(2\zeta\omega_n\omega_{IR})^2}} \tag{2.56}$$

The full steady-state solution is:

$$q_n(t)=\frac{\omega_{IR}I_{imp}}{\pi m\sqrt{(\omega_n^2-\omega_{IR}^2)^2+(2\zeta\omega_n\omega_{IR})^2}}\cos(\omega_{IR}t-\phi) \tag{2.57}$$

By tuning the laser repetition rate to match one of the cantilever's contact resonance frequencies $\omega_{IR}=\omega_n$, the amplitude of oscillation at resonance simplifies to:

$$A_{osc}=\frac{I_{imp}}{2\pi m\zeta\omega_n} \tag{2.58}$$

While both resonance-enhanced and ringdown AFM-IR rely on cantilever oscillations initiated by sample absorption, the maximum amplitude achieved under resonance conditions is typically greater than that from a single-pulse ringdown excitation. Using standard

solutions for a driven damped harmonic oscillator and an impulsively excited system, the ratio of the two amplitudes is given by:

$$\frac{A_{resoance}}{A_{ringdown}} = \frac{\frac{I_{imp}}{2\pi m\zeta\omega_n}}{\frac{I_{imp}}{m\omega_d}} = \frac{\sqrt{1-\zeta^2}}{2\pi\zeta} \tag{2.59}$$

For lightly damped systems ($\zeta \ll 1$), the damping ratio $\zeta$ can be replaced by the quality factor $Q = 1/2\zeta$. Substituting this into the amplitude ratio expression yields:

$$\frac{A_{resoance}}{A_{ringdown}} = \frac{\sqrt{4Q^2-1}}{2\pi} \tag{2.60}$$

Given that cantilevers typically exhibit quality factors much greater than one in both air and vacuum environments [107, 108, 109], the following approximation holds:

$$\frac{A_{resoance}}{A_{ringdown}} = \frac{Q}{\pi} \tag{2.61}$$

This ratio illustrates how resonance-enhanced detection amplifies the response relative to the ringdown mode. It is linearly proportional to the quality factor, making the enhancement particularly significant for low-damping, high-$Q$ cantilevers.

In the resonance-enhanced configuration, the photothermal expansion of the sample excites the AFM cantilever at its resonance frequency, selectively amplifying the AFM-IR signal, which can then be demodulated from the AFM deflection signal, as depicted in Fig. 2.13c and d. This resonance-enhanced AFM-IR technique achieves higher sensitivity than traditional ringdown measurements and is currently the most commonly employed paradigm in AFM-IR.

In resonance-enhanced measurements, it is crucial to match the pulse repetition rate with the cantilever's resonance frequency throughout the measurement. As the cantilever scans the sample surface during imaging, its resonance frequencies are influenced by the tip–sample contact stiffness. Softer materials typically cause the resonance peak to shift to lower frequencies, while harder materials shift it to higher frequencies [110]. If the pulse repetition rate is not adjusted accordingly this alters the AFM-IR signal amplitude. To address this issue, the laser repetition rate can be locked to the phase of the cantilever's resonance using a feedback loop, commonly known as a phase locked loop (PLL) [95]. This method monitors changes in the phase angle rather than the amplitude, which is necessary to maintain resonance-enhanced conditions throughout the scans. At the beginning of each measurement, the user sets a reference point corresponding to the phase angle of the contact resonance, along with a frequency range where variations are expected. The PLL then uses a PID controller to track the phase angle changes and adjust the laser pulse rate, ensuring consistent resonant excitation during the measurement.

### 2.3.3. Tapping Mode AFM-IR

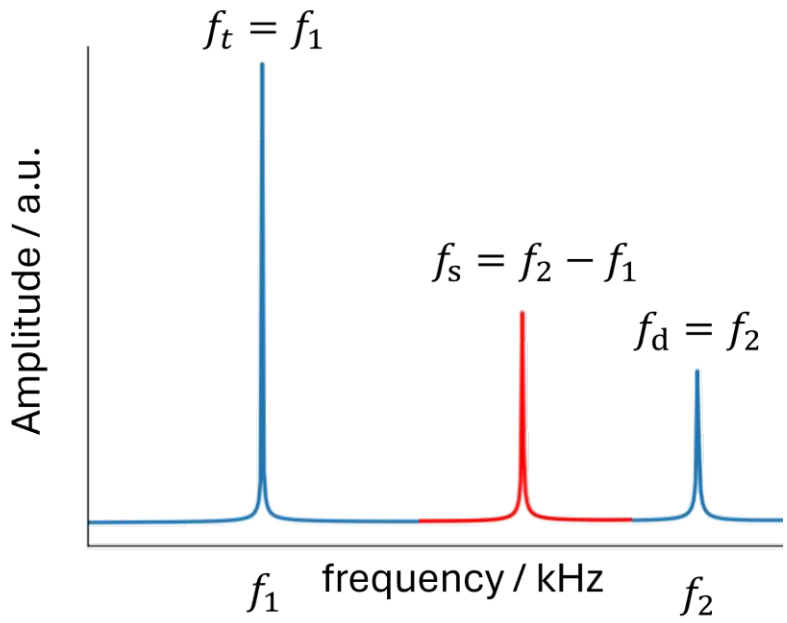


**Figure 2.14.:** Schematic representation of heterodyne mixing in the Tapping AFM-IR frequency domain. $f_1$ and $f_2$ represent the first and second resonance frequencies of the cantilever. The cantilever is driven at $f_t = f_1$, while the laser repetition rate is tuned to the frequency difference $f_2 - f_1$. Signal detection then occurs at the second resonance frequency $f_2$.

In tapping mode AFM-IR, the cantilever is driven to oscillate at one of its mechanical resonance frequencies and intermittently makes contact with the sample (similarly to tapping mode AFM). Concurrently, the sample is illuminated with a pulsed tunable IR laser with the laser repetition rate ($f_{IR}$) set to the difference between the cantilever's second ($f_2$) and first ($f_1$) resonance frequencies. This configuration facilitates a heterodyne detection scheme [80], enabling non-linear mixing of the cantilever's oscillation modes. Specifically, when the cantilever is driven at its first resonance frequency ($f_1$), setting $f_{laser} = f_2 - f_1$ results in the generation of a signal at $f_2$ due to the mixing process, as depicted in Fig. 2.14. The AFM-IR signal is consequently retrieved by demodulating the cantilever oscillation signal at the frequency $f_2$ using a lock-in amplifier [111]. The cantilever can also be driven at $f_2$, with the signal detected at $f_1$. This configuration has been shown to enable the acquisition of better quality tapping-mode AFM-IR spectra [112]. In this case, the laser repetition rate ($f_{IR}$) is still set to $f_2 - f_1$.

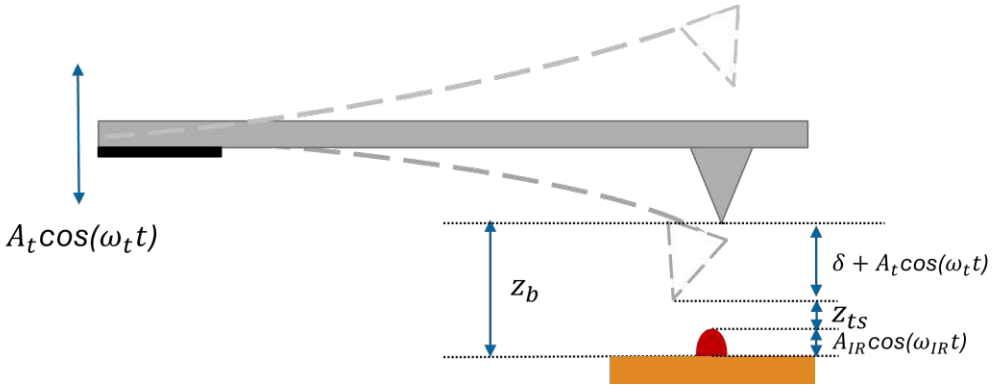


**Figure 2.15.:** Sketch of tapping mode AFM-IR working principle.

To understand tapping mode AFM-IR, we examine the mixer input, given by the tip–sample distance $z_{ts}$. The cantilever, typically actuated from the back using a piezo controller, oscillates harmonically at a resonance frequency ($f_t$), oscillating with an amplitude $A_t$ (Fig. 2.15). Its deflection $\delta$ representing the vertical displacement of the tip, reaches a maximum just before contacting the sample.

IR absorption in the sample induces localized heating, resulting in periodic thermal expansion. This expansion can be approximated as a harmonic function with thermal expansion amplitude $A_{IR}$ and laser repetition rate $f_{IR} = \omega_{IR}/2\pi$.

The tip-sample distance can be expressed as:

$$z_{ts}(t) = z_b - (\delta + (A_t \cos(\omega_t t)) - A_{IR} \cos(\omega_{IR} t) \tag{2.62}$$

where $z_b$ is the tip height setpoint, controlled by the tapping mode feedback loop at the resonance frequency $f_t$. $\delta$ is the cantilever displacement at $x = L$.

The Euler-Bernoulli beam equation (Eq. 2.35) can be solved by setting $z_b = 0$, under the assumption that the deflection $\delta = 0$ during the approach cycle of the cantilever [80, 113].

If we expand the tip-sample interaction force in a Taylor series up to the second order, we obtain:

$$F_{ts}(z_{ts}) = F_{ts}(z_b - \epsilon) = F_{ts}(z_b) - \frac{\partial F_{ts}(z_b)}{\partial z}\epsilon + \frac{1}{2}\frac{\partial^2 F_{ts}(z_b)}{\partial z^2}\epsilon^2 \tag{2.63}$$

The beating term is:

$$\epsilon = A_t \cos(\omega_t)t + A_{IR} \cos(\omega_{IR} t) \tag{2.64}$$

and the nonlinear mixing term is:

$$\begin{aligned}\epsilon^2 &= (A_t \cos(\omega_t t) + A_{IR} \cos(\omega_{IR} t))^2 \\ &= A_t^2 \cos^2(\omega_t t) + A_{IR}^2 \cos^2(\omega_{IR} t) + 2A_t \cos(\omega_t t) A_{IR} \cos(\omega_{IR} t) \\ &= A_t^2 \cos^2(\omega_t t) + A_{IR}^2 \cos^2(\omega_{IR} t) + A_t A_{IR}(\cos((\omega_t + \omega_{IR})t) + \cos((\omega_t - \omega_{IR})t))\end{aligned} \tag{2.65}$$

From the nonlinear mixing term, it becomes evident that the cantilever signal can be demodulated at $\omega_{mix} = \omega_t + \omega_{IR}$ or $\omega_{mix} = \omega_t - \omega_{IR}$. Therefore, the tip-sample interaction force at mixing frequency $\omega_{mix}$ is:

$$F_{mix}(t) = F_{mix,0} \cos(\omega_{mix} t) = \frac{1}{2} \frac{\partial^2 F_{ts}(z_b)}{\partial z^2} A_t A_{IR} \cos(\omega_{mix} t) \tag{2.66}$$

In the case where the driving frequency is at $f_1$, and the IR modulation frequency at $f_2 - f_1$. The detection frequency is given by $f_{det} = f_{mix} = f_1 + (f_2 - f_1) = f_2$, as depicted in Fig. 2.14.

Because in the tapping mode the cantilever's resonance frequency is less affected by the sample's mechanical properties [94], active frequency tracking is often not done. Moreover, this technique provides exceptional spatial resolution, achieving spectral resolutions as fine as 10 nm [95]. Tapping mode AFM-IR preserves the advantages of tapping mode AFM, making it ideal for analyzing soft [95, 114], sticky [111], or easily displaced samples [115], while expanding AFM-IR applications [94, 23, 21].

## 2.4. Current Limitations of AFM and AFM-IR

AFM and its infrared-enhanced counterpart, AFM-IR, have become essential tools for high-resolution nanoscale imaging and chemical analysis. While these techniques offer unique capabilities—such as sub-10 nm spatial resolution and localized chemical specificity—they are subject to several inherent limitations that restrict their broader applicability. These limitations can be broadly categorized into two areas: those related to AFM as a platform, and those specific to AFM-IR.

### 2.4.1. Limitations of AFM

Despite the powerful capabilities of AFM in achieving nanometer-scale resolution and exceptional surface sensitivity, several inherent limitations constrain its broader applicability.

A primary challenge in conventional AFM is slow imaging speed. Since data is acquired line-by-line, the technique is significantly slower than alternatives such as scanning electron microscope (SEM), making it less suitable for large-area mapping or dynamic, real-time imaging. High-speed atomic force microscopy (HS-AFM) has been developed to address this by employing miniaturized cantilevers with high resonance frequencies and optimized feedback systems [116]. HS-AFM enables video-rate imaging, particularly in liquid environments, and has proven valuable in capturing fast biological processes. However, this technique has trade-offs, including reduced force sensitivity, limited scan area, complex control requirements, and challenges in mechanical and chemical property mapping. As such, its use remains focused on niche applications.

Another limitation lies in the optical-lever detection scheme, which uses laser reflection onto a position-sensitive photodiode to track cantilever deflection [117]. While sensitive, this method requires bulky free-space optics and expensive lasers, and is vulnerable to misalignment and environmental noise [118, 119]. Additionally, AFM's temporal resolution is limited by thermal noise and mechanical inertia, requiring low-mass, high-Q cantilevers to achieve improved performance [120]. Further miniaturization for high-frequency operation (e.g., $>$1 MHz) is constrained by diffraction-limited optical detection [121, 122], ultimately impacting signal stability and readout accuracy.

### 2.4.2. Limitations of AFM-IR

AFM-IR enhances AFM by enabling nanoscale infrared spectroscopy through the detection of local photothermal expansion induced by infrared absorption. While this technique offers chemical mapping at resolutions far below the diffraction limit, it presents two major limitations: incomplete theoretical modeling and poor temporal resolution.

### Incomplete Theoretical Modeling

Early models of AFM-IR, such as those establishing a linear dependence of the signal on the imaginary part of the refractive index (i.e., optical absorption), provide only a limited understanding of the signal generation process. For example, the model proposed by Dazzi et al. [1] assumes idealized conditions and neglects important factors such as sample geometry, surrounding matrix, and material heterogeneity. Later, Morozovska et al. [3] developed a more rigorous approach by solving the full set of thermoelastic equations, thereby capturing how temperature distributions and mechanical displacements evolve across interfaces between adjacent materials. Schwartz et al. [123] showed that shorter laser pulses induce cantilever oscillations over a broader frequency spectrum, improving the system's responsiveness to materials with fast thermalization times.

Despite these advances, the current modeling framework remains insufficient for predicting signal behavior in realistic samples. In practice, AFM-IR systems often deviate significantly from the idealized geometries commonly assumed in the literature. Many samples of interest feature absorbers embedded within a surrounding matrix—such as inclusion bodies within cells [124], metal soaps in historical paint layers [125], or intracellular organelles [126]. In these heterogeneous environments, the AFM-IR signal arises from a complex interplay of optical absorption, thermal transport, and mechanical transduction, all modulated by spatially varying material properties. As a result, interpreting AFM-IR signals in such systems requires careful deconvolution of the measured response to isolate contributions from both the absorber and the surrounding matrix—a challenge often overlooked in simplified models.

Another underdeveloped area is the modeling of tapping mode AFM-IR. Despite its widespread use due to reduced lateral forces and improved imaging of soft materials, the theoretical treatment of signal generation in tapping mode remains incomplete. Existing models often oversimplify the influence of oscillation amplitude, tip-sample distance (setpoint), and phase dynamics. These time-dependent interactions modulate both thermal and mechanical transduction processes, yet are not fully captured in current analytical or numerical models.

### Limited Temporal Resolution

Another fundamental limitation of AFM-IR is its inability to capture fast dynamic changes in thermal expansion. The technique relies on detecting localized photothermal responses to pulsed infrared excitation, which cause thermal expansion and subsequent cantilever motion. However, the thermal diffusion and mechanical response occur on microsecond to millisecond timescales, fundamentally limiting the temporal resolution of the technique.

As a result, AFM-IR is not suitable for studying ultrafast or transient processes, such as rapid heat transport, fast molecular switching, or dynamic phase transitions. This limitation is further exacerbated by the mechanical bandwidth of the cantilever and the repetition rate of the IR source, which restrict the ability to resolve time-dependent absorption changes at the nanoscale [91]. While some efforts have been made to improve time resolution—such as single-pulse excitation or heterodyne detection—true time-resolved AFM-IR spectroscopy remains a significant challenge.

### 2.4.3. Addressing Current Challenges

To address the limitations of slow imaging speed, limited sensitivity, and poor temporal resolution—while also enabling new sensing modalities—recent advances in cavity optomechanics have demonstrated ultra-sensitive displacement detection of nanomechanical resonators, in some cases approaching or reaching the standard quantum limit [127, 128, 129, 130, 131]. These systems exploit evanescent coupling between a mechanical resonator and an optical microcavity, allowing for non-contact, highly sensitive displacement readout within compact, integrated platforms [132, 133, 134]. Such optomechanical approaches are promising candidates for integration into AFM systems [91, 102], offering enhanced signal stability, sensitivity, and scalability compared to conventional optical-lever detection schemes.

In the following section, we introduce the fundamental principles of photonic resonators and explore their application to optomechanical AFM probe systems. These developments and their potential impact on nanoscale imaging and spectroscopy are discussed in detail in Chapters 3.3, 3.4, and 3.5.

To overcome the limitations of current AFM-IR models, this work presents the development and validation of a point spread function (PSF) model that provides a comprehensive analytical framework for signal generation. The model accounts for optical absorption, photothermal expansion, and cantilever response, incorporating critical parameters such as absorber size, depth, and surrounding matrix properties. By employing Green's functions [135], the PSF model achieves closed-form solutions with significantly lower computational cost compared to conventional finite element method (FEM) simulations. Further details of this model and its implications are presented in Sections 2.1, 2,2. 3.1 and 3.2

To specifically address the limitations of tapping mode AFM-IR, we present extended theoretical derivations that explicitly incorporate the effects of the setpoint and tip–sample interaction dynamics. These developments are discussed in greater detail in Section 2.4. Nevertheless, the tapping-mode model proposed in this work remains theoretical and requires experimental validation to confirm its accuracy and practical applicability.

## 2.5. Photonic Resonators

In this section, the fundamentals of photonic resonators will be introduced, with a focus on the theoretical principles and optical properties of Bragg gratings, photonic crystals, and ring resonators.

Optical waveguides are key components in photonics, guiding light over various distances by confining it within a physical structure through total internal reflection [136, 137]. In integrated photonics, a common dielectric waveguide consists of a high-index silicon nitride ($Si_3N_4$) core surrounded by a lower-index cladding, such as air, with silicon dioxide ($SiO_2$) as the substrate (Fig. 2.16a). The mode profile, which describes the spatial distribution of the electromagnetic field, determines how light is confined and interacts with the material. In single-mode waveguides, this profile typically exhibits a Gaussian-like shape centered in the core, as shown in Fig. 2.16b from a FDTD simulation. The concept of effective refractive index $n_{eff}$ arises because the mode propagates through a medium that is neither purely core nor cladding; instead, $n_{eff}$ represents an averaged refractive index that determines the phase velocity of the guided mode.

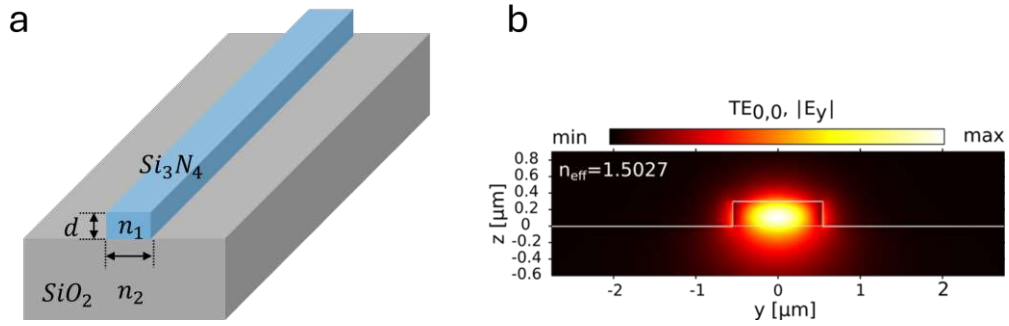


**Figure 2.16.:** (a) Schematic of a ridge waveguide consisting of a silicon nitride core atop a silicon dioxide substrate. (b) FDTD-simulated mode profile of the fundamental transverse electric (TE) mode in a dielectric waveguide, showing the spatial distribution of the electric field intensity predominantly confined within the high-index silicon core.

While waveguides confine and direct light along a defined path, additional control can be achieved through photonic resonators—localized structures that trap light at specific frequencies via interference and resonance effects [138]. These optical cavities enhance the local optical field through constructive interference, enabling discrete spectral resonances characterized by high quality factors (Q). Unlike waveguides that support continuous light propagation, photonic resonators provide precise control over optical properties such as

wavelength selectivity [139, 140, 141], field enhancement [142, 143], and slow light propagation [144, 145]. Resonant confinement is typically achieved by introducing reflective boundaries or defects—such as Bragg mirrors, periodic modulations, or photonic crystal patterns—into dielectric structures. Among the most widely used resonator geometries are Bragg gratings, photonic crystals, and ring resonators, each offering distinct advantages for applications in lasers, sensors, nonlinear optics, and cavity optomechanics.

Beyond their role in purely optical applications, photonic resonators also serve as the foundation for cavity optomechanics [127, 128, 129, 146]: a field that explores the interaction between light and mechanical motion at the nanoscale. Optomechanical systems based on photonic resonators utilize radiation pressure or gradient forces to drive and probe mechanical motion with high precision. In particular, micro-ring resonators [147, 148, 149], photonic crystal cavities [150, 131, 151], and Bragg gratings [152, 153] have been extensively studied for their ability to enhance optomechanical coupling, leading to applications in force sensing, displacement metrology, and quantum optomechanics.

In this section, we introduce the fundamental theory of Bragg gratings, photonic crystals, and ring resonators. These structures form the basis for various optical sensing platforms due to their high quality factors and strong light–matter interactions. In this thesis, we present the design and development of three distinct optomechanical AFM probes, each based on one of these resonator types: Bragg gratings, photonic crystals, and ring resonators. Detailed descriptions of these designs are provided in Sections 3.3, 3.4, and 3.5.

### 2.5.1. Bragg Gratings

Bragg gratings are fundamental optical elements with a periodic refractive index variation that selectively reflect or transmit light based on wavelength, acting as wavelength-selective filters or reflectors. They are widely used in optical sensing applications, telecommunications and signal processing [154, 155, 156, 157]. Integrated Bragg gratings offer the advantages of compact size and large-scale manufacturability and have gained significant attention due to their enhanced sensitivity and compact form factor. Recent advancements in silicon photonics have enabled the successful integration of Bragg gratings onto Silicon-on-Insulator (SOI) substrates, demonstrating their potential for advanced optical sensing applications [158, 159, 160].

In addition to sensing applications, Bragg gratings are also integral to photonic signal processing. Chirped Bragg gratings, where the periodicity gradually varies along the propagation direction, are especially effective in compensating for group velocity dispersion in optical fibers. This specificity restores pulse integrity and enables pulse compression, making these gratings essential for high-performance optical communication systems [161,

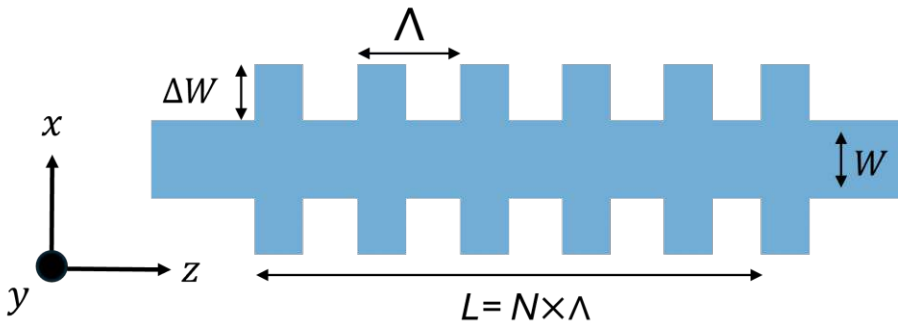


**Figure 2.17.:** Schematic of a uniform strip waveguide grating.

162].

In its simplest configuration, a Bragg grating is a structure with a periodic modulation of the effective refractive index along the propagation direction of the optical mode. This modulation is typically achieved by altering either the refractive index or the physical dimensions of the waveguide. At each boundary created by the modulation, a portion of the traveling light is reflected. The relative phase of the reflected light depends on both the grating period and the wavelength of the incident light.

The periodic modulation of the effective refractive index leads to multiple distributed reflections along the grating. These reflected signals interfere constructively only within a narrow spectral range centered around a specific wavelength, known as the Bragg wavelength. Within this range, light is strongly reflected. For other wavelengths, the reflections interfere destructively, canceling each other out, allowing the light to pass through the grating.

The Bragg grating structure used in this work consists of a waveguide with a central width of $W$ and sidewall corrugations of width $\Delta W$. Figure 2.17 illustrates a Bragg grating with square corrugations, periodically repeated with a period $\Lambda$. The total length of the grating is $L = N \times \Lambda$.

Based on coupled mode theory (CMT) [136, 163], and considering only the coupling between the forward and backward propagating fundamental modes with amplitudes $a(z)$ and $b(z)$, respectively, for a uniform grating, the CMT equation can be written as [164]:

$$\frac{d}{dz}\begin{pmatrix} a(z) \\ b(z) \end{pmatrix} = -i \begin{pmatrix} \Delta\beta & \kappa \\ -\kappa & -\Delta\beta \end{pmatrix} \cdot \begin{pmatrix} a(z) \\ b(z) \end{pmatrix} \tag{2.67}$$

Here, the time dependency is neglected and $\kappa$ is the coupling coefficient given by the grating strength and can be interpreted as the amount of the reflection per unit length. $z$

represents the propagation direction along the waveguide, symbol $i = \sqrt{-1}$ is the imaginary unit. $\Delta\beta$ represents the propagation constant offset from the Bragg wavelength (or the phase detuning factor), and is defined as [165]:

$$\Delta\beta = \beta_u + \kappa' + \frac{\pi}{\Lambda} \tag{2.68}$$

where $\beta_u$ is the propagation constant of the unperturbed waveguide, $\kappa'$ is the self-coupling coefficient and $\Lambda$ is the periodicity of the grating.

For the forward propagating mode, with the boundary condition $a(0) = 1, b(L) = 0$, where L is the length of the grating, the solution for $a(z)$ is given by:

$$a(z) = e^{\gamma z} \tag{2.69}$$

with

$$\gamma^2 = \kappa^2 - \Delta\beta^2 \tag{2.70}$$

The reflectance for a uniform grating is described by [164]:

$$R = \frac{\kappa^2 \sinh^2(\gamma L)}{\gamma^2 + \kappa^2 \sinh^2(\gamma L)} \tag{2.71}$$

The reflected wavelength($\lambda_B$) is known as Bragg wavelength, is given as:

$$\lambda_B = \frac{2\pi\Lambda n_{eff}}{\pi - \kappa'\Lambda} \tag{2.72}$$

where $n_{eff}$ is the average effective index of the Bloch mode [166](the natural eigenmodes of a wave in a periodic medium, described as a periodic function multiplied by a plane wave.) of the grating.

For the case where $\Delta\beta = 0$, the reflectance reaches its maximum with $\gamma = \kappa$. Using Eq. 2.71, the peak power reflectivity at the Bragg wavelength can be expressed as:

$$R_{peak} = \frac{\kappa^2 \sinh^2(\gamma L)}{\kappa^2(1 + \sinh^2(\gamma L))} = \frac{\sinh^2(\gamma L)}{\cosh^2(\gamma L)} = \tanh^2(\gamma L) \tag{2.73}$$

The bandwidth is also an important figure of merit for Bragg gratings, which determines the spectral range over which the grating efficiently reflects or filters light. This is crucial for applications such as wavelength-selective filtering, sensing, and optical signal processing [156]. A narrow bandwidth allows for high spectral selectivity—ideal for distinguishing closely spaced wavelengths—while a broader bandwidth can enhance tolerance to wavelength drift or fabrication imperfections [167].

The bandwidth between the first nulls around the resonance can be determined by:

$$\Delta\lambda = \frac{\lambda_B^2}{\pi n_g}\sqrt{\kappa^2 + (\pi/L)^2} \tag{2.74}$$

where $n_g = n - \lambda(\Delta n/\Delta\lambda)$ is the group index. Note that for long gratings, $\Delta\lambda = \lambda_B^2\kappa/(\pi n_g)$. Fig. 2.18 shows an example of a $Si_3N_4$ Bragg grating with a $SiO_2$ cladding, obtained using finite-difference time-domain (FDTD) simulations.

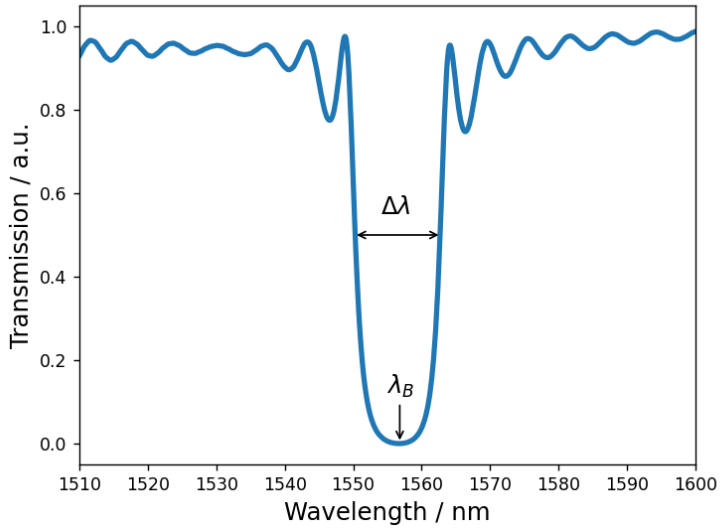


**Figure 2.18.:** FDTD-simulated transmission spectrum of a $Si_3N_4$ grating with a $SiO_2$ cladding, where the grating parameters are: width $w$ =1.35 µm, modulation depth $\Delta w$ =0.575 µm, period $\Lambda$ =0.456 µm, and number of periods $N = 240$.

When the self-coupling coefficient is neglected, Eq. 2.72 simplifies to $\lambda_B = 2\Lambda n_{eff}$, indicating that the Bragg wavelength depends only on the grating period and the effective index.

To determine the grating coupling coefficient parameter, we use reflection coefficients which are found by based on Fresnel equations. For a stepwise effective index variation:

$$\Delta n = n_{eff2} - n_{eff1}, \tag{2.75}$$

subscripts 1 and 2 correspond to the regions in the air and waveguide, respectively. The reflection at each interface can be written as $\Delta n/2n_{eff}$ according to the Fresnel equations. Each grating period contributes two reflections. For the case of a rectangular grating profile, the coupling coefficient is:

$$\kappa = 2\frac{\Delta n}{2n_{eff}}\frac{1}{\Lambda} = \frac{2\Delta n}{\lambda_B}\cdot\frac{\pi}{\pi - \kappa'\Lambda} \tag{2.76}$$

A specialized variant of Bragg gratings, known as phase-shifted Bragg gratings (PSBGs), incorporates a localized perturbation in the periodic structure, forming a first-order Fabry-Perot cavity between two Bragg reflectors [168]. This modification introduces a narrow spectral passband within the optical bandgap, making PSBGs particularly valuable for high-resolution biosensing [152], as well as temperature and strain sensing [153].

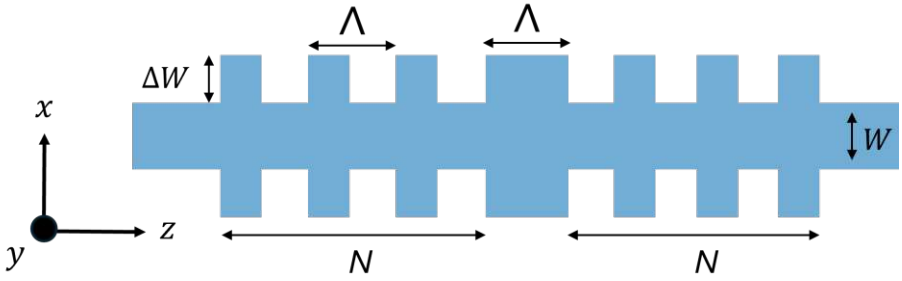


**Figure 2.19.:** Schematic of a quarter-wave phase shifted waveguide grating.

The phase shift primarily affects the spectrum by introducing a transmission peak at the center of the transmission stop-band and significantly increasing the bandwidth between between the first nulls. The bandwidth for the quarter-wave phase shifted Bragg grating is [169]:

$$\Delta\lambda = \frac{\lambda_B^2}{\pi n_g}\sqrt{\kappa^2 + (\pi/L)^2 + (2\pi/L)^2} \tag{2.77}$$

An additional term, $(2\pi/L)^2$, appears in the bandwidth expression compared to Eq.2.74, as a result of the phase shift introduced in the grating structure. This phase shift creates a defect mode — a localized resonance — within the photonic bandgap, allowing light at a specific wavelength within the stopband to transmit through the grating. The presence of this resonant cavity alters the dispersion characteristics and effectively broadens the spectral response. Consequently, the inclusion of the $(2\pi/L)^2$ term leads to a significant increase in bandwidth relative to a conventional Bragg grating without a phase shift, as illustrated in Fig. 2.20.

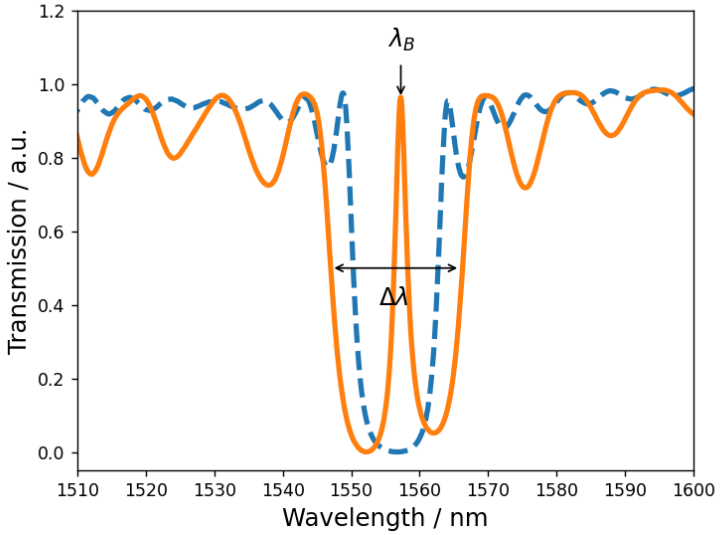


**Figure 2.20.:** FDTD-simulated transmission spectrum of $Si_3N_4$ grating with (orange solid line) and without (blue dashed line) the quarter-wave phase shift.

### 2.5.2. Photonic Crystals

Photonic crystals (PhCs) are materials with a periodically varying dielectric constant along specific directions, analogous to how electrons in semiconductors experience a periodic energy potential that forms allowed and forbidden energy bands [170]. Structurally, PhCs are similar to Bragg gratings, which manipulate light through periodic refractive index variations. However, the refractive index modulation in PhCs is significantly stronger than in typical Bragg gratings [171]. Moreover, unlike Bragg gratings, which are strictly one-dimensional (1D), PhCs can be one-, two-, or three-dimensional (1D, 2D, or 3D), influencing light propagation by creating photonic band gaps that restrict certain wavelengths from traveling through the material. 1D PhCs consist of alternating dielectric layers, resembling Bragg gratings [172, 173]. 2D PhCs have periodicity in two directions and are widely used in photonic crystal waveguides and cavities [174, 175]. 3D PhCs exhibit periodicity in all three directions, enabling the formation of a complete photonic band gap [176].

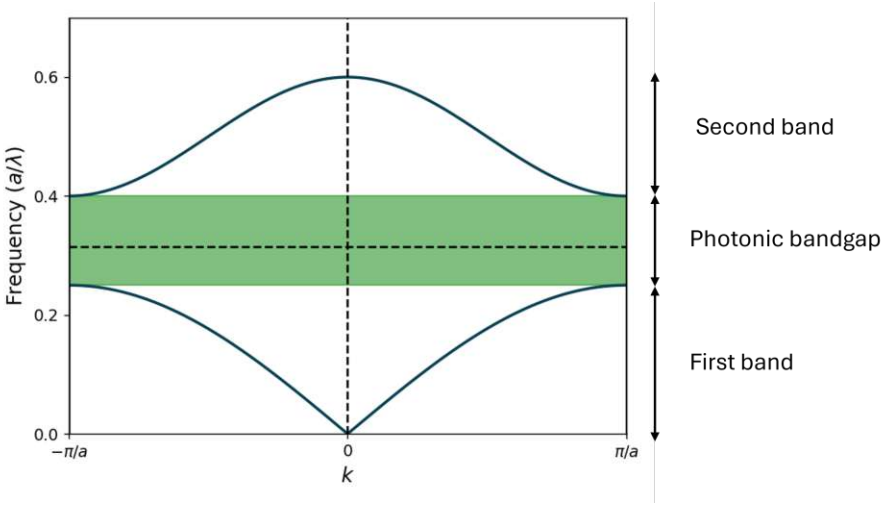


**Figure 2.21.:** Schematic of the band structure of a 1D photonic crystal. The first and second bands contain allowed modes, while the bandgap region hosts forbidden modes where light propagation is not permitted.

A key feature of PhCs is that the periodicity of the crystal induces photonic bandgaps (PBGs) in its band structure, preventing electromagnetic modes from existing within this frequency range. The propagating function $\mathbf{u}(z)$ is periodic, like Bloch modes [166], satisfying $\mathbf{u}(z+R) = e^{ikR}\mathbf{u(z)}$, where $R$ is an integer multiple of the spatial period $a$. However, within the bandgap (green area in Fig. 2.21), the wave vector becomes complex, expressed as $k = \Re(k) + i\kappa$. As a result, modes in the bandgap become evanescent, decaying exponentially [177].

$$\mathbf{H(r)} = e^{ikz}\mathbf{u}(z) = e^{i\Re(k)z}\mathbf{u}(z)e^{-\kappa z} \tag{2.78}$$

The imaginary component of the wave vector causes the decay on a length scale of $1/\kappa$.

While Eq. 2.78 is based on a plane wave approximation, this assumption becomes less accurate in small cavities, where wave effects dominate and ray-optics-based Bragg reflection conditions may not be strictly satisfied. As a result, the optical quality factor ($Q_o$) is greatly reduced. One solution is to extend the Bragg reflection effect in multiple directions. Introducing a small disorder or defect into the 2D or 3D photonic crystal to create a highly efficient photonic nanocavity with an extremely large $Q_o/V$ ratio [178]. The photonic bandgap effect is utilized for light confinement in the in-plane direction, while total internal reflection (TIR) at the interface between the slab and the air cladding governs the vertical direction. By combining the 2D photonic bandgap and 1D TIR, an ultrahigh $Q_0$ is achieved [178, 179].

### 2.5.3. Optical Ring Resonators

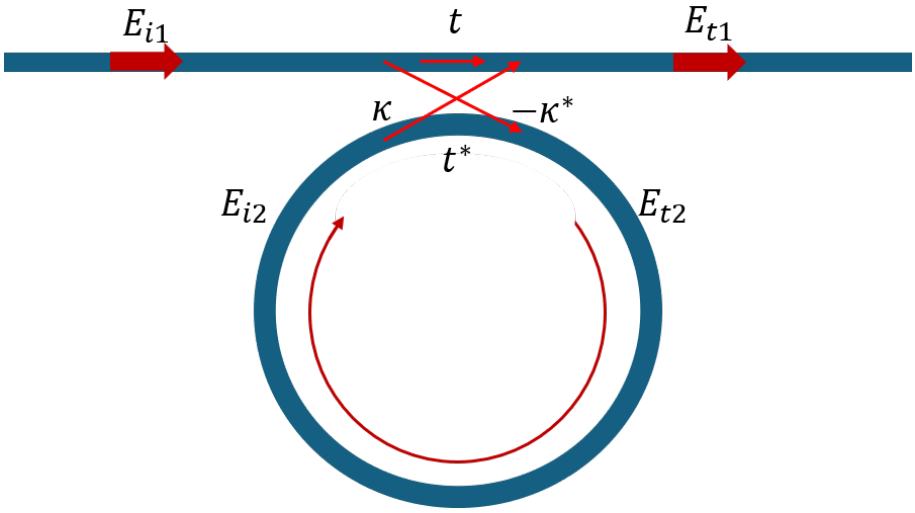


**Figure 2.22.:** schematic of a ring resonator.

The simplest configuration of an optical ring resonator is illustrated in Fig. 2.22. It consists of a straight waveguide (commonly referred to as the bus waveguide) that carries the light and is coupled to a ring waveguide.

The ring resonator can be interpreted as an optical feedback system [180]: light from the bus waveguide is partially coupled into the ring, where it circulates multiple times. During each round trip, the optical field accumulates a phase shift and experiences attenuation. Upon returning to the coupling region, the circulating field interferes with newly coupled light, leading to constructive or destructive interference depending on the phase conditions. Resonance occurs when the round-trip phase shift equals an integer multiple of $2\pi$ radians, resulting in periodic cavity resonances [181].

In the coupling region, light may either continue propagating in its original waveguide (bus or ring) or transfer to the other waveguide via evanescent coupling. This interaction is conveniently described using a scattering matrix [182] that relates the input fields ($E_{i1}$, $E_{i2}$) to the output fields ($E_{t1}$, $E_{t2}$), capturing both transmission and coupling behavior.

The strength of this coupling is governed by the coupling coefficient $\kappa$, which determines the fraction of light transferred between the waveguides. The transmission coefficient $t$ characterizes the portion of the field that remains in the original waveguide after the coupling interaction.

In the frequency domain, the output fields from the coupling region are related to the input fields through the following unitary scattering matrix [182]:

$$\begin{pmatrix} E_{t1} \\ E_{t2} \end{pmatrix} = \begin{pmatrix} t & \kappa \\ -\kappa^* & t^* \end{pmatrix} \cdot \begin{pmatrix} E_{i1} \\ E_{i2} \end{pmatrix} \tag{2.79}$$

where, the $*$ denotes the conjugated complex value of $t$ and $\kappa$, respectively. The symmetry of the matrix arises from the reciprocity of the network under consideration:

$$|\kappa^2| + |t^2| = 1 \tag{2.80}$$

To account for propagation effects within the ring, two key parameters are introduced: the amplitude transmission coefficient $\alpha$ and the round-trip phase accumulation $\theta$. The coefficient $\alpha$ (with $0 \leq \alpha \leq 1$) accounts for optical losses during a single circulation around the ring, where $\alpha = 1$ corresponds to a lossless ring.

The phase relationship between the field just before completing a round trip, $E_{t2}$, and the field just after $E_{i2}$, is described by a multiplicative factor $e^{i\theta}$. The phase accumulation $\theta$ is given by

$$\theta = \frac{2\pi R\omega}{c} \tag{2.81}$$

where $R$ is the radius of the ring measured from the center of the ring too the center of the waveguide, $c = c_0/n_{eff}$ is the phase velocity of the ring mode, and $n_{eff}$ is the effective index.

To simplify the analysis, it is common to normalize the input electric field amplitude by setting $E_{i1} = 1$. Taking into account the round-trip losses characterized by the amplitude transmission coefficient $\alpha$, the electric field re-entering the coupling region after one full circulation in the ring is given by:

$$E_{i2} = \alpha \cdot e^{i\theta} E_{t2} \tag{2.82}$$

From Eq.2.79 and 2.82, we could therefore obtain:

$$\begin{aligned} E_{t2} &= \frac{-\kappa *}{1 - t^* \alpha e^{j\theta}} \\ E_{t1} &= \frac{te^{-j\theta} - \alpha}{e^{-j\theta} - \alpha t^*} \\ E_{i2} &= \frac{-\alpha \kappa^*}{e^{-j\theta} - \alpha t^*} \end{aligned} \tag{2.83}$$

This leads to the transmission $T$ at the output waveguide:

$$T = |E_{t1}|^2 = \frac{te^{-j\theta} - \alpha}{e^{-j\theta} - \alpha t^*} \cdot \frac{t^* e^{j\theta} - \alpha^*}{e^{j\theta} - \alpha^* t} = \frac{tt^* + \alpha^2 - \alpha(te^{-j\theta} + t^* e^{j\theta})}{1 + \alpha^2 tt^* - \alpha(te^{-j\theta} + t^* e^{j\theta})} \tag{2.84}$$

If we define the complex transmission coefficient as $t = |t|e^{j\phi}$, where $|t|$ represents the coupling losses and $\phi$ denotes the phase of the coupler, Eq. 2.84 can be simplified as:

$$T = \frac{|t|^2 + \alpha^2 - 2\alpha|t|\cos(\phi - \theta)}{1 + \alpha^2|t|^2 - 2\alpha|t|\cos(\phi - \theta)} \tag{2.85}$$

At the resonance wavelength, the phase term $\phi - \theta = 2n\pi$ ($n = 0, 1, 2, ...$ is the number of the resonance modes in the ring), the transmission is further simplified as:

$$T = \frac{(|t| - \alpha)^2}{(1 - \alpha|t|)^2} \tag{2.86}$$

In the case where the coupling losses $t$ are equal to the internal losses of the ring $\alpha$, the transmission drops to zero. This condition, known as critical coupling, occurs when the coupling rate into the resonator exactly matches the internal loss rate. The maximum transmission under the critical coupling condition occurs when $\phi - \theta = (2n + 1)\pi$, leading to:

$$T_{max} = \frac{4\alpha^2}{(1 + \alpha^2)^2} \tag{2.87}$$

Since $\alpha$ lies between 0 and 1, it is evident that $T_{max}$ increases with $\alpha$, meaning higher transmission occurs when internal losses are low. Therefore, to achieve a large output power, it is desirable to operate in the range where $|t| \approx \alpha \approx 1$, ensuring minimal losses in the ring and weak coupling between the ring and the waveguide.

Recalling that the round-trip phase accumulation is given by Eq. 2.81, which can be rewritten in terms of the vacuum wavelength $\lambda$ as:

$$\theta = \frac{4\pi^2 R n_{eff}}{\lambda} \tag{2.88}$$

Resonance occurs when the total phase shift accumulated during a round trip in the ring results in constructive interference at the coupling region. Since this condition can be satisfied at multiple wavelengths, the ring resonator exhibits periodic resonances across the optical spectrum.

The distance between two adjacent resonance peaks, denoted as $\Delta\lambda$ in Fig. 2.23, is known as the free spectral range (FSR) and is defined as [182]:

$$FSR = \Delta\lambda = -\frac{1}{R}\left(\frac{\partial\beta}{\partial\lambda}\right)^{-1} \tag{2.89}$$

where $\beta = 2\pi n_{eff}/\lambda$ is the propagation constant of the electromagnetic wave in the ring. Neglecting the wavelength dependence of the refractive index, Eq. 2.89 can be rewritten as:

$$FSR = \frac{\lambda^2}{2\pi R \cdot n_{eff}} \tag{2.90}$$

The FSR is inversely proportional to the radius of the ring and effective index.

The finesse ($F$) of a ring resonator is defined as the ratio of the FSR to the full width at half maximum (FWHM) of the resonance spectrum peak:

$$F = \frac{FSR}{FWHM} \tag{2.91}$$

The quality factor ($Q_0$) of a resonator, also characterizes the sharpness of the resonance and is closely related to finesse. It is defined as the ratio of the operating wavelength to the resonance width (FWHM). In the case of weak coupling ($\kappa \ll 1$), $Q_0$ can be expressed as [182]:

$$Q_0 = F \cdot \frac{\lambda}{FSR} = \frac{\lambda}{FWHM} = \frac{2\pi^2 R \cdot n_{eff}}{\lambda \kappa^2} \tag{2.92}$$

Fig. 2.23 presents a FDTD-simulated transmission spectrum of a Si resonator on a $SiO_2$ substrate, with a radius of $R$ =3.1 µm, where the FSR and resonance width $\delta\lambda$ are indicated.

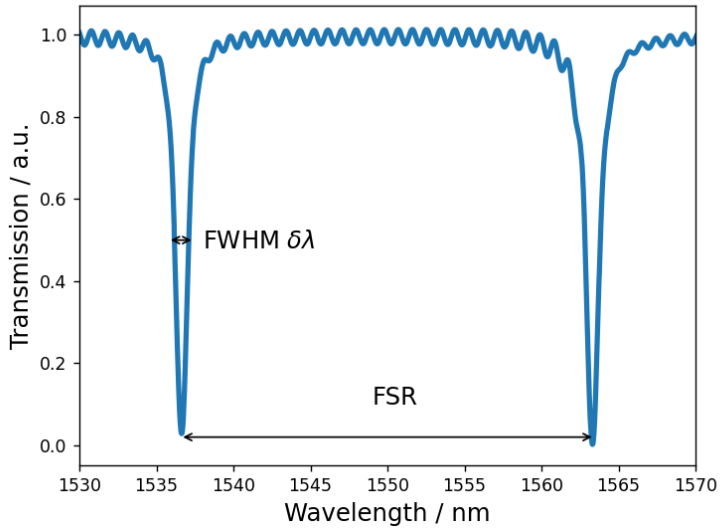


**Figure 2.23.:** FDTD-simulated transmission spectrum of a Si ring resonator on a $SiO_2$ substrate, with a radius of $R$ =3.1 µm.

# 3. Modeling AFM-IR Signal

## 3.1. Point Spread Function of AFM-IR in Cylindrical Coordinates

In Section 1.3.1, we discussed the AFM-IR signal and the limitations of existing analytical models for photothermal expansion, the primary mechanism inducing cantilever oscillations. A key limitation of these models is their assumption of laterally homogeneous samples, where the surface expansion is directly proportional to the temperature change following a laser pulse. Under these conditions, the AFM-IR signal can be described by considering only sample heating and thermal conduction [91].

However, to accurately study spatial resolution in AFM-IR, models must account for laterally heterogeneous samples. In such cases, the surface displacement is influenced not only by thermal expansion but also by the sample's elastic response [3]. A non-uniform absorber distribution leads to spatially varying heating, which induces inhomogeneous strain in the surrounding material, affecting the overall sample's photothermal response and therefore the AFM-IR signal. To address this complexity, we employ Green's function methods [183], which allow the solution of differential equations with inhomogeneous source terms to be expressed in terms of integral operators. This approach provides a powerful and efficient framework for modeling spatially resolved signal generation in laterally inhomogeneous systems.

To further investigate these effects, we developed an analytical model in cylindrical coordinates for the AFM-IR signal that incorporates three key components: transient laser heating, heat conduction within the sample, and thermo-elastic deformation of the material. In this new model, we consider that the laser energy is initially absorbed by the absorber according to its absorption coefficient, leading to internal heat generation at a rate of $g(r, \theta, z, t)$ per unit volume with unit $(W/m^3)$, where $t$ is time, $r$ is the radial distance, $z$ represents the vertical (axial) distance.

For simplicity, we assume homogeneous illumination of the absorber, meaning that the incident laser intensity is uniform across the illuminated area. While this is a reasonable approximation for the present case, it is important to note that the model neglects spatial variations in the beam profile.

Assuming a homogeneous heat distribution in the $r$-plane, the heat source and resulting temperature changes depend only on $r$, $z$ and $t$. Therefore, throughout the analysis, the heat generation function simplifies to $g(r, \theta, z, t) = g(r, z, t)$, eliminating any dependence on $\theta$. In such conditions, the time dependent heating source term can be expressed as:

$$g(r, z, t) = g_V(r, z) * \prod \left( \frac{t}{t_p} \right) \tag{3.1}$$

$\prod\left(\frac{t}{t_p}\right)$ is the rectangular box function of length $t_p$. $g_V(r,z)$ is the product of the optical absorption coefficient and the optical fluence defined as:

$$g_V(r,z) = \mu_a \cdot P/A_f \tag{3.2}$$

where $\mu_a$ is the optical absorption coefficient, $P$ is the excitation laser power and $A_f$ is the optical fluence area.

The sample's geometry consists of a single absorber embedded within a matrix, which is deposited on a semi-infinite thick substrate and covered by air, as shown in Fig. 3.1. In the following sections, we first solve the heat equation for this system in cylindrical coordinates to determine the temperature distribution. This solution is then incorporated into Navier's equations to obtain the thermo-elastic displacement at the surface, which is considered the AFM-IR signal.

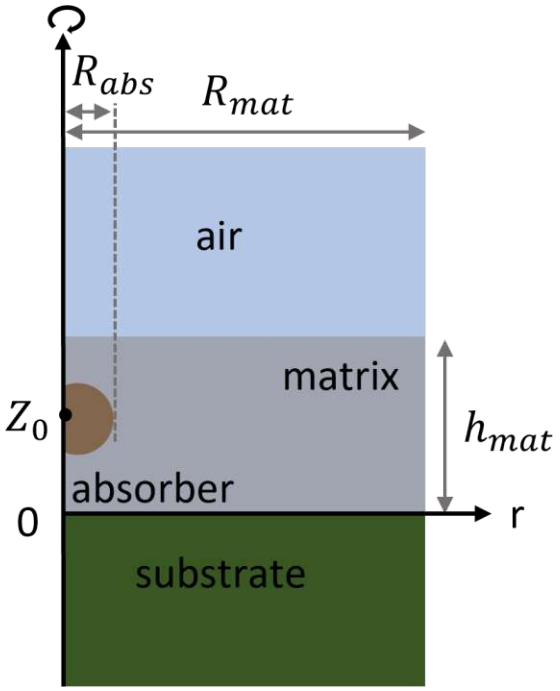


**Figure 3.1.:** Schematic of the modeled, cylindrically symmetric system composed of a single spherical absorber surrounded by a matrix, deposited on a non-absorbing substrate.

### 3.1.1. Heat Equation in Cylindrical Coordinates

The whole system can be treated as either a semi-infinite body over the domain $0 < r < \infty$ or as a finite body with a radius of $R_{mat}$, provided that $R_{mat}$ is sufficiently large such

that the boundary has a negligible influence on the thermal and mechanical behavior in the region surrounding the absorber. The system is described by Fourier's law:

$$\frac{\partial^2 T(r,z,t)}{\partial r^2} + \frac{1}{r}\frac{\partial T(r,z,t)}{\partial r} + \frac{\partial^2 T(r,z,t)}{\partial z^2} + \frac{g(r,z,t)}{\kappa} = \frac{1}{\alpha}\frac{\partial T(r,z,t)}{\partial t} \quad for \quad t \geq 0 \tag{3.3}$$

With the following initial conditions (IC) and boundary conditions (BC):

$$\begin{aligned}
&BC1: && \frac{\partial T(r,z,t)}{\partial r} = 0 \quad at \quad r = 0 && \text{(symmetry)} \\
&BC2: && T(r = R_{mat}, z, t) = 0 && \text{(Dirichlet boundary condition)} \\
&BC3: && T(r, z = 0, t) = 0 && \text{(substrate is a perfect heat sink)} \\
&BC4: && \frac{\partial T(r,z,t)}{\partial z} = 0 \quad at \quad z = h_{mat} && \text{(air is insulating)} \\
&IC: && T(r, z, t = 0) = F(r, z)
\end{aligned} \tag{3.4}$$

where $\kappa$ is the thermal conductivity. To facilitate the Green's function solution of the heat conduction equation, an initial heat distribution $F(r,z)$ is assumed. This distribution is not necessarily physical but serves as a mathematical construct representing the initial condition from which the system's response to an arbitrary heat source can be derived.
In the following, we take room temperature as zero, $T$ is variant above room temperature, and $\alpha$ is the thermal diffusivity defined as:

$$\alpha = \frac{\kappa}{\rho C_p} \tag{3.5}$$

where $\rho$ is the density and $C_p$ is the specific heat capacity.

Note: BC1 is the symmetry condition, BC2 implies that the sample is a finite cylinder with a constant temperature at the sides. This boundary condition was chosen over the alternative assumption of a semi-infinite sample, as it enables a more tractable analytical solution. Besides, if $R_{mat}$ is large enough the solutions are almost identical. BC3 and BC4 indicate that the sample is finite in the $z$ direction with a constant temperature at sample/substrate interface and insulation condition at the top sample/air interface.
To determine the desired Green's function, we consider the homogeneous version of the problem defined above, i.e. the version without the heating term $\frac{g(r,z,t)}{\kappa}$, denoted as $\Psi(r,z,t)$, within the same spatial and temporal domain:

$$\frac{\partial^2 \Psi(r,z,t)}{\partial r^2} + \frac{1}{r}\frac{\partial \Psi(r,z,t)}{\partial r} + \frac{\partial^2 \Psi(r,z,t)}{\partial z^2} = \frac{1}{\alpha}\frac{\partial \Psi(r,z,t)}{\partial t} \quad in \quad 0 \leq r \leq R_{mat}, 0 \leq z \leq h_{mat} \tag{3.6}$$

Now, with all homogeneous boundary conditions, we split our solution into three independent functions:

$$\Psi(r,z,t) = R(r)Z(z)\Gamma(t) \tag{3.7}$$

which after substitution into Eq. 3.6 yields:

$$\frac{1}{R}\left(\frac{d^2R}{dr^2} + \frac{1}{r}\frac{dR}{dr}\right) + \frac{1}{Z}\frac{d^2Z}{dz^2} = \frac{1}{\alpha\Gamma}\frac{d\Gamma}{dt} = -\lambda^2 \tag{3.8}$$

The solution of the separated ordinary differential equation (ODE) in the $t$ dimension leads to the expected form:

$$\Gamma(t) = C_1 e^{-\alpha\lambda^2 t} \tag{3.9}$$

with the remaining terms of Eq. 3.8 yielding:

$$\frac{1}{R}\left(\frac{d^2R}{dr^2} + \frac{1}{r}\frac{dR}{dr}\right) + \lambda^2 = -\frac{1}{Z}\frac{d^2Z}{dz^2} = \eta^2 \tag{3.10}$$

The solution of the $z$-dimension ODE yields the desired solution form:

$$Z(z) = C_2 \cos\eta z + C_3 \sin\eta z \tag{3.11}$$

Applying BC3 yields constant $C_2 = 0$, while applying BC4 results in eigenvalues(for integer values of $n$):

$$\eta = \frac{\pi}{2h_{mat}}(2n+1), \quad n = 0,1,2,... \tag{3.12}$$

If we now consider the remaining $r$ terms of Eq. 3.10, where we first let $\beta^2 = \lambda^2 - \eta^2$, and then multiply both sides by the function $R$, yielding:

$$\frac{d^2R}{dr^2} + \frac{1}{r}\frac{dR}{dr} + \beta^2 R = 0 \tag{3.13}$$

This is the Bessel equation of order zero, and the elementary solutions are [135]:

$$R(r) = C_4 J_0(\beta r) + C_5 Y_0(\beta r) \tag{3.14}$$

where $J_0(\beta r)$ and $Y_0(\beta r)$ are the Bessel functions of order zero. The requirement of the symmetry condition stated by BC1 eliminates the $Y_0(\beta r)$ term, while BC2 then yields:

$$C_4 J_0(\beta_m R_{mat}) = 0 \quad for \quad m = 0,1,2,3,.. \tag{3.15}$$

Now, $\lambda_{nm}$ is:

$$\lambda_{nm}^2 = \beta_m^2 + \eta_n^2 \tag{3.16}$$

Since the eigenvalues and eigenfunctions are, now, defined for both spatial dimensions, we form a product solution of the separated functions and sum over all possible solutions:

$$\Psi(r,z,t) = \sum_{n=0}^{\infty}\sum_{m=0}^{\infty} C_{nm} J_0(\beta_m r) sin(\eta_n z) e^{-\alpha\lambda_{nm}^2 t} \tag{3.17}$$

By applying the initial conditions:

$$\Psi(t=0) = F(r,z) = \sum_{n=0}^{\infty}\sum_{m=0}^{\infty} C_{nm} J_0(\beta_m r) sin(\eta_n z) \tag{3.18}$$

To find the Fourier coefficients, we use the property of orthogonality of our two enigenfunctions over their respective intervals, by applying successively the following operators to both sides of Eq. 3.18 [183]:

$$* \int_{z=0}^{h_{mat}} sin(\eta_i z) dz \quad and * \int_{r=0}^{R_{mat}} r J_0(\beta_j r) dr \tag{3.19}$$

which yields:

$$C_{nm} = \frac{\int_{z=0}^{h_{mat}} \int_{r=0}^{R_{mat}} F(r,z) r J_0(\beta_m r) sin(\eta_n z) dr dz}{\int_{z=0}^{h_{mat}} \int_{r=0}^{R_{mat}} r J_0^2(\beta_m r) sin^2(\eta_n z) dr dz} \tag{3.20}$$

The solution of the integrals in the denominator are [135]:

$$\int_{r=0}^{R_{mat}} r J_0(\beta_m r) dr = \frac{R_{mat}}{\beta_m} J_1(\beta_m R_{mat}) \tag{3.21}$$

$$\int_{r=0}^{R_{mat}} r J_0^2(\beta_m r) dr = \frac{R_{mat}^2}{2} J_1^2(\beta_m R_{mat}) \tag{3.22}$$

$$\int_{z=0}^{h_{mat}} sin^2(\eta_n z) dz = \frac{h_{mat}}{2} \tag{3.23}$$

The solution in our general form, introducing the Fourier constants, namely,

$$\begin{aligned} \Psi(r,z,t) = &\sum_{n=0}^{\infty}\sum_{m=0}^{\infty} \frac{4 J_0(\beta_m r) sin(\eta_n z) e^{-\alpha \lambda_{nm}^2 t}}{h_{mat} R_{mat}^2 J_1^2(\beta_m R_{mat})} \\ &\times \int_{z'=0}^{h_{mat}} \int_{r'=0}^{R_{mat}} F(r',z') r' J_0(\beta_m r') sin(\eta_n z') dr' dz' \end{aligned} \tag{3.24}$$

We now reformulate the above solution into:

$$\begin{aligned} \Psi(r,z,t) = &\int_{z'=0}^{h_{mat}} \int_{r'=0}^{R_{mat}} \left[ \sum_{n=0}^{\infty}\sum_{m=0}^{\infty} \frac{4 J_0(\beta_m r) sin(\eta_n z) e^{-\alpha \lambda_{nm}^2 t}}{h_{mat} R_{mat}^2 J_1^2(\beta_m R_{mat})} J_0(\beta_m r') sin(\eta_n z') \right] \\ &\times F(r',z') r' dr' dz' \end{aligned} \tag{3.25}$$

The solution of the homogeneous problem of Eq. 3.6 in terms of Green's function is given as:

$$\Psi(r,z,t) = \int_{z'=0}^{L} \int_{r'=0}^{b} G(r,z,t|r',z',t')|_{t'=0} F(r',z') r' dr' dz' \tag{3.26}$$

By comparing this solution with Eq. 3.24, we readily conclude that $G(r,z,t|r',z',t')|_{t'=0}$ is given by:

$$G(r,z,t|r',z',t')|_{t'=0} = \sum_{n=0}^{\infty}\sum_{m=0}^{\infty} \frac{4 J_0(\beta_m r) sin(\eta_n z)}{h_{mat} R_{mat}^2 J_1^2(\beta_m R_{mat})} J_0(\beta_m r') sin(\eta_n z') e^{-\alpha \lambda_{nm}^2 t} \tag{3.27}$$

Green's function $G(r,z,t|r',z',t')$ is now determined by replacing $t$ with $t-t'$, yielding the result [183]:

$$G(r,z,t|r',z',t') = \sum_{n=0}^{\infty}\sum_{n=0}^{\infty}\sum_{m=0}^{\infty} \frac{4J_0(\beta_m r)sin(\eta_n z)}{h_{mat}R_{mat}^2 J_1^2(\beta_m R_{mat})} J_0(\beta_m r')sin(\eta_n z')e^{-\alpha\lambda_{nm}^2(t-t')} \tag{3.28}$$

Then, the solution of the non-homogeneous problem of Eq. 3.3 in terms of the above Greens's function is given, according to Eq. 3.28, as [183]:

$$\begin{aligned} T(r,z,t) = &\int_{z'=0}^{h_{mat}}\int_{r'=0}^{R_{mat}} G(r,z,t|r',z',t')|_{t'=0}F(r',z')r'dr'dz' \\ &+ \frac{\alpha}{\kappa}\int_{t'>0}^{t}\int_{z'=0}^{h_{mat}}\int_{r'=0}^{R_{mat}} G(r,z,t|r',z',t')g(r',z',t')r'dr'dz' \\ &- \alpha\int_{t'=0}^{t}\int_{z'=0}^{h_{mat}}\left[r'\frac{\partial' G(r,z,t|r',z',t')}{\partial r'}\right]_{r'=b} f(t')dt' \\ &+ \alpha\int_{t'=0}^{t}\int_{r'=0}^{R_{mat}}\left[r'\frac{\partial' G(r,z,t|r',z',t')}{\partial z'}\right]_{z'=0} f(t')dt' \\ &- \alpha\int_{t'=0}^{t}\int_{r'=0}^{R_{mat}}\left[r'\frac{\partial' G(r,z,t|r',z',t')}{\partial z'}\right]_{z'=h_{mat}} f(t')dt' \end{aligned} \tag{3.29}$$

where $f(t)$ is a prescribed temperature maintained at the boundaries. In our case, the medium is initially at room temperature with no temperature variation, and the temperature at the boundary is not maintained. So $F(r,z)=0$ and $f(t)=0$. Then, the solution of the non-homogeneous problem defined by Eq. 3.3 can then be expressed in terms of the Green's function, yielding the following integral form:

$$T(r,z,t) = \frac{\alpha}{\kappa}\int_{t'>0}^{t}\int_{z'=0}^{h_{mat}}\int_{r'=0}^{R_{mat}} G(r,z,t|r',z',t')g(r',z',t')r'dr'dz' \tag{3.30}$$

Introducing the Green's function of Eq. 3.28 into Eq. 3.30. We define the heat source as:

$$g(r',z',t') = g_V(r',z') * \prod(\frac{t'}{t_p}), \quad in \quad 0 \le r' \le a, z_0 - R_{abs} \le z' \le z_0 + R_{abs}, t \ge 0 \tag{3.31}$$

By substituting the above equation and Green's function of Eq. 3.28 into Eq. 3.30 yields the overall temperature solution:

$$\begin{aligned} T(r,z,t) =& \frac{\alpha}{\kappa}\int_{t'=0}^{t_p}\int_{z'=z_0-R_{abs}}^{z_0+R_{abs}}\int_{r'=0}^{R_{abs}}\sum_{n=0}^{\infty}\sum_{m=0}^{\infty}\frac{4J_0(\beta_m r)sin(\eta_n z)}{h_{mat}R_{mat}^2 J_1^2(\beta_m R_{mat})} \\ &\times r'J_0(\beta_m r')sin(\eta_n z')e^{-\alpha\lambda_{nm}^2(t-t')}g_V(r',z')\prod(\frac{t'}{t_p})dr'dz'dt' \\ =& \sum_{n=0}^{\infty}\sum_{m=0}^{\infty} A(\beta_m,\eta_n)J_0(\beta_m r)sin(\eta_n z)\begin{cases} 1-e^{-\alpha\lambda_{nm}^2 t} & \text{in} \quad 0 \le t \le t_p \\ (e^{\alpha\lambda_{nm}^2 t_p}-1)e^{-\alpha\lambda_{nm}^2 t} & \text{for} \quad t > t_p \end{cases} \end{aligned} \tag{3.32}$$

where $A(\beta_m, \eta_n) = \frac{8R_{abs}g_V}{\kappa h_{mat}R_{mat}^2} \frac{J_1(\beta_m R_{abs})sin(\eta_n z_0)sin(\eta_n R_{abs})}{J_1^2(\beta_m R_{mat})\lambda_{nm}^2 \beta_m \eta_n}$.

While until now, we only considered a single pulse, to model the pulse chain, we set the laser repetition rate parameter as $f_{rep}$, and a single pulse period is defined by $1/f_{rep}$. Therefore, Eq. 3.32 can be modified as:

$$T(r,z,t) = \sum_{N=1}^{\infty}\sum_{n=0}^{\infty}\sum_{m=0}^{\infty} A(\beta_m,\eta_n)J_0(\beta_m r)sin(\eta_n z) \times \begin{cases} 1 - e^{-\alpha\lambda_{nm}^2(t-\frac{1}{f_{rep}}(N-1))} & \text{in} \quad \frac{1}{f_{rep}}(N-1) \leq t \leq t_p + \frac{1}{f_{rep}}(N-1) \\ (e^{\alpha\lambda_{nm}^2 t_p} - 1)e^{-\alpha\lambda_{nm}^2(t-\frac{1}{f_{rep}}(N-1))} & \text{in} \quad t_p + \frac{1}{f_{rep}}(N-1) < t < \frac{1}{f_{rep}}N \end{cases} \tag{3.33}$$

In this section, we applied the Green's function method to solve for the temperature distribution resulting from localized heat generation within the sample. This thermal field serves as a foundational step in understanding how heterogeneous absorber distributions influence heat propagation in AFM-IR. However, it is not the temperature alone, but the resulting surface displacement—arising from thermo-elastic expansion—that determines the measured signal. To complete the description of the AFM-IR signal generation process, it is therefore essential to evaluate how the thermal field induces mechanical displacement in the sample. In the following section, we address this by solving the coupled thermo-elastic equations, establishing a direct link between localized heating and cantilever deflection.

### 3.1.2. Thermo-Elastic Equation in Cylindrical Coordinates

Following Noda et al. [184], the Navier's equations for axisymmetric thermo-elastic problems without the body forces can be expressed as:

$$\nabla^2 u_z + \frac{1}{1-2v}\frac{\partial e}{\partial z} - 2\alpha_z(\frac{1+v}{1-2v})\frac{\partial T}{\partial z} = 0 \tag{3.34}$$

where:

$$\nabla^2 = \frac{\partial^2}{\partial r^2} + \frac{1}{r}\frac{\partial}{\partial r} + \frac{\partial^2}{\partial z^2} \tag{3.35}$$

where $E$ is the material's Young's modulus, $\alpha_z$ its coefficient of linear thermal expansion, $v$ the Poisson ratio, and $e$ is the dilatation defined by the sum of strain components:

$$e = \epsilon_{xx} + \epsilon_{yy} + \epsilon_{zz} \tag{3.36}$$

The solution of Naviers equations without body forces can be expressed by Goodiers thermo-elastic displacement potential $\Phi$ and Boussinesq harmonic functions $\varphi$ and $\psi$ under the axisymmetric conditions.

$$u_z = \frac{\partial \Phi}{\partial z} + \frac{\partial \varphi}{\partial z} + z\frac{\partial \psi}{\partial z} - (3-4v)\psi \tag{3.37}$$

in which the Goodiers thermo-elastic displacement potential $\Phi$ must satisfy the governing equations:

$$\bigtriangledown^2 \Phi = KT, \tag{3.38}$$

where $K$ is the Restraint coefficient defined as [184]:

$$K = \frac{\beta}{\lambda + 2\mu} = \left(\frac{1+v}{1-v}\right)\alpha_z \tag{3.39}$$

where $\beta$ is the thermo-elastic constant, $\lambda$ and $\mu$ are the Lamé elastic constants, and $\alpha_z$ the coefficient of the linear thermal expansion. Boussinesq harmonic functions $\varphi$ and $\psi$ must satisfy the governing equations:

$$\bigtriangledown^2 \varphi = \frac{\partial^2 \varphi}{\partial r^2} + \frac{1}{r}\frac{\partial \varphi}{\partial r} + \frac{\partial^2 \varphi}{\partial z^2} = 0 \tag{3.40}$$

$$\bigtriangledown^2 \psi = \frac{\partial^2 \psi}{\partial r^2} + \frac{1}{r}\frac{\partial \psi}{\partial r} + \frac{\partial^2 \psi}{\partial z^2} = 0 \tag{3.41}$$

The components of the stress are represented by the Goodier thermo-elastic displacement potential $\Phi$ and Boussinesq harmonic functions $\varphi$, $\psi$ are:

$$\sigma_{rr} = 2G\left(\frac{\partial^2 \Phi}{\partial r^2} - KT + \frac{\partial^2 \varphi}{\partial r^2} + z\frac{\partial^2 \psi}{\partial r^2} - 2v\frac{\partial \psi}{\partial z}\right) \tag{3.42}$$

$$\sigma_{\theta\theta} = 2G\left(\frac{1}{r}\frac{\partial \Phi}{\partial r} - KT + \frac{1}{r}\frac{\partial \varphi}{\partial r} + \frac{z}{r}\frac{\partial \psi}{\partial r} - 2v\frac{\partial \psi}{\partial z}\right) \tag{3.43}$$

$$\sigma_{zz} = 2G\left[\frac{\partial^2 \Phi}{\partial z^2} - KT + \frac{\partial^2 \varphi}{\partial z^2} + z\frac{\partial^2 \psi}{\partial z^2} - 2(1-v)\frac{\partial \psi}{\partial z}\right] \tag{3.44}$$

$$\sigma_{zr} = 2G\left[\frac{\partial^2 \Phi}{\partial r \partial z} + \frac{\partial^2 \varphi}{\partial r \partial z} + z\frac{\partial^2 \psi}{\partial r \partial z} - (1-2v)\frac{\partial \psi}{\partial r}\right] \tag{3.45}$$

Referring to Eq.3.41 and 3.40, the functions $\varphi$ and $\psi$ can be expressed by use of integrals satisfying the solution form as shown on [184] under the axial symmetric condition:

$$\varphi = \sum_{n=0}^{\infty}\sum_{m=0}^{\infty} BJ_0(\beta_m r)e^{-\beta_m z} \tag{3.46}$$

$$\psi = \sum_{n=0}^{\infty}\sum_{m=0}^{\infty} C J_0(\beta_m r) e^{-\beta_m z} \tag{3.47}$$

The Goodier thermo-elastic displacement potential $\Phi$ can be expressed as:

$$\Phi(r,z,t) = \sum_{n=0}^{\infty}\sum_{m=0}^{\infty} \frac{-A(\beta_m,\eta_n)K}{\beta_m^2+\eta_n^2} J_0(\beta_m r) sin(\eta_n z)\mathcal{T}(t) \tag{3.48}$$

Substituting Eq.3.46, 3.47, and 3.48 into 3.37, the displacement becomes:

$$\begin{aligned} u_z(r,z,t)) = \sum_{n=0}^{\infty}\sum_{m=0}^{\infty}\Bigg[ & \frac{-A(\beta_m,\eta_n)K\eta_n}{\beta_m^2+\eta_n^2} J_0(\beta_m r) cos(\eta_n z)\mathcal{T}(t) \\ & + ((B+zC)\beta_m - (3-4v)C) J_0(\beta_m r) e^{-\beta_m z}\Bigg] \end{aligned} \tag{3.49}$$

The boundary conditions on the traction free surface are:

$$\sigma_{zz} = 0, \quad \sigma_{zr} = 0 \quad on \quad z = h_{mat} \tag{3.50}$$

The unknown functions $B$ and $C$ can be determined from the boundary conditions 3.50:

$$C = -\frac{A(\beta_m,\eta_n)K}{\beta_m e^{-\beta_m h_{mat}}}\left(\frac{\eta_n^2}{\beta_m^2+\eta_n^2}+1\right)\mathcal{T}(t) \tag{3.51}$$

$$B = -\frac{1-2v+h_{mat}\beta_m}{\beta_m} C \tag{3.52}$$

Substituting Eq.3.52 and 3.51 into 3.49, the displacements at surface can be simplified as:

$$u_z(r,h_{mat},t) = \sum_{n=0}^{\infty}\sum_{m=0}^{\infty} \frac{2(1+v)A(\beta_m,\eta_n)\alpha_z}{\beta_m}\left(\frac{\eta_n^2}{\beta_m^2+\eta_n^2}+1\right) J_0(\beta_m r)\mathcal{T}(t) \tag{3.53}$$

While analytical solutions offer valuable physical insight and computational efficiency, they often rely on simplifying assumptions that may not fully capture the complexity of real experimental conditions—particularly in the case of irregular geometries, material heterogeneity, or boundary conditions. To complement the analytical model and validate its predictions, we next employ FEM simulations. FEM provides a flexible and powerful numerical framework for solving the coupled thermal and mechanical equations under more realistic sample configurations. In the following section, we describe the implementation of FEM simulations used to model AFM-IR signal generation, and compare the results with those obtained from the analytical point spread function model.

### 3.1.3. Finite Element Method Simulations for Model Validation

The FEM is a powerful numerical technique for solving partial differential equations (PDEs) over complex geometries and material domains [185]. It works by discretizing a continuous domain into a finite number of smaller subdomains, or elements, over which the governing equations are approximated using local interpolation functions. This method is particularly well-suited for multi-physics problems, such as those encountered in AFM-IR, which involve coupled thermal and mechanical phenomena under nontrivial boundary and material conditions. Unlike analytical models, which often require simplifying assumptions (e.g., symmetry or idealized geometries), FEM enables accurate simulation of real-world scenarios, including heterogeneous absorber distributions, layered structures, and anisotropic material properties.

Prior to comparing the analytical model with experimental results, it is important to assess whether the model's assumptions limit its relevance to real AFM-IR conditions. To address this, we constructed a finite element model that replicates the same physical scenario under comparable parameters. This numerical simulation provides a reference against which the analytical results can be evaluated. Comparing both approaches helps reveal the effects of the approximations used in the analytical framework and clarifies how they influence the predicted AFM-IR response. Such benchmarking is essential for establishing the validity and reliability of the analytical model before applying it to experimental data.

The FEM model was developed using COMSOL Multiphysics software to simulate heat transfer and solid mechanics in heterostructures. For this purpose, we employed a two-dimensional asymmetric model, complemented by an extra-fine free triangular mesh. This approach enabled a detailed analysis of heat transfer both within the absorber and across the interfaces between different materials, allowing for precise modeling of thermal behavior in the system.

In the thermal expansion module, we coupled the *heat transfer in solids and fluids* interface with solid mechanics to accurately simulate the thermo-elastic response of the structure. The boundary conditions for this model were carefully chosen to mirror the physical setup of the system. Adiabatic boundary conditions were applied at the outer boundaries, depicted as red lines in the heat transfer model shown in Fig. 3.2a, to represent the isolation of the system. The matrix/air interface was assigned free surface boundary conditions to enable surface displacement, while the substrate/air interface was subjected to fixed constraint boundary conditions, ensuring the integrity of the substrate during thermal expansion, as illustrated in Fig. 3.2b.

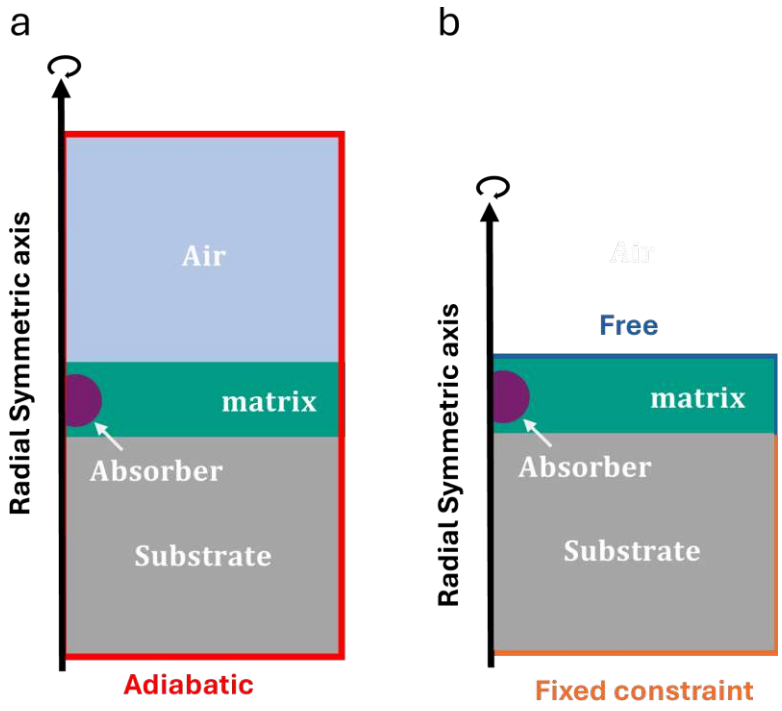


**Figure 3.2.:** (a) Boundary conditions used to model the photothermal heating in the finite element method simulations. (b) Boundary conditions used in the thermo-elastic simulations.

### 3.1.4. Comparison Analytical Model and FEM

To ensure that the assumptions underlying the analytical model did not compromise its ability to describe actual AFM-IR experiments, we compared the model's integrated temperature and surface displacement profiles with those obtained from the FEM simulation. The FEM model represents a spherical polymethyl methacrylate (PMMA) absorber embedded in a polyethylene (PE) matrix on a silicon (Si) substrate (see Fig. 3.2). The absorber and matrix were assigned literature values for the thermal and mechanical properties of PMMA and PE, respectively (see Table 3.1). Unlike a perfect heat sink assumption for the substrate, we modeled a 5 µm-thick Si layer, and instead of an insulating boundary at the cover layer, heat dissipation through thermal diffusion in air (5 µm) was included. The material parameters used for the simulations are listed in Supplementary Table 3.1. Unless otherwise stated, the following parameters remained constant in both FEM and PSF models: absorber radius $R_{abs} = 70\,\text{nm}$, matrix thickness $h_{mat} = 1\,\mu\text{m}$, the matrix radius is $R_{mat} = 5\,\mu\text{m}$ (see Fig. 3.1a for a sketch of the sample geometry). The simulations consider a peak laser power of 4.5 mW, and a beam diameter $r_{laser} = 10\,\mu\text{m}$.

Both models yielded nearly identical integrated temperature values across all tested pulse widths (see Fig. 3.3a for results at 100 ns, 300 ns, and 500 ns). Similarly, the surface displacement trends showed strong agreement between the two models as a function of pulse width (Fig. 3.3b). In both cases, integrated temperature and surface displacement increased with pulse width. However, the surface displacement profile was significantly broader than the temperature profile, confirming that the absorber's thermo-elastic displacement exhibits a non-linear relationship with temperature due to the inhomogeneous heat source distribution, which induces non-uniform strains in adjacent materials.

Both models also revealed distinct dependencies of integrated temperature and surface displacement on absorber depth (Fig. 3.3c,d). When the absorber was positioned closer to the surface, the surface displacement exhibited higher amplitude and a narrower profile. In contrast, the shape of the integrated temperature profile was mainly governed by heat diffusion, becoming narrower when the absorber was closer to the substrate.

Overall, the PSF model of AFM-IR shows strong agreement with the FEM simulations, with a mean percentage difference below 3 % for integrated temperature and displacement data across all tested pulse widths and absorber depths (see Fig. 3.4). This confirms that the simplifications in the PSF models are valid and do not significantly impact its accuracy.

**Table 3.1.:** Parameters used in finite-difference time domain model and PSF model of AFM-IR simulations. The thermal, mechanical and thermo-mechanical properties are listed below.

| Property* | PMMA | PE | air | silicon |
|---|---|---|---|---|
| absorption coefficient (1/cm) | 960 [186] | - | - | - |
| coefficient of thermal expansion (1/k) | $193.6 \times 10^{-6}$ [187] | $150 \times 10^{-6}$ [188] | - | $2.6 \times 10^{-6}$ [189] |
| thermal conductivity (W/(m· k)) | 0.192 [190] | 0.25 [191] | 0.025 [192] | 130 [189] |
| density ($kg/m^3$) | 1190 [193] | 930 [194] | 1.2 [192] | 2329 [189] |
| heat capacity (J/(kg·k)) | 1420 [195] | 1900 [196] | 1015 [192] | 700 [189] |
| Young's modulus (GPa) | 2.4 [197] | 1 [194] | - | 170 [198] |
| Poisson's ratio | 0.37 [197] | 0.46 [194] | - | 0.28 [198] |

*These values are treated as exact numbers for the purpose of simulations.

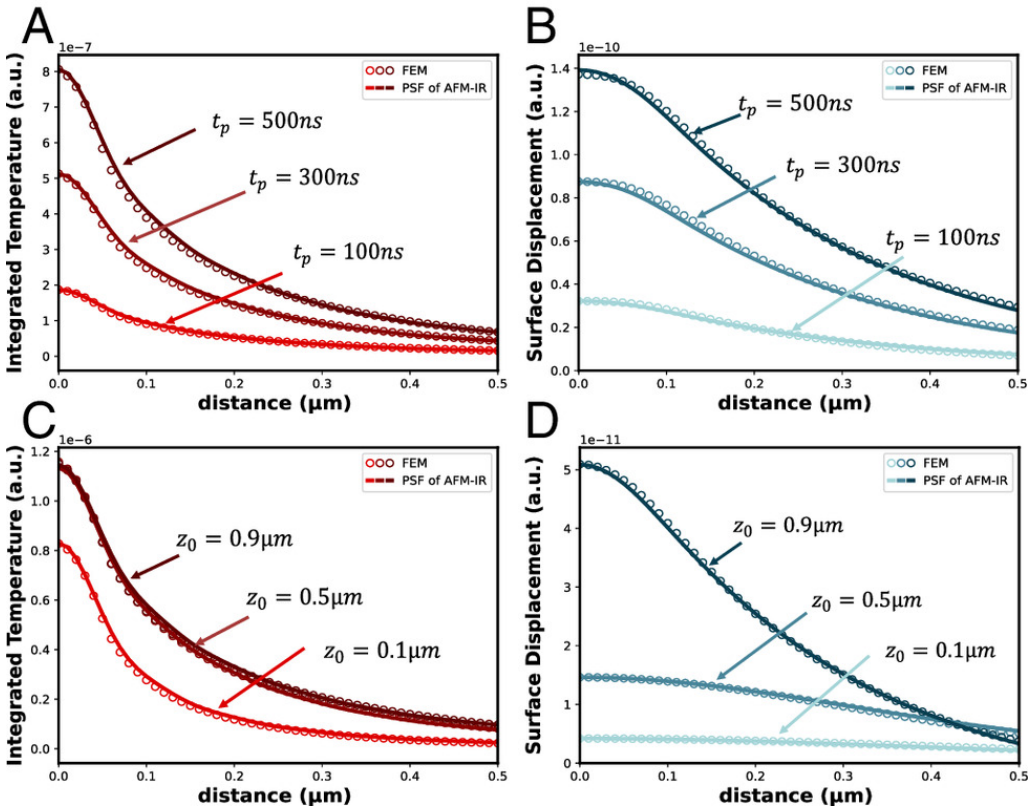


**Figure 3.3.:** Integrated temperature and displacement profiles for varying laser pulse widths and absorber depths. Temperature and thermo-elastic displacement profiles are analyzed under different excitation conditions using the analytical model from [103]. a) Temperature distribution and (b) resulting thermoelastic surface displacement are shown for three different laser pulse widths: 100 ns, 400 ns, and 500 ns, with the absorber positioned at a depth of $z_0 = 0.9\,\mu m$. c) Temperature distribution and (d) surface displacement are plotted for three absorber depths: $z_0 = 0.9\,\mu m$, $0.5\,\mu m$ and $0.1\,\mu m$, under a fixed pulse width of 100 ns. All cases assume a laser repetition rate of 500 kHz.

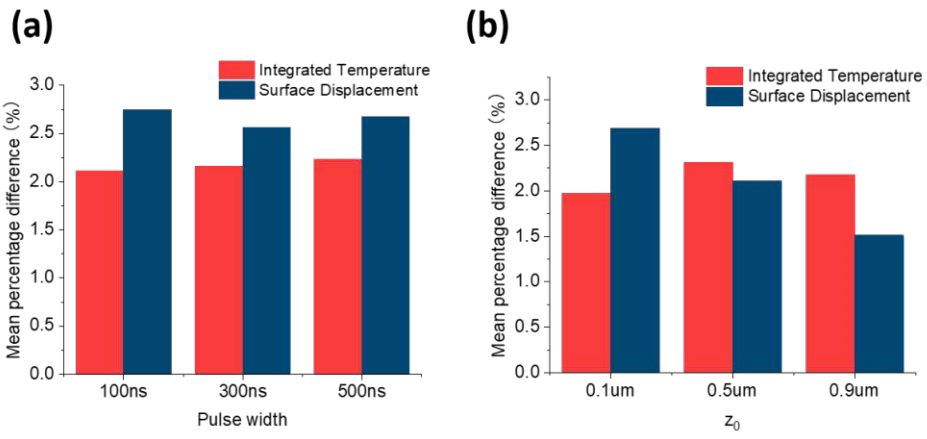


**Figure 3.4.:** Mean percentage difference analysis of integrated temperature and displacement between the PSF model of AFM-IR and the FEM simulations for the tested pulse widths and depth positions of the absorber.

## 3.2. One Dimensional Photothermal Model

In the previous section, we presented the development of a two-dimensional photothermal model suitable for heterogeneous sample structures. While this model captures essential features of spatially varying absorption and thermal diffusion, it does not explicitly account for one of the most practically relevant geometries: multilayer thin-film systems. Such systems are widely encountered in material science, electronics, and biosensing, where multiple stacked layers interact thermally and mechanically under IR excitation. Notably, many existing models neglect the influence of the underlying substrate, often assuming idealized heat sink boundary conditions at the bottom of the domain. While this simplification facilitates analytical treatment, it can overlook important thermal feedback effects from the substrate, particularly in thin or thermally insulating films.

To address this, we introduce in this section a general analytical framework for multilayer thin-film structures under varied boundary conditions, enabling a more accurate description of the coupled thermal and thermo-elastic response in layered systems. By exploiting rotational symmetry in the heat equation, we reduce the spatial dimensionality of the problem, simplifying both analytical and numerical analyses. In particular, axisymmetric conditions transform the full three dimensional heat diffusion problem into an effectively one dimensional form, which not only speeds up computation but also allows for more straightforward implementation of boundary conditions.

Therefore, we now consider a sandwich structure consisting of two distinct homogeneous materials, denoted as materials A and B, occupying the region $0 \leq z \leq L_3$, and both characterized by low thermal conductivity. This layered region is deposited on a substrate of thickness $L$ spanning the region $L_3 \leq z \leq L_4$, and is covered with air in the region $-\infty \leq z \leq 0$. We analyze a one-dimensional heat conduction problem within this finite layered structure. The upper surface at $z = 0$ and the lower boundary at $z = L4$ are exposed to air, establishing appropriate boundary conditions. The complete structure thus comprises three distinct layers, as illustrated schematically in Figure 3.5.

The sample is initially at a temperature distribution given by $F(z)$. For time $t > 0$, the entire volume of the structure is illuminated by an excitation laser, resulting in internal heat generation throughout the volume. This internal heating process is mathematically described by the heating function g(z,t), presenting the spatial and temporal distribution of energy absorption within the structure.

$$g(z,t) = g \cdot \prod(\frac{t}{t_p}) \cdot e^{-\beta z} \tag{3.54}$$

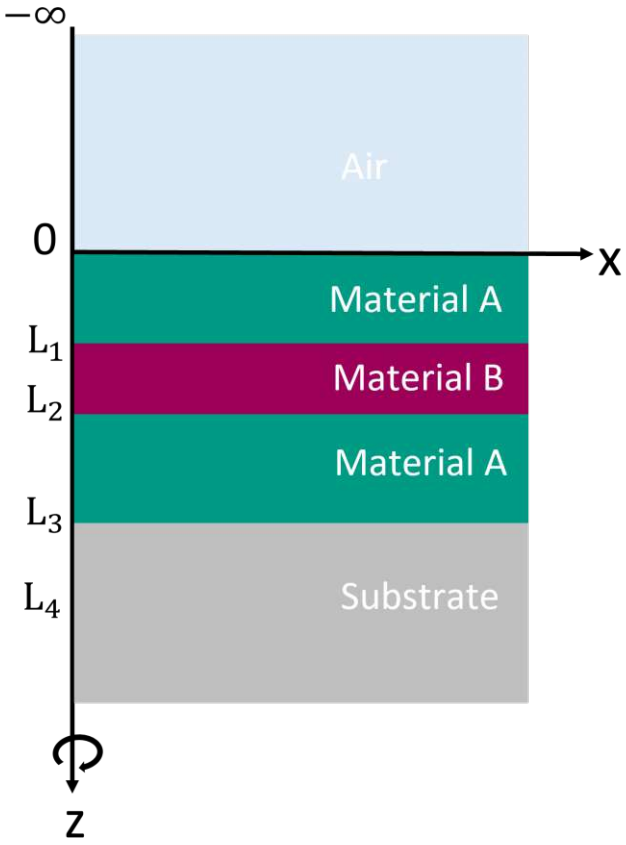


**Figure 3.5.:** Schematic figure of the multilayer sample geometry

Here, $g$ is a constant heat source term proportional to the optical absorption coefficient, the excitation laser power, and the optical fluence area. The temporal profile of the excitation laser pulse is represented by the function $\prod(\frac{t}{t_p})$, where $t_p$ is the pulse width. Additionally, the spatial decay of optical energy penetration into the sample is described by the exponential function $e^{-\beta z}$, where $\beta$ is the optical penetration coefficient.

In the following analysis, we divide the system into three distinct regions:

1. **Region 1** $(0 \leq z \leq L_3)$: the sandwich structure containing the heat source,
2. **Region 2** $(L_3 \leq z \leq L_4)$: the substrate layer without internal heating,
3. **Region 3** $(-\infty \leq z \leq 0)$: air, also without internal heating.

The mathematical formulation of this problem is given as:

In Region 1:

$$\frac{\partial^2 T_1(z,t)}{\partial z^2} + \frac{g(z,t)}{\kappa_1} = \frac{1}{\alpha_1}\frac{\partial T_1(z,t)}{\partial t} \tag{3.55}$$

In Region 2:

$$\frac{\partial^2 T_2(z,t)}{\partial z^2} = \frac{1}{\alpha_2}\frac{\partial T_2(z,t)}{\partial t} \tag{3.56}$$

In Region 3:

$$\frac{\partial^2 T_3(z,t)}{\partial z^2} = \frac{1}{\alpha_3}\frac{\partial T_3(z,t)}{\partial t} \tag{3.57}$$

where $\alpha_i (i = 1, 2, 3)$ denotes the thermal diffusivity in each region.

Initial and boundary conditions are:

$$\begin{aligned}
&BC1: \quad -\kappa_1 \frac{\partial T_1}{\partial z}|_{z=0} = -\kappa_3 \frac{\partial T_3}{\partial z}|_{z=0} \quad \text{continuity of heat flux at interface} \\
&BC2: \quad T_1(0,t) = T_3(0,t) \quad \text{continuity of temperature at interface} \\
&BC3: \quad T_3(z=-\infty) = 0 \quad \text{no temperature change at infinity} \\
&BC4: \quad T_1(L_3,t) = T_2(L_3,t) \quad \text{continuity of temperature at interface} \\
&BC5: \quad -\kappa_1 \frac{\partial T_1}{\partial z}|_{z=L_3} = -\kappa_2 \frac{\partial T_2}{\partial z}|_{z=L_3} \quad \text{continuity of heat flux at interface} \\
&BC6: \quad \frac{\partial T_2}{\partial z}|_{z=L_4} = 0 \quad \text{air is insulating at the bottom interface} \\
&IC: \quad T_1(z,t=0) = F(z) \quad \text{initial conditions}
\end{aligned} \tag{3.58}$$

where $\kappa_i (i = 1, 2, 3)$ is the thermal conductivity in each region.

The general approach involves solving the homogeneous heat conduction equation to obtain the Green's function in Region 1, which accounts for the response of the system to localized heat sources under the specified boundary conditions.

$$\frac{\partial^2 \Psi_1(z,t)}{\partial z^2} = \frac{1}{\alpha_1}\frac{\partial \Psi_1(z,t)}{\partial t} \quad in \quad 0 \le z \le L_3 \tag{3.59}$$

With the boundary condition homogeneous, we assume a separation of the form:

$$\Psi_1(z,t) = Z_1(z)\Gamma_1(t) \tag{3.60}$$

Substitution of equation 3.60 into 3.59 yields:

$$\frac{1}{Z_1}\frac{d^2 Z_1}{dz^2} = \frac{1}{\alpha_1 \Gamma_1}\frac{d\Gamma_1}{dt} = -\lambda^2 \tag{3.61}$$

This equation introduces the separation constant $\lambda$. The resulting ODE in the time dimension yields the solution:

$$\Gamma_1(t) = C_1 e^{-\alpha_1 \lambda^2 t} \tag{3.62}$$

while the space-variable ODE produces the solution:

$$Z_1(z) = C_2 \cos \lambda z + C_3 \sin \lambda z \tag{3.63}$$

Since the heat equation in Region 3 (air region) is homogeneous and the temperature decays with increasing depth (BC3), we adopt the same analytical approach used for Region 1 to obtain the corresponding Green's function.

$$\Psi_3(z,t) = Z_3(z)\Gamma_3(t) = Z_3(z)C_4 e^{-\alpha_3\lambda^2 t} \tag{3.64}$$

and

$$Z_3(z) = C_5 e^{-\lambda z} \tag{3.65}$$

In Region 2,

$$\Psi_2(z,t) = Z_2(z)\Gamma_2(t) = Z_2(z)C_6 e^{-\alpha_2\lambda^2 t} \tag{3.66}$$

and

$$Z_2(z) = C_7 \cos\lambda(z - L_3) + C_8 \sin\lambda(z - L_3) \tag{3.67}$$

Applying BC1 and BC2, we have

$$\begin{aligned} \kappa_1(\lambda C_3) &= \kappa_3(-\lambda C_5) \\ C_2 &= C_5 \end{aligned} \tag{3.68}$$

Rearranging,

$$Z_1(z) = C_2(\cos\lambda z - \frac{\kappa_3}{\kappa_1}\sin\lambda z) \tag{3.69}$$

and

$$Z_3(z) = C_2 e^{-\lambda z} \tag{3.70}$$

Typically, the thermal conductivity of air ($0.0284\,\mathrm{W/(m\,K)}$)[199] is significantly lower than that of polymer materials, which generally range from $0.11\,\mathrm{W/(m\,K)}$ to $0.44\,\mathrm{W/(m\,K)}$[200].

### 3.2.1. Thermal Conductivity of Materials Significantly Exceeds that of Air

In the case where the thermal conductivity of the materials in Region 1 significantly exceeds that of air, the term involving the ratio $\frac{\kappa_3}{\kappa_1}$ becomes negligible. Under this assumption, Eq. 3.69 simplifies to:

$$Z_1(z) = C_2 \cos\lambda z \tag{3.71}$$

Applying BC4, BC5 and BC6, we have:

$$\begin{aligned} &C_2 \cos\lambda L_3 = C_7 \\ &\kappa_1(-\lambda C_2 \sin\lambda L_3) = \kappa_2(\lambda C_8) \\ &\lambda(-C_7 \sin\lambda(L_4 - L_3) + C_8 \cos\lambda(L_4 - L_3)) = 0 \end{aligned} \tag{3.72}$$

Rearranging, and replacing the difference $L_4 - L_3$ by the substrate thickness $L$:

$$\begin{aligned} C_7 &= C_2 \cos\lambda L_3 \\ C_8 &= -\frac{\kappa_1}{\kappa_2} C_2 \sin\lambda L_3 \end{aligned} \tag{3.73}$$

The eigenfunctions in all regions are governed by the following differential equations:

$$\tan \lambda_n L = -\frac{\kappa_1}{\kappa_2} \tan \lambda_n L_3, \quad \text{n=1,2,3..} \tag{3.74}$$

Taking Eq. 3.73 into Eq. 3.67, yielding

$$Z_2(z) = C_2(\cos \lambda L_3 \cos \lambda(z - L_3) - \frac{\kappa_1}{\kappa_2} \sin \lambda L_3 \sin \lambda(z - L_3)) \tag{3.75}$$

Common substrates used in AFM-IR, such as silicon (139.4 W/(mK)), ZnO (50 W/(mK)), SiN (30 W/(mK)), ZnS (25.1 W/(mK)), and $CaF_2$ (9.71 W/(mK)), typically have thermal conductivities significantly greater (often by more than an order of magnitude) than those of polymer samples. Consequently, the term involving the ratio $\frac{\kappa_1}{\kappa_2}$ approaches zero. Under this assumption, Eq. 3.74 simplifies to the following non-trivial solution:

$$\sin \lambda_n L = 0 \tag{3.76}$$

Which gives the eigenvalues:

$$\lambda_n = \frac{n\pi}{L}, \quad \text{n=1,2,3,...} \tag{3.77}$$

This approximation results in a boundary condition of zero temperature change at the sample-substrate interface, effectively treating the substrate as an ideal heat sink.

The sum over all possible mode solutions, yielding

$$\Psi_1(z,t) = \sum_{n=0}^{\infty} c_n cos\lambda_n z e^{-\alpha\lambda_n^2 t} \tag{3.78}$$

Where $c_n = C_1C_2$. Application of the initial condition yields the Fourier integral expansion of the initial temperature distribution F(z), namely,

$$F(z) = \sum_{n=0}^{\infty} c_n cos\lambda_n z \tag{3.79}$$

Multiply both sides by the orthogonal function for an arbitrary eigenvalue, say $cos\lambda_i z$:

$$* \int_{z=0}^{L_3} cos\lambda_i z dz \tag{3.80}$$

This operation eliminates all terms of the summation except one, yielding:

$$c_n = \frac{2}{L_3} \int_{z'=0}^{L_3} F(z') cos\lambda_n z' dz' \tag{3.81}$$

Substitution of equation 3.81 into equation 3.78 yields the expression:

$$\Psi_1(z,t) = \frac{2}{L_3} \int_{z'=0}^{L_3} F(z') \sum_{n=0}^{\infty} e^{-\alpha\lambda_n^2 t} cos\lambda_n z cos\lambda_n z' dz' \tag{3.82}$$

Now we consider a Green's function approach for the solution, which takes the form of:

$$\Psi_1(z,t) = \frac{2}{L_3}\int_{z'=0}^{L_3} F(z')G(z,t|z',\tau)dz' \tag{3.83}$$

By comparing equation 3.83 with equation 3.82, we readily conclude that $G(z,t|z',\tau)|_{\tau=0}$ is given by:

$$G(z,t|z',\tau)|_{\tau=0} = \frac{2}{L_3}\sum_{n=0}^{\infty} e^{-\alpha\lambda_n^2 t} cos\lambda_n z cos\lambda_n z' \tag{3.84}$$

Green's function $G(z,t|z',\tau)$ is now determined by replacing $t$ with $t-\tau$ in equation 3.84, yielding the result:

$$G(z,t|z',\tau) = \frac{2}{L_3}\sum_{n=0}^{\infty} e^{-\alpha\lambda_n^2 (t-\tau)} cos\lambda_n z cos\lambda_n z' \tag{3.85}$$

Then the solution of the non-homogeneous problem of equation (3.3) in terms of the above Green's function without prescribed boundary temperature is given as[183]:

$$\begin{aligned} T(z,t) = &\int_{z'=0}^{\infty} G(z,t|z',\tau)|_{\tau=0} F(z')dz' \\ &+ \frac{\alpha}{\kappa_1}\int_{\tau=0}^{t}\int_{z'=L_1}^{L_2} G(z,t|z',\tau)g(z',\tau)dz' \\ &+ \alpha\sum_{1}^{N}\left\{\int_{\tau=0}^{t} G(z,t|z',\tau)|z' = z_i\frac{1}{k}f_i(\tau)d\tau\right\} \end{aligned} \tag{3.86}$$

Where $f(t)$ is a prescribed temperature maintained at the boundaries. In our case, the system starts at uniform room temperature, and no boundary temperature is enforced. Therefore, we assume zero initial and boundary conditions, setting $F(r,z) = 0$, $f(t) = 0$. The resulting solution $T(z,t)$ then describes the temperature evolution driven purely by internal heat sources. Tthe solution of the non-homogeneous problem defined by Eq. 3.3, which is given in terms of the Green's function becomes in variable form:

$$T(z,t) = \frac{\alpha}{\kappa_1}\int_{\tau=0}^{t}\int_{z'=L_1}^{L_2} G(z,t|z',\tau)g(z',\tau)dz'd\tau \tag{3.87}$$

Substitution of the above and Green's function 3.85 into equation 3.87 yielding the overall temperature solution:

$$\begin{aligned} T_1(z,t) &= \frac{\alpha_1}{\kappa_1}\int_{\tau=0}^{t}\int_{z'=L_1}^{L_2}\frac{2}{L_3}\sum_{n=0}^{\infty} e^{-\alpha_1\lambda_n^2(t-\tau)} cos\lambda_n z cos\lambda_n z' g\prod(\frac{\tau}{t_p})e^{-\beta(z'-L_1)}dz'd\tau \\ &= \frac{2g\alpha_1}{\kappa_1 L_3}\cdot\sum_{n=0}^{\infty}\int_{\tau=0}^{t} e^{-\alpha_1\lambda_n^2(t-\tau)}\prod(\frac{\tau}{t_p})d\tau\cdot cos\lambda_n z\int_{z'=L_1}^{L_2} cos\lambda_n z' e^{-\beta(z'-L_1)}dz' \end{aligned} \tag{3.88}$$

Time dependent function $\Gamma_1(t)$:

$$\Gamma_1(t) = \int_{\tau=0}^{t} e^{-\alpha_1\lambda_n^2(t-\tau)} \prod(\frac{\tau}{t_p})d\tau = \frac{1}{\alpha_1\lambda_n^2} \begin{cases} 1 - e^{-\alpha_1\lambda_n^2 t} & \text{in} \quad 0 \le t \le t_p \\ (e^{\alpha_1\lambda_n^2 t_p} - 1)e^{-\alpha_1\lambda_n^2 t} & \text{for} \quad t > t_p \end{cases} \tag{3.89}$$

Space dependent function $I_n(z)$:

$$I_n = cos\lambda_n z \int_{z'=L_1}^{L_2} cos\lambda_n z' e^{-\beta(z'-L_1)} dz' \tag{3.90}$$

Let set:

$$u = z' - L_1 \Rightarrow du = dz' \tag{3.91}$$

$$u = z' - L_1 \Rightarrow du = dz' \tag{3.92}$$

Rewriting the Eq. 3.90 in terms of $u$:

$$\begin{aligned} I_n &= cos\lambda_n z \int_{u=0}^{L_2-L_1} cos\lambda_n(u + L_1)e^{-\beta u} du \\ &= cos\lambda_n z(\cos\lambda_n L_1 \int_{u=0}^{L_2-L_1} cos\lambda_n u e^{-\beta u} du - \sin\lambda_n L_1 \int_{u=0}^{L_2-L_1} sin\lambda_n u e^{-\beta u} du) \\ &= cos\lambda_n z(I_1 + I_2) \end{aligned} \tag{3.93}$$

Where:

$$\begin{aligned} I_1 &= \cos\lambda_n L_1 \int_{u=0}^{L_2-L_1} cos\lambda_n u e^{-\beta u} du \\ &= \cos\lambda_n L_1 (\frac{\lambda_n \sin\lambda_n(L_2 - L_1) - \beta\cos\lambda_n(L_2 - L_1)}{\lambda_n^2 + \beta^2} e^{-\beta(L_2-L_1)} + \frac{\beta}{\lambda_n^2 + \beta^2}) \end{aligned} \tag{3.94}$$

$$\begin{aligned} I_2 &= -\sin\lambda_n L_1 \int_{u=0}^{L_2-L_1} sin\lambda_n u e^{-\beta u} du \\ &= \sin\lambda_n L_1 (\frac{\lambda_n \cos\lambda_n(L_2 - L_1) + \beta\sin\lambda_n(L_2 - L_1)}{\lambda_n^2 + \beta^2} e^{-\beta(L_2-L_1)} - \frac{\lambda_n}{\lambda_n^2 + \beta^2}) \end{aligned} \tag{3.95}$$

Now we adding up $I_1$ and $I_2$:

$$\begin{aligned} I_1 + I_2 = (&\frac{\lambda_n(\cos\lambda_n L_1 \sin\lambda_n(L_2 - L_1) + \sin\lambda_n L_1 \cos\lambda_n(L_2 - L_1)}{\lambda_n^2 + \beta^2} \\ &+ \frac{\beta(\sin\lambda_n L_1 \sin\lambda_n(L_2 - L_1) - \cos\lambda_n L_1 \cos\lambda_n(L_2 - L_1))}{\lambda_n^2 + \beta^2})e^{-\beta(L_2-L_1)} \\ &+ \frac{\beta\cos\lambda_n L_1 - \lambda_n \sin\lambda_n L_1}{\lambda_n^2 + \beta^2} \\ = &\frac{\lambda_n(\sin\lambda_n L_2 e^{-\beta(L_2-L_1)} - \sin\lambda_n L_1) + \beta(\cos\lambda_n L_1 - \cos\lambda_n L_2 e^{-\beta(L_2-L_1)})}{\lambda_n^2 + \beta^2} \end{aligned} \tag{3.96}$$

In the case of small penetration coefficient, in which case, $\beta = 0$ can be applied, then Eq. 3.96 can be simplified to:

$$I_1 + I_2 = \frac{\sin \lambda_n L_2 - \sin \lambda_n L_1}{\lambda_n} \tag{3.97}$$

The corresponding temperature distributions in Region 2 and 3, the solutions are:

$$T_2(z,t) = (I_1 + I_2) Z_2(z) \sum_{n=0}^{\infty} \int_{\tau=0}^{t} e^{-\alpha_2 \lambda_n^2 (t-\tau)} \prod (\frac{\tau}{t_p}) d\tau \tag{3.98}$$

$$T_3(z,t) = Z_3(z) \sum_{n=0}^{\infty} \int_{\tau=0}^{t} e^{-\alpha_3 \lambda_n^2 (t-\tau)} \prod (\frac{\tau}{t_p}) d\tau \tag{3.99}$$

Solving the temperature distribution in both air (Region 2) and substrate (Region 3) is essential because these layers govern how heat dissipates from the absorbing region. The air layer influences surface cooling, while the high-conductivity substrate acts as a thermal sink that limits temperature rise in the sample. Together, they determine the degree of thermal confinement and directly impact both the amplitude and spatial resolution of the AFM-IR signal.

### 3.2.2. Thermal Conductivity of Materials Comparable to that of Air

When the thermal conductivity of the materials is comparable to that of air, the term involving the ratio $\frac{\kappa_3}{\kappa_1}$ cannot be neglected. The eigenfunction in Region 1 is given by the following solution:

$$Z_1(z) = C_2(\cos \lambda z - \frac{\kappa_3}{\kappa_1} \sin \lambda z) \tag{3.100}$$

Applying BC4, BC5 and BC6, we have:

$$\begin{aligned} &C_2(\cos \lambda L_3 - \frac{\kappa_3}{\kappa_1} \sin \lambda L_3) = C_7 \\ &\kappa_1(-\lambda C_2 \sin \lambda L_3 - \lambda C_2 \frac{\kappa_3}{\kappa_1} \cos \lambda L_3) = \kappa_2(\lambda C_8) \\ &\lambda(-C_7 \sin \lambda L + C_8 \cos \lambda L) = 0 \end{aligned} \tag{3.101}$$

Rearranging, we have the eigensolutions governed by:

$$\tan \lambda_n L = -\frac{1}{\kappa_2} \frac{\kappa_1 \tan \lambda_n L_3 + \kappa_3}{\kappa_1 - \kappa_3 \tan \lambda_n L_3} \tag{3.102}$$

The eigenfunctions in Region 2 is given by:

$$Z_2(z) = C_2[(\cos \lambda_n L_3 - \frac{\kappa_3}{\kappa_1} \sin \lambda_n L_3) \cos \lambda_n (z - L_3) - \frac{\kappa_1}{\kappa_2} (\sin \lambda_n L_3 + \frac{\kappa_3}{\kappa_1} \cos \lambda_n L_3) \sin \lambda_n (z - L_3)] \tag{3.103}$$

Sum over all possible mode solutions in Region 1, yielding:

$$\Psi_1(z,t) = \sum_{n=0}^{\infty} c_n(\cos\lambda_n z - \frac{\kappa_3}{\kappa_1}\sin\lambda z)e^{-\alpha\lambda_n^2 t} \tag{3.104}$$

Where $c_n = C_1C_2$. The application of the initial condition yields the Fourier integral expansion of the initial temperature distribution F(z), namely,

$$F(z) = \sum_{n=0}^{\infty} c_n(\cos\lambda_n z - \frac{\kappa_3}{\kappa_1}\sin\lambda_n z) \tag{3.105}$$

Multiply both sides by the orthogonal function for an arbitrary eigenvalue, say $cos\lambda_i z$:

$$* \int_{z=0}^{L_3} (\cos\lambda_i z - \frac{\kappa_3}{\kappa_1}\sin\lambda_i z)dz \tag{3.106}$$

This operation eliminates all terms of the summation except one:

$$A_n = \frac{L_3}{2}(1 + \frac{k_3^2}{k_1^2}) \tag{3.107}$$

Yielding:

$$c_n = \frac{1}{A_n}\int_{z'=0}^{L_3} F(z')(\cos\lambda z' - \frac{\kappa_3}{\kappa_1}\sin\lambda z')dz' \tag{3.108}$$

Substitution of equation 3.81 into equation 3.104 yields the expression:

$$\Psi_1(z,t) = \frac{1}{A_n}\int_{z'=0}^{L_3}\sum_{n=0}^{\infty} F(z')(\cos\lambda z - \frac{\kappa_3}{\kappa_1}\sin\lambda z)(\cos\lambda z' - \frac{\kappa_3}{\kappa_1}\sin\lambda z')dz'e^{-\alpha\lambda_n^2 t} \tag{3.109}$$

Green's function $G(z,t|z',\tau)$ is given by:

$$G(z,t|z',\tau) = \frac{1}{A_n}\sum_{n=0}^{\infty} e^{-\alpha\lambda_n^2(t-\tau)}(\cos\lambda z - \frac{\kappa_3}{\kappa_1}\sin\lambda z)(\cos\lambda z' - \frac{\kappa_3}{\kappa_1}\sin\lambda z') \tag{3.110}$$

The overall temperature solution is:

$$\begin{aligned} T_1(z,t) &= \frac{\alpha_1}{\kappa_1}\int_{\tau=0}^{t}\int_{z'=L_1}^{L_2}\frac{1}{A_n}\sum_{n=0}^{\infty}(\cos\lambda z - \frac{\kappa_3}{\kappa_1}\sin\lambda z)(\cos\lambda z' - \frac{\kappa_3}{\kappa_1}\sin\lambda z') \\ &\quad \times e^{-\alpha_1\lambda_n^2(t-\tau)}g\prod(\frac{\tau}{t_p})e^{-\beta(z'-L_1)}dz'd\tau \\ &= \frac{g\alpha_1}{\kappa_1 A_n}\cdot\sum_{n=0}^{\infty}\int_{\tau=0}^{t} e^{-\alpha_1\lambda_n^2(t-\tau)}\prod(\frac{\tau}{t_p})d\tau \\ &\quad \times (\cos\lambda z - \frac{\kappa_3}{\kappa_1}\sin\lambda z)\int_{z'=L_1}^{L_2}(\cos\lambda z' - \frac{\kappa_3}{\kappa_1}\sin\lambda z')e^{-\beta(z'-L_1)}dz' \end{aligned} \tag{3.111}$$

Space dependent function $I_n(z)$:

$$I_n = (\cos\lambda z - \frac{\kappa_3}{\kappa_1}\sin\lambda z)\int_{z'=L_1}^{L_2}(\cos\lambda z' - \frac{\kappa_3}{\kappa_1}\sin\lambda z')e^{-\beta(z'-L_1)}dz' \tag{3.112}$$

Let set:

$$u = z' - L_1 \Rightarrow du = dz' \tag{3.113}$$

Rewriting the Eq. 3.112 in terms of $u$:

$$\begin{aligned} I_n &= (\cos\lambda z - \frac{\kappa_3}{\kappa_1}\sin\lambda z)\int_{u=0}^{L2-L1}(cos\lambda_n(u+L1) - \frac{\kappa_3}{\kappa_1}\sin\lambda(u+L1))e^{-\beta u}du \\ &= (\cos\lambda z - \frac{\kappa_3}{\kappa_1}\sin\lambda z)(I_1 - \frac{\kappa_3}{\kappa_1}I_2) \end{aligned} \tag{3.114}$$

Where:

$$\begin{aligned} I_1 &= \int_0^{L_2-L_1}\cos\lambda(u+L_1)e^{-\beta u}du \\ &= \frac{\lambda_n(\sin\lambda_n L_2 e^{-\beta(L2-L1)} - \sin\lambda_n L_1) + \beta(\cos\lambda_n L1 - \cos\lambda_n L_2 e^{-\beta(L2-L1)})}{\lambda_n^2+\beta^2} \end{aligned} \tag{3.115}$$

$$\begin{aligned} I_2 &= \int_0^{L_2-L_1}\sin\lambda(u+L_1)e^{-\beta u}du \\ &= -\cos\lambda L_1(\frac{\lambda_n\cos\lambda_n(L2-L1)+\beta\sin\lambda_n(L2-L1)}{\lambda_n^2+\beta^2}e^{-\beta(L2-L1)} - \frac{\lambda_n}{\lambda_n^2+\beta^2}) \\ &\quad + \sin\lambda L_1(\frac{\lambda_n\sin\lambda_n(L2-L1)-\beta\cos\lambda_n(L2-L1)}{\lambda_n^2+\beta^2}e^{-\beta(L2-L1)} + \frac{\beta}{\lambda_n^2+\beta^2}) \\ &= \frac{\lambda_n(-\cos\lambda_n L_2 e^{-\beta(L2-L1)} + \cos\lambda_n L_1) + \beta(\sin\lambda_n L1 - \sin\lambda_n L_2 e^{-\beta(L2-L1)})}{\lambda_n^2+\beta^2} \end{aligned} \tag{3.116}$$

Combining $I_1$ and $I_2$:

$$I_n = (\cos\lambda z - \frac{\kappa_3}{\kappa_1}\sin\lambda z)(I_1 - \frac{k_3}{k_1}I_2) \tag{3.117}$$

In Region 2, the final solution is:

$$T_2(z,t) = (I_1 - \frac{k_3}{k_1}I_2)Z_2(z)\sum_{n=0}^{\infty}\int_{\tau=0}^{t}e^{-\alpha_2\lambda_n^2(t-\tau)}\prod(\frac{\tau}{t_p})d\tau \tag{3.118}$$

## 3.3. One Dimensional Photoacoustic Model

Having discussed the photothermal effects in the previous section, we now turn our focus to the photoacoustic phenomena. Unlike the direct thermal effects, which primarily involve the thermal expansion of the material, the photoacoustic effect arises from the rapid absorption of light followed by acoustic wave generation due to the rapid thermal expansion. This distinction is crucial for understanding the broader implications of light-matter interactions in nanoscale sensing applications.

Although the photoacoustic effect was not the primary focus of this thesis, we developed a one-dimensional photoacoustic model tailored for liquid samples to complement our photothermal analysis. This simplified model captures the essential physics of acoustic wave generation and propagation following pulsed IR absorption in fluid environments. While preliminary in scope, it lays the groundwork for future studies aimed at integrating photoacoustic detection with AFM-based techniques, particularly in scenarios where acoustic contrast may offer additional chemical or structural information beyond what is accessible through thermal expansion alone.

Building upon the previous discussion of thermal effects, we now introduce the thermal effect equation of motion in solids, as described by Achenbach [201]. This equation provides a framework for understanding how thermal energy influences the mechanical behavior of materials, particularly in the context of photoacoustic and photothermal phenomena. The equation is:

$$(\lambda + \mu)\nabla\nabla \cdot \mathbf{u} + \mu\nabla^2\mathbf{u} - \alpha(3\lambda + 2\mu)\nabla T + \rho\mathbf{f} = \rho\ddot{\mathbf{u}} \tag{3.119}$$

Where $\lambda$ and $\mu$ are the Lame elastic constants, $\mathbf{f}$ is the external force and $\rho$ is the density of the sample.

If we consider our samples are in liquids and no external force applies in our case, then the shear waves can be neglected ($\mu = 0$), and the equation 3.119 can be simplified as:

$$\lambda\nabla\nabla \cdot \mathbf{u} - 3\alpha\lambda\nabla T = \rho\ddot{\mathbf{u}} \tag{3.120}$$

Taking differentiate in time on both side of the above equation, we obtain:

$$\lambda\nabla\nabla \cdot \dot{\mathbf{u}} - 3\alpha\lambda\nabla\dot{T} = \rho\,\ddot{\mathbf{u}} \tag{3.121}$$

In the following, we define the velocity potential $\dot{\mathbf{u}} = \nabla\varphi$, the pressure $p = -\rho\dot{\varphi}$, the velocity $c^2 = \lambda/\rho$, and the volumetric thermal-elastic constant $\beta = 3\alpha$. The equation 3.121 can, then, be rewritten as:

$$\lambda\nabla\nabla \cdot \nabla\varphi - \beta\lambda\nabla\dot{T} = \rho\nabla\ddot{\varphi} \tag{3.122}$$

We integrate in volume from both side, one $\nabla$ will be cancelled, then differentiate in time again on both side:

$$\lambda\nabla^2\dot{\varphi} - \beta\lambda\ddot{T} = \rho\,\dddot{\varphi} \tag{3.123}$$

Replacing $\dot{\varphi}$ by $-p/\rho$, we have:

$$\lambda\nabla^2(-p/\rho) - \beta\lambda\ddot{T} = -\ddot{p} \tag{3.124}$$

Then:

$$\ddot{p} - c^2\nabla^2 p = \beta\lambda\ddot{T} = \frac{3\alpha c^2}{\rho}\ddot{T} \tag{3.125}$$

We can write the wave equation with a general heat source in one-dimension Cartesian coordinates:

$$p_{tt} - c^2 p_{zz} = f(z,t) \tag{3.126}$$

Suppose the arbitrary boundary conditions:

$$p(z,0) = \phi(z) \tag{3.127}$$

$$p_t(z,0) = \psi(z) \tag{3.128}$$

We use the superposition principle to expect the solution of equation 3.83 be the form:

$$p(z,t) = p^p(z,t) + p^h(z,t) \tag{3.129}$$

Where $p^p(z,0)$ is a *particular solution* of equation 3.126 satisfying homogeneous boundary conditions:

$$p^p(z,0) = 0 \tag{3.130}$$

$$p^p_t(z,0) = 0 \tag{3.131}$$

And $p^h(z,t)$ is a solution of the corresponding: *homogeneous equation*

$$\begin{aligned} p^h_{tt} - c^2 P^h_{zz} &= 0 \\ p^h(z,0) &= \phi(z) \\ p^h_t(z,0) &= \psi(z) \end{aligned} \tag{3.132}$$

The general solution of the homogeneous part of the solution is given by:

$$p^h(z,t) = \frac{1}{2}(\phi(z+ct) + \phi(z-ct)) + \frac{1}{2c}\int_{z-ct}^{z+ct}\psi(\tau)d\tau \tag{3.133}$$

And the particular part of the solution is:

$$p^p(z,t) = \frac{1}{2c}\int_0^t\int_{z-c(t-s)}^{z+c(t-s)} f(y,s)dyds \tag{3.134}$$

The temperature change is the heat source of the pressure wave, so the function $f(z,t) = \frac{3\alpha c^2}{\rho} f(z)f(t)$ should take the form as equation 3.97:

$$f(z) = \frac{2\alpha g}{\kappa L \lambda_n^3} cos\lambda_n z(sin\lambda_n L_2 - sin\lambda_n L_1) \tag{3.135}$$

$$f(t) = \begin{cases} -\alpha^2 \lambda_n^4 e^{-\alpha\lambda_n^2 t} & \text{in} \quad 0 \le t \le t_p \\ \\ \alpha^2 \lambda_n^4 (e^{\alpha\lambda_n^2 t_p} - 1) e^{-\alpha\lambda_n^2 t} & \text{for} \quad t > t_p \end{cases} \tag{3.136}$$

Both the temperature and pressure variations are zero at the initial condition, therefore:

$$\begin{aligned} \phi(z) &= 0 \\ \psi(z) &= 0 \end{aligned} \tag{3.137}$$

Then,

$$p^h(z,t) = 0 \tag{3.138}$$

In this case, we don't have a solution to the homogeneous wave equation with inhomogeneous boundary conditions. And:

$$\begin{aligned} p^p(z,t) &= \frac{1}{2c} \int_0^t \int_{z-c(t-s)}^{z+c(t-s)} f(y,s) dy ds \\ &= \frac{1}{2c} \int_0^t \frac{2\alpha g}{\kappa L \lambda_n^3} * \frac{3\alpha c^2}{\rho} \frac{1}{\lambda_n} sin(\lambda_n y)|_{z-c(t-s)}^{z+c(t-s)} (sin\lambda_n L_2 - sin\lambda_n L_1) f(s) ds \\ &= \frac{6\alpha^2 cg}{\kappa \rho L \lambda_n^4} cos\lambda_n z(sin\lambda_n L_2 - sin\lambda_n L_1) \int_0^t sin\lambda_n c(t-s) f(s) ds \\ &= \frac{6\alpha^4 cg}{\kappa \rho L} cos\lambda_n z(sin\lambda_n L_2 - sin\lambda_n L_1) \begin{cases} -e^{-\alpha\lambda_n^2 t} & \text{in} \quad 0 \le t \le t_p \\ \\ (e^{\alpha\lambda_n^2 t_p} - 1) e^{-\alpha\lambda_n^2 t} & \text{for} \quad t > t_p \end{cases} \end{aligned} \tag{3.139}$$

The solution of the integrals are:

$$\begin{aligned} \int_0^t sin\lambda_n c(t-s) ds &= \int_0^t (sin\lambda_n ct cos\lambda_n cs - cos\lambda_n ct sin\lambda_n cs) ds \\ &= \frac{1}{\lambda_n c} (sin\lambda_n ct * sin\lambda_n ct + cos\lambda_n ct * (cos\lambda_n ct - 1)) \\ &= \frac{1}{\lambda_n c} (1 - cos\lambda_n ct) \end{aligned} \tag{3.140}$$

$$
\begin{aligned}
\int cos\lambda_n cse^{-\alpha\lambda_n^2 s}ds &= \frac{1}{\lambda_n c}\int_0^t e^{-\alpha\lambda_n^2 s}dsin\lambda_n cs \\
&= \frac{1}{\lambda_n c}(e^{-\alpha\lambda_n^2 s}sin\lambda_n cs + \alpha\lambda_n^2\int_0^t e^{-\alpha\lambda_n^2 s}sin\lambda_n csds) \\
&= \frac{1}{\lambda_n c}(e^{-\alpha\lambda_n^2 s}sin\lambda_n cs - \frac{\alpha\lambda_n}{c}\int_0^t e^{-\alpha\lambda_n^2 s}dcos\lambda_n cs) \\
&= \frac{1}{\lambda_n c}(e^{-\alpha\lambda_n^2 s}sin\lambda_n cs - \frac{\alpha\lambda_n}{c}e^{-\alpha\lambda_n^2 s}cos\lambda_n cs - \frac{\alpha^2\lambda_n^3}{c}\int_0^t e^{-\alpha\lambda_n^2 s}cos\lambda_n csds)) \\
&= \frac{e^{-\alpha\lambda_n^2 s}(c * sin\lambda_n cs - \alpha\lambda_n^2 cos\lambda_n cs)}{\lambda_n(c^2+\alpha^2\lambda_n^2)}
\end{aligned}
\tag{3.141}
$$

$$
\begin{aligned}
\int sin\lambda_n cse^{-\alpha\lambda_n^2 s}ds &= -\frac{1}{\lambda_n c}\int_0^t e^{-\alpha\lambda_n^2 s}dcos\lambda_n cs \\
&= -\frac{1}{\lambda_n c}(e^{-\alpha\lambda_n^2 s}cos\lambda_n cs + \alpha\lambda_n^2\int_0^t e^{-\alpha\lambda_n^2 s}cos\lambda_n sds) \\
&= -\frac{1}{\lambda_n c}(e^{-\alpha\lambda_n^2 s}cos\lambda_n cs + \frac{\alpha\lambda_n}{c}\int_0^t e^{-\alpha\lambda_n^2 s}dsin\lambda_n cs) \\
&= -\frac{1}{\lambda_n c}(e^{-\alpha\lambda_n^2 s}cos\lambda_n cs + \frac{\alpha\lambda_n}{c}e^{-\alpha\lambda_n^2 s}sin\lambda_n cs + \frac{\alpha^2\lambda_n^3}{c}\int_0^t e^{-\alpha\lambda_n^2 s}sin\lambda_n csds) \\
&= -\frac{e^{-\alpha\lambda_n^2 s}(c * cos\lambda_n cs + \alpha\lambda_n^2 sin\lambda_n cs)}{\lambda_n(c^2+\alpha^2\lambda_n^2)}
\end{aligned}
\tag{3.142}
$$

For $0 < t \leq t_p$:

$$
\begin{aligned}
A &= \int_0^t sin\lambda_n c(t-s)e^{-\alpha\lambda_n^2 s}ds \\
&= (sin\lambda_n ct\int_0^t cos\lambda_n cse^{-\alpha\lambda_n^2 s}ds - cos\lambda_n ct\int_0^t sin\lambda_n cse^{-\alpha\lambda_n^2 s}ds) \\
&= (sin\lambda_n ct\frac{e^{-\alpha\lambda_n^2 s}(c * sin\lambda_n cs - \alpha\lambda_n^2 cos\lambda_n cs)}{\lambda_n(c^2+\alpha^2\lambda_n^2)}|_0^t + cos\lambda_n ct\frac{e^{-\alpha\lambda_n^2 s}(c * cos\lambda_n cs + \alpha\lambda_n sin\lambda_n^2 cs)}{\lambda_n(c^2+\alpha^2\lambda_n^2)}|_0^t) \\
&= \frac{c * e^{-\alpha\lambda_n^2 t} + \alpha\lambda_n^2 sin\lambda_n ct - c * cos\lambda_n ct}{\lambda_n(c^2+\alpha^2\lambda_n^2)}
\end{aligned}
\tag{3.143}
$$

For $t > t_p$:

$$
\begin{aligned}
B &= \int_0^{t_p} sin\lambda_n c(t-s)(e^{\alpha\lambda_n^2 t_p}-1)e^{-\alpha\lambda_n^2 s}ds \\
&= (e^{\alpha\lambda_n^2 t_p}-1)(sin\lambda_n ct\frac{e^{-\alpha\lambda_n^2 s}(c*sin\lambda_n cs-\alpha\lambda_n^2 cos\lambda_n cs)}{\lambda_n(c^2+\alpha^2\lambda_n^2)}|_0^{t_p} \\
&\quad + cos\lambda_n ct\frac{e^{-\alpha\lambda_n^2 s}(c*cos\lambda_n cs+\alpha\lambda_n sin\lambda_n cs)}{\lambda_n(c^2+\alpha^2\lambda_n^2)}|_0^{t_p}) \\
&= (e^{\alpha\lambda_n^2 t_p}-1)\frac{e^{-\alpha\lambda_n^2 t_p}(c*cos\lambda_n c(t-t_p)+\alpha\lambda_n^2 sin\lambda_n c(t_p-t))+\alpha\lambda_n^2 sin\lambda_n ct-c*cos\lambda_n ct}{\lambda_n(c^2+\alpha^2\lambda_n^2)}
\end{aligned}
\tag{3.144}
$$

Now, if we add A and B, we will obtain the complete solution of the equation 3.139:

$$
p^p(z,t) = \frac{6\alpha^4 cg}{\kappa\rho L}cos\lambda_n z(sin\lambda_n L_2 - sin\lambda_n L_1)\begin{cases} A \quad \text{in} \quad 0 \le t \le t_p \\ \\ B \quad \text{for} \quad t > t_p \end{cases} \tag{3.145}
$$

Together, these derivations yield a one-dimensional photoacoustic model that captures the temporal and spatial evolution of acoustic pressure in liquid environments, providing a foundational framework for interpreting photoacoustic signal generation in AFM-based measurements.

# 4. Introduction to the Publications

## 4.1. An Analytical Model of Label-Free Nanoscale Chemical Imaging

AFM-IR spectroscopy has emerged as a powerful technique for nanoscale chemical imaging, enabling spatial resolutions beyond the diffraction limit [46, 22, 88]. By combining the high spatial resolution of AFM with the chemical specificity of infrared spectroscopy, AFM-IR provides unique insights into the composition and structure of a wide range of samples, including polymers [96, 97], biological tissues [54, 50, 98], and nanomaterials [99, 100]. Despite the technique's growing relevance, understanding and predicting the factors influencing AFM-IR signal generation and spatial resolution remain challenging, especially when dealing with complex, inhomogeneous samples [124, 126, 125].

Existing theoretical models have contributed valuable perspectives on signal formation mechanisms. Dazzi et al. [1, 2] introduced foundational models focused on homogeneous samples, while Morozovska et al. [3] and Schwartz et al. [4] expanded the understanding to interfaces and temporal dynamics. However, these models often fall short when addressing samples composed of absorbers embedded within a matrix—a common scenario in practical applications such as imaging organelles within cells [202] or detecting contaminants in polymer films [203]. These complex sample geometries introduce additional variables, including interfacial thermal resistance [204, 205] and heterogeneous thermal and mechanical properties, that significantly influence the AFM-IR response.

This publication presents the development and validation of a point spread function (PSF) model for AFM-IR, providing an analytical framework to describe the entire signal generation process. The model accounts for light absorption, photothermal expansion, and subsequent detection by the AFM cantilever, incorporating critical factors such as absorber size, position, and the surrounding matrix properties. By employing Green's functions [135], the PSF model delivers exact mathematical solutions while maintaining computational efficiency superior to conventional FEM simulations.

Experimental validation and FEM comparisons confirm the PSF model's accuracy, demonstrating strong agreement in predicting how parameters like laser pulse width, modulation frequency, and sample composition affect signal amplitude and spatial resolution. Notably, the model highlights the dominant role of demodulation frequency in controlling spatial resolution [4], independent of pulse width, and underscores the significance of interfacial thermal resistance in interpreting AFM-IR signals [91, 206].

Beyond enhancing fundamental understanding, the PSF model offers practical advantages for experimental optimization and opens avenues for advanced AFM-IR techniques, including surface-sensitive imaging [21], tapping mode AFM-IR [21], and frequency-

dependent tomography. By bridging theoretical rigor with experimental applicability, this work provides a versatile tool for researchers seeking to exploit the full potential of AFM-IR in nanoscale chemical imaging. This work has been published in The Proceedings of the National Academy of Sciences (PNAS) (https://doi.org/10.1073/pnas.2403079122).

# Analytical model of label-free nanoscale chemical imaging reveals avenues towards improved spatial resolution and sensitivity.

**Yide Zhang**[a,c], **Ufuk Yilmaz**[a], **Gustavo Vinicius Bassi Lukasievicz**[d], **Liam O'Faolain**[c], **Bernhard Lendl**[a], **and Georg Ramer**[a,b,1]

This manuscript was compiled on April 11, 2025

**Atomic force microscopy-infrared spectroscopy (AFM-IR) is a photothermal scanning probe technique that combines nanoscale spatial resolution with the chemical analysis capability of mid-infrared spectroscopy. Using this hybrid technique, chemical identification down to the single molecule level has been demonstrated. However, the mechanism at the heart of AFM-IR, the transduction of local photothermal heating to cantilever deflection, is still not fully understood. Existing physical models only describe this process in few special cases but not in many of the types of sample geometries encountered in the practical use of AFM-IR. In this work an analytical expression for modeling the temperature and photothermal expansion process is introduced, verified with finite element simulations and validated with AFM-IR experiments. This method describes AFM-IR signal amplitudes in vertically and laterally heterogeneous samples and allows studying the effect of position and size of an absorber, pump laser repetition rate and pulse width on AFM-IR signal amplitudes and spatial resolution.**

**The analytical model can be used to identify optimal AFM-IR experimental settings in conventional and advanced AFM-IR modes (e.g., tapping mode, surface sensitive mode). The model also paves the way for signal inversion based super-resolution AFM-IR.**

Atomic force microscopy-infrared | nanoscale chemical imaging | analytical modeling | photothermal expansion

## Significance Statement

AFM-IR is a widely used scanning probe technique for label-free photothermal nanoscale chemical imaging, with diverse applications spanning single protein spectroscopy to analyzing nanoscale chemical, physical, and optical phenomena. However, the understanding of spatial resolution of the technique is limited to few specific, simple geometries (spheres, pillars, etc.). We introduce an analytical model of AFM-IR verified by numerical simulations and experiments that describes experimental data well for complex sample geometries. The model allows to reason about the spatial resolution and sensitivity of the technique and can give guidance for optimizing experimental parameter for sensitivity and resolution and interpreting results. Beyond this, it can be a stepping stone towards super-resolution AFM-IR or nanoscale chemical tomography.

AFM-IR is a near-field technique combining atomic force microscopy (AFM) and mid-infrared (IR) spectroscopy, which achieves nanoscale spatial resolution optical imaging independent of the wavelength (1–3) and thus enables chemical analysis based on infrared spectroscopy orders if magnitude below the diffraction limit (4–8).

A typical AFM-IR setup consists of a pulsed laser focused onto a sample at the location of the tip of an AFM cantilever (see Figure 1a). In general, the working principle of this technique (2, 9) is described by focusing on the change of the sample's density, which induces a localized sample expansion. The partial or total absorption of light from the pulsed laser by molecules distributed in the sample results in a local temperature increase affecting the density and refractive index of the sample at the place of absorption. A train of laser pulses will thus generate a modulated temperature change in the sample leading to photothermal and photoacoustic waves that propagate within the sample. AFM-IR employs the the spatially resolved detection of the photothermal expansion of the sample by the AFM's cantilever upon illumination with a pulsed light source (see Figure 1b).

Absorption of light from the laser pulse leads to local temperature increase and concurrent thermal expansion (Figure 1c). As the heat is redistributed within the sample this local expansion subsides.

Using a laser with adjustable pulse repetition rate, the mechanical resonances of the cantilever can selectively be excited (10) when the laser repetition rate matches the selected mode of the cantilever. In this scenario, the photothermal expansion stimulates the AFM cantilever at its oscillation's resonance frequency (Figure 1d), hereby selectively amplifying the AFM-IR signal which can be demodulated from the AFM deflection signal.

This general working principle is well accepted in the community and the ability of AFM-IR for chemical imaging is well established, with applications ranging from materials (11, 12) to biological samples (6, 13, 14) and photonics, perovskites (15), and semiconductors (2, 16). Several groups have studied the AFM-IR imaging contrast mechanism. The initial theoretical description of AFM-IR signal generation and transduction was established by Dazzi et al. (17, 18),

Author affiliations: [a]Institute of Chemical Technologies and Analytics, TU Wien, Vienna, 1060, Austria; [b]Christian Doppler Laboratory for Advanced MIR Laser Spectroscopy in (Bio-)Process Analytics, TU Wien, Vienna, 1060, Austria; [c]Centre for Advanced Photonics and Process Analysis, Munster Technological University, Cork, T12P928, Ireland; [d]Department of Physics, Universidade Tecnológica Federal do Paraná, Medianeira PR 85884-000, Brazil

Y.Z. and U.Y. prepared samples, performed experiments and drafted the manuscript. Y.Z. performed FEM simulations and developed the PSF model with input from G.R.. G.R. supervised U.Y. and Y.Z. in all experiments and evaluations. G. V. B. L. provided support in thermal modeling. G.R., L.O'F. and B.L. conceptualized the study, proposed the project and acquired the funding. All authors have read and revised the manuscript.

The authors declare no competing interest..

[1]To whom correspondence should be addressed. E-mail: georg.ramer@tuwien.ac.at

who considered a homogeneous sample without accounting for geometry, illuminated with single pulse laser. While this model does not describe the spatial resolution of AFM-IR, it shows that the thermal expansion is linearly proportional to the local absorption.

Later, Morozovska et al., studied the contrast formation mechanism of T-shape boundary between two materials in nanoscale IR spectroscopy (19). In this model, using two semi-infinite materials with an interface orthogonal to the AFM scanning plane temperature distribution and mechanical displacement of both absorber and the neighboring material is described, taking into account various factors, including different IR-radiation absorption coefficients, thermo-physical and elastic properties of the two materials. These properties encompass thermal diffusivities, thermal conductivities, and elastic stiffness, as well as thermal expansion coefficients. This model indicates higher modulation frequency would provide a significantly higher spatial resolution. Schwartz et al. (20) devised an analytical model to depict the photothermal expansion of a homogenous sample, factoring in a single laser pulse. They considered the laser heating profile and performed numerical simulations on heterogeneous samples comprising two adjacent materials. This study aimed to elucidate the dependence of signal transduction efficiency and spatial resolution on laser pulse width, pulse shape, sample thermalization time and interfacial thermal resistance, etc. and found this model in good agreement with their previous experimental investigations (21, 22).

However, in many cases AFM-IR samples do not conform to the geometries described in literature. Particularly, many samples consist of absorbers embedded within a larger matrix, such as inclusion bodies inside a cell (23), metal soaps in paint layers (24) or even organelles (25).

Interpreting AFM-IR signals poses a challenge due to sample heterogeneity. This challenge - often overlooked - requires deconvolution of the signal generation from sample contributions. Our study addresses this crucial aspect, emphasizing its significance not only for AFM-IR but also for scanning probe techniques in a more broad sense.

In the present work, we develop a model describing the whole AFM-IR signal generation process, starting with light absorption by an absorber embedded in a matrix until detection of the sample's surface expansion. This model takes into account thermal and mechanical properties of materials, as well as the size and position of the absorber. The vertically and laterally inhomogeneous sample comprising an analyte embedded in a matrix is relevant to a wide range of common AFM-IR applications such as the detection of organelles within a cell (26) or contamination within a polymer layer (27).

Our approach uses an analytical description of the time-dependent heating and sample deformation based on Green's functions. This model is a better match to real-world problems encountered in the life and material sciences than previously described analytical models, such as lumped linear proportional models. It provides exact mathematical expressions for the variables of interest, yielding clear insights into their relationships in an easily interpretable form. While models based on finite element modeling (FEM) are able to incorporate more details, here, our approach excels in computational efficiency.

This Green's function approach, whereby the response of a system to an excitation is determined by convolving the distribution of the absorbers and the time domain shape of the pump laser pulse with a system response function has some interesting parallels to signal processing and optical microscopy: along the temporal axis, the sample can be understood to act as a low pass filter upon the excitation pulse shape and in the spatial dimension, our model exhibits similarities to a point spread function (PSF) that is typically used to understand and characterize spatial resolution in optical imaging. Thus, this "PSF model of AFM-IR" enables us to directly compare the spatial resolution in optical imaging techniques and with those achieved in AFM-IR. Furthermore, it allows the efficient modeling of the response of samples with arbitrary absorber distribution.

To arrive at a PSF model of AFM-IR that can be algebraically handled, certain assumptions regarding the sample geometry and properties need to be made. To ensure the validity of these assumptions, we compare the PSF model to finite element simulations which we can validate against experimental AFM-IR data. Through this validation process, we observe a strong agreement between the PSF model of AFM-IR, finite element simulations, and experimental results.

With the validated PSF model of AFM-IR, we are able to make general predictions regarding the spatial resolution and signal intensity in AFM-IR. Specifically, we can investigate how these parameters are influenced by factors such as the pulse width and repetition rate of the excitation laser, as well as the thermal and mechanical properties of the sample. By leveraging the PSF model, we gain valuable insights into the fundamental aspects of AFM-IR and its performance characteristics.

We show that this model will help to understand how experimental parameters (pulse rate, pulse width, sample stiffness, sample geometry,...) influence the performance of advanced AFM-IR techniques, such as tapping mode AFM-IR (28), or the recently introduced surface sensitive AFM-IR (29).

## Results and discussion

**Modeling the AFM-IR signal.** In laterally homogeneous samples, the surface expansion is proportional to the temperature change of the sample after a laser pulse, hence for such samples the signal can fairly accurately be described if only sample heating and thermal conduction are taken into account (7). However, to study spatial resolution in AFM-IR, models that describe laterally heterogeneous samples are required. Here, surface displacement also depends on the elastic response of the sample (19), as the inhomogeneous, absorber distribution dependent heating and creates inhomogeneous strain in the neighboring material. There are three components in our description of AFM-IR: transient laser heating of the sample, heat conduction within the sample and thermo-elastic deformation of the sample.

More specifically, laser heating is described as a time-dependent volumetric heat source $g(\mathbf{x},t)$, where $\mathbf{x}$ represents any location in the domain. Thermal conduction is described by Fourier's law

$$\nabla^2 T(\mathbf{x},t) + \frac{1}{\kappa} g(\mathbf{x},t) = \frac{1}{\alpha}\frac{\partial T(\mathbf{x},t)}{\partial t} \qquad [1]$$

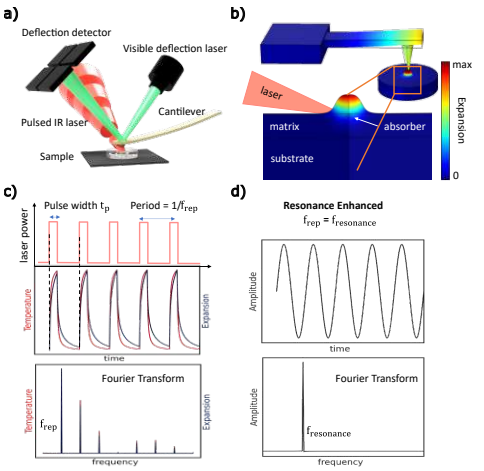


**Fig. 1. Schematic illustration of the resonance enhanced AFM-IR. a)** Sketch illustrating the AFM-IR setup. The sample is placed on a piece of silicon (gray) and illuminated from the top with a pulsed, tunable, infrared beam (red). **b)** The sample location that absorbs the energy of IR laser which is then transformed into temperature change and thermal expansion. The sample's photothermal expansion excites the cantilever into oscillations. **c)** In the excitation process, temperature and expansion increase during the pulse time ($t_p$) and repeat the same process with the repetition frequency ($f_{rep}$). The signal in frequency domain will only present at the $f_{rep}$ and it's higher order modes . While operating AFM-IR at contact mode, in the resonance-enhanced operation **d)**, $f_{rep}$ matches the selected resonance frequency of the cantilever to resonantly exciting it, thereafter, the enhanced AFM-IR signal is proportional to the mode's quality factor.

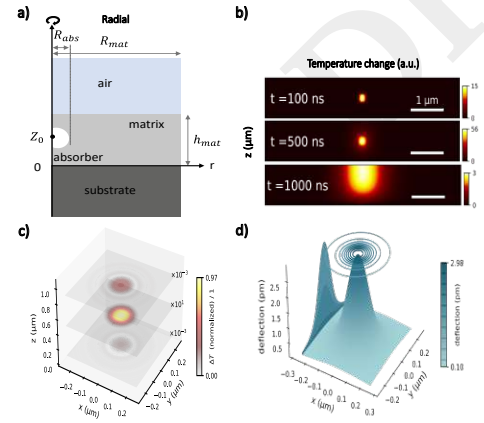


**Fig. 2. Using the PSF model to describe the AFM-IR signal: a)** Schematic of the modeled, cylindrically symmetric system composed of a single spherical absorber surrounded by a matrix, deposited on a non-absorbing substrate. **b)** Lateral and vertical temperature change at different times during and after illumination with 500 ns length laser pulse. (Absorber position at $z_0$ = 0.5 µm). **c)** Amplitude of temperature change at several depths in the sample. **d)** Amplitude of thermo-elastic displacement at the surface. At 500 kHz and a pulse width of 500 ns.

where $\kappa$ is the thermal conductivity and $\alpha$ is the thermal diffusivity. In the equilibrium state, thermo-elastic sample deformation without external force is described by Navier's equations of thermoelasticity (30),

$$\mu \bigtriangledown^2 \mathbf{u}_i + (\lambda + \mu) \frac{\partial e}{\partial \mathbf{x}_i} - \beta \frac{\partial T(\mathbf{x}, t)}{\partial \mathbf{x}_i} = 0 \qquad [2]$$

where $e$ is dilatation, $i \in \{1, 2, 3\}$ are indices of Cartesian coordinates, $\lambda$ and $\mu$ are the Lamé elastic constants, and $\beta$ is the thermo-elastic constant. The AFM-IR signal is proportional to the surface displacement. Depending on the type of transducer either the amplitude of displacement at a specific frequency (4) or the time-dependent surface displacement (10) is recorded in AFM-IR. Considering the insignificance of the photoacoustic signal in AFM-IR measurements compared to the photothermal signal, along with its tendency to introduce artifacts (29), we have made the decision not to include it in the current model.

Assuming the system is in thermal equilibrium before excitation with a laser pulse, its response is determined through convolution of $g(\mathbf{x}', t)$ with a Green's function $G(\mathbf{x}, t|\mathbf{x}', t')$. Green's function represents the temperature at any location $\mathbf{x}$ within the domain, at any time $t$, due to an instantaneous volumetric source, located at the position $\mathbf{x}'$, releasing its energy spontaneously at time $t = t'$ into a medium at steady-state conditions. To find $G$ and solve Eq. (1) and Eq. (2), we use assumptions that have been previously shown to describe the thermal behavior of AFM-IR experiments well (7): (1) the sample is a homogeneous material of known thickness that is (2) placed on a substrate acting as a heat sink and (3) covered by an insulating layer (air) (see Figure 2a).

In the following sections we will first develop the analytical model, then verify that our model does not give significantly different results from a model that uses finite thermal conductivities for the cover layer and the substrate, by comparing the results from the analytical model with those calculated using a finite element model (FEM).

Model results are additionally compared to experimental AFM-IR data of a polymethyl methacrylate (PMMA) absober embedded in a polyethylene (PE) matrix. In the discussion section, we intend to present predictions regarding the resolution and signal intensity dependencies on the depth positions of the absorber, its size and the repetition rates of the laser.

The FEM simulations take into account additional factors, heat transfer between different materials, temperature distribution, thermal expansion in equilibrium states, and interfacial thermal conductance in agreement with other work (9, 20, 31). For AFM-IR experiments, we prepared samples with PMMA beads embedded in PE matrix, and performed a series measurements with different laser pulse widths and repetition rates.

**A Green's function solution describing the AFM-IR signal.** We choose a cylindrical coordinate system, for two reasons: in analogy to PSFs, it allows an axisymmetric, quasi-2D representation that is more illustrative than a three-dimensional one, without loss of generality, and has significantly lower computational cost for FEM modeling, required for comparison.

The heat equation in cylindrical coordinates reads

$$\frac{\partial^2 T(r,z,t)}{\partial r^2}+\frac{1}{r}\frac{\partial T(r,z,t)}{\partial r}+\frac{\partial^2 T(r,z,t)}{\partial z^2}+\frac{g(r,z,t)}{\kappa}=\frac{1}{\alpha}\frac{\partial T(r,z,t)}{\partial t} \quad [3]$$

using a finite, axisymmetric cylindrical sample of radius $R_{mat}$ and height $h_{mat}$. Using the boundary conditions as outlined in the previous section the canonical Green's function solution (32) is

$$T(r,z,t)=\frac{\alpha}{\kappa}\int_{t'=0}^{t}\int_{z'=0}^{h_{mat}}\int_{r'=0}^{R_{mat}} G(r,z,t|r',z',t') \times g(r',z',t')r'dr'dz'dt' \quad [4]$$

with a Green's function

$$G(r,z,t|r',z',t')=\sum_{n=0}^{\infty}\sum_{m=0}^{\infty}\frac{4J_0(\beta_m r)sin(\eta_n z)}{h_{mat}R_{mat}^2 J_1^2(\beta_m R_{mat})} \times J_0(\beta_m r')sin(\eta_n z')e^{-\alpha\lambda_{nm}^2(t-t')} \quad [5]$$

where $\beta_m$, $\eta_n$ and $\lambda_{mn}$ are eigenvalues obtained according to boundary conditions (see Supplementary section S1). While $G$ contains an infinite sum of modes, the decay time of each mode is $1/\alpha\lambda_{mn}^2$, which decreases as integer values $m$ and $n$ increase. Hence, the sum can be truncated once sufficiently short time scales have been reached.

The overall sample deformation in AFM-IR is on the order of picometers (7) and experimental parameters are chosen to not change sample properties (e.g. not to cause phase transitions or damage to the sample) during the experiment. Hence, we can split the time-dependent, volumetric heat source in to a spatial and a temporal component $g(\mathbf{x},t)=g_V(\mathbf{x})g_t(t)$. The time domain variation in the illumination intensity is described by $g_t(t)$, while $g_V(\mathbf{x})$ describes the location and intensity of heating, i.e., location and magnitude of light absorption inside the sample (in the following discussion, we neglect optical effects such as interference upon the signal. These effects can be added by multiplying the absorption coefficient with the local light intensity to arrive at a modified $g_V$ (32)). Splitting $g(\mathbf{x},t)$ allows us to also split the convolution in Eq. (5) into two parts, one that describes the mode amplitude and shape in $r$ and $z$, and one that describes the time domain behaviour of each mode:

$$T(r,z,t)=\sum_{n=0}^{\infty}\sum_{m=0}^{\infty}A(\beta_m,\eta_n)\underbrace{J_0(\beta_m r)sin(\eta_n z)}_{\text{spatial}}\underbrace{\mathcal{T}_{nm}(t)}_{temporal} \quad [6]$$

where $A(\beta_m,\eta_n)$ depends on the correlation between $g_V(r,z)$ and $J_0(\beta_m r)sin(\eta_n z)$ and

$$\mathcal{T}_{nm}(t)=\int_{t'=0}^{t}g_t(t')e^{-\alpha\lambda_{nm}^2(t-t')}dt' \quad [7]$$

i.e. the convolution of $g_t(t)$ and $e^{-\alpha\lambda_{nm}^2 t}$. $g_V(r,z)$ is the product of the optical absorption coefficient and the optical fluence, as defined in Eq. (S2). By utilizing Eq. (6), we can generate spatial temperature distributions within the absorber and matrix at various time points (Figure 2b). In frequency domain $\mathcal{T}$ is the product of the Fourier transforms of $g_t(t)$ and $e^{-\alpha\lambda_{nm}^2 t}$, allowing an easy way to study location dependent amplitudes of temperature changes (see Figure 2c).

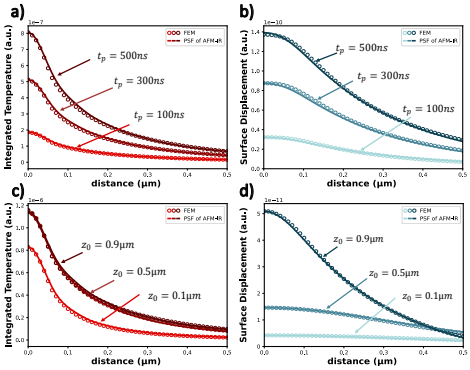


**Fig. 3. Integrated temperature and displacement profile for three different laser pulse widths and depth positions of the absorber. a)** Temperature profile and **b)** thermo-elastic displacement profile are examined for three different pulse widths at a laser repetition rate of 500 kHz. The absorber is positioned at a depth of $z_0$ = 0.9 μm. **c)** Temperature profile and **d)** thermo-elastic displacement profile are examined for three different depth positions of the absorber. At a laser repetition rate of 500 kHz and a pulse width of 100 ns.

Once $T(r,z,t)$ is known, following Noda et al.(30), the vertical sample displacement $u_z$ at the surface can be determined from Navier's equations for axisymmetric thermoelastic problems in cylindrical coordinates as (see Supplementary section S2):

$$u_z(r,h_{mat},t)=2(1+v)\alpha_z\sum_{n=0}^{\infty}\sum_{m=0}^{\infty}\frac{A(\beta_m,\eta_n)}{\beta_m} \times\left(\frac{\eta_n^2}{\beta_m^2+\eta_n^2}+1\right)\underbrace{J_0(\beta_m r)}_{\text{spatial}}\underbrace{\mathcal{T}_{nm}(t)}_{\text{temporal}} \quad [8]$$

where $K$ is the restraint coefficient (see Eq. (S39)), $\alpha_z$ is the coefficient of thermal expansion and

$$A(\beta_m,\eta_n)=\frac{4}{\kappa h_{mat}R_{mat}^2}\frac{\iint_V r'J_0(\beta_m r')sin(\eta_n z')g(r',z')dr'dz'}{J_1^2(\beta_m R_{mat})\lambda_{nm}^2} \quad [9]$$

for a sphere, it is:

$$A(\beta_m,\eta_n)=\frac{8R_{abs}g_V}{\kappa h_{mat}R_{mat}^2}\frac{J_1(\beta_m R_{abs})sin(\eta_n z_0)sin(\eta_n R_{abs})}{J_1^2(\beta_m R_{mat})\lambda_{nm}^2\beta_m\eta_n} \quad [10]$$

Again, time domain and spatial domain behavior separated in Eq. (8).

Where $R_{abs}$ is the radius of the absorber. Eq. (8) provides us with ability to represent the surface displacement either in the time domain or the frequency domain. This is illustrated in Figure 2d as an example.

**Comparison PSF model and FEM.** To verify that the assumptions taken for the PSF model did not affect its ability to describe an actual AFM-IR experiment, the integrated temperature and surface displacement profiles calculated by the model were compared with those calculated using a FEM model of a spherical absorber consisting of PMMA embedded into a PE matrix placed on a silicon substrate. The displacement profiles conformed well to reality: spherical

absorber and matrix were assigned literature values for thermal and mechanical properties of PMMA and PE, respectively. The substrate was not set to be a perfect heat sink but a Si layer (5 µm) and instead of an insulating boundary at the cover layer, here heat transduction through thermal diffusion in air (5 µm) was modeled. The material properties for simulations are listed in Supplementary S3 Table 1. Unless stated otherwise, the following parameters remain constant in simulations involving the FEM and PSF models of AFM-IR: $R_{abs} = 70$ nm, matrix thickness $h_{mat} = 1$ µm, the matrix radius is $R_{mat} = 5$ µm (see Figure 2a for a sketch of the sample geometry).

Both models yield virtually identical integrated temperatures for all tested pulse widths (see Figure 3a for the variation of integrated temperature at pulse widths of 100 ns, 300 ns and 500 ns). Both models also agree well when it comes to the dependence of surface displacement on pulse width (Figure 3b).

However, there are deviations between the Green's function model and the FEM model when using substrates (such as $SiO_2$) that do not act similar to a perfect heat sink for the polymer sample (see Figure S18). It should be noted that $SiO_2$ is not a common substrate for AFM-IR due to its strong infrared absorption. The effects of interfacial thermal resistance and thermal conductivity of the substrate are reduced at higher laser repetition rates and for absorbers far from the substrate (see Figure S19). "Far" in this case can be understood in terms of the thermal diffusion length $\mu = \sqrt{\frac{\alpha}{\pi f}}$. This result matches studies on thermal behavior of thin films (33). In case of very thin films modifications to the Green's function model are required. However, in such samples models that assume vertical homogeneity might be more adept, such as those by Schwartz et al. (20), Morozovska et al. (19) or Dazzi's original study of the AFM-IR signal (34).

Both integrated temperature and surface displacement increase with increasing pulse width. However, it is evident that the surface displacement profile is much broader than the temperature profile. These results confirm that the thermo-elastic displacement has a nonlinear relationship with the temperature variation due to the presence of an inhomogeneous distribution of the heat source, which induces non-uniform strains in adjacent materials.

Furthermore, both models reveal distinct dependencies of integrated temperature and surface displacement on the absorber position (see Figure 3c,d). Evidently, when the absorber is positioned closer to the surface, the surface displacement exhibits higher amplitude and a narrower profile, while the shape of the integrated temperature profile mainly depends on how quickly the heat can diffuse away from the absorber (i.e. it is narrower closer to the substrate). Likewise, a comparable dependency is evident in the surface temperature profiles (see Figure S1).

Despite the PSF model of AFM-IR being designed for scenarios where the absorber is fully beneath the surface, we used the FEM model to understand how an absorber that extends partially beyond the surface would behave in AFM-IR. Surprisingly, we observed minimal difference in the displacement profile and amplitude for a bead that is just below the surface and one that is half below and half above the surface, as depicted in Figure S2. In general

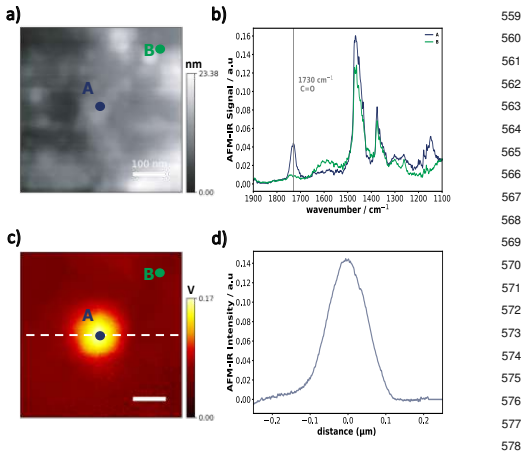


**Fig. 4. PMMA bead measurement with laser repetition rate 508 kHz, pulse width 200 ns. a)** AFM topography image of a PMMA nanoparticle. **b)** AFM-IR spectra obtained on the position A and B, respectively. **c)** Corresponding AFM-IR chemical map at 1730 $cm^{-1}$. The dashed line corresponds to the profile in d). **d)** Cross section profile of the AFM-IR signal distribution.

there is a high level of agreement between the PSF model of AFM-IR and the FEM simulations, with a mean percentage difference between both models for integrated temperature and displacement data below 3 % for all tested pulse widths and depth positions of the absorber (see Figure S3), meaning that the simplifications of the PSF model do not noticeably affect its accuracy.

The same agreement was found when other experimental parameters were adjusted, such as sample size $R_{abs}$, specific heat capacity $C_p$ and thermal conductivity $\kappa$ (see Figure S4). These results indicate that the surface displacement magnitude is roughly in proportion to the absorber's volume (Figure S4a), while the full width at half maximum (FWHM) of the displacement profile does not show a proportional increase with the absorber's size (see Figure S4b). Moreover, the physical properties of the matrix material play a crucial role in the signal intensity and and the spatial resolution (given by the shape of the surface displacement). A matrix material with low heat capacity and thermal conductivity leads to higher signal intensity at the surface (Figure S4c,e). This occurs due to the rapid heating characteristic of a material with low specific heat capacity, coupled with its limited thermal conductivity that impedes efficient heat conduction. Consequently, heat is redistributed from the absorber into the matrix material more slowly, resulting in a higher temperature and corresponding higher thermal expansion. On the other hand, a matrix material with high specific heat capacity and low thermal conductivity shows narrower surface displacement profiles. The increased heat capacity facilitates superior thermal confinement, reducing the spread of heat and enhancing the spatial resolution of the imaging (Figure S4d). Additionally, the low thermal conductivity helps to minimize heat dissipation, further enhancing the resolution of AFM-IR imaging (Figure S4f).

**Comparison of model and experiment.** A sample resembling the simulated structure using FEM and PSF model was prepared using PMMA beads with diameters of approximately 140 nm. These beads were suspended in a PE matrix and subsequently microtomed into thin slices with a thickness of 1 µm (refer to the Methods section for more details). The buried absorber (see Figure 4a) was detected using the 1730 $cm^{-1}$ carbonyl band of PMMA (see Figure 4b) which can be clearly distinguished from the matrix spectrum. The AFM-IR absorption image (also referred to as "chemical image") at 1730 $cm^{-1}$ shows a single PMMA bead (see Figure 4c) with a FWHM determined from the cross section through the chemical image of 121 nm.

Here, we find another utility of the FEM based model, namely that it also allows us to model the heat flow across the interface between PMMA and PE, such as interfacial roughness, compositional disorder, or general interfacial thermal resistance (ITR) (35, 36) which could affect the thermal diffusion and thus the AFM-IR signal. To address these potential effects, we incorporated ITR between PMMA and PE ($R_{PMMA/PE}$) into the finite element simulations. However, to the best of our knowledge, no literature values exist for $R_{PMMA/PE}$ and ITR values are generally associated with high uncertainties (37, 38). Our approach consisted of utilizing reported ITR values of polymers in the model, such as the ITR in BN@PEI/PVA ($2.15 \times 10^{-6}\,m^2\,K\,W^{-1}$) and in BN/PVA ($3.03 \times 10^{-6}\,m^2\,K\,W^{-1}$) (39). Thus, by choosing the ITR in a range between the two reported values described before, and in accordance with our FEM simulations, we found that our selected value has a good agreement with experimental results (see Figure 5). These values are comparable to those used by others to simulate AFM-IR experiments (20).

The model and experiment both show an increasing peak amplitude at constant pulse width and increasing repetition rate (see Figure 5c,e). The increasing peak amplitude can be attributed to the increasing duty cycle and thus increasing energy deposited in the absorber. The peak amplitude at the highest tested frequency (1231 kHz) deviates from the trend seen for the other frequency but follows the FWHM trend (see Figure S20 and Figure 5f). This is due to the fact that at this setting a duty cycle of 12.3 % had been reached which goes beyond the specifications of the laser used. In this regime the EC-QCLs control circuit will skip every other pulse so as to stay within the maximum duty cycle specifications of the device and avoid damage, leading to a 50 % reduction in peak amplitude. The FWHM is not affected by this.

We use the FWHM of the AFM-IR signal distribution profile, as depicted in Figure 5f to determine the achievable spatial resolution. Experiments and models agree that increasing the laser repetition rates led to a decrease in FWHM, indicating improved spatial resolution (see Figure 5d). In the following section, we show that this effect can be understood through the PSF model.

The model and simulation also agree well when it comes to the effect of pulse width. When keeping the repetition rate around 282 kHz and varying the pulse width from 100 ns to 500 ns at constant peak pulse power, a linear dependence of peak and integrated amplitude on the pulse width is found (see Figure 6). To compare modeled and measured amplitude a scaling factor is required, as the models directly output surface displacement, while the AFM-IR signal is proportional to surface displacement but has several sensitivity constants that are difficult to determine (17). We have determined a scaling factor of $(13.61 \pm 1.14)$ nm/V as described in **Methods** to show that the linear relation seen in the simulation is matched by the behavior in the experiment. However, it should be noted that this factor only relates experimental AFM-IR signal amplitude to simulated surface displacement. The actual experimental surface displacement is thus proportional to the simulated one but not equal to it, as this factor depends on the type of cantilever, the AFM instrument, the resonance mode, laser power and laser profile on the surface.

This effect, too, is due to the increasing duty cycle and thus increasing energy deposited in the absorber. This effect is not true for arbitrary long pulse widths, as will be discussed below.

**Effects of experimental parameters on the AFM-IR signal.** Having established that the PSF and FEM model and FEM model and experiment, respectively, agree well, we can now leverage the analytical description of the PSF model to understand the effects of experimental parameters on the AFM-IR signal.

As the PSF model can describe the signal of a three-dimensional absorber, in addition to time/frequency domain behaviour (9) it can also describe the lateral extension of the deflection caused by an absorber, which allows to determine the spatial resolution of the AFM-IR measurement. In general, modes with higher $\beta_m$ will lead to a narrower profile due to the only $r$ dependent term $J_0(\beta_m r)$ in Eq. (8). These narrower modes will have a faster decay in time as $\lambda_{mn}$ increases with $m$ affecting the time-dependent term $\mathcal{T}_{nm}(t)$ defined in Eq. (7).

Thus, resonance enhanced AFM-IR at higher frequencies and other AFM-IR techniques that use high frequencies by default, such as tapping mode AFM-IR and surface sensitive AFM-IR, provide a better lateral spatial resolution.

The PSF model also shows a relationship between the FWHM of the surface displacement and the distance $h_{mat} - z_0$ of the absorber from the surface. The further the absorber is from the surface the wider the FWHM (see Figure 7a). This behaviour can be explained by looking at the $z_0$ dependence of $A(\beta_m, \eta_n)$. For a spherical absorber this can be easiest explained through the following part of $A(\beta_m, \eta_n)$ $\sin(\eta_n z_0) \sin(\eta_n R_{abs})$ (see Eq. (10)). This expression will always be positive for low $z_0$ but for $z_0 \approx h_{mat}$ will be positive for even $n$ be positive and for odd $n$ be negative. As the mode shape in $r \propto J_0(\beta_m r)$ this means that for absorbers close to the surface the wider lower order modes in $m$ for $n = 0$ are counteracted by negative contributions from $n > 0$. The $\sin(\eta_n z_0) \sin(\eta_n R_{abs})$ term also explains the higher surface displacement for absorbers close to the surface: at $z_0 \propto 0$, $\sin(\eta_n z_0)$ will also be close to zero.

Taking a closer look at the frequency dependence of the spatial resolution, Eq. (7) allows us to understand the effect of pulse width on the achievable spatial resolution. For a rectangular pulse $\prod\left(\frac{t}{t_p}\right)$ (e.g. in the case of an EC-QCL), in the frequency domain

$$\mathcal{T}_{nm}(f) = \frac{2\alpha\lambda_{mn}^2}{\alpha^2\lambda_{mn}^4 + 4\pi^2 f^2} \cdot t_p \,\mathrm{sinc}(t_p f) \qquad [11]$$

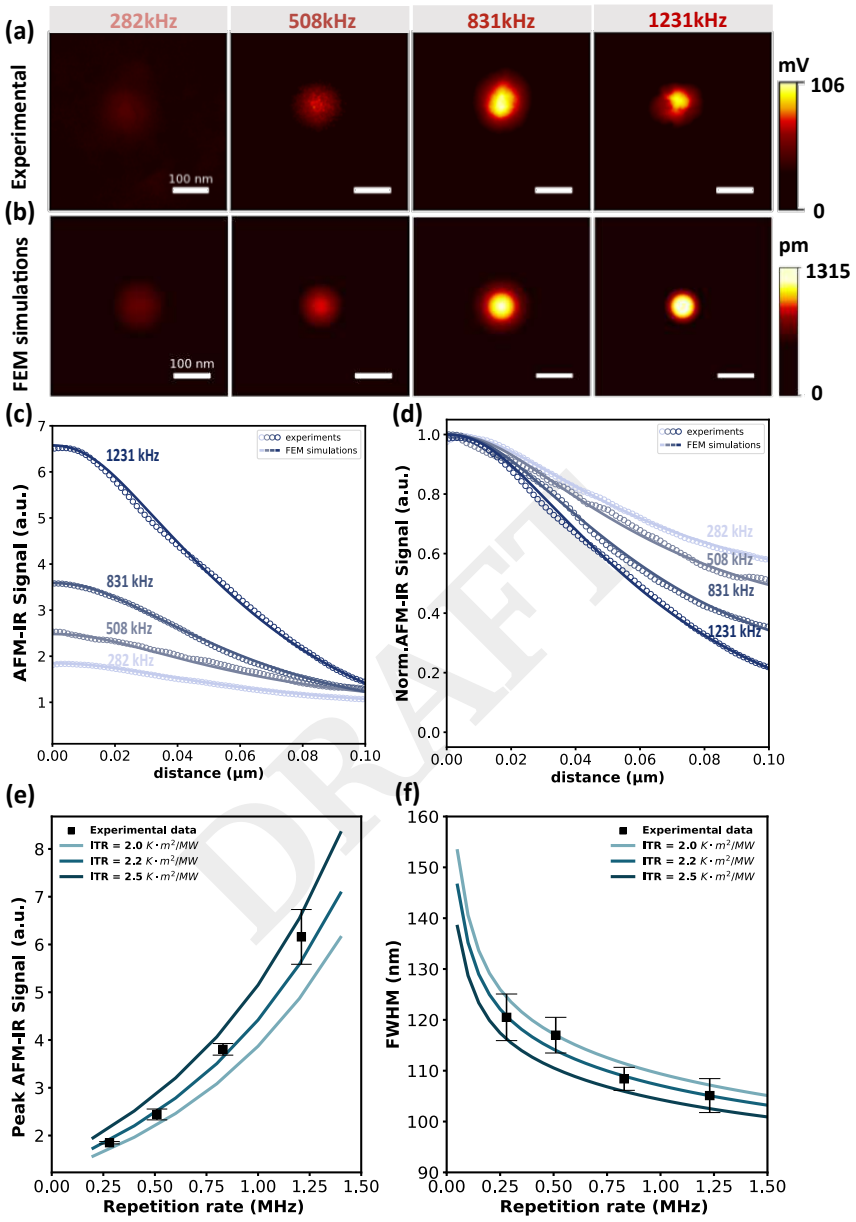


**Fig. 5. AFM-IR images were obtained for various laser repetition rates. a)** Experimental AFM-IR images were obtained using a series of laser repetition rates at a pulse width of 100 ns. **b)** Simulated AFM-IR images under the same experimental parameters. Considering a peak laser power of 4.5 mW, beam diameter $r_{laser} = 10\,\mu m$, diameter of 140 nm for the absorber, positioned at a depth of 0.93 μm, tightly under the surface. **c)** The AFM-IR signal at each examined frequency is scaled to a baseline value, with solid lines representing the FEM simulations at each corresponding frequency. **d)** The AFM-IR signal at each examined frequency is normalized to its local peak value, with solid lines representing the FEM simulations at each corresponding frequency. **e)** Peak amplitudes of AFM-IR signal in dependence on laser repetition rates. The simulated line represents the trend of the peak surface displacement based on FEM simulations. **f)** FWHM of AFM-IR signal cross section was measured at laser repetition rates of 282 kHz, 508 kHz, 831 kHz, and 1231 kHz. The reported measurements include the mean value as well as the maximum deviation from repeated measurements. The FEM simulated line represents the trend of the FWHM as a function of laser repetition rates. The simulation presented in Figure S7 is based on the PSF model and does not include consideration for the thermal resistance at the interface.

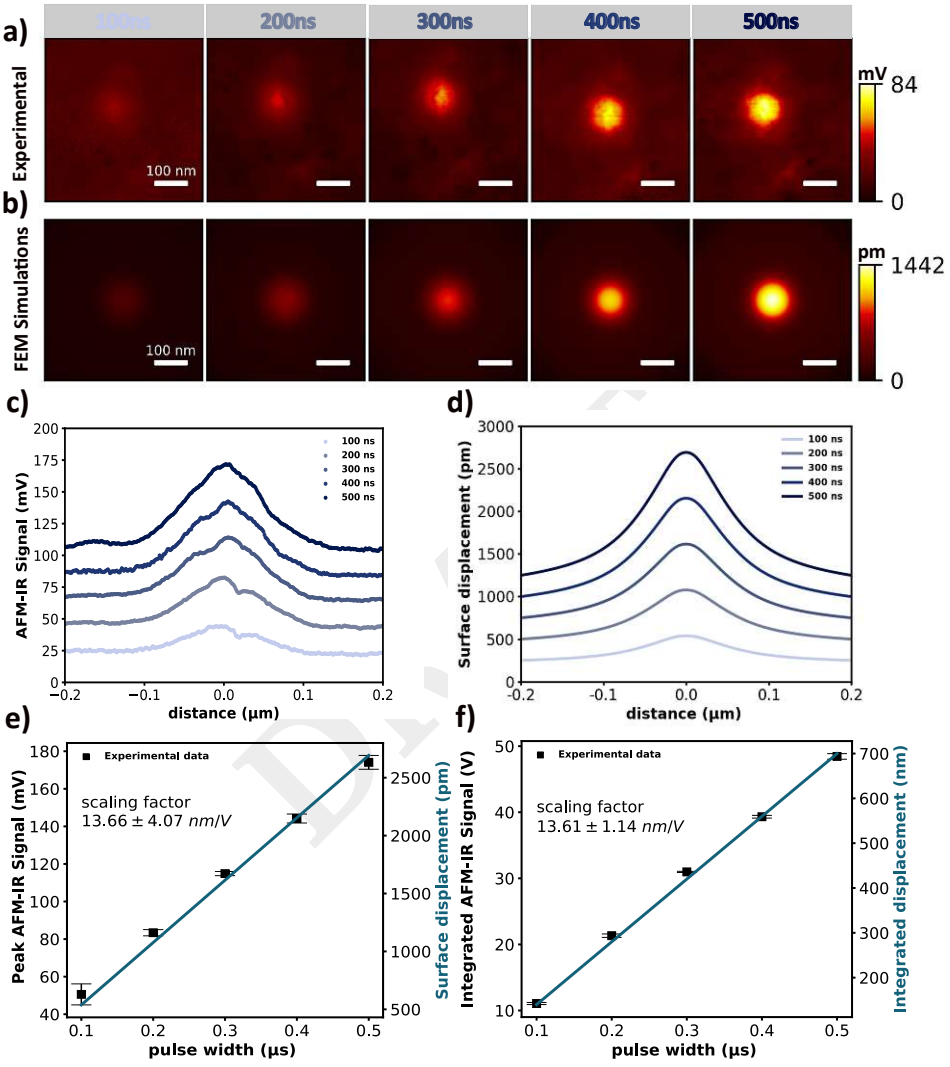


**Fig. 6. AFM-IR signal dependence on pulse width. a)** Experimental AFM-IR images were obtained using a series of laser pulse widths ranging from 100 ns to 500 ns at a laser repetition rate of 282 kHz. To highlight the distinct contrast between the figures acquired at different frequencies, all images were subtracted by their respective minimum values. The figures displaying the original minimum values are presented in Figure S8. **b)** Simulated AFM-IR images under the same experimental parameters. Considering laser power 4.5 mW, a diameter of 100 nm for the absorber, positioned at a depth of 0.93 μm. **c)** The experimental AFM-IR signal profile over axial displacement measured at different pulse widths. **d)** FEM simulation of surface displacement profiles at different pulse widths. **e)** Peak AFM-IR signal and simulated peak surface displacement in dependence on pulse widths. The reported measurements represent the mean values with the maximum deviation from repeated measurements. **f)** Integrated AFM-IR signal and simulated integrated surface displacement over the radial coordinate from –2 μm to 2 μm depending on pulse widths.

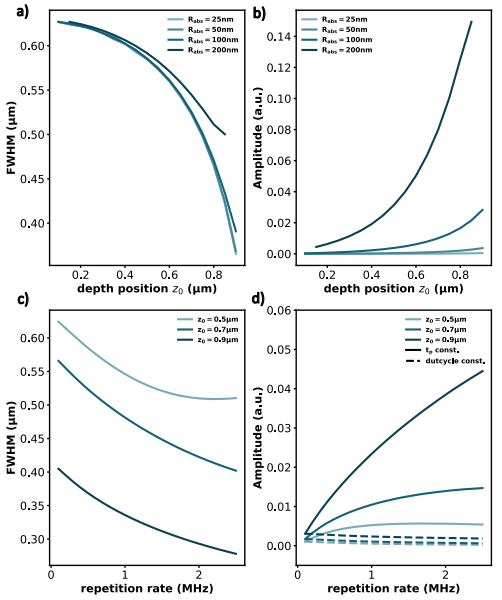


**Fig. 7. FWHM and amplitude exhibit dependencies on the position of absorber depths and laser repetition rates. a)** FWHM and **b)** amplitude are examined at various absorber depth positions for four different absorber sizes. The laser pulse has a duration of 100 ns, and the repetition rate is 500 kHz. **c)** FWHM and **d)** amplitude are examined at different laser repetition rates for three distinct absorber depth positions. Solid lines represent simulations at a constant laser pulse duration of 100 ns, and dash lines represent simulations with a constant duty cycle of 1 %. The absorber has a radius of 50 nm.

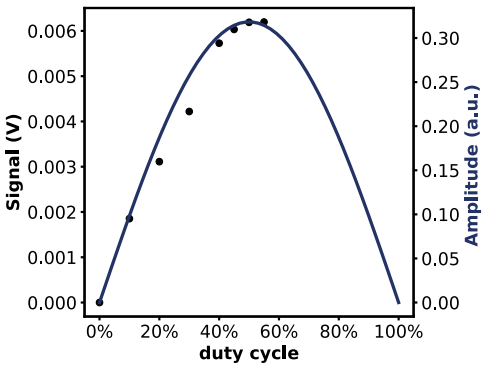


**Fig. 8.** The measured laser power and calculated signal amplitude as a function of duty cycle.

For a pulse train of repetition rate $f_{rep}$, the above expression is multiplied by a Dirac comb

$$f_{rep} \sum_{k=-\infty}^{\infty} \delta\left(f - k\, f_{rep}\right) \qquad [12]$$

with $\delta$ being Dirac's delta. In this case, typically the signal is demodulated at $f_{rep}$ or one of its multiples.

Thus, when the laser is pulsed at a fixed frequency, the Fourier transformed $\prod$ merely acts as a scaling factor that affects all $A(\beta_m, \eta_n)$ in the same way. Pulse width thus only affects the signal amplitude but not the spatial resolution. We can also see that the pulse width does affect overall signal amplitude. It reaches a maximum at $t_p = \frac{1}{2f}$ and then decreases back down to 0 at $t_p = \frac{1}{f}$. Note that $f$ here is not necessarily the laser repetition rate $f_{rep}$ but the frequency at which the signal is demodulated. Hence, when demodulating the AFM-IR signal at a multiple of the laser repetition rate (as is sometimes done to reach cantilever resonances beyond the maximum pulse repetition rate of the laser) care has to be taken, that the product of the demodulation frequency and pulse width $ft_p \leq 0.5$ (see the relationship between laser amplitude and duty cycle in Figure 8). Increasing $ft_p > 0.5$ does not increase the amplitude of the signal and only leads to unnecessary sample heating. (Illustrations of the relationship between pulse width, signal amplitude and frequency can be found in Figure S5). Even though the highest signal is achieved at 50 % duty cycler, there is a good reason to keep the pulse width as short as possible when exciting the cantilever with a train of pulses: sample heating. While at constant peak pulse power the maximum signal amplitude is achieved at 50 % duty cycle, when instead keeping the average power constant, the signal at duty cycles below 10 % is more than 1.5 times higher than that at 50 % (see Figure S5e).

Consideration of cantilever dynamics, including mode analysis and beam slope, becomes crucial when higher resonances of the cantilever are excited (40). The contributions from the cantilever act as a transfer function to the final detected signal, as detailed in the original work by Dazzi et al. (17). Figure S17 illustrates the product of the calculated beam slope and the simulated surface displacement. It plots the peak value at each mode frequency, demonstrating a good agreement with the experiments. More details can be found in the Supporting Information.

As mentioned above, increasing the pulse repetition rate will narrow the FWHM of the surface displacement (i.e. improve spatial resolution). However, this does not affect absorbers at all depths in the same way (see Figure 7c). Here, for absorbers buried deeper below the surface a "levelling out" effect can be seen, whereby further increase of the repetition rate does not improve the spatial resolution.

Finally, the PSF model also helps to explain the depth resolution of the surface sensitive AFM-IR (see Figure 7d). At constant pulse width, the peak amplitude caused by an absorber buried deeper inside the sample plateaus at lower frequencies than that of those closer to the surface (continuous lines). When the experiment is conducted at constant duty cycle, this appears as an overall decrease of the peak amplitude of the buried absorber compared to that of absorbers closer to the surface (dashed lines).

## Conclusions

This work establishes an analytical expression that describes, for the first time, the surface displacement caused by a three-dimensional absorber embedded within a matrix in an AFM-IR experiment. This point spread function model provides a detailed understanding of the photothermal expansion and AFM-IR signal generation processes. Based on this model we can understand the effect of experimental parameters and sample geometry on signal amplitude and spatial resolution.

The PSF model was rigorously validated through comparisons with finite element method (FEM) simulations and experimental data.

The developed PSF model explains that increasing the pulse width enhances the signal as long as the product of pulse width and demodulation frequency is kept below 0.5. Furthermore, our experimental data agree with the PSF model, which also does not find a direct relation between pulse width and spatial resolution, aligning with the findings of other researchers (20).

The demodulation frequency is found to be the main factor under the control of the AFM-IR user for a given sample and cantilever that affects spatial resolution. Higher frequency improves resolution. At constant pulse width it also increases peak amplitude.

The PSF model can also be used to study vertical resolution of high frequency AFM-IR modes, showing that the peak signal amplitude from absorber far from the surface will decay with increasing demodulation frequency.

In comparing experimental data and FEM model we have identified the interfacial thermal resistance between phases as a significant contribution to the AFM-IR signal. While the determination of interfacial thermal resistance in AFM-IR using custom transducers has previously been demonstrated (7, 41), specialized, high frequency AFM-IR tips were demonstrated for the determination of this often elusive parameter, our results hint at alternative approach that leverages the frequency dependent AFM-IR image combined with modeling. In this work, the interfacial thermal resistance between PMMA absorber and PE $R_{PMMA/PE}$ was found to be $\approx 2.2 \times 10^{-6}\,\mathrm{m^2\,K\,W^{-1}}$.

The combination of optical and photo-elastic effects in AFM-IR also need to be taken into account when evaluating spectra, as peak amplitude caused by an absorber not only depend on its vertical but also its lateral extension.

Our study confirms the following properties of the AFM-IR signal that have also been found in previous work that did not model an inhomogeneous sample:

1. The AFM-IR signal linearly depends on the coefficient of thermal expansion $\alpha_z$.
2. Higher modulation frequencies / pulse rates lead to higher spatial resolution.
3. The spatial resolution in AFM-IR remains independent of the pulse width/duty cycle of the laser (see point 10 for limits).
4. In small spherical absorbers it is the volume rather than the height that is proportional to the AFM-IR signal – this remains true even for buried spheres.
5. High thermal conductivity of the matrix reduces the signal amplitude and degrades spatial resolution.

Beyond confirming these established properties of the AFM-IR signal our study also allows us to deduce the following relationships:

6. With increasing depth (distance from the surface) the apparent size of absorbers increases.
7. The spatial resolution of AFM-IR remains independent of Young's modulus, Poisson's ratio, and the thermal expansion coefficient.
8. The AFM-IR signal amplitude decreases for absorbers located deeper within the sample.
9. Modulation at higher frequencies preferentially generates signal from absorbers closer to the surface.
10. When exciting with a pulse train, the signal at duty cycle $< 10\,\%$ is more than 1.5 times higher than that at $50\,\%$ at the same average power.

While our model does not take into account acoustic waves, Chae et al. reported the detection of such waves in the air in an AFM-IR experiment using a nanophotonic transducer (7), and Raschke et al. studied them in the context of photoinduced force experiments (42). Despite regarding the acoustic wave as negligible in our current study, investigating the coupling of photothermal and photoacoustic effects would constitute a valuable addition and could potentially contribute to a better understanding of how to either use these phenomena to gain additional insight into the sample or better understand how to remove their contribution to the AFM-IR signal.

Furthermore, assumptions underlying this model preclude its direct application to some interesting sample configurations that have been analyzed with AFM-IR. For example, in the graphene on $SiO_2$ substrate sample analyzed by Menges et al. (43) it is not the sample layer or the graphene absorber that produces the thermal expansion required for AFM-IR but the $SiO_2$ substrate. Likewise, substrates with low thermal conductivity in comparison to that of the sample (44) or high coefficient of thermal expansion will require a modification of the model. In such cases verification of the validity of the assumptions underlying the Green's function approach using FEM is prudent. The comparison between experimental data and FEM model also demonstrates the importance of interfacial thermal resistance on the AFM-IR signal amplitude and spatial resolution. This point should be taken into account when studying interfaces.

The developed PSF model of AFM-IR provides researchers with a powerful tool for quantitative analysis and optimization of nanoscale chemical imaging experiments. Beyond the applications and results shown in this work, a conversion to Cartesian coordinates can be envisioned. This would allow to study more complex samples. As the PSF model is significantly more efficient than a comparable FEM approach it can provide deeper insights into advanced, non-linear AFM-IR techniques, such as surface sensitive AFM-IR. Potentially, the model could also be used to combine AFM-IR images taken at different frequencies to perform tomography to determine the vertical makeup of a sample.

**Author Affiliations.** ORCID
Yide Zhang: 0000-0002-2675-739X
Ufuk Yilmaz: 0009-0009-3572-5267
Gustavo Vinicius Bassi Lukasievicz: 0000-0002-6754-7057
Liam O'Faolain: 0000-0003-1160-7441
Bernhard Lendl: 0000-0003-3838-5842
Georg Ramer: 0000-0001-8307-5435

## Supporting Information Appendix (SI).

***SI file.*** A PDF file including of additional figures S1 to S20, table S1 and the additional derivations for equations in the main text is available free of charge.

***SI Code and raw data.*** Code and raw data to generate all figures are available on Zenodo: https://doi.org/10.5281/zenodo.10518024

## Materials and Methods

**Sample Preparation.** The PE/PMMA sample was prepared by melting and mixing a polyethylene (PE) matrix (average Mw 35.000, Sigma Aldrich) just above the melting temperature (Tm = 116 °C) while keeping in motion through, vigorous stirring and subsequently adding nano-beads of Poly(methyl methacrylate) (PMMA, Tm = 160 °C) with average diameter 140 nm (PolyAn Pink, PolyAn GmbH). The beads are dispersed in a water solution with a solid content of 1 % and were pipetted onto the molten PE. This evaporates the water but does not melt PMMA. Stirring was continued until beads were thoroughly mixed into the PE. Then the mixture was cooled to room temperature. For further drying, the sample was placed into an oven (105 °C) for 3 hours.

The sample was ultra-cryomicrotomed to a thickness of 1 µm and placed on Si substrates for measurements.

**AFM-IR experimental and data collection.** All AFM-IR data were collected using a nanoIR3s (Bruker) controlled by Analysis Studio (Anasys Instruments, v3.15).

Experiments were conducted using an overall gold coated contact mode cantilever (Cont-GB-C, BudgetSensors Innovative Solutions Bulgaria Ltd.) with a nominal first resonance frequency of $(13 \pm 4)$ kHz and a nominal spring constant between $0.04\,\mathrm{N\,m^{-1}}$ and $0.40\,\mathrm{N\,m^{-1}}$. As source for photothermal excitation a mid-IR external cavity quantum cascade laser (EC-QCL) (MIRcat-QT, DRS Daylight Solutions Inc.) was used. All AFM-IR measurements were performed in resonance enhanced contact mode AFM-IR. For AFM-IR images a 500 nm × 500 nm area was scanned with a line rate of 0.1 Hz (lateral speed $100\,\mathrm{nm\,s^{-1}}$) and a resolution of 400 pixels per line at 200 lines. For chemical imaging the distinct carbonyl-stretching band of PMMA (C=O) at $1730\,\mathrm{cm^{-1}}$ was selected and pulse peak power was set as 15 mW. The polarization of the laser source is set to 0 degrees in respect to the sample plane. The laser repetition rate was kept at the frequency of the contact resonance of the cantilever using a phase-locked loop (PLL).

The experiments were performed at a series of laser pulse widths of 100 ns, 200 ns, 300 ns, 400 ns, 500 ns each at laser repetition rates of 282 kHz, 508 kHz, 831 kHz, and 1231 kHz. For each laser – pulse width and repetition rate setting three IR images were collected. Simultaneously with the IR images (trace and retrace), also height images (trace and retrace), deflection channel (trace and retrace) and the PLL frequency channel (trace and retrace) were recorded.

The AFM-IR instrument and laser beam paths were encased and purged with dry air.

**Scaling factor determination.** The original figures of Figure 5 and 6 with the their respective minimum values are presented in Figure S6 and S8. Figure 5c and d illustrate the cross section through the chemical images and FEM simulations at different pulse widths from Figure 5a and b. In the absence of consideration for the interfacial thermal resistance between PMMA beads and PE, the simulated surface displacement profiles exhibit much greater width compared to the cross-section profiles observed in the experiments, as depicted in Figure S9.

Figure 6e and f depict that the simulated peak and integrated surface displacement exhibit a linear growth trend with the pulse width. When compared with the experimental results, scaling factors (accounting for a range of experimental sensitivity factors) of $(13.66 \pm 4.07)$ nm/V and $(13.61 \pm 1.14)$ nm/V were obtained for the surface displacement and the AFM-IR signal, respectively, by calculating the mean ratio of the deflection signal amplitude and the model surface deformation. Calculated scaling factors for the surface displacement and the AFM-IR signal at each pulse width are shown on Figure S10.

**Laser power duty cycle measurement.** A custom EC-ICL (ALPES Lasers SA) was used to probe the behavior of the AFM-IR signal at high duty cycle (see Figure 8). The device emits between $2800\,\mathrm{cm^{-1}}$ to $3100\,\mathrm{cm^{-1}}$ and achieves pulse widths of up to 3000 ns at repetition rates up to 180 kHz at >10 mW peak power and up to 100 % duty cycle.

**ACKNOWLEDGMENTS.** This work was funded with financial support from the European Union's Horizon 2020 research and innovation programme. The authors Y.Z., L.O'F., G.R., and B.L. acknowledge the Marie Skłodowska-Curie project "OPTAPHI" under grant agreement No. 860808. U.Y., and G.R. acknowledge the European Commissions's Horizon 2020 project "PeroCUBE" under grant agreement No. 861985. G.R. also acknowledges support from European Commissions's Horizon 2020 project "TUMOR-LN-oC" under grant agreement number 953234. G. V. B. Lukasievicz acknowledges support from Conselho Nacional de Desenvolvimento Científico e Tecnológico (CNPq) under grant agreement No. 307415/2022-8. The financial support by the Austrian Federal Ministry for Labour and Economy and the National Foundation for Research, Technology and Development and the Christian Doppler Research Association is gratefully acknowledged. The authors would like to thank Andrew Cashman for his valuable input and the discussions. Furthermore, the authors would also like to thank Jakob Gruber and Karin Whitmore for microtoming some samples using facilities at the University Service Centre for Transmission Electron Microscopy (USTEM), TU Wien.

The authors would also like to thank Dr. Andrea Centrone for pointing out a mistake in the pre-print.

1. A Centrone, Infrared Imaging and Spectroscopy Beyond the Diffraction Limit. *Annu. Rev. Anal. Chem.* **8**, 101–126 (2015).
2. A Dazzi, CB Prater, AFM-IR: Technology and Applications in Nanoscale Infrared Spectroscopy and Chemical Imaging. *Chem. Rev.* **117**, 5146–5173 (2017).
3. AM Katzenmeyer, et al., Mid-infrared spectroscopy beyond the diffraction limit via direct measurement of the photothermal effect. *Nanoscale* **7**, 17637–17641 (2015).
4. A Dazzi, et al., AFM–IR: Combining Atomic Force Microscopy and Infrared Spectroscopy for Nanoscale Chemical Characterization. *Appl. Spectrosc.* **66**, 1365–1384 (2012).
5. ACV dos Santos, B Lendl, G Ramer, Systematic analysis and nanoscale chemical imaging of polymers using photothermal-induced resonance (AFM-IR) infrared spectroscopy. *Polym. Test.* **106**, 107443 (2022).
6. FS Ruggeri, B Mannini, R Schmid, M Vendruscolo, TPJ Knowles, Single molecule secondary structure determination of proteins through infrared absorption nanospectroscopy. *Nat. Commun.* **11**, 2945 (2020).
7. J Chae, et al., Nanophotonic Atomic Force Microscope Transducers Enable Chemical Composition and Thermal Conductivity Measurements at the Nanoscale. *Nano Lett.* **17**, 5587–5594 (2017).
8. G Ramer, VA Aksyuk, A Centrone, Quantitative chemical analysis at the nanoscale using the PTIR technique. *Anal. Chem.* **89**, 13524–13531 (2017).
9. J J. Schwartz, D S. Jakob, A Centrone, A guide to nanoscale IR spectroscopy: resonance enhanced transduction in contact and tapping mode AFM-IR. *Chem. Soc. Rev.* **51**, 5248–5267 (2022) Publisher: Royal Society of Chemistry.
10. F Lu, M Jin, MA Belkin, Tip-enhanced infrared nanospectroscopy via molecular expansion force detection. *Nat. Photonics* **8**, 307–312 (2014).

11. AC V. D. dos Santos, D Tranchida, B Lendl, G Ramer, Nanoscale chemical characterization of a post-consumer recycled polyolefin blend using tapping mode AFM-IR. *The Analyst* **147**, 3741–3747 (2022).
12. F Tang, P Bao, Z Su, Analysis of Nanodomain Composition in High-Impact Polypropylene by Atomic Force Microscopy-Infrared. *Anal. Chem.* **88**, 4926–4930 (2016).
13. L Baldassarre, et al., Mapping the amide I absorption in single bacteria and mammalian cells with resonant infrared nanospectroscopy. *Nanotechnology* **27**, 075101 (2016).
14. A Dazzi, et al., Chemical mapping of the distribution of viruses into infected bacteria with a photothermal method. *Ultramicroscopy* **108**, 635–641 (2008).
15. Y Yuan, et al., Photovoltaic Switching Mechanism in Lateral Structure Hybrid Perovskite Solar Cells. *Adv. Energy Mater.* **5**, 1500615 (2015).
16. J Houel, et al., Ultraweak-Absorption Microscopy of a Single Semiconductor Quantum Dot in the Midinfrared Range. *Phys. Rev. Lett.* **99**, 217404 (2007).
17. A Dazzi, F Glotin, R Carminati, Theory of infrared nanospectroscopy by photothermal induced resonance. *J. Appl. Phys.* **107**, 124519 (2010).
18. A Dazzi, PhotoThermal Induced Resonance. Application to Infrared Spectromicroscopy in *Thermal Nanosystems and Nanomaterials*, ed. S Volz. (Springer Berlin Heidelberg, Berlin, Heidelberg) Vol. 118, pp. 469–503 (2009) Series Title: Topics in Applied Physics.
19. AN Morozovska, et al., Photothermoelastic contrast in nanoscale infrared spectroscopy. *Appl. Phys. Lett.* **112**, 033105 (2018).
20. JJ Schwartz, G Pavlidis, A Centrone, Understanding Cantilever Transduction Efficiency and Spatial Resolution in Nanoscale Infrared Microscopy. *Anal. Chem.* **94**, 13126–13135 (2022).
21. B Lahiri, G Holland, A Centrone, Chemical Imaging Beyond the Diffraction Limit: Experimental Validation of the PTIR Technique. *Small* **9**, 439–445 (2013).
22. L Quaroni, Understanding and Controlling Spatial Resolution, Sensitivity, and Surface Selectivity in Resonant-Mode Photothermal-Induced Resonance Spectroscopy. *Anal. Chem.* **92**, 3544–3554 (2020).
23. AC V. D. dos Santos, et al., Nanoscale Infrared Spectroscopy and Chemometrics Enable Detection of Intracellular Protein Distribution. *Anal. Chem.* **92**, 15719–15725 (2020).
24. X Ma, et al., Nanoscale IR spectroscopy: From Principles to Nanoscale Imaging and Identification of Metal Soaps. *Microsc. Microanal.* **27**, 2814–2815 (2021).
25. S Kenkel, et al., Chemical imaging of cellular ultrastructure by null-deflection infrared spectroscopic measurements. *Proc. Natl. Acad. Sci.* **119**, e2210516119 (2022) Publisher: Proceedings of the National Academy of Sciences.
26. F Bai, R Bertram, BR Karamched, A closed-loop multi-scale model for intrinsic frequency-dependent regulation of axonal growth. *Math. Biosci.* **344**, 108768 (2022).
27. S Kenkel, S Mittal, R Bhargava, Closed-loop atomic force microscopy-infrared spectroscopic imaging for nanoscale molecular characterization. *Nat. Commun.* **11**, 3225 (2020).
28. J Mathurin, A Deniset-Besseau, A Dazzi, Advanced Infrared Nanospectroscopy Using Photothermal Induced Resonance Technique, AFMIR: New Approach Using Tapping Mode. *Acta Phys. Polonica A* **137**, 29–32 (2020).
29. J Mathurin, et al., Photothermal AFM-IR spectroscopy and imaging: Status, challenges, and trends. *J. Appl. Phys.* **131**, 010901 (2022).
30. N Noda, RB Hetnarski, Y Tanigawa, *Thermal stresses*. (Taylor & Francis, New York), 2nd ed edition, (2003).
31. G Balasubramanian, IK Puri, Heat conduction across a solid-solid interface: Understanding nanoscale interfacial effects on thermal resistance. *Appl. Phys. Lett.* **99**, 013116 (2011).
32. KD Cole, ed., *Heat conduction using Green's functions*, Series in Computational and Physical Processes in Mechanics and Thermal Sciences. (CRC Press, Boca Raton), 2. ed edition, (2011).
33. ED Black, IS Grudinin, SR Rao, KG Libbrecht, Enhanced photothermal displacement spectroscopy for thin-film characterization using a Fabry-Perot resonator. *J. Appl. Phys.* **95**, 7655–7659 (2004).
34. A Dazzi, F Glotin, R Carminati, Theory of infrared nanospectroscopy by photothermal induced resonance. *J. Appl. Phys.* **107**, 124519 (2010) Publisher: American Institute of Physics.
35. PE Hopkins, Thermal Transport across Solid Interfaces with Nanoscale Imperfections: Effects of Roughness, Disorder, Dislocations, and Bonding on Thermal Boundary Conductance. *ISRN Mech. Eng.* **2013**, 1–19 (2013).
36. J Song, Y Zhang, Effect of an interface layer on thermal conductivity of polymer composites studied by the design of double-layered and triple-layered composites. *Int. J. Heat Mass Transf.* **141**, 1049–1055 (2019).
37. K Zheng, J Zhu, YM Ma, DW Tang, FS Wang, Interfacial thermal resistance between high-density polyethylene (HDPE) and sapphire. *Chin. Phys. B* **23**, 107307 (2014).
38. MD Losego, L Moh, KA Arpin, DG Cahill, PV Braun, Interfacial thermal conductance in spun-cast polymer films and polymer brushes. *Appl. Phys. Lett.* **97**, 011908 (2010).
39. K Ruan, X Shi, Y Guo, J Gu, Interfacial thermal resistance in thermally conductive polymer composites: A review. *Compos. Commun.* **22**, 100518 (2020).
40. U Rabe, J Turner, W Arnold, Analysis of the high-frequency response of atomic force microscope cantilevers. *Appl. Phys. A* **66**, S277–S282 (1998).
41. M Wang, et al., High Throughput Nanoimaging of Thermal Conductivity and Interfacial Thermal Conductance. *Nano Lett.* **22**, 4325–4332 (2022).
42. BT O'Callahan, J Yan, F Menges, EA Muller, MB Raschke, Photoinduced Tip–Sample Forces for Chemical Nanoimaging and Spectroscopy. *Nano Lett.* **18**, 5499–5505 (2018).
43. F Menges, et al., Substrate-enhanced photothermal nano-imaging of surface polaritons in monolayer graphene. *APL Photonics* **6**, 041301 (2021).
44. S Rizevsky, K Zhaliazka, T Dou, M Matveyenka, D Kurouski, Characterization of Substrates and Surface-Enhancement in Atomic Force Microscopy Infrared Analysis of Amyloid Aggregates. *The J. Phys. Chem. C* **126**, 4157–4162 (2022) Publisher: American Chemical Society.

## 4.2. Nanoscale Chemical Imaging for Subsurface Complex Structures

AFM-IR has become an essential tool for nanoscale chemical characterization, offering spatial resolution beyond the diffraction limit of conventional infrared spectroscopy. This unique capability enables the study of subsurface structures [207] and compositional variations in a wide range of materials [94, 21]. However, much of the existing research has focused on relatively simple geometries, with limited exploration into how complex three-dimensional structures and surface topographies influence the AFM-IR signal.

Understanding the interplay between sample geometry and AFM-IR signal generation is crucial for accurate interpretation of chemical images. While previous studies have investigated depth sensitivity through variations in laser parameters [207, 208, 209], the impact of absorber size, shape, and position—particularly in the presence of non-flat surfaces—remains underexplored. This gap is significant, as non-planar surfaces and heterogeneous sample structures are common in practical applications such as nanoelectronics [210], energy materials [211], and defect analysis in manufacturing processes [212].

Alternative infrared-based scanning probe techniques, such as scattering-type scanning near-field optical microscopy (s-SNOM) and nano-FTIR, have been used to investigate subsurface features [213, 214]. While these methods provide valuable insights, their application to complex geometries has been limited, often requiring simplified sample designs like thin films or stepped structures [215]. Consequently, there is a growing need for comprehensive models that accurately predict how both absorber geometry and surface topography affect the AFM-IR signal.

In our previous work, we established an analytical model describing the dependence of AFM-IR signal intensity and spatial resolution on the size and depth of spherical absorbers beneath flat surfaces [103]. Although this model provided valuable insights, the experimental validation was limited by indirect knowledge of absorber positioning and the assumption of flat sample surfaces. To overcome these limitations, this study employs advanced nano-fabrication techniques to create samples with well-controlled absorber geometries and complex surface features. This approach enables direct investigation of how variations in absorber size, shape, position, and surface topography influence the chemical imaging capabilities of AFM-IR.

By combining experimental measurements with FEM simulations and an improved analytical model, we explore the relationship between sample geometry and AFM-IR signal generation. Our findings reveal that both the FWHM of chemical images and the signal intensity are strongly dependent on the underlying absorber dimensions. Moreover, we

demonstrate distinct differences in the chemical imaging mechanisms when exciting absorbers beneath the surface compared to those within the covering layer. These effects are particularly pronounced in complex structures, such as logo-shaped patterns, where surface topography plays a significant role in shaping the detected signal.

The insights gained from this work enhance the understanding of AFM-IR's subsurface imaging capabilities and highlight the importance of considering sample geometry in both experimental design and data interpretation. These findings have broad implications for fields requiring high-resolution chemical imaging of buried structures, including materials science, nanotechnology, and microelectronics. The work has been submitted for publication. A pre-print is available at doi:10.26434/chemrxiv-2025-slt6r.

# Experimental and Theoretical Insights into Nanoscale AFM-IR Imaging of Complex Heterogeneous Structures

Yide Zhang,[†,‡,¶] Ufuk Yilmaz ,[†] Artem S. Vorobev,[‡,¶] Simone Iadanza,[§,‖] Liam O'Faolain,[‡,¶] Bernhard Lendl,[†] and Georg Ramer*[,†]

†*Institute of Chemical Technologies and Analytics, TU Wien, Vienna, Austria*

‡*Centre for Advanced Photonics and Process Analysis, Munster Technological University, Cork, Ireland*

¶*Tyndall National Institute, Cork, Ireland*

§*Laboratory of Nano and Quantum Technologies PaulScherrer-Institut, Villigen, Switzerland*

‖*Ecole Polytechnique Federale de Lausanne, Lausanne, Switzerland*

E-mail: georg.ramer@tuwien.ac.at

**Abstract**

Nanoscale chemical imaging enabled by atomic force microscopy-infrared spectroscopy (AFM-IR) provides valuable insights into the complex structures and chemical compositions of materials and biological samples. While AFM-IR has been applied to subsurface imaging, the underlying mechanisms, particularly in non-planar geometries, complex, heterogeneous structures, remain underexplored. This study presents a theoretical analysis and experimental validation of AFM-IR for imaging subsurface features within organic multilayer structures, uncovering how image broadening depends on

whether the excitation occurs in the subsurface or covering layer. An analytical model based on the sample geometry demonstrates that the lateral size of the absorber significantly impacts both the signal intensity and spatial resolution in AFM-IR chemical imaging. These findings are experimentally validated, and a more representative finite element method (FEM) model was subsequently created, resulting in strong agreement with the experimental data. The model reveals how irregular structures directly impact photothermal expansion, providing an explanation for the distinct image broadening observed with infrared excitation of different layers. Additionally, a linear relationship is observed between feature size, chemical images, and AFM-IR signal intensity. These findings contribute significantly to the understanding of the AFM-IR signal, providing insights into resolution, sensitivity, paving the way for more advanced nanoscale chemical imaging capabilities.

# Introduction

Achieving nanoscale chemical imaging with high spatial resolution remains a challenge, particularly for subsurface structures where traditional techniques struggle to provide accurate depth information. Atomic force microscopy-infrared spectroscopy (AFM-IR) overcomes this limitation by combining the high spatial resolution of atomic force microscopy (AFM) with the chemical specificity of infrared (IR) spectroscopy, enabling sub-diffraction-limited chemical imaging.[1–3] AFM-IR provides detailed chemical and structural insights into materials at the nanoscale,[4–8] making it a valuable tool in fields such as materials science, biology, and nanotechnology.[1,2,9–12]

The working principle of AFM-IR lies in detection of thermal expansion of the sample area beneath the cantilever tip after the absorption of focused, pulsed IR radiation. A sequence of laser pulses induces a modulated temperature change in the sample, generating photothermal and photoacoustic effects due to radiation absorption.[13] This results in a rapid thermal expansion and a height change of the sample surface, which then induces an oscillatory

motion in the cantilever, detected through the cantilever deflection signal. The extent of this deflection is directly proportional to both the wavelength-dependent absorption coefficient and the thermal expansion coefficient of the sample.[4] This enables AFM-IR to provide images based on local infrared absorption, i.e., chemical imaging.

While the cantilever tip scans the sample surface only, the AFM-IR signal is not just from the top-most part of the sample. Several studies have investigated depth sensitivity by optimizing laser parameters. For instance, Prine et al.[14] demonstrated tunable depth sensitivity in bilayer polymer films by controlling laser energy and pulse frequency, while Jakob et al.[15] explored how signal intensity varies with sample thickness. Dazzi et al.[16] established an empirical relationship between probing depth and laser repetition rate. These studies have highlighted the value of AFM-IR as a non-destructive technique for observing subsurface features at the nanoscale.

However, these prior studies focused on simplified layered structures with uniform interfaces, where depth profiling could be predicted with well-controlled conditions. In real-world applications, many materials exhibit complex three-dimensional geometries, irregular sample topographies, and lateral heterogeneities that affect AFM-IR signal generation and spatial resolution. The mechanisms governing AFM-IR response in such systems remain largely unexplored.

The need for non-destructive subsurface imaging[17] is critical for understanding defects and dislocation layers beneath the surface,[18] particularly in micro- and nano-device manufacturing for detecting buried defects,[19] energy science for probing subsurface morphologies that influence charge transport and stability,[20] and semiconductors for imaging nanoscale buried interfaces essential for device optimization.[21]

While conventional techniques, such as optical microscopy lack nanoscale resolution,[22] while AFM struggles with subsurface detection.[23] Other infrared-based scanning probe microscopy techniques, such as scattering-type scanning near-field optical microscopy (s-SNOM)[24,25] and nano-FTIR spectroscopy,[26] have emerged as promising alternatives for surface and sub-

surface measurements. These techniques offer spatial resolution in the order of the tip radius, typically around 25 nm, providing valuable insights into nanotomography and enabling simultaneous chemical composition and topography measurements. They also allow depth probing up to 100 nm.[26,27] However, these measurements were limited to simple structures, such as thin-film or stair-shaped samples. Furthermore, they did not fully account for the sample's geometry and the influence of sample size has been largely overlooked.

Our recent work demonstrated the depth and size dependence of spherical absorbers on signal intensity and spatial resolution in AFM-IR.[28] However, knowledge about the absorber position in this work was only indirect and the sample surface was required to be flat. Further experimental validation and a non-trivial extension of the model are needed to understand the AFM-IR signal of subsurface absorbers in complex geometries.

In this study, we improve upon our previous work and the state of the art in several crucial ways: We now use nano-fabrication to create our samples. This yields well controlled complex, heterogeneous structures. We thus have direct knowledge about absorber size, shape and position and the sample surface no longer is flat, enabling us to explore the effect of surface topography on the AFM-IR signal. Nano-fabrication also means that sample dimensions can easily be changed through nano-fabrication, which allows verification of the models across a large parameter space. With these controlled structures, we establish a direct correlation between experimental observations and theoretical predictions. Furthermore, we experimentally confirm a linear relationship between absorber size and AFM-IR signal broadening, providing new insights into spatial resolution and signal interpretation in AFM-IR imaging.

## Results and discussion

Samples were fabricated on silicon substrates with 1 µm-high SU-8 (a high contrast, epoxy-based electron beam resist) structures using electron-beam lithography (EBL). The sample

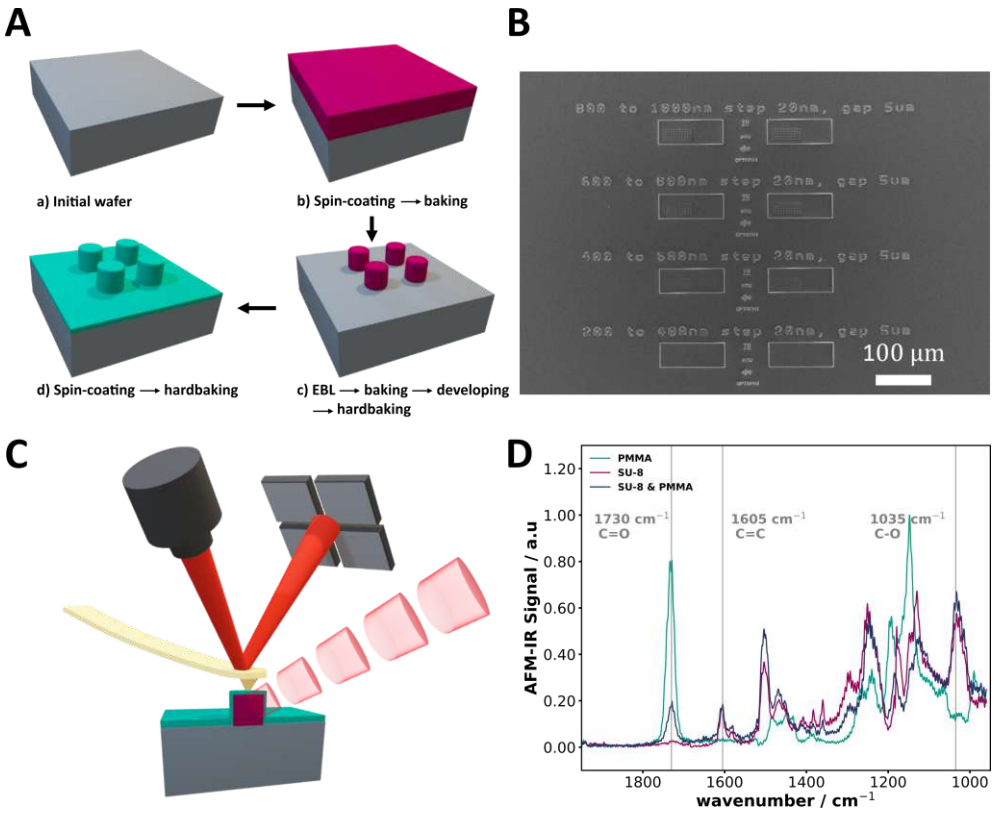


Figure 1: (A) Fabrication steps for the sample (details are discussed in Methods Section). The SU-8 layer is depicted in purple, while the PMMA layer is depicted in turquoise. (B) SEM image of the fabricated sample, featuring a 1 µm thick layer of SU-8 on a silicon substrate, encased by a 185 nm layer of PMMA. The pillars have diameters ranging from 480 nm to 1000 nm, with steps of 20 nm, along with various logo-shaped structures on the same chip. (C) Illustration of the AFM-IR setup. (D) AFM-IR spectra were obtained from the SU-8 and SU-8 & PMMA samples, respectively.

.

structures are depicted in step c of Figure 1A and are referred to as "SU-8" in figures and throughout this work. The patterned SU-8 was then coated with a 185 nm-thick PMMA layer, illustrated in step d of Figure 1A. This bilayer sample is referred to as "SU-8 & PMMA" throughout the manuscript. The resulting patterns are illustrated in Figure 1B.

In the experiments, we employed tapping-mode AFM-IR,[11,13,29–31] which utilizes the mechanical resonance of the cantilever and heterodyne mixing of the cantilever tapping motion

and surface expansion to enhance signal detection. Unlike other modes, the resonance frequency is minimally influenced by variations in the sample's mechanical properties.[9] Moreover, this approach delivers exceptional spatial resolution, achieving spectral resolutions as fine as 10 nm.[29] The AFM-IR spectrum of SU-8 was obtained from the SU-8 sample, while the spectrum of PMMA was obtained from the SU-8 & PMMA sample, specifically from the surrounding area of pillars. SU-8 is characterized by the presence of the C=C stretching vibration near 1605 $cm^{-1}$ and the C-O stretching vibration around 1035 $cm^{-1}$.[32] In contrast, PMMA exhibits a distinct absorption band at 1730 $cm^{-1}$, attributed to the C=O vibrational mode of the ester moiety. Positioning the cantilever tip atop of the nanopillar, produced a combination from both SU-8 and PMMA spectra, shown as the dark-blue curve in Figure 1D.

To investigate the dependence of AFM-IR signal intensity and spatial resolution on the size of absorbers, we designed and fabricated nanopillars with identical height but varying diameters, ranging from 480 nm to 1000 nm, as shown in Figure 1B. AFM-IR experiments were performed at laser wavelengths corresponding to the absorption bands of the underlying SU-8 and the covering PMMA layers. The same AFM cantilever was used throughout all pillar measurements to minimize any mechanical variability between probes that could affect the signal intensity. Topography and chemical images were collected at each wavenumber over a 10 µm by 10 µm area containing four pillars (a single pillar measurement is presented in Figure S2). For more measurement details, see the Methods Section.

Figure 2A shows an SEM image of four pillars. Pillars aligned in the same column in the top and bottom rows are identical in size. The pillars in the right column have a diameter that is 20 nm larger than those in the left column. SEM measurements provided a rough estimate of pillar dimensions, the fidelity of the fabrication process. To map the C=C stretch band of SU-8, chemical images at 1605 $cm^{-1}$ were recorded (Figure 2B). Areas of strong absorption in Figure 2B correspond to the higher (white) regions in the topography image (Figure 2C). By tuning the laser to 1730 $cm^{-1}$ and exciting PMMA's C=O vibrational

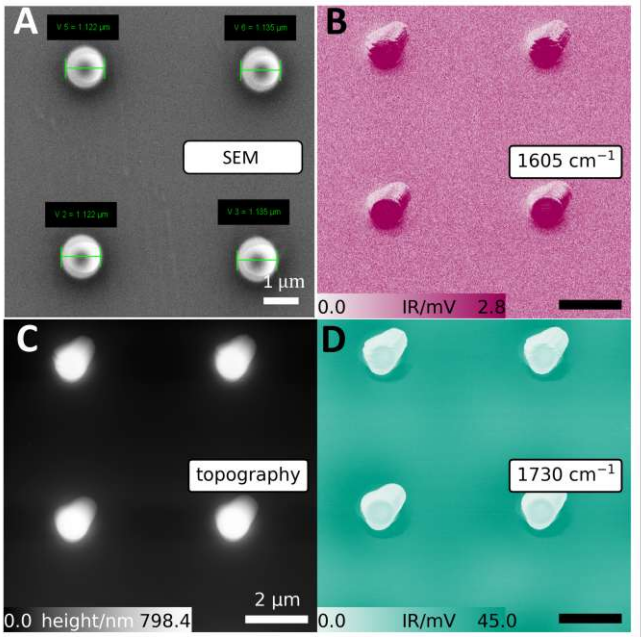


Figure 2: (A) SEM image of fabricated SU-8 pillars covered by PMMA. The first column shows SU-8 pillars with a designed diameter of 800 nm, and the second column 820 nm. After covering the PMMA layer, the pillars were measured using SEM, revealing diameters of 1122 nm and 1135 nm in the first and second columns, respectively. Note that the turquoise markings include the thickness of the covering PMMA layer. (B) Corresponding AFM-IR chemical map at 1605 cm$^{-1}$. (C) AFM topography image. (D) Corresponding AFM-IR chemical map at 1730 cm$^{-1}$. The scale bar is consistent across panels B, C, and D.

mode, we recorded a chemical image of the same area (Figure 2D). While the distinct shape of the pillars remains clearly visible, the highest IR signal is observed in the surrounding area rather than at the pillars themselves.

Based on the topographic and chemical imaging measurements of the nanopillars, we analyzed the dependence of AFM-IR signal intensity and resolution on the absorber size. To achieve this, we generated cross-sectional profiles through the center of each nanopillar, measured the FWHM, and averaged the IR signal in the integrated area for each, as shown in Figure S3. Figure S4A shows the cross-sectional profiles of the pillars in the first row of Figure 2B and C, while Figure S4B presents the profiles from the first row of Figure 2C and D.

To better understand the physical origins of the measured AFM-IR signal and to account for possible influencing factors, we developed an analytical model by solving the heat transfer and thermoelastic equations.

We analyzed the AFM-IR signal by examining the thermal expansion of the sample and considered laser heating as a time-dependent cylindrical volumetric heat source $g(r, z, t)$, where $r$ and $z$ represent any location in the domain. Heat is generated internally throughout the solid absorber at a rate of $g(r, z, t)$ per unit volume. Thermal conduction in cylindrical coordinates was described using Fourier's law[33]

$$\frac{\partial^2 T(r,z,t)}{\partial r^2} + \frac{1}{r}\frac{\partial T(r,z,t)}{\partial r} + \frac{\partial^2 T(r,z,t)}{\partial z^2} + \frac{g(r,z,t)}{\kappa} = \frac{1}{\alpha}\frac{\partial T(r,z,t)}{\partial t} \tag{1}$$

where $\kappa$ is the thermal conductivity and $\alpha$ is the thermal diffusivity. In the equilibrium state, the solution of the Navier's equations of thermoelasticity[34] without external force in the cylindrical coordinates can be expressed by the Boussinesq harmonic functions:

$$u_z = \frac{\partial \Phi}{\partial z} + \frac{\partial \varphi}{\partial z} + z\frac{\partial \psi}{\partial z} - (3 - 4v)\psi \tag{2}$$

$$u_r = \frac{\partial \Phi}{\partial r} + \frac{2}{\partial r}\frac{\partial \varphi}{\partial r} + z\frac{\partial \psi}{\partial \theta} + z\frac{\partial \psi}{\partial r} \tag{3}$$

where $v$ is Poisson's ratio, Goodiers thermoelastic displacement potential $\Phi$ and Boussinesq harmonic functions $\varphi$ and $\psi$ must satisfy governing equations[34], as shown in Supplementary Section Equation S58, S60 and S61.

In this study, tapping-mode AFM-IR is utilized, ensuring that the cantilever tip remains perpendicular to the sample surface. This configuration effectively eliminates lateral tip–sample forces[35]. Consequently, lateral forces are negligible, and only the vertical displacement $u_z$ is considered as the primary factor contributing to surface deformation.

Assuming that both the buried and covering layers are perfect cylindrical shapes with vertical sidewalls, the surface displacement can be derived and simplified as follows (see

Supplementary Section S2):

$$u_z(r,t) = \sum_{n=0}^{\infty}\sum_{m=0}^{\infty} \frac{2(1+v)A(\beta_m,\eta_n)\alpha_z}{\beta_m}\left(\frac{\eta_n^2}{\beta_m^2+\eta_n^2}+1\right)\underbrace{J_0(\beta_m r)}_{\text{spatial}}\underbrace{\mathcal{T}(t)}_{temporal} \tag{4}$$

Here, $\beta_m$ and $\eta_n$ represent eigenvalues determined by the boundary conditions. However, two boundary conditions - thermal insulation at $r = R_{mat}$ and $z = H_{mat}$ - are not included in the model. Incorporating these conditions would prevent the use of separation of variables. Nevertheless, comparisons with FEM simulations confirm that this simplification has minimal impact on the results. The term $A(\beta_m, \eta_n)$ is the modal amplitude (refer to Supplementary Section S1 Equation S52).

$$A(\beta_m,\eta_n) \propto \frac{g_V R_{abs} J_1(\beta_m R_{abs})}{\kappa \lambda_{mn}^2 \beta_m} \tag{5}$$

This term primarily depends on the product of absorber size $R_{abs}$ and solutions of first order Bessel functions $J_1(\beta_m R_{abs})$, volumetric heat source $g_V$ (the product of the optical absorption coefficient and optical fluence), and the eigenvalue solutions.

From Eqs. 4, 5, it is evident that the amplitude of surface displacement depends linearly on the optical absorption coefficient and thermal expansion coefficient $\alpha_z$, aligning with previous findings.[4,28] Additionally, it is inversely proportional to the thermal diffusivity $\kappa$.

The AFM-IR signal also exhibits a distinct dependence on absorber size. As shown in Figure 3A, the average signal scales with absorber volume for sizes below approximately 840 nm, while beyond this threshold, it transitions to a linear relationship with absorber diameter. Within the absorber diameter range of the fabricated samples, the averaged signal follows a linear trend, as highlighted in the inset of Figure 3A.

Moreover, the FWHM of the surface displacement profile closely follows the absorber diameter, increasing linearly from 200 nm to 1500 nm. For diameters below 200 nm, this trend deviates, reaching a minimum of 270 nm. Beyond 1500 nm, the FWHM tends to match the absorber diameter, as shown in Figure 3B. These findings highlight the strong

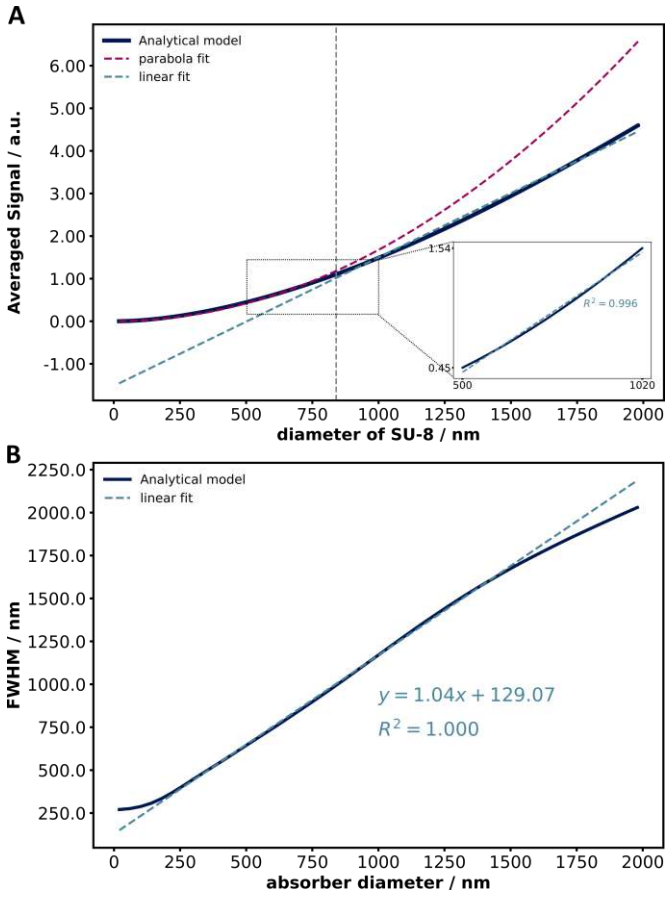


Figure 3: (A) The simulated averaged signal and (B) the full width at half maximum (FWHM) of the surface displacement profiles are plotted as functions of the SU-8 diameter, based on the analytical model. The linear fit in (B) was performed for SU-8 diameters ranging from 200 nm to 1500 nm. The analytical simulations were conducted at a laser repetition rate of 710 kHz and a laser pulse width of 220 ns, matching the experimental conditions.

dependence of AFM-IR spatial resolution on absorber size.

To accurately model the nanopillar structure while reflecting its real-world fabricated characteristics, we analyzed an SU-8 pillar with 800 nm diameter, by measuring its height from topography images of both the SU-8 and SU-8 & PMMA samples. Cross-sectional profiles through the pillar centers (Figure 4A) show that the sidewalls are not perfectly vertical but exhibit a tilt, particularly in the SU-8 & PMMA sample. This effect cannot be accurately modeled using an analytical approach. Therefore, we developed a more realistic

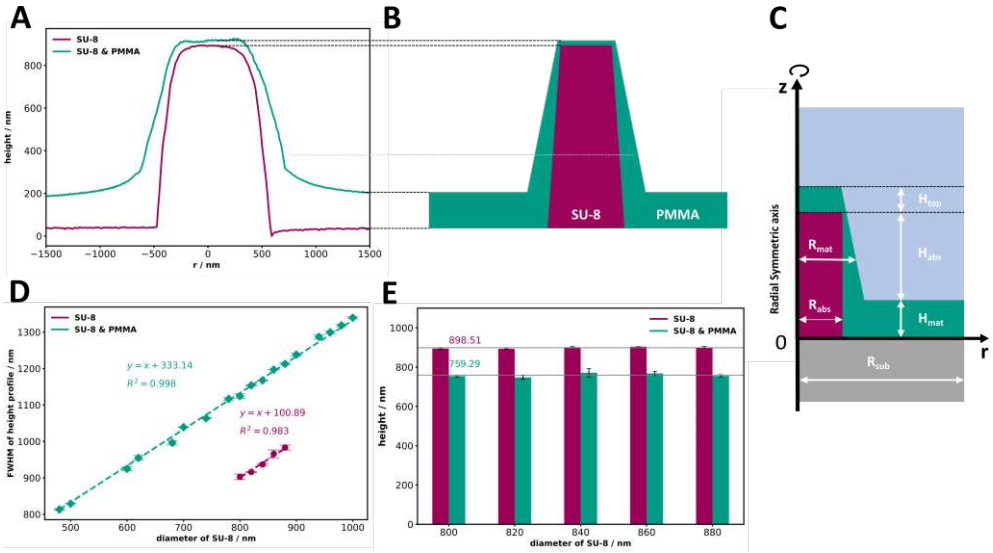


Figure 4: (A) Cross-sectional height profiles of a nanopillar with an 800 nm diameter were obtained for SU-8 and SU-8 & PMMA samples. (B) Schematic representation of the modeled nanopillar. In the graph, the dashed line indicates the reference height from panel A, reflecting the geometry of the SU-8 and PMMA layers. (C) Cylindrically symmetric system composed of a single cylindrical absorber surrounded by a matrix, deposited on a non-absorbing substrate. (D) FWHM of the cross-sectional height profiles of the SU-8 and SU-8 & PMMA samples. Error bars indicate the maximum deviation from the mean values. (E) Height of each nanopillar at different designed diameter of SU-8.

FEM model to compare the results with experimental data. Detailed descriptions of the simulations are provided in the Supplementary Section S4. In our model, we assume tilted sidewalls with flat surfaces for both the SU-8 and PMMA covering layers, as depicted in Figure 4B and C. A cylindrical coordinate system was used to achieve an axi-symmetric, quasi-3D representation. This approach is more intuitive than a full 3D model, while still retaining generality, and offers significantly lower computational cost, making it more suitable for comparison between the analytical model and numerical model.

Furthermore, to ensure the accuracy of the simulations, we conducted measurements on the SU-8 sample to determine the height and FWHM of each nanopillar (see Figure S4). The FWHM of each nanopillar was determined from its height cross-sectional profiles, revealing a linear relationship with the diameter of SU-8 for both SU-8 and SU-8 & PMMA samples, as

shown in Figure 4D, confirming consistency between the design and the fabrication process. From the linear fit, the sidewall thickness was calculated as the difference of the radius of the PMMA layer ($R_{mat}$) and SU-8 pillar ($R_{abs}$). Using the measured values, the thickness is given by: $R_{mat} - R_{abs} = 333.14\,\text{nm}/2 - 100.89\,\text{nm}/2 = 116.1\,\text{nm}$.

The height of examined nanopillars exhibited only minor variations within each sample, as depicted in Figure 4E. Notably, the average height of the SU-8 sample is greater than that of the SU-8 & PMMA sample, suggesting an inhomogeneous coverage of PMMA on the substrates and SU-8 structures. Using the measured average heights of selected pillars, we calculated $H_{abs}+H_{mat} = 898.5\,\text{nm}$, $H_{top}+H_{abs} = 759.3\,\text{nm}$, where $H_{abs}$ the hight of absorber, $H_{mat}$ the PMMA layer thickness on the substrate, $H_{top}$ the PMMA layer thickness on the SU-8 nanopillar, as as illustrated in Figure 4C. The PMMA layer thickness on substrate was determined by height measurements at six locations using a profilometer, yielding an average thickness of $H_{mat} = 171.9\,\text{nm}$. From this, the PMMA layer thickness on SU-8 nanopillar was calculated as $H_{top} = 32.7\,\text{nm}$.

The material properties used for simulations are provided in Supplementary Table 1. Unless stated otherwise, the following parameters remained constant in simulations involving the FEM model: side wall thickness 116 nm, $H_{mat} = 170\,\text{nm}$, $H_{top} = 30\,\text{nm}$, $R_{sub} = 5\,\mu\text{m}$ (see Figure 4C for a sketch of the sample geometry).

Figure 5A and B compare 3D FEM simulations and experimental observations when the SU-8 (underlying layer) is excited. The laser is tuned to $1605\,\text{cm}^{-1}$ matching the SU-8 absorption making it the heat source. The simulated displacement is shown in color, representing the normalized magnitude, along with the deformed shapes. The cross-sectional profiles from Figures 5A and B show good overlap between the simulation and experimental results, as illustrated in Figure 5C. When the laser is tuned to $1730\,\text{cm}^{-1}$, the heat source transitions from the underlying layer to the covering layer. The deformed shapes align well with experimental data (Figures 5D and 5E), showing strong agreement in the cross-sectional profiles (Figure 5F).

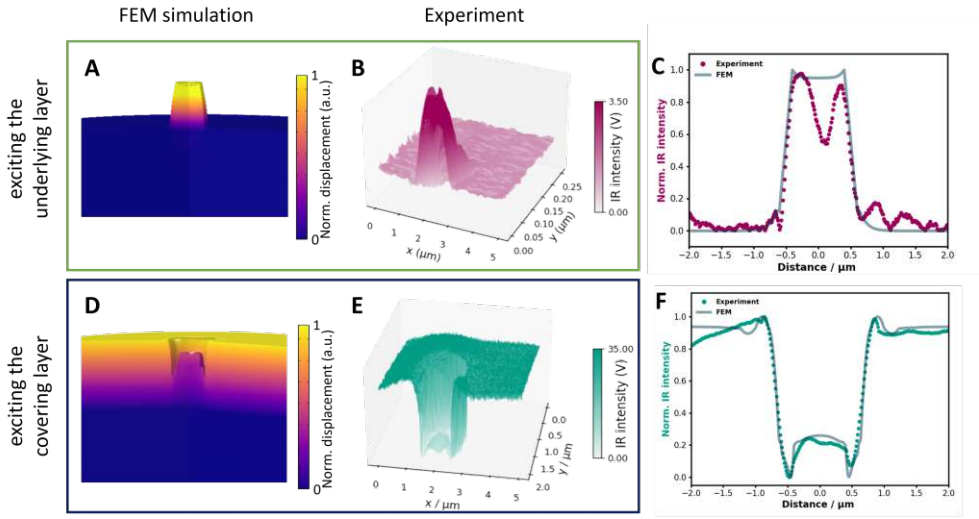


Figure 5: We examine the case of 800 nm pillar. (A) and (D) show 3D FEM simulations of displacement with SU-8 and PMMA as heat sources, respectively, with amplitudes exaggerated for clarity. (B) and (E) represent the corresponding experiments with SU-8 and PMMA excited, respectively. The cross-sectional profiles of the normalized IR intensity from experimental data (B) and (E) , compared with the corresponding FEM simulation data from (A) and (D) are shown in (C) and (F), respectively.

Furthermore, by integrating the green areas, as illustrated in Figures S3A, Figure 6A shows that the averaged IR signal at a wavenumber of 1605 $cm^{-1}$ increases nearly linearly with the diameter of SU-8, consistent with FEM simulation results and theoretical prediction (Figure 3A). Likewise, when tuning to 1730 $cm^{-1}$ the signal decreases as the pillar size increases. This means that the lateral extent of the structure affects the local AFM-IR amplitude. In the case of the SU-8 pillar a change by a factor of 2 in size causes an increase of the signal amplitude by 50%.

While the size of the pillar structures in the chemical images increase linearly with feature size, the FWHM of the structure depends on whether the SU-8 subsurface structure or the PMMA covering layer is excited. The same structure when measured at a wavelength absorbed by the subsurface material appears about 358 nm smaller than when measured at a wavelength corresponding to the cover layer, and around 103 nm smaller than the height image. This calculation is based on the intercept difference obtained from the linear fitting

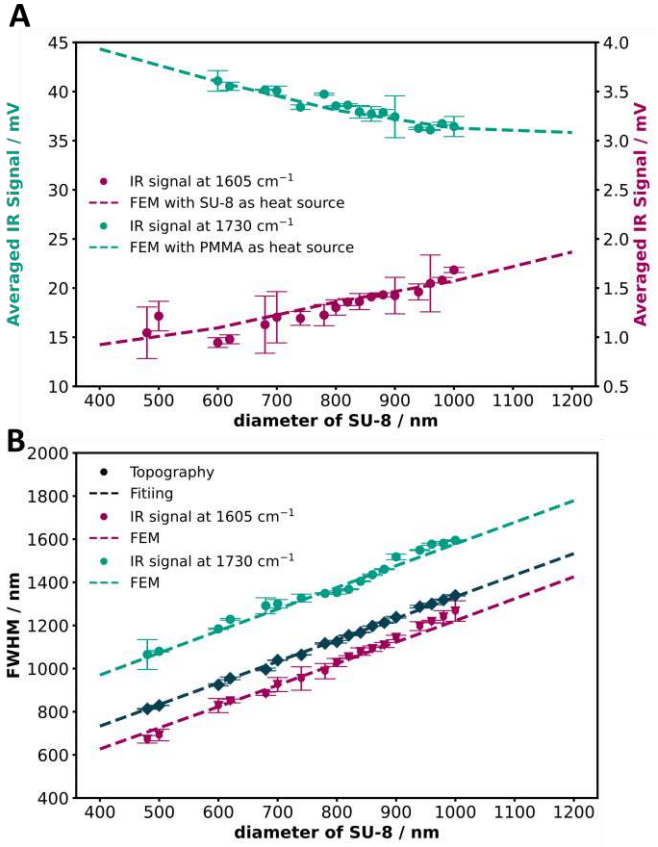


Figure 6: (A) The averaged AFM-IR signal of the examined pillars is plotted as a function of the SU-8 diameter. (B) The FWHM extracted from the cross-sectional profiles of chemical images is shown alongside the corresponding FEM-simulated data. The FEM simulation results were scaled using a consistent arbitrary factor for both SU-8 and PMMA as heat sources, enabling direct comparison with experimental data. Error bars indicate the maximum deviation from the mean values.

of the experimental data. Fitted results are shown in Figure S8. This trend is represented by the experimental data, along with the corresponding simulated lines in Figure 6B, aligning closely with the analytical simulation shown in Figure 3B.

This effect is observed not only in pillar structures but also in more complex geometries, such as the one shown in Figure 7. As before, the structure appears smaller when exciting the subsurface layer (SU-8 at 1035 cm$^{-1}$, see Figure 7A) compared to when exciting the cover layer (PMMA at 1730 cm$^{-1}$, see Figure 7C).

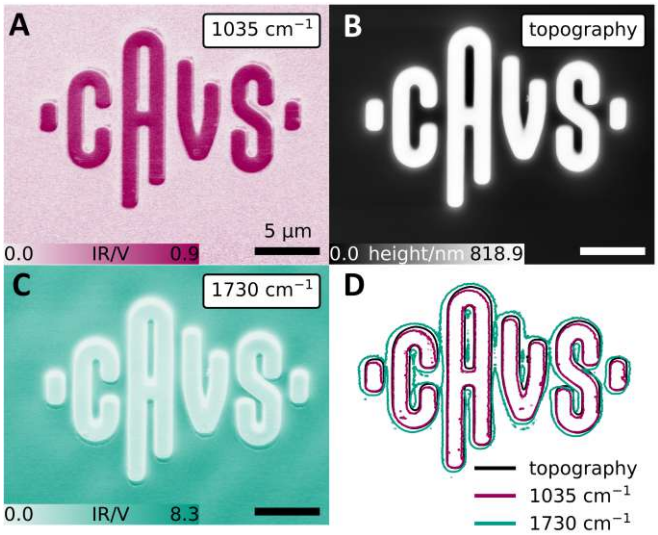


Figure 7: (A) AFM-IR chemical map at 1035 cm$^{-1}$. (B) AFM topography image. (C) Corresponding AFM-IR chemical map at 1730 cm$^{-1}$. (D) Contour lines of the topography image, chemical map at 1035 and 1730 cm$^{-1}$.

Higher IR signals were observed at pillar edges compared to the center, as confirmed by simulations shown in Figure 5C. This phenomenon can be primarily attributed to the tilted, uneven sidewall coverage of the pillar. It is not observed when the SU-8 pillar and the covering layers are vertical (Figure S9A) or when the SU-8 pillar is flush with the surrounding PMMA matrix (Figure S9B). Other contributing factors include differences in thermal expansion coefficients between the materials: PMMA has a thermal expansion coefficient nearly four times higher than that of SU-8. Additionally, the potential presence of interfacial thermal resistance (ITR) between PMMA and SU-8 may also play a role.

To investigate the influence of these factors, we performed FEM simulations, where the SU-8 pillar was modeled as a perfect vertical cylinder, while the PMMA covering layer had a tilted sidewall with the same minimum width as the SU-8 pillar. By varying the tilt angle of the sidewall from 0 to 10 degrees, the results in Figure 8A show that for sidewall angles below 5 degrees, the signal amplitude at the edge of the pillar is significantly higher than at the center. This effect was found to be relatively insensitive to the thermal expansion

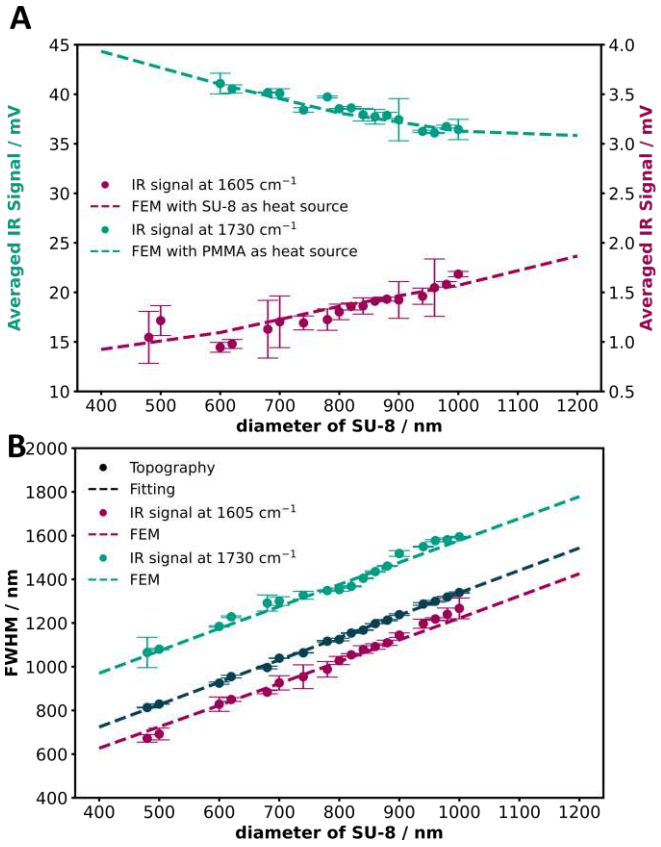


Figure 8: (A) The normalized amplitude of the minimum surface deformation at different radial positions with varying tilted angles of the sidewalls. (B) The normalized amplitude of the minimum surface deformation at different radial positions with varying ITR values.

coefficient. As shown in Figure S7, even when the thermal expansion coefficient of PMMA was assumed to be equal to that of SU-8, the observed signal distribution at the edge and center remained similar.

Additionally, we explored the effect of varying the ITR between the materials. With a 5-degree tilted sidewall, increasing the ITR, resulted in significantly higher signal amplitude at the edge compared to the center, as shown in Figure 8B. While ITR between PMMA and SU-8 may contribute to this effect, it was not explicitly included in our model in order to avoid unnecessary complexity. Future studies quantifying ITR could improve simulation accuracy and provide a more comprehensive understanding of the underlying mechanisms.

# Conclusions and outlook

In summary, we developed an analytical model to provide a straightforward overview of how sample geometry and material properties influence the AFM-IR signal. These findings were further verified through experiments and FEM modeling on precisely controlled, fabricated samples.

Our study constitutes the most detailed view of the capability of AFM-IR for subsurface structural analysis yet. We provided experimental evidence supported by theoretical descriptions and modelling of the influence of the surface topography on the chemical image of a subsurface structure for the first time.

A key finding is the variation in the observed structure size in AFM-IR images when exciting the subsurface versus the covering layers caused by the sample geometry. This is observed in our experimental data and also described by the FEM model. Beyond this, the FEM model allows us to explain the detailed features of the the AFM-IR signal, attributing them to the surface geometry — specifically, the tilted sidewalls of the pillars.

We also present the first experimental evidence demonstrating that AFM-IR spatial resolution is directly linked to the absorber's diameter, as demonstrated in Figure 6B and Figure S8. Additionally, we observed a linear increase in signal intensity with absorber diameter. These results align excellently with the theoretical predictions. We believe these findings directly contribute to improved accuracy when determining the actual size of chemically distinct structures using AFM-IR.

Overall, our findings advance the understanding of AFM-IR's capabilities, particularly in subsurface imaging and the role of absorber geometry on signal intensity and spatial resolution. These insights pave the way for future research and applications in nanotechnology and materials science.

# Methods

## Sample preparations

After the initial design of the structures, the fabrication process began with spin-coating a SU-8 (SU-8-2) resist layer (approximately 1000 nm thick) onto a silicon wafer and soft-baking 90 °C for 300 s. To improve polymer adhesion, the wafer was first cleaned using oxygen plasma treatment, followed by a dehydration baking step at 90 °C for 300 s. The desired device layout was patterned onto the SU-8 resist using electron beam lithography (EBL) at 100 kV and 50 pA. After exposure, the sample was post baked at 90 °C for 400 s, developed in an EC-solvent for 60 s and subjected to a final bake at 200 °C for 30 mins. Next, a (185 nm-thick) PMMA (PMMA A4) resist layer was spin-coated over the fabricated sample and hard-baked at 150 °C for 10 mins.

## AFM-IR measurements

All AFM-IR measurements were conducted using a Bruker nano-IR 3s system coupled to a MIRcat-QT external cavity quantum cascade laser array (EC-QCL) from Daylight Solutions, with a spectral range from 910 $cm^{-1}$ to 1950 $cm^{-1}$. Spectra were acquired using AFM-IR in tapping-mode with a heterodyne detection scheme.

For pillar measurements, the cantilever was driven at its first resonance frequency ($f_1 \approx$ 128 kHz), and the AFM-IR signal was demodulated at the second resonance frequency ($f_2 \approx$ 839 kHz) using a digital lock-in amplifier (MFLI, Zurich Instruments). The laser repetition rate was adjusted to $f_L = f_2 - f_1 \approx 711$ kHz. A overall gold-coated cantilever with a nominal first free resonance frequency of 150 ± 75 kHz and a nominal spring constant between 5 and 20 $N\,m^{-1}$ (Tap150GB-G from BudgetSensors) was used. The laser pulse width was set to 220 ns. Laser power was adjusted to 14.75% of the original power using metal mesh attenuators resulting in a pulse peak power of up to 15 mW for 1605 $cm^{-1}$ and 24 mW for 1730 $cm^{-1}$. AFM-IR images were obtained over a 10 µm × 10 µm area at a line-scan rate of

0.1 Hz (lateral speed 100 nm $s^{-1}$) and a resolution of 400 pixels per line.

During measurements of the "CAVS" nanostructure, the cantilever was driven at its first resonance frequency ($f_1 \approx 242$ kHz), and the AFM-IR signal was demodulated at the second resonance frequency ($f_2 \approx 1534$ kHz) using a digital lock-in amplifier (MFLI, Zurich Instruments). The laser repetition rate was set to $f_L = f_2 - f_1 \approx 1292$ kHz. A overall gold-coated cantilever with a nominal first free resonance frequency of 300 ± 100 kHz and a nominal spring constant between 20 and 75 N $m^{-1}$ (Tap300GB-G from BudgetSensors) was used. The laser was set to emit pulses with a pulse width of 160 ns. Laser power was adjusted to 14.75% of the original power using metal mesh attenuators resulting in a pulse peak power of up to 7 mW for 1035 $cm^{-1}$ and 22 mW for 1730 $cm^{-1}$. For AFM-IR images a 25 µm × 20 µm area was scanned with a line rate of 0.1 Hz (lateral speed 100 nm $s^{-1}$) and a resolution of 800 pixels per line.

All spectra were recorded at each location with a spectral resolution of 1 $cm^{-1}$. Dry air generated by an adsorptive dry air generator was used to purge the instrument and all beam paths.

## Supporting Information

A PDF file including of additional Figures S1 to S9, Table 1 and the additional derivations for equations in the main text is available free of charge. Code and raw data to generate all figures is available on Zenodo (DOI:10.5281/zenodo.14812045)[36]

# Author information


### Corresponding Author

**Georg Ramer**- Institute of Chemical Technologies and Analytics, TU Wien, Vienna, Austria; Email: georg.ramer@tuwien.ac.at

ORCID

Yide Zhang: 0000-0002-2675-739X

Ufuk Yilmaz: 0009-0009-3572-5267

Artem S.Vorobev: 0000-0002-3642-5225

Simone Iadanza: 0000-0001-8470-4600

Liam O'Faolain: 0000-0003-1160-7441

Bernhard Lendl: 0000-0003-3838-5842

Georg Ramer: 0000-0001-8307-5435

### Author Contributions

Y.Z. and A.S.V. fabricated samples and drafted the manuscript. Y.Z. and U.Y. performed experiments, prepared figures and drafted the manuscript. Y.Z. developed the model with input from G.R.. S.I provided support in sample fabrications. G.R. supervised U.Y. and Y.Z. in all experiments and evaluations. G.R., L.O. and B.L. conceptualized the study, proposed the project and acquired the funding. All have read and revised the manuscript. Y.Z. and U.Y. contributed equally to this study.

## Acknowledgement

This work was funded with financial support from the European Union's Horizon 2020 research and innovation programme. The authors Y.Z., A.S.V., L.O., G.R., and B.L. acknowledge the Marie Skłodowska-Curie project "OPTAPHI" under grant agreement No. 860808. U.Y., and G.R. acknowledge the project "PeroCUBE" under grant agreement No. 861985. G.R. also acknowledges European Union's Horizon 2020 research and innovation programme in project Tumor-LN-oC (grant agreement no. 953234). The financial support by the Austrian Federal Ministry for Labour and Economy and the National Foundation for Research, Technology and Development and the Christian Doppler Research Association is gratefully acknowledged.

The authors would like to thank Camille Barbier from Tyndall National Institute and Nikolaus Hondl from TU Wien for the initial measurements of SU-8 pillars with AFM.

## Declarations

The authors declare that they have no known competing financial interests or personal relationships that could have appeared to influence the work reported in this paper.

## References

(1) Centrone, A. Infrared Imaging and Spectroscopy Beyond the Diffraction Limit*. *Annual Review of Analytical Chemistry* **2015**, *8*, 101–126, Publisher: Annual Reviews.

(2) Dazzi, A.; Prater, C. B. AFM-IR: Technology and Applications in Nanoscale Infrared Spectroscopy and Chemical Imaging. *Chemical Reviews* **2017**, *117*, 5146–5173, Publisher: American Chemical Society.

(3) Katzenmeyer, A. M.; Holland, G.; Chae, J.; Band, A.; Kjoller, K.; Centrone, A. Mid-infrared spectroscopy beyond the diffraction limit via direct measurement of the photothermal effect. *Nanoscale* **2015**, *7*, 17637–17641, Publisher: The Royal Society of Chemistry.

(4) Dazzi, A.; Prater, C. B.; Hu, Q.; Chase, D. B.; Rabolt, J. F.; Marcott, C. AFM–IR: Combining Atomic Force Microscopy and Infrared Spectroscopy for Nanoscale Chemical Characterization. *Applied Spectroscopy* **2012**, *66*, 1365–1384.

(5) dos Santos, A. C. V.; Lendl, B.; Ramer, G. Systematic analysis and nanoscale chemical imaging of polymers using photothermal-induced resonance (AFM-IR) infrared spectroscopy. *Polymer Testing* **2022**, *106*, 107443.

(6) Ruggeri, F. S.; Mannini, B.; Schmid, R.; Vendruscolo, M.; Knowles, T. P. J. Single molecule secondary structure determination of proteins through infrared absorption nanospectroscopy. *Nature Communications* **2020**, *11*, 2945.

(7) Chae, J.; An, S.; Ramer, G.; Stavila, V.; Holland, G.; Yoon, Y.; Talin, A. A.; Allendorf, M.; Aksyuk, V. A.; Centrone, A. Nanophotonic Atomic Force Microscope Transducers Enable Chemical Composition and Thermal Conductivity Measurements at the Nanoscale. *Nano Letters* **2017**, *17*, 5587–5594.

(8) Ramer, G.; Aksyuk, V. A.; Centrone, A. Quantitative chemical analysis at the nanoscale using the PTIR technique. *Analytical Chemistry* **2017**, *89*, 13524–13531.

(9) Kurouski, D.; Dazzi, A.; Zenobi, R.; Centrone, A. Infrared and Raman chemical imaging and spectroscopy at the nanoscale. *Chemical Society Reviews* **2020**, *49*, 3315–3347, Publisher: Royal Society of Chemistry.

(10) Mathurin, J.; Deniset-Besseau, A.; Bazin, D.; Dartois, E.; Wagner, M.; Dazzi, A. Photothermal AFM-IR spectroscopy and imaging: Status, challenges, and trends. *Journal of Applied Physics* **2022**, *131*, 010901.

(11) J. Schwartz, J.; S. Jakob, D.; Centrone, A. A guide to nanoscale IR spectroscopy: resonance enhanced transduction in contact and tapping mode AFM-IR. *Chemical Society Reviews* **2022**, *51*, 5248–5267, Publisher: Royal Society of Chemistry.

(12) V. D. Dos Santos, A. C.; Hondl, N.; Ramos-Garcia, V.; Kuligowski, J.; Lendl, B.; Ramer, G. AFM-IR for Nanoscale Chemical Characterization in Life Sciences: Recent Developments and Future Directions. *ACS Measurement Science Au* **2023**, *3*, 301–314.

(13) Mathurin, J.; Deniset-Besseau, A.; Dazzi, A. Advanced Infrared Nanospectroscopy Using Photothermal Induced Resonance Technique, AFMIR: New Approach Using Tapping Mode. *Acta Physica Polonica A* **2020**, *137*, 29–32.

(14) Prine, N.; Cardinal, C.; Gu, X. Understanding and controlling the depth sensitivity of scanning probe based infrared imaging and nanospectroscopy for buried polymeric structures. *Nanoscale* **2023**, *15*, 10244–10253.

(15) Jakob, D. S.; Schwartz, J. J.; Pavlidis, G.; Grutter, K. E.; Centrone, A. Understanding AFM-IR signal dependence on sample thickness and laser excitation: experimental and theoretical insights. *Analytical Chemistry* **2024**, *96*, 16195–16202, Publisher: American Chemical Society.

(16) Dazzi, A.; Mathurin, J.; Leclere, P.; Nickmilder, P.; De Wolf, P.; Wagner, M.; Hu, Q.; Deniset-Besseau, A. Photothermal AFM-IR Depth Sensitivity: An Original Pathway to Tomographic Reconstruction. *Analytical Chemistry* **2024**, *96*, 17931–17940.

(17) Mukherjee, S.; Gowen, A. A review of recent trends in polymer characterization using non-destructive vibrational spectroscopic modalities and chemical imaging. *Analytica Chimica Acta* **2015**, *895*, 12–34.

(18) Xie, J.; Yan, J.; Zhu, D.; He, G. Atomic-Level Insight into the Formation of Subsurface Dislocation Layer and Its Effect on Mechanical Properties During Ultrafast Laser Micro/Nano Fabrication. *Advanced Functional Materials* **2022**, *32*, 2108802.

(19) Shin, C.; Kim, K.; Kim, J.; Ko, W.; Yang, Y.; Lee, S.; Jun, C. S.; Kim, Y. S. Fast, exact and non-destructive diagnoses of contact failures in nano-scale semiconductor device using conductive AFM. *Scientific Reports* **2013**, *3*, 2088.

(20) Cui, Z.; Sun, J.; Landerer, D.; Sprau, C.; Thelen, R.; Colsmann, A.; Hölscher, H.; Ma, W.; Chi, L. Seeing Down to the Bottom: Nondestructive Inspection of All-Polymer Solar Cells by Kelvin Probe Force Microscopy. *Advanced Materials Interfaces* **2016**, *3*, 1600446.

(21) Xu, J.; Wu, H.; Mun, J.; Ning, R.; Wang, W.; Wang, G. N.; Nikzad, S.; Yan, H.; Gu, X.;

Luo, S.; Zhou, D.; Tok, J. B.; Bao, Z. Tuning Conjugated Polymer Chain Packing for Stretchable Semiconductors. *Advanced Materials* **2022**, *34*, 2104747.

(22) Soliman, M.; Ding, Y.; Tetard, L. Nanoscale subsurface imaging. *Journal of Physics: Condensed Matter* **2017**, *29*, 173001.

(23) Farokh Payam, A.; Passian, A. Imaging beyond the surface region: Probing hidden materials via atomic force microscopy. *Science Advances* **2023**, *9*, eadg8292.

(24) Mooshammer, F.; Sandner, F.; Huber, M. A.; Zizlsperger, M.; Weigand, H.; Plankl, M.; Weyrich, C.; Lanius, M.; Kampmeier, J.; Mussler, G.; Grützmacher, D.; Boland, J. L.; Cocker, T. L.; Huber, R. Nanoscale Near-Field Tomography of Surface States on (Bi $_{0.5}$ Sb $_{0.5}$ ) $_2$ Te $_3$. *Nano Letters* **2018**, *18*, 7515–7523.

(25) Govyadinov, A. A.; Mastel, S.; Golmar, F.; Chuvilin, A.; Carney, P. S.; Hillenbrand, R. Recovery of Permittivity and Depth from Near-Field Data as a Step toward Infrared Nanotomography. *ACS Nano* **2014**, *8*, 6911–6921.

(26) Mester, L.; Govyadinov, A. A.; Chen, S.; Goikoetxea, M.; Hillenbrand, R. Subsurface chemical nanoidentification by nano-FTIR spectroscopy. *Nature Communications* **2020**, *11*, 3359.

(27) Ho, K.; Kim, K. S.; Gilburd, L.; Mirzoyan, R.; De Beer, S.; Walker, G. C. Nanoscale Subsurface Morphologies in Block Copolymer Thin Films Revealed by Combined Near-Field Infrared Microscopy and Mechanical Mapping. *ACS Applied Polymer Materials* **2019**, *1*, 933–938.

(28) Zhang, Y.; Yilmaz, U.; Lukasievicz, G. V. B.; O'Faolain, L.; Lendl, B.; Ramer, G. An analytical model of label-free nanoscale chemical imaging reveals avenues toward improved spatial resolution and sensitivity. *Proceedings of the National Academy of Sciences* **2025**, *122*, e2403079122.

(29) Wieland, K.; Ramer, G.; Weiss, V. U.; Allmaier, G.; Lendl, B.; Centrone, A. Nanoscale chemical imaging of individual chemotherapeutic cytarabine-loaded liposomal nanocarriers. *Nano Research* **2019**, *12*, 197–203.

(30) Tuteja, M.; Kang, M.; Leal, C.; Centrone, A. Nanoscale partitioning of paclitaxel in hybrid lipid–polymer membranes. *The Analyst* **2018**, *143*, 3808–3813.

(31) V. D. dos Santos, A. C.; Tranchida, D.; Lendl, B.; Ramer, G. Nanoscale chemical characterization of a post-consumer recycled polyolefin blend using tapping mode AFM-IR. *The Analyst* **2022**, *147*, 3741–3747.

(32) Wang, Y.; Pai, J.-H.; Lai, H.-H.; Sims, C. E.; Bachman, M.; Li, G. P.; Allbritton, N. L. Surface graft polymerization of SU-8 for bio-MEMS applications. *Journal of Micromechanics and Microengineering* **2007**, *17*, 1371–1380.

(33) Cole, K. D., Ed. *Heat conduction using Green's functions*, 2nd ed.; Series in Computational and Physical Processes in Mechanics and Thermal Sciences; CRC Press: Boca Raton, 2011.

(34) Noda, N.; Hetnarski, R. B.; Tanigawa, Y. *Thermal stresses*, 2nd ed.; Taylor & Francis: New York, 2003.

(35) Aliano, A. et al. In *Encyclopedia of Nanotechnology*; Bhushan, B., Ed.; Springer Netherlands: Dordrecht, 2012; pp 99–99.

(36) Zhang, Y.; Yilmaz, U.; Vorobev, A. S.; Iadanza, S.; O'Faolain, L.; Lendl, B.; Ramer, G. Data and Code for "Probing the Depths: Experimental and Simulated Insights into Nanoscale AFM-IR Imaging of Complex Heterogeneous Structures". 2025; `https://doi.org/10.5281/zenodo.14812045`.

In Section 1.2, we introduced AFM and its applications. Despite its advantages, AFM faces several challenges, particularly in improving measurement sensitivity, resolution, and operational efficiency. The performance of AFM-based techniques is heavily influenced by the mechanical properties of the cantilever, especially its resonant frequency and stiffness. These factors directly impact the application range, image acquisition speed, and temporal resolution, ultimately affecting both efficiency and practicality.

AFM cantilevers deflect in response to tip-sample interactions, and this deflection is commonly measured using the optical-lever technique. In this method, a weak laser beam reflects off the backside of the cantilever onto a position-sensitive photodiode detector [117]. However, this approach requires long optical paths, leading to a bulky readout system that complicates high-throughput AFM implementations [118, 119].

Achieving higher resonant frequencies in the MHz range requires reducing cantilever dimensions. However, miniaturization introduces challenges when using free-space optical methods, as strong diffraction effects arise when the cantilever width becomes smaller than the beam waist [121].

Recent advancements in cavity optomechanics [127, 128, 129] have enabled highly sensitive displacement measurements of nanomechanical resonators, surpassing quantum limits [130, 131]. These systems detect mechanical motion via evanescent wave coupling to an optical cavity, where a nanomechanical resonator interacts with a micro-resonator in the near field [132].

Leveraging cavity optomechanics, researchers have demonstrated significant potential for enhancing AFM performance. Pierre et al. introduced a ring-shaped probe integrating a nanoscale apex with a ring resonator on a silicon chip. This design enabled operation at extremely high frequencies ($> 100\,\mathrm{MHz}$) with sub-nanometer oscillation amplitudes [133]. Similarly, Kartik et al. fabricated a cantilever positioned near a micro-ring disk on a silicon device, achieving sub-$\mathrm{fm}/(\mathrm{Hz})^{1/2}$ sensitivity to cantilever motion with a broad stiffness range from $0.01\,\mathrm{N/m}$ to $290\,\mathrm{N/m}$ [134, 216].

Building on these nanophotonic transducers, Chase et al. demonstrated AFM-based chemical composition and thermal conductivity measurements at the nanoscale [91]. Wang et al. extended these capabilities to chemical imaging of thermal conductivity and interfacial thermal conductance [102]. These advancements go beyond conventional AFM topographical imaging, enabling precise material property characterization through integrated nanophotonic transducers.

In this section, we introduce three AFM probe designs that integrate optomechanical cavities, leveraging their unique capabilities to enhance measurement sensitivity, resolution, and operational efficiency. These designs address key AFM limitations by improving force

detection, achieving high mechanical resonance, and enabling advanced nanoscale material characterization.

## 4.3. Ring Resonator-Based Optomechanical Transducers for Atomic Force Sensing

In recent years, the integration of optical and mechanical systems has garnered significant attention in advancing high-precision sensing technologies. One such advancement is the development of optomechanical devices, which leverage the coupling between optical micro-resonators and mechanical resonators to achieve exceptional displacement sensitivity. These devices offer unique advantages, including high bandwidth, precise wavelength control, and strong coupling between optical and mechanical modes, making them ideal candidates for various applications in force and displacement sensing [127, 128, 129].

Traditional sensing systems often face limitations in terms of sensitivity, bandwidth, and integration complexity, especially when coupled with the demands of high-throughput measurements. To address these challenges, the use of silicon-on-insulator (SOI) wafers has emerged as a promising platform due to their compatibility with integrated photonics and mechanical components [217]. The integration of optical micro-ring resonators with suspended cantilevers on SOI wafers provides a compact, robust solution with tunable mechanical properties, enabling the realization of sensors capable of detecting forces in the femtonewton range, super fast resonance frequencies [133, 82] and achieving unprecedented displacement sensitivity [216, 134].

In this work, we present the design, simulation, and experimental validation of a novel optomechanical sensor that combines optical micro-ring resonators with suspended cantilevers fabricated on SOI wafers. By leveraging the unique characteristics of these integrated systems, we achieve displacement sensitivities below sub-fm/$\mathrm{Hz}^{1/2}$, which enhances the capabilities of force and displacement sensing at the nanoscale [216, 91]. Our device also offers the ability to tune in-plane mechanical frequencies and stiffness, providing a versatile platform for a wide range of sensing applications, from material characterization to biological studies [133, 102].

This paper outlines the development of the device, including detailed simulations using finite-difference time-domain (FDTD) and finite element method (FEM) techniques, along with experimental characterization that validates the predicted performance. By demonstrating the strong coupling between the optical and mechanical modes, we highlight the potential of these optomechanical sensors for high-precision force and displacement measurements, with implications for future advancements in nanoscale measurement technologies [218, 82]. The paper has been submitted for publication. A pre-print is available at doi:10.26434/chemrxiv-2025-fz4km.

# Single-Mode Ring Resonator-Based Optomechanical Transducers for Advanced Atomic Force Sensing

Yide Zhang,[†,‡,¶] Artem S.Vorobev,[‡,¶] Savda Sam,[†,‡,¶] S. Hadi Badri,[‡,¶] Mauro David,[§] Bernhard Lendl,[†] Georg Ramer,[*,†,‖] and Liam OFaolain[*,‡,¶]

†*Institute of Chemical Technologies and Analytics, TU Wien, Vienna, Austria*

‡*Centre for Advanced Photonics and Process Analysis, Munster Technological University, Cork, Ireland*

¶*Tyndall National Institute, Cork, Ireland*

§*Institute of Solid State Electronics, TU Wien, Vienna, Austria*

‖*Christian Doppler Laboratory for Advanced Mid-Infrared Laser Spectroscopy in (Bio-)process Analytics, TU Wien, Vienna, Austria*

E-mail: georg.ramer@tuwien.ac.at; William.Whelan-Curtin@mtu.ie

**Abstract**

Atomic force microscopy (AFM) is a widely used technique for high-resolution imaging and force sensing, yet its performance is fundamentally constrained by the cantilever size, spring constants, and mechanical frequencies. To overcome these limitations, we present a compact and highly efficient single-mode ring resonator-based optomechanical transducer on an silicon-on-insulator (SOI) platform. Unlike conventional designs that rely on whispering gallery modes (WGMs) resonators, our approach ensures mode stability, facilitates straightforward signal interpretation, and enhances measurement

reliability by eliminating mode-splitting effects and complex optical responses. Coupled with a picogram-scale cantilever, our system achieves exceptional displacement sensitivity of $6.7 \times 10^{-16}\,\mathrm{m/Hz^{1/2}}$ and force detection down to $5.0 \times 10^{-14}\,\mathrm{N}$, providing a high-performance alternative to existing optomechanical AFM transducers. The tunable mechanical resonance frequency (1.3 MHz to 22.5 MHz) and adjustable stiffness (0.46 N/m to 3.54 N/m) enable precise force sensing across a broad range of applications, from soft matter characterization to high-speed imaging. Importantly, our results exhibit strong agreement with theoretical predictions, ensuring accurate and direct displacement measurements. This is a key advantage over WGM-based approaches that suffer from optical mode instability. Our results establish this single-mode optomechanical transducer as a robust, high-sensitivity platform for next-generation AFM and nanoscale sensing applications, offering a compact, scalable, and highly precise alternative to traditional free-space optical detection methods. The combination of high displacement sensitivity, mode stability, and tunable performance establishes this optomechanical transducer as a promising advancement in integrated nanoscale sensing and AFM applications.

# Introduction

Atomic Force Microscopy (AFM)[1,2] has become an essential tool for high-resolution imaging and force sensing across diverse fields, including nanotechnology, materials science, and biology. Unlike optical and electron microscopy, AFM relies on physical interactions[3–8] between a nanoscale probe and a sample surface, enabling nanoscale characterization of mechanical,[9] electrical,[10] biological,[11] and thermal[12] properties. Furthermore, when combined with pulsed IR lasers for sample excitation, AFM can also achieve chemical characterization[13,14] with nanoscale resolution. However, AFM performance is fundamentally constrained by the mechanical properties of the cantilever, particularly its resonance frequency, stiffness, and displacement detection method.

Traditional optical-lever detection methods, which track cantilever deflection via laser reflection onto a position-sensitive photodiode,[2] remain widely used due to its sensitivity. However, these approaches rely on bulky free-space optics and expensive tunable lasers and expensive tunable laser, while remaining prone to alignment challenges and environmental disturbances.[15,16] The time resolution of AFM is fundamentally constrained by the thermal limit of the cantilever,[17] necessitating low mass and high quality factors to minimize thermal noise off resonance.[18] To achieve high resonant frequencies (>1 MHz), which are essential for faster imaging and rapid force spectroscopy,[19,20] cantilever miniaturization is often required. However, the resulting reduced dimensions are limited by optical diffraction,[21,22] further making it impossible for displacement detection and signal stability.

To address these limitations, integrated cavity optomechanics[23–25] have emerged as a powerful alternative. By leveraging the interaction between a high-quality optical resonator and a mechanical oscillator, this approach enables displacement transduction with sensitivities close to the quantum limit.[26–28] In optomechanical systems, evanescent wave coupling allows precise motion detection,[29] making them well-suited for AFM applications.

Despite their advantages, prior optomechanical AFM transducers face several key challenges. Microdisk-based transducers[30,31] achieve high optical Q-factors but rely on multimode whispering gallery modes (WGMs), which introduce mode splitting, unpredictable optical responses, and complex signal interpretation. High-frequency optomechanical sensors[32] demonstrated impressive performance with mechanical frequencies exceeding 100 MHz, providing exceptional displacement sensitivity. However, their fixed ultra-high stiffness (40 kN/m) makes them unsuitable probing of soft materials. Additionally, multi-mode resonators exhibit non-trivial coupling effects, further reducing the reliability of direct displacement measurements in AFM applications.

In this work, we present a single-mode ring resonator-based optomechanical transducer on an silicon-on-insulator (SOI) platform, enabling both for direct displacement measurement with fast and high-accuracy sensing (200 nm dynamic range) and an AFM feedback-assisted

mode for structured samples requiring larger displacement tracking. Our system achieves a displacement sensitivity below femtometer/$Hz^{1/2}$ and force detection in the tens of femtonewtons range, while maintaining tunable mechanical frequencies from 1.3 MHz to 22.5 MHz and adjustable stiffness from 0.46 N/m to 3.54 N/m by modifying the ring resonator geometry.

This new design shows promise as a compact and versatile alternative to free-space optical detection of cantilever displacement, making it adaptable to a wide range of sensing applications. By demonstrating a strong correlation between experimental optical resonance shifts and theoretical predictions, this work establishes the SOI-based optomechanical transducer as a viable solution for high-frequency applications, thereby advancing optomechanical AFM sensing and expanding its applicability in material characterization, photothermal imaging, and biological research.

# Results and discussion

## Device Design and Simulation

The device is fabricated on an SOI wafer, consisting of a 220 nm top silicon layer, 3 µm silicon dioxide underlayer and a 725 µm silicon handle layer. Fabrication was carried out using electron beam lithography (EBL), with process details provided in Methods section.

A scanning electron microscope (SEM) image of a fabricated device is shown in Figure 1a. The structure consists of a tapered waveguide that evanescently couples light into and out of a single-mode optical micro-ring resonator. The narrowest section of the tapered waveguide, as well as the ring width, is 500 nm, ensuring support for a single TE mode. The device operates at telecom wavelengths and under critical coupling conditions with a 60 nm gap between the ring and tapered waveguide. This gap was initially determined through finite-difference time-domain (FDTD) simulations during the design process and later validated experimentally. To optimize light coupling efficiency, the gap distance was finely adjusted in 10 nm steps, ranging from 50 nm to 100 nm, as detailed in Supporting Information Section

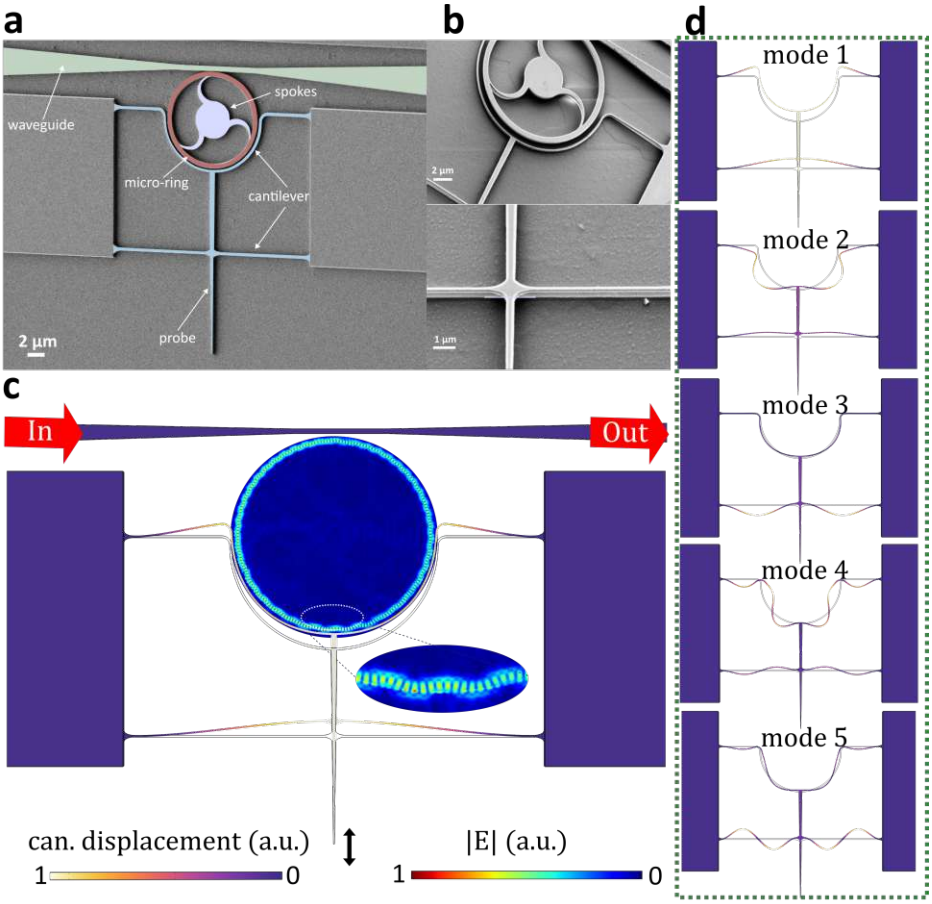


Figure 1: (a) False-colored SEM image of the micro-ring cantilever with a 5 µm ring radius, characterized in this study to illustrate the device geometry. The applied color scheme distinctly highlights the waveguide, micro-ring, supporting spokes, and cantilever, enhancing structural clarity. (b) Magnified SEM micrograph showing the suspended cantilever in greater detail. (c) Illustration of the devices working principle. The gray regions represent the device in its equilibrium state, while the colored regions depict the deformed shape of the micro-ring cantilever in its first in-plane mechanical mode, as simulated via FEM. The micro-ring has a 10 µm radius and a 500 nm width, supported by three curved spokes. The cantilever is connected via two 10 µm arms, with a probe width of 100 nm and a length of 20 µm. The entire device has a thickness of 220 nm. A color map within the ring resonator cavity shows the normalized electric field amplitude at a resonance wavelength of 1556.34 nm, calculated using FDTD simulations, with the cantilever positioned 10 nm away. The cantilevers motion modulates the optical mode of the resonator, enabling signal transduction. (d) Simulated first five in-plane mechanical modes of the cantilever, with amplitudes scaled by a factor of 10,000 for visual clarity.

S1.

The blue rendering in Figure 1a illustrates the flexible cantilever-probe unit, which is positioned adjacent to the ring resonator in the fabricated optomechanical transducer. The cantilever part consists of both semicircular and straight sections. The semicircular section, curved around the edge of the ring, features a width and a gap of 200 nm to maximize interaction with the optical ring. The gap determines the dynamic range of the cantilevers movement relative to the ring, enabling direct measurement compared to previous designs[30,32,33] that rely on AFM feedback. This design choice allows for faster signal tracking and a simpler readout.

The cantilever is clamped at both ends and includes a 20 µm-long probe, supported by a straight cantilever positioned 10 µm away from the probe tip. The probe width is chosen to be 100 nm for mechanical characterization; however, it can be thinned down to tens of nanometers for high spatial resolution microscopy.[34] This design ensures the cantilever remains free-standing, allowing optimized in-plane motion for strong coupling with the ring resonator.[30]

The cantilever is released through selective etching of the sacrificial oxide layer down to a thickness of 700 nm using buffered HF (7:1 ratio) (see Figure S2). The undercutting process is carefully controlled to ensure free vibration of the cantilever, while keeping the micro-ring and tapered waveguide securely anchored to the substrate. The suspended cantilever is shown in Figure 1b. To improve mechanical stability, the micro-ring is supported by three curved spokes, which have been optimized to minimize optical scattering losses.

The cantilever deforms under applied force at the tip or vibrates due to thermal-mechanical noise. In both cases, the gap between the cantilever and the ring changes, causing a local variation in the refractive index near the ring. This directly affects the propagation of optical modes at the rings edge, leading to an optical resonance shift as well as a corresponding intensity change. Figure S4 presents an FDTD simulation illustrating the optical modes of the device without the cantilever. When the cantilever is positioned 10 nm from the ring

resonator, its presence modifies the optical modes, as depicted in Figure 1c.

The mechanical modes of the cantilever are analyzed using finite-element method (FEM) simulations, with the first five modes shown in Figure 1d. Since our design primarily utilizes in-plane motion, we focus on even-symmetry in-plane modes, which exhibit strong coupling with the optical modes of the ring resonator. These modes are particularly relevant to AFM applications, enabling high-sensitivity force and displacement sensing.

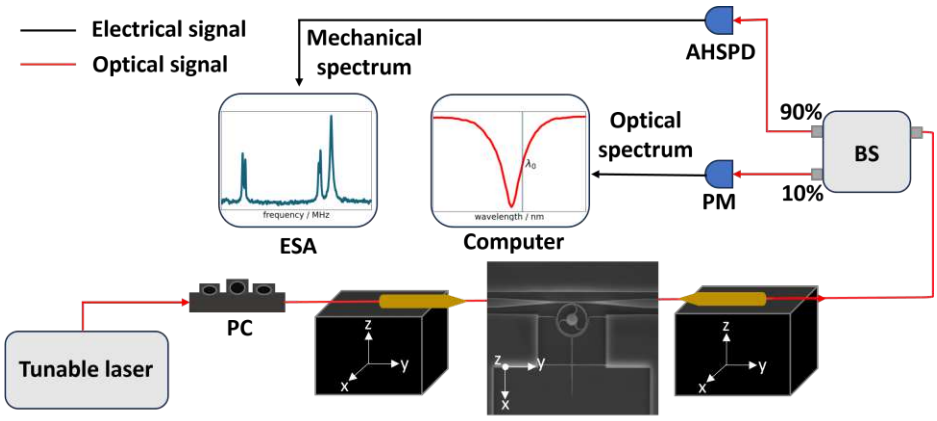


Figure 2: Schematic of the characterization setup: A power-controlled near-infrared tunable laser first passes through a polarization controller (PC) before being coupled into and collected from the devices using micro-lensed fibers. These fibers are mounted on three-dimensional nano-positioning stages, integrated with a custom-built visualization system. The inset displays an optical image captured using this system. After collection, the light is split in a 90:10 ratio using a fiber beam splitter (BS): 10% of the light is directed to a multichannel power meter (PM) to a computer for optical power monitoring. The remaining 90% is sent to an amplified high-speed photodetector (AHSPD) and then to an electrical spectrum analyzer (ESA) to extract the devices mechanical response.

## Optomechanical Detection

The fabricated devices are characterized using a home-built optomechanical setup, schematically shown in Figure 2. This setup allows for the characterization of multiple devices on the same chip, while simultaneously collecting optical spectra and mechanical resonance data. A tunable laser (Santec TSL-570), operating over a wide wavelength range of 1480 nm to 1640 nm, is used for excitation. The laser light is polarization-controlled before being cou-

pled into a micro-lensed fiber, which injects the light into the device. After passing through the device, the light is collected and split into two branches.

10% of the collected light is directed to a multi-port optical power monitor (Santec MPM-215), which is interfaced with computer-controlled software to record optical spectra. After identifying an optical mode with a high optical quality factor ($Q_o$), a wavelength is selected at the inflection point of the cavity resonance to maximize sensitivity to mechanical vibrations. The remaining 90% of the transmitted signals is sent to an amplified high-speed photodetector (FPD510-FC-NIR, Thorlabs Inc.). This signal is then analyzed using an electrical spectrum analyzer (FSV4, Rohde & Schwarz GmbH), providing direct access to the thermo-mechanical resonance spectrum of the cantilever.

Using the optomechanical setup described above, we performed air-based measurements on devices with ring radii of 5 µm, 7 µm, and 10 µm. In these experiments, thermal noise induces random oscillations of the cantilever, which occur at its mechanical resonance frequencies. The normalized transmission spectra across the full wavelength range for these devices are shown in Figure 3a, c, and e, along with zoomed-in scans of individual optical resonances.

The $Q_o$ was extracted by fitting the experimental spectra with Lorentzian functions. The measured $Q_o$ values are 2141, 3756 and 4275 for the 5 µm, 7 µm, and 10 µm rings, respectively, showing an increase in $Q_o$ with ring size. This trend is attributed to reduced bending losses in larger rings, whereas smaller rings experience higher bending losses.[35]

To determine the response of the transducer, the laser was tuned to the inflection point of the TE cavity mode, as shown in the zoomed-in spectra of Figure 3a, c, and e. The corresponding mechanical spectra covering 1 to 25 MHz are presented in Figure 3b, d, and f. The observed peaks arise from thermally driven cantilever motion, as confirmed by FEM simulations. These peaks primarily correspond to the first five in-plane even-symmetry modes, as illustrated in Figure 1d. However, in the 5 µm device, the first two mechanical modes are not clearly visible, likely due to a low cavity-cantilever coupling factor, which

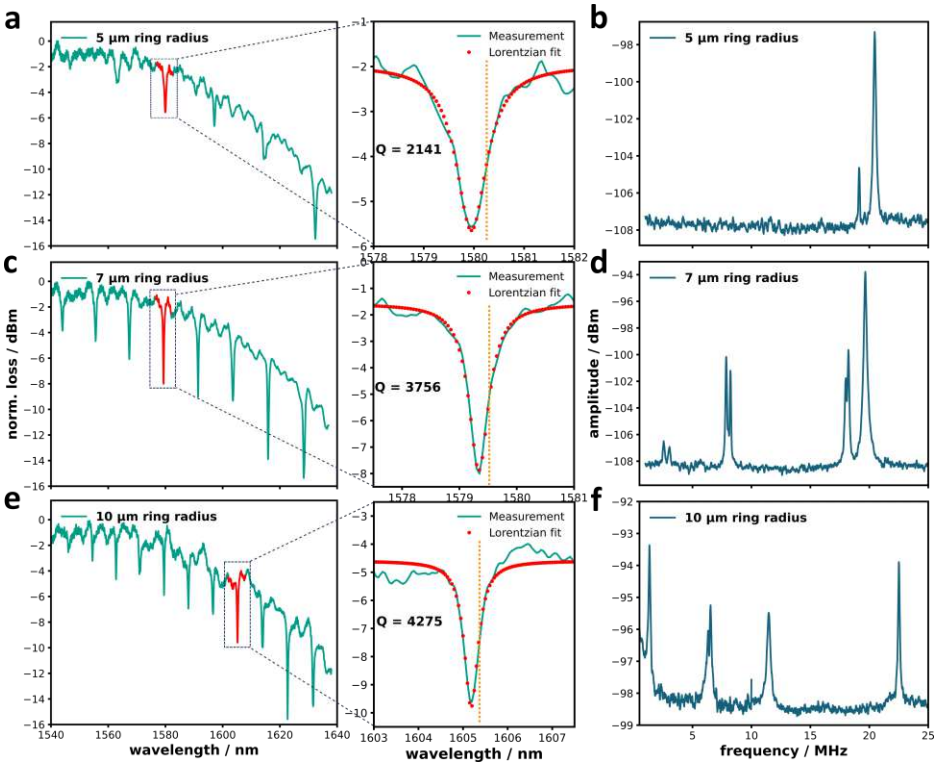


Figure 3: Optical and mechanical spectra of devices with different ring radii: Panels (a), (c), and (e) display the optical spectra for devices with ring radii of 5 µm, 7 µm, and 10 µm, respectively. Panels (b), (d), and (f) show the corresponding mechanical spectra for the same devices. The right-hand plots in (a), (c), and (e) provide zoomed-in views of the red traces from the left-hand plots. Orange dashed lines in the zoomed-in figures indicate the wavelengths used for mechanical spectrum measurements.

reduces the optical transduction efficiency for these modes.

Moreover, FEM simulations indicate that the mechanical frequency of the device decreases as the size of the ring increases. The measured frequencies from the examined devices, shown in Figure 4, align well with the theoretical predictions.

The measured mechanical quality factors ($Q_M$) values for these modes range from approximately $Q_M \approx 6$ for mode 1 of the 10 µm device to $Q_M \approx 247$ for mode 3 of the 5 µm device. Additionally, for each individual device, we observe that $Q_M$ increases for higher-order modes.

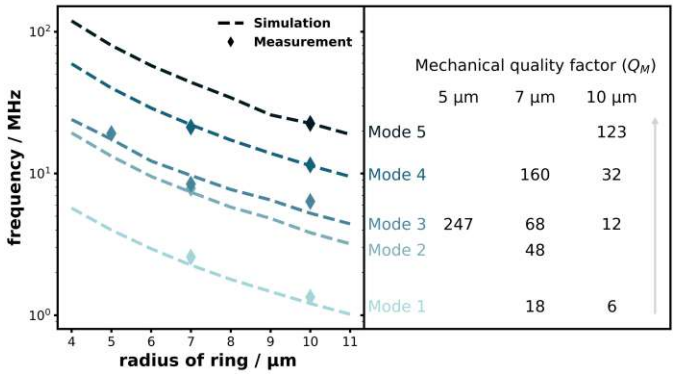


Figure 4: Left panel: Simulated mechanical frequencies for devices with ring radii ranging from 4 µm to 11 µm, alongside experimentally measured results from the tested devices. Right panel: Calculated mechanical quality factors ($Q_M$) corresponding to each vibrational mode.

## Transduction Efficiency

To further evaluate the capability of our devices as displacement and force sensors, we modified the optomechanical setup by incorporating a three-dimensional closed-loop controlled piezo stage (MAX381/M, Thorlabs Inc.) with a 3D-printed probe holder mounted on top. A straight tungsten probe with a 500 nm tip diameter (Micro Support Co., Ltd.) was inserted into the probe holder and positioned at a 15° angle relative to the device surface, as shown in Figure 5a. The probe position was precisely controlled using a stepper motor, allowing to approach the probe tip to the end of the cantilever.

Transmission spectra were recorded before probe contact, labeled as "0 nm" in Figure 5d and g. After making contact, the probe incrementally displaced the cantilever in 20 nm steps with transmission spectra collected at each step (Figure 5d, 7 µm device). As the probe pushed the cantilever closer to the ring, the optical resonance shifted toward longer wavelengths. The observed resonance shift, $\Delta\lambda$, referenced to the equilibrium state, increases with probe displacement. The nonlinear dependence of the resonance shift on cantilever movement arises from the nonlinear variation in the local refractive index near the ring

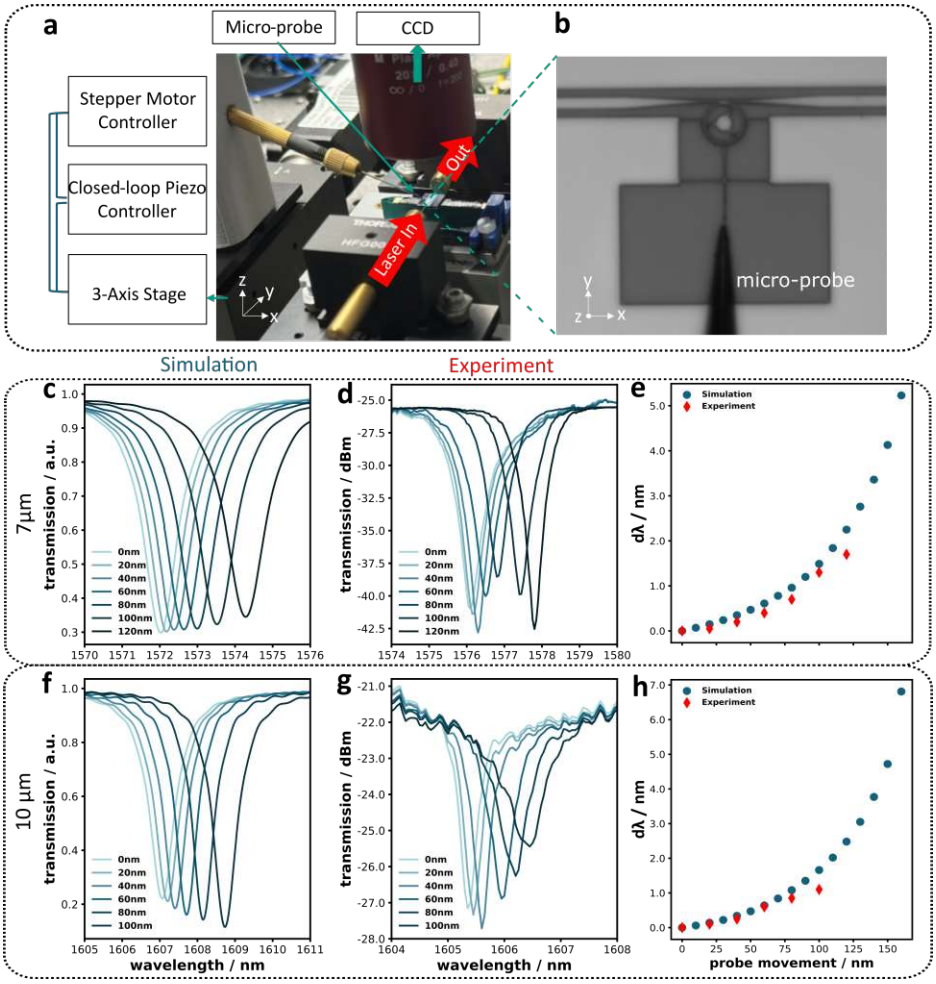


Figure 5: (a) Micro-probe measurement setup used for the mechanical characterization of micro-ring cantilevers. (b) Optical image captured using the custom-built visualization system, showing a fine probe in contact with the micro-ring cantilever. (c, f) FDTD-simulated optical spectra depicting the effect of cantilever motion toward the ring resonator in 20 nm steps, for devices with ring radii of 7 µm and 10 µm, respectively. (d, g) Corresponding experimental results validating the simulated optical response. (e, h) Resonance wavelength shift ($\Delta\lambda$) referenced to the equilibrium state (0 nm cantilever motion), plotted as a function of probe displacement.

resonator, which in turn affects the optical mode confinement and effective index of the ring. The experimental results align closely with simulations, confirming the capability to use the developed device.

Based on the results shown in Figures 5e and h, the optomechanical coupling factor was

determined through FEM simulations, confirmed by experimental findings. This factor is defined as

$$g_{OM}/2\pi = \frac{d\omega_O}{dx} \tag{1}$$

where $d\omega_O$ is the angular optical cavity mode frequency shift and $dx$ represents the cantilever displacement. For the probe displacement range in this study, $g_{OM}/2\pi$ varies from 0.3 GHz/nm to 1.7 GHz/nm for the 7 µm device, and from 0.6 GHz/nm to 1.3 GHz/nm for the 10 µm device. The experimentally achieved values are consistent with previously reported $g_{OM}/2\pi$ values for silicon microdisk AFM probes,[30] which were based solely on simulations. Furthermore, $g_{OM}/2\pi$ increases as the gap between the ring and cantilever decreases, confirming the strong optomechanical interaction in our system.

The minimum detectable force $F_{min}$ is calculated based on[36]

$$F_{min} = \sqrt{\frac{4kk_BTB}{2\pi f_M Q_M}} \tag{2}$$

where $B$ is the measurement bandwidth, $T$ the temperature (300 K), and cantilever stiffness $k$ and $k_B$ is the Boltzmann constant.

The stiffness of the optomechanical cantilever depends on the ring size, with values of 0.46 N/m for 5 µm device and 3.54 N/m for 10 µm, as shown in Figure S3. Taking a common bandwidth of $B = 50$ Hz, consistent with prior studies for comparison to other experiments,[30,36] the calculated $F_{min}$ for the first mode of the 7 µm device is $5.0 \times 10^{-14}$ N. For the 10 µm device, $F_{min}$ is $2.4 \times 10^{-13}$ N. This fivefold increase is consistent with the stiffness-dependent force detection limit, where higher stiffness reduces mechanical responsiveness to weak forces.

The device's displacement measurement sensitivity is calibrated using thermal-mechanical noise measurements. The detection sensitivity limit is $6.7\times10^{-16}$ m/Hz$^{1/2}$ and $8.3\times10^{-16}$ m/Hz$^{1/2}$ for the 7 µm and 10 µm devices, respectively, with detailed calculations provided in the Meth-

ods section.

The achieved displacement and force sensitivity closely align with previously reported values[30,32] (see comparison table in Supporting Information Section S2), demonstrating comparable or improved sensitivity while maintaining a large dynamic measurement range. Furthermore, unlike previous studies that relied on controlled nitrogen or vacuum environments, our device achieves its sensitivities in ambient air and improves upon other high-sensitivity optomechanical AFM probes used for AFM-IR[33] by more than an order of magnitude, underscoring its robustness for real-world AFM applications. Such fast, highly sensitive probes are essential for detecting weak interactions in nanoscale systemsfrom transient thermal phenomena and thermal conductivity imaging to van der Waals forces and single-molecule interactions.

## Conclusion and Discussion

In summary, we have developed and demonstrated a novel optomechanical device based on an SOI platform, integrating optical micro-ring resonators with suspended cantilevers. The device operates under a single TE mode, ensuring stable optical performance with high wavelength control precision. Through a combination of FDTD and FEM simulations, supported by experimental validation, we characterized the optical and mechanical properties of devices with varying ring sizes, confirming their suitability for high-precision sensing applications.

The device exhibits strong optomechanical coupling, achieving a balance between moderate optical quality factors. Experimentally, the optomechanical coupling factor $g_{OM}/2\pi$ ranges from 0.3 GHz/nm to 1.7 GHz/nm, aligning well with simulated values. This strong coupling enables the optical modes to transduce the cantilevers megahertz-frequency motion with a displacement sensitivity of $6.7 \times 10^{-16}\,\mathrm{m/Hz^{1/2}}$ while operating in ambient air. The mechanical quality factors $Q_M$ and stiffness values were characterized, revealing clear dependencies on device size and mode order. Furthermore, the minimum detectable force was

calculated to be as low as $5.0 \times 10^{-14}$ N, underscoring the devices capability for high-precision displacement and force sensing.

These findings establish our optomechanical transducer as robust platforms for high-precision sensing, leveraging the synergy between integrated photonics and nanomechanics. The demonstrated performance paves the way for advancements in high-throughput scanning and integrated photonic-based metrology. Future work will focus on systematic measurements by fully releasing the cantilever and integrating the optomechanical transducer into an AFM system using fiber bonding techniques. Additionally, we aim to explore further applications in advanced metrology and near-field imaging.

# Methods

## Detection sensitivity

The thermal-mechanical spectra are shown in Figure 3b, d and f. The cantilever is driven by the thermal noise of room temperature. The displacement sensitivity induced by the thermal noise can be described by.[31,37]

$$[S_{xx}(\omega)]^{1/2} = \left( \frac{4k_B T \omega_M / Q_M}{m_{eff}((\omega^2 - \omega_M^2)^2 + \omega^2 \omega_M^2 / Q_M^2)} \right)^{1/2} \tag{3}$$

where $\omega_M$ is angular mode frequency ($2\pi f_M$). The effective mass for the fundamental mode is $m_{eff} = 0.73 m_0$.[38] $m_0 = 11.45$ pg for the 7 µm device and $m_0 = 14.26$ pg for the 10 µm device. These values have been observed from FEM simulations. The limit of detection sensitivity is $6.7 \times 10^{-16}$ m/Hz$^{1/2}$ and $8.3 \times 10^{-16}$ m/Hz$^{1/2}$ for 7 µm and 10 µm device, receptively. The thermal-mechanical displacement is $[S_{xx}(\omega)\Delta f]^{1/2}$,[38] where $\Delta f$ is the measurement bandwidth.

## Simulation

The optical ring resonator and cantilevers were designed using the Python Gdspy module, and the resulting designs were exported as .gds files. These files were utilized for optical transmission simulations, solid mechanical simulations, and final fabrication, ensuring consistency across all stages of the process.

Optical transmission simulations were conducted using finite-difference time-domain (FDTD) methods with a 3D-FDTD commercial software package from Ansys, Inc. To optimize simulation performance, a quasi-2D simulation approach was employed within the 3D-FDTD solver. This approach enhances computational efficiency while preserving simulation accuracy. Mechanical mode and stiffness simulations of the cantilevers were conducted using the finite element method (FEM) with the 3D Solid Mechanics module in COMSOL Multiphysics software 6.2.

## Device fabrication

A thermally oxidized bulk Silicon wafer with a deposited layer of poly-Si (220 nm thick) from the SOITEC Corp. was utilized. Initially, a ZEP 520A resist layer (450 nm thick) was spin-coated onto the wafer at 190 °C for 3 minutes. The desired device layouts were then defined on the resist using electron beam lithography (EBL) with a voltage of 100 kV and 1 nA current, followed by development in a bath of n-Amyl Acetate solution for 90 seconds and rinsing with IPA. Subsequently, the patterns were transferred to the SOI layer through an inductively coupled plasma (ICP) etching process using $O_2$:$CHF_3$ chemistry in 8:42 ratio (with an etch rate of approximately 35 nm/min). The remaining resist mask was removed via an $O_2$ plasma ashing step followed by immersion in MICROPOSIT 1165 remover for 10 minutes. Finally, a cleaning cycle involving Piranha etching, Acetone, and IPA were conducted to conclude the fabrication process step.

For the tip releasing the additional EBL exposure step was implemented. PMMA-A14 resist layer (2 µm thick) was spin-coated onto the sample and soft-baked at 150 °C for

3 minutes. The desired opening regions were then defined on the resist using second stage alignment EBL (50 nm alignment error) with a voltage of 100 kV and 10 nA current, followed by development in a bath of MIBK and IPA solution for 120 seconds and rinsing with IPA with following by a 150 °C 20 minutes hard baking step. The $SiO_2$ layer in the opening regions was partially etched using the buffered hydrofluoric acid solution with a 7:1 ratio. The etching process was conducted for 7 minutes at an approximate etch rate of 100 nm/min. Finally, a cleaning cycle was performed, consisting of a 10-minute immersion in acetone to dissolve the PMMA protection layer, followed by rinsing with IPA for thorough cleaning.

## Author Affiliations

Corresponding Author

Georg Ramer

*Email: georg.ramer@tuwien.ac.at

Liam OFaolain

*Email:William.Whelan-Curtin@mtu.ie

ORCID

Yide Zhang: 0000-0002-2675-739X

Artem S.Vorobev: 0000-0002-3642-5225

Savda Sam: 0009-0008-1310-8906

S. Hadi Badri: 0000-0003-2295-6276

Mauro David: 0000-0003-3695-436X

Liam OFaolain: 0000-0003-1160-7441

Bernhard Lendl: 0000-0003-3838-5842

Georg Ramer: 0000-0001-8307-5435

## Author Contributions

Y.Z. designed the devices, developed and performed FEM and FDTD simulations, and drafted the manuscript. A.S.V. fabricated the samples. Y.Z. and M. D. performed buffered HF etching. Y.Z. and S.S. conducted the characterization experiments on the fabricated devices. S.H.B contributed to the discussions of the design and FDTD simulations. L.O. supervised Y.Z. in the design and simulations and guided A.S.V. in sample fabrications. G.R. supervised Y.Z. in building the setup for the characterization experiments. G.R., L.O., and B.L. conceptualized the study, proposed the project. All authors reviewed and revised the manuscript.

# Acknowledgement

This work was funded with financial support from the European Unions Horizon 2020 research and innovation programme. The authors Y.Z., A.S.V., S.S., B.L., L.O'F. and G.R. acknowledge the Marie Skodowska-Curie project OPTAPHI under grant agreement No.860808. The financial support by the Austrian Federal Ministry for Labour and Economy and the National Foundation for Research, Technology and Development and the Christian Doppler Research Association is gratefully acknowledged. B.L. and G.R. acknowledge funding from the Austrian Science Fund (FWF) [doi.org/10.55776/COE7].

The authors thank the Center for Micro- and Nanostructures (ZMNS) for providing the cleanroom facilities as well as Alois Lugstein from TU Wien for the support with the HF etching of the devices. The further authors thank Katharina Rauchenwald from TU Wien for the support with SEM imaging.

## Supporting Information Available

A PDF file including of additional figures S1 to S4 and table S1. Code and raw data to generate all figures is available on Zenodo (DOI:10.5281/zenodo.15077551).[39]

## References


(1) Binnig, G.; Quate, C. F.; Gerber, C. Atomic Force Microscope. *Physical Review Letters* **1986**, *56*, 930–933.

(2) Meyer, G.; Amer, N. M. Novel optical approach to atomic force microscopy. *Applied Physics Letters* **1988**, *53*, 1045–1047.

(3) Kawai, S.; Foster, A. S.; Bjrkman, T.; Nowakowska, S.; Bjrk, J.; Canova, F. F.; Gade, L. H.; Jung, T. A.; Meyer, E. Van der Waals interactions and the limits of isolated atom models at interfaces. *Nature Communications* **2016**, *7*, 11559.

(4) Zhou, N.; Wang, R.; Zhou, X.; Song, H.; Xiong, X.; Ding, Y.; L, J.; Gan, L.; Zhai, T. PGaSe/N$MoS_2$ Vertical Heterostructures Synthesized by van der Waals Epitaxy for Photoresponse Modulation. *Small* **2018**, *14*, 1702731.

(5) Eaton, P. J.; West, P. *Atomic force microscopy*; Oxford university press: Oxford, 2018.

(6) Dazzi, A.; Prater, C. B. AFM-IR: Technology and Applications in Nanoscale Infrared Spectroscopy and Chemical Imaging. *Chemical Reviews* **2017**, *117*, 5146–5173.

(7) Centrone, A. Infrared Imaging and Spectroscopy Beyond the Diffraction Limit. *Annual Review of Analytical Chemistry* **2015**, *8*, 101–126.

(8) Zhang, Y.; Yilmaz, U.; Lukasievicz, G. V. B.; OFaolain, L.; Lendl, B.; Ramer, G. An analytical model of label-free nanoscale chemical imaging reveals avenues toward improved spatial resolution and sensitivity. *Proceedings of the National Academy of Sciences* **2025**, *122*, e2403079122.

(9) Rico, F.; Gonzalez, L.; Casuso, I.; Puig-Vidal, M.; Scheuring, S. High-Speed Force Spectroscopy Unfolds Titin at the Velocity of Molecular Dynamics Simulations. *Science* **2013**, *342*, 741–743.

(10) Leblebici, S. Y. et al. Facet-dependent photovoltaic efficiency variations in single grains of hybrid halide perovskite. *Nature Energy* **2016**, *1*, 16093.

(11) Dufrne, Y. F.; Ando, T.; Garcia, R.; Alsteens, D.; Martinez-Martin, D.; Engel, A.; Gerber, C.; Mller, D. J. Imaging modes of atomic force microscopy for application in molecular and cell biology. *Nature Nanotechnology* **2017**, *12*, 295–307.

(12) Laraoui, A.; Aycock-Rizzo, H.; Gao, Y.; Lu, X.; Riedo, E.; Meriles, C. A. Imaging thermal conductivity with nanoscale resolution using a scanning spin probe. *Nature Communications* **2015**, *6*, 8954.

(13) Dazzi, A.; Prater, C. B.; Hu, Q.; Chase, D. B.; Rabolt, J. F.; Marcott, C. AFMIR: Combining Atomic Force Microscopy and Infrared Spectroscopy for Nanoscale Chemical Characterization. *Applied Spectroscopy* **2012**, *66*, 1365–1384.

(14) V. D. Dos Santos, A. C.; Tranchida, D.; Lendl, B.; Ramer, G. Nanoscale chemical characterization of a post-consumer recycled polyolefin blend using tapping mode AFM-IR. *The Analyst* **2022**, *147*, 3741–3747.

(15) Sadeghian, H.; Herfst, R.; Dekker, B.; Winters, J.; Bijnagte, T.; Rijnbeek, R. High-throughput atomic force microscopes operating in parallel. *Review of Scientific Instruments* **2017**, *88*, 033703.

(16) Lim, S.-H. .; Raorane, D.; Satyanarayana, S.; Majumdar, A. Nano-chemo-mechanical sensor array platform for high-throughput chemical analysis. *Sensors and Actuators B: Chemical* **2006**, *119*, 466–474.

(17) Schumacher, Z.; Spielhofer, A.; Miyahara, Y.; Grutter, P. The limit of time resolution in frequency modulation atomic force microscopy by a pump-probe approach. *Applied Physics Letters* **2017**, *110*, 053111.

(18) Albrecht, T. R.; Grtter, P.; Horne, D.; Rugar, D. Frequency modulation detection using high- $Q$ cantilevers for enhanced force microscope sensitivity. *Journal of Applied Physics* **1991**, *69*, 668–673.

(19) Viani, M. B.; Schffer, T. E.; Paloczi, G. T.; Pietrasanta, L. I.; Smith, B. L.; Thompson, J. B.; Richter, M.; Rief, M.; Gaub, H. E.; Plaxco, K. W.; Cleland, A. N.; Hansma, H. G.; Hansma, P. K. Fast imaging and fast force spectroscopy of single biopolymers with a new atomic force microscope designed for small cantilevers. *Review of Scientific Instruments* **1999**, *70*, 4300–4303.

(20) Ando, T.; Kodera, N.; Takai, E.; Maruyama, D.; Saito, K.; Toda, A. A high-speed atomic force microscope for studying biological macromolecules. *Proceedings of the National Academy of Sciences* **2001**, *98*, 12468–12472.

(21) Kouh, T.; Karabacak, D.; Kim, D. H.; Ekinci, K. L. Diffraction effects in optical interferometric displacement detection in nanoelectromechanical systems. *Applied Physics Letters* **2005**, *86*, 013106.

(22) Braunsmann, C.; Seifert, J.; Rheinlaender, J.; Schffer, T. E. High-speed force mapping on living cells with a small cantilever atomic force microscope. *Review of Scientific Instruments* **2014**, *85*, 073703.

(23) Aspelmeyer, M.; Kippenberg, T. J.; Marquardt, F. Cavity optomechanics. *Reviews of Modern Physics* **2014**, *86*, 1391–1452.

(24) Van Thourhout, D.; Roels, J. Optomechanical device actuation through the optical gradient force. *Nature Photonics* **2010**, *4*, 211–217.

(25) Favero, I.; Karrai, K. Optomechanics of deformable optical cavities. *Nature Photonics* **2009**, *3*, 201–205.

(26) Schliesser, A.; Arcizet, O.; Rivire, R.; Anetsberger, G.; Kippenberg, T. J. Resolved-sideband cooling and position measurement of a micromechanical oscillator close to the Heisenberg uncertainty limit. *Nature Physics* **2009**, *5*, 509–514.

(27) Clerk, A. Facing Heisenberg at the nanoscale. *Nature Nanotechnology* **2009**, *4*, 796–798.

(28) Eichenfield, M.; Camacho, R.; Chan, J.; Vahala, K. J.; Painter, O. A picogram- and nanometre-scale photonic-crystal optomechanical cavity. *Nature* **2009**, *459*, 550–555.

(29) Anetsberger, G.; Arcizet, O.; Unterreithmeier, Q. P.; Rivire, R.; Schliesser, A.; Weig, E. M.; Kotthaus, J. P.; Kippenberg, T. J. Near-field cavity optomechanics with nanomechanical oscillators. *Nature Physics* **2009**, *5*, 909–914.

(30) Srinivasan, K.; Miao, H.; Rakher, M. T.; Davano, M.; Aksyuk, V. Optomechanical Transduction of an Integrated Silicon Cantilever Probe Using a Microdisk Resonator. *Nano Letters* **2011**, *11*, 791–797.

(31) Liu, Y.; Miao, H.; Aksyuk, V.; Srinivasan, K. Wide cantilever stiffness range cavity optomechanical sensors for atomic force microscopy. *Optics Express* **2012**, *20*, 18268.

(32) Schwab, L.; Allain, P. E.; Mauran, N.; Dollat, X.; Mazenq, L.; Lagrange, D.; Gly, M.; Hentz, S.; Jourdan, G.; Favero, I.; Legrand, B. Very-high-frequency probes for atomic force microscopy with silicon optomechanics. *Microsystems & Nanoengineering* **2022**, *8*, 32.

(33) Chae, J.; An, S.; Ramer, G.; Stavila, V.; Holland, G.; Yoon, Y.; Talin, A. A.; Allendorf, M.; Aksyuk, V. A.; Centrone, A. Nanophotonic Atomic Force Microscope Transducers Enable Chemical Composition and Thermal Conductivity Measurements at the Nanoscale. *Nano Letters* **2017**, *17*, 5587–5594.

(34) Wang, M.; Ramer, G.; Perez-Morelo, D. J.; Pavlidis, G.; Schwartz, J. J.; Yu, L.; Ilic, R.; Aksyuk, V. A.; Centrone, A. High Throughput Nanoimaging of Thermal Conductivity and Interfacial Thermal Conductance. *Nano Letters* **2022**, *22*, 4325–4332.

(35) McKinnon, W. R.; Xu, D. X.; Storey, C.; Post, E.; Densmore, A.; Delge, A.; Waldron, P.; Schmid, J. H.; Janz, S. Extracting coupling and loss coefficients from a ring resonator. *Optics Express* **2009**, *17*, 18971.

(36) Torbrgge, S.; Schaff, O.; Rychen, J. Application of the KolibriSensor to combined atomic-resolution scanning tunneling microscopy and noncontact atomic-force microscopy imaging. *Journal of Vacuum Science & Technology B, Nanotechnology and Microelectronics: Materials, Processing, Measurement, and Phenomena* **2010**, *28*, C4E12–C4E20.

(37) Saulson, P. R. Thermal noise in mechanical experiments. *Physical Review D* **1990**, *42*, 2437–2445.

(38) Ekinci, K. L.; Roukes, M. L. Nanoelectromechanical systems. *Review of Scientific Instruments* **2005**, *76*, 061101.

(39) Zhang, Y.; Vorobev, A. S.; Sam, S.; Badri, S. H.; Mauro, D.; Liam, O.; Lendl, B.; Ramer, G. Datasets for "Single-Mode Ring Resonator-Based Optomechanical Transducers for Advanced Atomic Force Sensing". 2025; `https://doi.org/10.5281/zenodo.15077551`.

## 4.4. Photonic Crystal-Based AFM Transducer

To expand the applications of microcantilevers beyond AFM, researchers have proposed designs that incorporate photonic crystal (PhC) waveguides and PhC resonators into the cantilever structure as sensing elements. These designs include stress sensors [59], displacement measurement [219], force and strain sensors [220, 221, 222]. The cantilever sensor has also been characterized for its performance in both air and water environments [223]. PhC cavities are favored as advanced platforms due to their exceptionally high quality factor (Q) relative to their volume (V), which significantly enhances light-matter interactions and makes them highly suitable for investigation as optomechanical resonators [150, 224, 225].

PhC cavities are particularly attractive for sensing applications due to their exceptionally high-quality factor ($Q_0$) relative to their small volume, which enhances light-matter interactions and makes them highly suitable for use as optomechanical resonators [150, 131, 151].

In this work, we propose a novel photonic transducer that integrates a PhC cavity with a micro-ring cantilever on a silicon nitride ($Si_3N_4$) platform. The strong optomechanical coupling afforded by the PhC structure enables highly sensitive detection of mechanical motion through optical readout—either via transmission intensity changes or wavelength shifts.

We further explore the integration of this optomechanical transducer into an AFM system to enable linear and highly sensitive force and displacement measurements. By varying the radius of the micro-ring cantilever, we demonstrate tunability of its first three in-plane mechanical resonance frequencies and effective spring constants, offering a versatile platform for dynamic sensing applications.

# Silicon Nitride Photonic Crystal-Cantilever Sensor for Quantitative Force and Displacement Measurements

YIDE ZHANG,[1,2,3] GAUTHAM PAIKKATH,[2,3], BERNHARD LENDL,[1] GEORG RAMER,[1,4] AND LIAM O'FAOLAIN[2,3]

[1] *Institute of Chemical Technologies and Analytics, TU Wien, Vienna, 1060 Austria*
[2] *Centre for Advanced Photonics and Process Analysis, Munster Technological University, Cork, Ireland*
[3] *Tyndall National Institute, Cork, Ireland*
[4] *Christian Doppler Laboratory for Advanced Mid-Infrared Laser Spectroscopy in (Bio-)process Analytics, TU Wien, Vienna, Austria*
[*] *William.Whelan-Curtin@mtu.ie*

**Abstract:** We present a purely photonic, optomechanical sensing approach for atomic force microscopy (AFM) by integrating a silicon nitride (SiN) photonic crystal cavity with a ring-shaped cantilever. This design eliminates the need for conventional AFM feedback loops by providing direct on-chip readout of cantilever motion via transmission-intensity changes or resonance-wavelength shifts over a 100 nm range. Crucially, both readouts exhibit a linear response with respect to cantilever displacement, enabling straightforward calibration and quantitative force/displacement measurements. Leveraging a high-quality factor ($>3 \times 10^5$) ensures strong optomechanical coupling, enabling intensity changes up to 7 %/nm and wavelength shifts of 21 pm/nm. By varying the ring radius, we tune mechanical frequencies from 400 kHz to 75.12 MHz and spring constants from 0.3 N/m to 39 N/m, thus broadening the applicability of high-sensitivity AFM measurements in compact or challenging environments.

## 1. Introduction

Conventional atomic force microscopy (AFM) relies on optical-lever detection, which, while achieving nanometer-scale spatial resolution and effective force sensing [1–4], is limited by bulky optical paths, alignment sensitivity, and difficulties in high-frequency operation [5–7]. Conventional cantilever-based AFM techniques face two significant challenges. First, many dynamic nanoscale phenomena, particularly those occurring below the microsecond timescale, are either too fast or too weak for direct AFM detection [8, 9]. Second, quantifying nanoscale forces often requires complex modeling [10], experimental transfer function measurements [11, 12], or machine learning approaches instead of direct force measurements [13]. These approaches introduce uncertainties and complicate data interpretation, thus limiting the effectiveness of AFM in certain applications.

To address these challenges, optomechanical AFM probes based on high-Q optical cavities have been developed, significantly enhancing displacement and force sensitivity. Recent advancements in cavity optomechanics [14–17] have led to substantial improvements in measurement capabilities. By coupling high-quality optical resonators with nano/micro-mechanical cantilevers [18, 19], or by utilizing optical cavities as mechanical resonators themselves [8], researchers have achieved highly precise radiation-pressure force measurements [20]. These advancements have enabled oscillator displacement measurements with sensitivities below the quantum limit [21, 22]. Building on these nanophotonic transducers, researchers have demonstrated the ability to measure chemical composition and image thermal conductivity at the nanoscale [9, 23].

Despite achieving high-frequency and high-sensitivity measurements, existing nanophotonic transducers have yet to demonstrate ultra-fast thermal dynamics or fully linear force and displacement detection. To bridge this gap, we propose a novel photonic transducer based on a photonic crystal cavity (PhC) integrated with a ring-shaped cantilever on a silicon nitride

(SiN) platform. Photonic crystals have attracted significant attention due to their ability to confine light within extremely small volumes while maintaining high quality factors (Q), thereby enhancing light-matter interactions and making them highly suitable for optomechanical resonator applications [22, 24, 25]. This strong optomechanical coupling facilitated by PhCs has enabled their use in various sensors, including those for stress [26], displacement measurement [27], and force and strain sensing [28–30].

In this study, we demonstrate an integrated optomechanical sensor for highly sensitive and linear force and displacement measurements in AFM. By reading out either the transmission-intensity change or the resonance-wavelength shift in a ring-shaped PhC, we eliminate the need for external free-space optics and alignment-sensitive feedback loops. Moreover, by varying the ring radius, we tune the first three in-plane mechanical frequencies and spring constants, offering broad adaptability for different measurement regimes. Monolithically fabricated in SiN, the entire optomechanical transducer is embedded directly in the cantilever structure, resulting in a purely on-chip photonic mechanism that reduces complexity, alignment challenges, and system footprint while providing direct and linear readout of nanomechanical motion.

This research not only addresses the current limitations of AFM but also lays the groundwork for future innovations in nanoscale measurement technologies. By providing a more robust and sensitive approach to force and displacement detection, the proposed sensor could enable new applications in fields ranging from material characterization to biological research.

## 2. Design and modelling

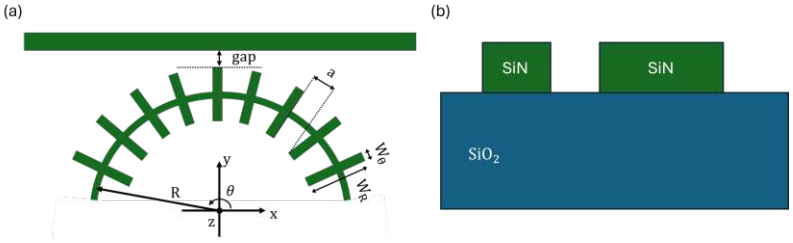


Fig. 1. (a) Top view of the schematic representation of the curved photonic crystal cavity. The structure consists of a curved photonic crystal pattern integrated onto a silicon nitride (SiN) platform. (b) The cross-section illustrates the layered composition, with SiN components supported by a silicon dioxide ($SiO_2$) substrate.

SIN cavity designed in this work consists of a periodic array of rectangular SiN pillars, hereafter referred to as "nanosticks". These SiN nanosticks separated by air gaps and supported on a $SiO_2$ substrate. This structure functions as a wavelength-selective mirror, similar to high-contrast Bragg gratings. The cavity is formed by gradually tapering the width of the nanosticks, thereby introducing a localized defect in the photonic bandgap. This defect leads to a confined optical mode with a Gaussian-shaped electric field distribution along the cavity, effectively minimizing optical losses [31].

For this work, the tapering function of the cavity is defined as [32]:

$$W_R(i) = W_R(0) + \frac{i^2}{i_{max}^2}[W_R(i_{imax}) - W_R(0)] \tag{1}$$

where $W_R(i)$ is the width of the $i-th$ nanostick along the radial (R-) direction in the $x-y$ plane, with $i$ denoting the stick index and $i_{max}$ being the total number of nanosticks on either

side of the central stick (where $i = 0$). The central nanostick has a width of $W_R(0)$ while the outermost nanosticks at both ends of the photonic crystal (PhC) cavity have a width of $W_R(i_{max})$, as illustrated in Fig. 1.

The length of each nanostick along the azimuthal ($\theta$-) direction in the $x - y$ plane, denoted as $W_\theta$, remains constant. This one-dimensional (1D) PhC cavity is designed on a 300 nm-thick SiN platform, which has a refractive index $n = 2.00$ in the telecom range. This platform is supported by a 2 µm-thick $SiO_2$ layer with a refractive index of $n = 1.45$.

The curved geometry, defined by a radius $R$ alters the photonic band structure, facilitating tighter mode confinement and leading to a single resonance. The optical mode confinement of the PhC cavity is shown in Fig. 2(a), which depicts the normalized intensity profile of the electric filed. The optical mode is designed to resonate in the S-band, with a wavelength around 1500 nm. To achieve the high optical Q-factor and single resonance, parameters such as $W_\theta$, $W_R$ and curvature $R$ are optimized through 3D finite difference time domain (FDTD) simulations. The cavity exhibits a single resonance spectrum within the 1450 nm to 1600 nm range, as illustrated in Fig. 2(b), with a calculated optical Q-factor of approximately $3 \times 10^5$ with air cladding.

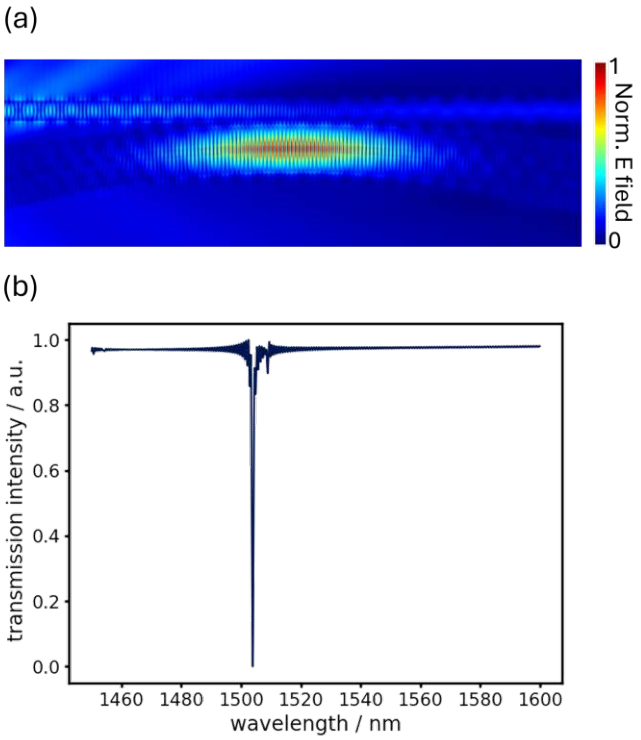


Fig. 2. (a) FDTD-calculated normalized electric field amplitude at its resonance wavelength 1506.77 nm. (b) FDTD-calculated transmittance versus optical wavelength.

The curved structure further enhances optomechanical interactions by better aligning the mechanical motion with the optical field distribution, thereby improving sensitivity and coupling efficiency. Building on the curved PhC cavity design, we propose an optomechanical device

by integrating a ring-shaped cantilever with the PhC cavity on the same SiN platform. The ring-shaped cantilever is supported by two 500 nm-wide arms, which allow for back-etching of the underlying substrate, enabling the structure to be suspended in air while allowing the probe apex to protrude from the device. The ring is positioned 100 nm away from the PhC cavity, as illustrated in Fig. 3(a). Hereafter, we refer to the device as the PhC-ring sensor.

As the ring-shaped cantilever moves relative to the PhC, the optical wave transmitted at the edge of the PhC experiences a modulation in the surrounding refractive index, altering the effective optical path length of the PhC's resonant modes. This results in a spectral shift in the resonance wavelengths [19, 33].

To analyze this interaction, the cantilever deformation at its first resonance mode was simulated using the finite element method (FEM). The deformed cantilever structure was then incorporated into a FDTD simulation with the PhC cavity. One example where the optical resonance mode was computed with 10 nm gap between the ring and the PhC. The results, presented in Fig. 3(b), demonstrate that the normalized electric field distribution is perturbed by the presence of the ring, indicating strong optomechanical coupling.

The mechanical modes are designed to maximize optomechanical coupling and achieve high resonance frequencies. We examined a ring with 5 µm radius, supported by two 5 µm-long arms on each side. The first three in-plane mechanical mode shapes and their corresponding resonance frequencies are shown in Fig. 3(c).

In addition to the first-order in-plane mode of the suspended cantilever, the second- and third-order in-plane modes also influence the spectral position of the PhC due to their in-plane motion relative to the cavity. However, since the first-order in-plane mode exhibits the strongest optomechanical coupling, our analysis will primarily focus on this mode in the following discussions.

## 3. Results

In this study, we investigated the optical response of the transmitted light in the PhC while varying the gap between the ring-shape and the PhC cavity. The quasi-3D finite-difference time-domain (FDTD) method was employed to compute the transmission spectrum, incorporating the deformed ring-shaped cantilever at its first-order in-plane mode, as obtained from the FEM simulation.

As the ring moves closer to the PhC cavity, the shrinking gap increases the effective refractive index, enhancing light transmission from the PhC cavity to the ring. This results in two key effects: 1. A redshift (longer wavelength shift) in the optical resonance, and 2. a decrease in the extinction ratio (reduction in resonance contrast).

Figure 4(a) presents the simulated resonance peaks of the PhC-ring sensor for different ring–PhC gap values. To quantify the transmission intensity change, we select the inflection point on the resonance curve of the static cantilever at wavelength $\lambda_0$ and measure the transmission intensity at this wavelength for different gaps. This allows us to plot the percentage intensity change as a function of the ring-shaped cantilever's displacement, which exhibits a linear increase, as shown in Fig. 4(b).

Additionally, by tracking the resonance wavelength shift at the minimum transmission point (Fig. 4(d)), we observe that the wavelength shift also increases linearly with cantilever displacement. However, in the last 30 nm of displacement, as the ring moves further from the PhC cavity, the slope of this shift steepens, indicating a stronger optomechanical interaction in this regime.

By applying a linear fit to the relationship between the percentage intensity change and the displacement of the cantilever, the slope of the fitted function represents the PhC-ring sensor's displacement sensitivity. Since the radius of the ring is the key design factor-while keeping the waveguide width fixed at 500 nm to ensure high optical coupling—we examined four different ring radii: 5 , 10 , 15 , 20 µm. We then performed simulations similar to those shown in Fig.

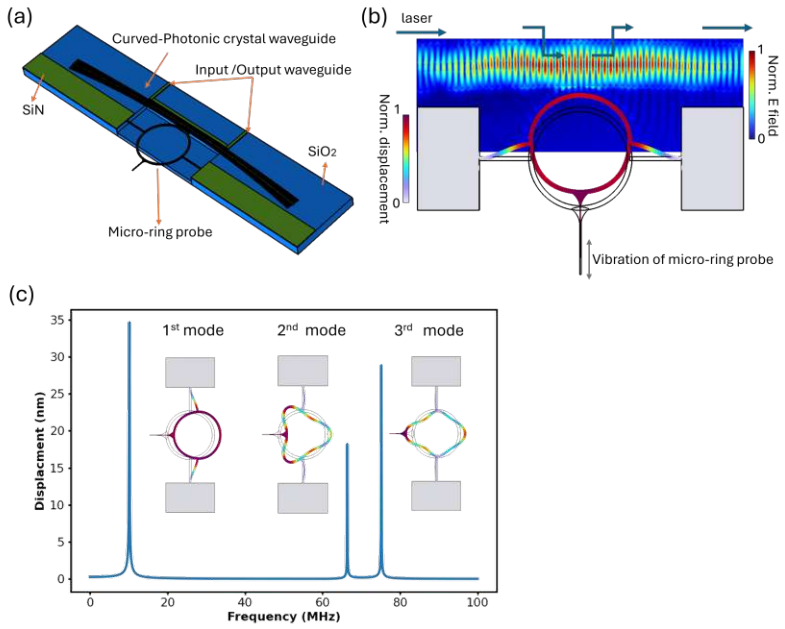


Fig. 3. (a) A 3D illustration of the PhC-cantilever device, featuring a ring-shaped cantilever positioned 100 nm away from the center of the curved photonic crystal cavity. (b) The working principle of the PhC-cantilever device is illustrated. The gray parts represent the device in its equilibrium state, while the colored ring-shaped cantilever shows the FEM-calculated deformed shape in its first in-plane mechanical mode. The ring has a radius of 5 µm, supported by two 5 µm arms, with a probe width of 100 nm, length of 2 µm and a thickness of 300 nm. The colored map in the curved photonic crystal cavity indicates the FDTD-calculated normalized electric field amplitude when the ring is positioned 10 nm away. The mechanical motion of the ring-shaped cantilever is transduced by its influence on the optical mode of the PhC. (c) First three mechanical modes of cantilever.

4, and Fig. 5(a) illustrates the percentage sensitivity $\Delta T/\Delta x$ for different ring radii, where $\Delta x$ represents the cantilever displacement. We observe that larger rings exhibit higher sensitivity, as a greater interaction area with the PhC cavity enhances optomechanical coupling efficiency. A similar trend is observed in Fig. 5(c), where the wavelength shift sensitivity ($\Delta\lambda/\Delta x$) increases with larger ring radii. This further confirms that increasing the interaction region between the ring and the PhC cavity enhances the sensor's performance.

Additionally, we calculated the spring constants and the first three in-plane mechanical modes of the ring-shaped cantilever and plotted them as functions of the ring radius in Fig. 5(b). The spring constant ranges from 0.3 N/m to 39 N/m, with a pronounced decrease between 5 and 10 µm. Notably, the spring constant follows a power-law dependence on the ring radius, as revealed in Fig. 5(b). Once this parameter is established—through either simulation or empirical calibration—quantitative force measurements can be made directly from the optical displacement signals.

A similar trend is observed in the mechanical resonance frequencies of the first three in-plane modes, which decrease as the ring radius increases, as depicted in Fig. 5(d). This behavior

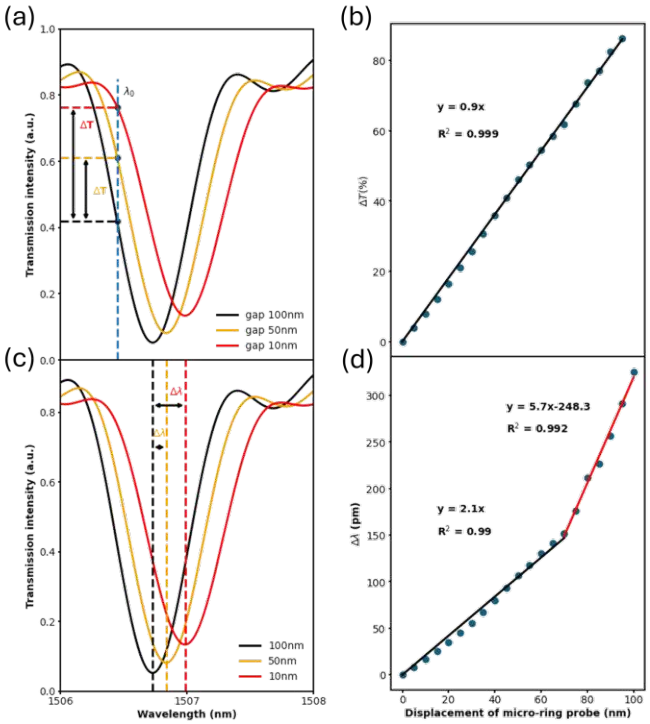


Fig. 4. (a) As the ring-shaped cantilever displaces towards the PhC, the gap between the PhC and the cantilever decreases. By fixing the laser wavelength at 40% of the maximum transmission, which lies on the linear part of the slope, the transmitted intensity increases. The change in transmitted intensity is linearly proportional to the displacement of the cantilever, as shown in (b). (c) The displacement of the cantilever also causes a resonance shift towards longer wavelengths. This wavelength shift is linearly proportional to the displacement of the ring-shaped cantilever within the first 70 nm and the last 30 nm, as illustrated in (d).

suggests that larger rings exhibit lower stiffness and mechanical frequency, which can influence the sensor's dynamic response and optomechanical coupling efficiency. Based on the results in Fig. 5(d), the optomechanical coupling factor, defined as $g_{OM}/2\pi = \frac{d\omega_O}{dx}$, increases linearly as the gap between the cantilever and the PhC shrinks, where $d\omega_O$ represents the shift in the angular frequency of the optical cavity mode.

Notably, because the PhC's resonance shift directly encodes the cantilever's displacement, no external or secondary feedback mechanism is necessary. Conventional AFM sensors depend on an external laser beam and quadrant photodiode for deflection readout; here, the entire detection pathway is integrated on the chip. This simplifies high-frequency measurements, since the bandwidth is not limited by bulky free-space optics or complicated electronics. Instead, the photonic resonator responds instantaneously to ring motion, yielding a purely photonic displacement or force signal.

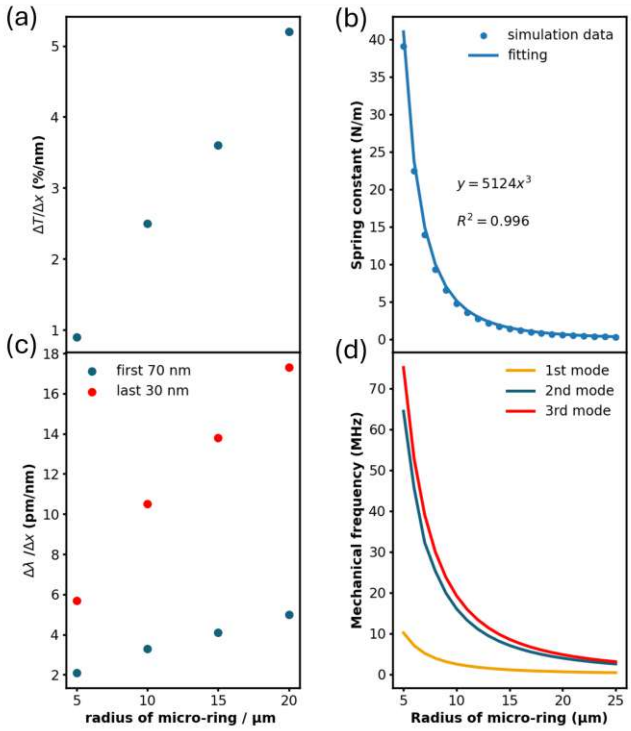


Fig. 5. (a) and (c) illustrate the optical sensitivities, whereas (b) and (d) depict the mechanical properties, all as functions of ring radius. In (a), the slope of the percentage intensity change versus cantilever displacement is shown, while (c) presents the slope of the resonance wavelength shift versus displacement. Meanwhile, (b) shows the resulting spring constants, and (d) indicates the first three in-plane mechanical resonance frequencies.

## 4. Conclusion

In summary, our ring-shaped photonic crystal cantilever demonstrates direct and highly sensitive displacement/force transduction, achieved without the need for the standard AFM optical lever or electronic feedback loop. By relying solely on the shift in photonic crystal resonance, we obtain linear and quantitative measurements of nanomechanical motion. This integrated, purely photonic readout significantly reduces setup complexity and opens new avenues for miniaturized, high-throughput force sensors that can be deployed in real-world conditions—be it fluidic environments, vacuum systems, or multi-probe arrays. Future work will focus on further optimizing the Q-factor and exploring additional functionalization routes, paving the way for an even broader range of nanoscale characterization tasks.

## 5. Acknowledgments

This work was funded with financial support from the European Union's Horizon 2020 research and innovation programme. The authors Y.Z., G.P., B.L., G.R. and L.O'F. acknowledge the Marie Skłodowska-Curie project "OPTAPHI" under grant agreement No. 860808. The financial

support by the Austrian Federal Ministry for Labour and Economy and the National Foundation for Research, Technology and Development and the Christian Doppler Research Association is gratefully acknowledged.

## References


1. G. Binnig, C. F. Quate, and C. Gerber, "Atomic Force Microscope," Phys. Rev. Lett. **56**, 930–933 (1986).
2. G. Meyer and N. M. Amer, "Novel optical approach to atomic force microscopy," Appl. Phys. Lett. **53**, 1045–1047 (1988).
3. C. Gerber and H. P. Lang, "How the doors to the nanoworld were opened," Nat. Nanotechnol. **1**, 3–5 (2006).
4. W. Bao, M. Melli, N. Caselli, *et al.*, "Mapping Local Charge Recombination Heterogeneity by Multidimensional Nanospectroscopic Imaging," Science **338**, 1317–1321 (2012).
5. H. Sadeghian, R. Herfst, B. Dekker, *et al.*, "High-throughput atomic force microscopes operating in parallel," Rev. Sci. Instruments **88**, 033703 (2017).
6. S.-H. im, D. Raorane, S. Satyanarayana, and A. Majumdar, "Nano-chemo-mechanical sensor array platform for high-throughput chemical analysis," Sensors Actuators B: Chem. **119**, 466–474 (2006).
7. T. Kouh, D. Karabacak, D. H. Kim, and K. L. Ekinci, "Diffraction effects in optical interferometric displacement detection in nanoelectromechanical systems," Appl. Phys. Lett. **86**, 013106 (2005).
8. P. E. Allain, L. Schwab, C. Mismer, *et al.*, "Optomechanical resonating probe for very high frequency sensing of atomic forces," Nanoscale **12**, 2939–2945 (2020).
9. J. Chae, S. An, G. Ramer, *et al.*, "Nanophotonic Atomic Force Microscope Transducers Enable Chemical Composition and Thermal Conductivity Measurements at the Nanoscale," Nano Lett. **17**, 5587–5594 (2017).
10. H. Söngen, R. Bechstein, and A. Kühnle, "Quantitative atomic force microscopy," J. Physics: Condens. Matter **29**, 274001 (2017).
11. K. Gadelrab, S. Santos, J. Font, and M. Chiesa, "Single cycle and transient force measurements in dynamic atomic force microscopy," Nanoscale **5**, 10776 (2013).
12. M. Stark, R. W. Stark, W. M. Heckl, and R. Guckenberger, "Inverting dynamic force microscopy: From signals to time-resolved interaction forces," Proc. National Acad. Sci. **99**, 8473–8478 (2002).
13. A. Chandrashekar, P. Belardinelli, M. A. Bessa, *et al.*, "Quantifying nanoscale forces using machine learning in dynamic atomic force microscopy," Nanoscale Adv. **4**, 2134–2143 (2022).
14. M. Aspelmeyer, T. J. Kippenberg, and F. Marquardt, "Cavity optomechanics," Rev. Mod. Phys. **86**, 1391–1452 (2014).
15. D. Van Thourhout and J. Roels, "Optomechanical device actuation through the optical gradient force," Nat. Photonics **4**, 211–217 (2010).
16. I. Favero and K. Karrai, "Optomechanics of deformable optical cavities," Nat. Photonics **3**, 201–205 (2009).
17. G. Anetsberger, O. Arcizet, Q. P. Unterreithmeier, *et al.*, "Near-field cavity optomechanics with nanomechanical oscillators," Nat. Phys. **5**, 909–914 (2009).
18. K. Srinivasan, H. Miao, M. T. Rakher, *et al.*, "Optomechanical Transduction of an Integrated Silicon Cantilever Probe Using a Microdisk Resonator," Nano Lett. **11**, 791–797 (2011).
19. Y. Liu, H. Miao, V. Aksyuk, and K. Srinivasan, "Wide cantilever stiffness range cavity optomechanical sensors for atomic force microscopy," Opt. Express **20**, 18268 (2012).
20. A. Schliesser, O. Arcizet, R. Rivière, *et al.*, "Resolved-sideband cooling and position measurement of a micromechanical oscillator close to the Heisenberg uncertainty limit," Nat. Phys. **5**, 509–514 (2009).
21. A. Clerk, "Facing Heisenberg at the nanoscale," Nat. Nanotechnol. **4**, 796–798 (2009).
22. M. Eichenfield, R. Camacho, J. Chan, *et al.*, "A picogram- and nanometre-scale photonic-crystal optomechanical cavity," Nature **459**, 550–555 (2009).
23. M. Wang, G. Ramer, D. J. Perez-Morelo, *et al.*, "High Throughput Nanoimaging of Thermal Conductivity and Interfacial Thermal Conductance," Nano Lett. **22**, 4325–4332 (2022).
24. H. Li and M. Li, "Optomechanical photon shuttling between photonic cavities," Nat. Nanotechnol. **9**, 913–919 (2014).
25. J. Gomis-Bresco, D. Navarro-Urrios, M. Oudich, *et al.*, "A one-dimensional optomechanical crystal with a complete phononic band gap," Nat. Commun. **5**, 4452 (2014).
26. T.-W. Lu and P.-T. Lee, "Ultra-high sensitivity optical stress sensor based on double-layered photonic crystal microcavity," Opt. Express **17**, 1518 (2009).
27. F. Galeotti, I. Seršić Vollenbroek, M. Petruzzella, *et al.*, "On-chip waveguide-coupled opto-electro-mechanical system for nanoscale displacement sensing," APL Photonics **5**, 026103 (2020).
28. B. Li, F.-L. Hsiao, and C. Lee, "Configuration analysis of sensing element for photonic crystal based NEMS cantilever using dual nano-ring resonator," Sensors Actuators A: Phys. **169**, 352–361 (2011).
29. C. Lee and J. Thillaigovindan, "Optical nanomechanical sensor using a silicon photonic crystal cantilever embedded with a nanocavity resonator," Appl. Opt. **48**, 1797 (2009).
30. T. T. Mai, F.-L. Hsiao, C. Lee, *et al.*, "Optimization and comparison of photonic crystal resonators for silicon microcantilever sensors," Sensors Actuators A: Phys. **165**, 16–25 (2011).
31. Q. Quan, P. B. Deotare, and M. Loncar, "Photonic crystal nanobeam cavity strongly coupled to the feeding waveguide," Appl. Phys. Lett. **96**, 203102 (2010).

246 32. S. Iadanza, J. H. Mendoza-Castro, T. Oliveira, *et al.*, "High-Q asymmetrically cladded silicon nitride 1D photonic
247 crystals cavities and hybrid external cavity lasers for sensing in air and liquids," Nanophotonics **11**, 4183–4196
248 (2022).
249 33. T. J. Kippenberg and K. J. Vahala, "Cavity Optomechanics: Back-Action at the Mesoscale," Science **321**, 1172–1176
250 (2008).

## 4.5. Understanding the Mechanical Stress-Induced Effects on Electromagnetic Wave Simulations.

Microcantilevers are suspended beam-like structures, fixed at one end, that bend or vibrate in response to an applied load [226]. As fundamental micro- and nanoelectromechanical (MEMS/NEMS) structures, they are widely used for force, mass, and strain sensing, as well as biosensing, chemical detection, and imaging [227, 228, 229, 230, 231].

Advances in silicon photonics have enabled the integration of Bragg gratings onto Silicon-on-Insulator (SOI) slabs, demonstrating their potential for optical sensing [158, 159, 160]. Silicon photonics, particularly utilizing waveguide Bragg gratings (WBGs), has shown promise in integrating mechanical probes and optical cavities into miniaturized sensing devices. However, conventional free-space optical detection methods face limitations at the microscale due to diffraction effects, especially when cantilever widths approach or fall below the detection laser's beam waist.

To overcome these limitations, this paper introduces an optomechanical sensor design that integrates a waveguide Bragg grating onto a silicon-on-insulator (SOI) cantilever. The cantilever bending induced by external forces results in strain-dependent refractive index changes, causing measurable shifts in the optical resonance wavelength. A comprehensive numerical model based on finite element simulations (COMSOL Multiphysics) is developed to incorporate stress-induced effects into a full simulation of a waveguide Bragg grating. This approach enables a deeper understanding and optimization of the interactions, offering valuable insights for future sensor design, fabrication, and characterization.

A preliminary version of this modeling approach was presented at the COMSOL Conference 2023 and is available online (https://www.comsol.fr/paper/design-and-simulation-of-bragg-grating-based-optomechanical-sensor-for-atomic-force-microscopy-122231.)

# Design and Simulation of Cantilever Beam with a Bragg Grating based Optomechanical Senor for Atomic Force Microscopy in COMSOL

Yide Zhang[1,2], Liam O'Faolain[2] and Georg Ramer[1]

1. Institute of Chemical Technologies and Analytics, TU Wien, Vienna, 1060 Austria

2. Centre for Advanced Photonics and Process Analysis, Munster Technological University, Cork, T12P928, Ireland

E-mail: yide.zhang@tuwien.ac.at



## Abstract:

Silicon photonics has shown great potential in bringing together mechanical probes and optical cavity as compact sensors for many sensing applications. In this work, we present the integration of a waveguide Bragg grating (WBG) onto a cantilever beam, utilizing a Silicon-on-insulator (SOI) structure as an optomechanical sensor for atomic force microscopy (AFM). The flexibility of the COMSOL Multiphysics software enables us to model the mechanical characteristics of the cantilever and link the mechanical bending effects to the optical transmission simulations. Within these simulations, the nanoscale force applied to the cantilever tip results in cantilever beam deformation, represented by a picometer scale shift in optical resonance frequency. The simulation is carried out for the proposed Bragg grating design, featuring 80 gratings, and attains a force sensitivity approximately 16 m/N, corresponding to a cantilever stiffness 0.06 N/m.

Keywords: silicon photonics, waveguide Bragg grating, cantilever, AFM

## 1.Introduction

Atomic force microscopy (AFM) has been widely acknowledged as a crucial tool for surface imaging, force measurement, and localization. It serves as a standard technique for nanoscale force spectroscopy [1,2]. Recent advancements in MEMS and nanophotonics have demonstrated the potential to enhance conventional AFM performance, offering a broad range of cantilever stiffnesses [3], exceptionally high frequencies and quality factors [4], and cost-effective, rapid fabrication on a single silicon chip [5]. Consequently, silicon photonics has emerged as a promising avenue for integrating mechanical probes with optical cavities, creating compact sensors for diverse sensing applications.

Latest developments in silicon photonics have enabled the successful integration of Bragg gratings onto the Silicon-on-insulator (SOI) slab, demonstrating their potential for optical sensing applications, as demonstrated in references [6, 7, 8]. Leveraging the capabilities of waveguide Bragg gratings (WBG) on the SOI platform, we investigate the fusion of WBG with a cantilever, leading to the development of compact sensors for atomic force measurements. Within this framework, micro scale cantilevers are employed, a size range challenging to efficiently transduce using free-space optical methods due to pronounced diffraction effects. These effects arise when the cantilever's width falls below the detection beam waist, competing with the reflection of the detection laser at the cantilever tip and limiting the AFM sensitivity. Microscale cantilever-based optomechanical

sensors typically involve a vibrating cantilever that incorporates an optical cavity on its surface. When a force is exerted in the cantilever's tip, the resulting bending strain induces a change in the refractive index within the core, leading to a shift in the wavelength of the resonance. Consequently, an optical readout system that relies on the changes in transmitted or reflected power at the wavelength of interest is employed, effectively eliminating the need for a deflection laser in the process.

In this context, the resonance shift phenomenon is influenced by various factors, including the strain induced on the WBG due to the bending of the cantilever, deformation of the straight waveguide, and three-dimensional alterations in refractive index. These effects should all be taken into account. As a result, there is a critical need for a numerical model capable of simulating the entire process of light transmission and its response to cantilever deformation caused by applied force. This model, relying on finite element simulations, will grant a comprehensive comprehension of this intricate process. Its significance lies in its role as a pivotal instrument for guiding design improvements, streamlining fabrications, and providing valuable support for characterization of the fabricated devices.

## 2. Design and Simulation

The structure of the proposed cantilever-based optomechanical sensor is illustrated in Figure 1. It consists of a silicon dioxide (SiO2) cantilever, silicon (Si) waveguides, and a cantilever tip. WBG is specifically designed with a Si core, SiO2 substrate, and air cladding.

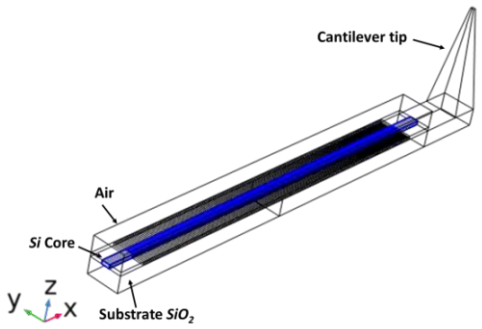


**Figure 1**. Schematic of waveguide Bragg grating cantilever. Blue: Core with gratings.

The silicon WBGs operate based on Bragg reflection. When the signal propagates through the Bragg grating, it undergoes reflection at all interfaces, leading to a relative phase difference between the input signal and the reflected light. Accordingly, after multiple reflections, only those wavelengths achieving constructive interference are highly reflected, while others cancel each other out and pass through the grating. These reflected signals are confined to a narrow band centred around the Bragg wavelength. Any change in the core's refractive index causes a shift in the reflected wavelength, allowing for force sensing by monitoring the wavelength shift or reflected power change of the resonant wavelength peak. The Bragg wavelength ($\lambda_B$) associated with peak reflectivity can be determined using Bragg's equation,

$$\lambda_B = 2 \cdot \Lambda \cdot n_{eff}$$

where $\Lambda$ is the grating period, $n_{eff}$ is the effective refractive index.

The parameters for the width and height of the rectangular waveguide core layer are determined using the effective refractive index method [9] and the guided mode cutoff condition [10]. In our WBG simulation model design, we select a waveguide width for the Bragg grating, equal to 540 µm to ensure single-mode transmission within the waveguide. The geometric model of the silicon waveguide is established based on the single-mode transmission condition of a rectangular waveguide with a width of 500 µm. The thickness of the silicon waveguide in the chosen device layer is 220 nm. Silicon is chosen as the core material for the waveguide, with a refractive index of 3.46 at 1550 nm. Silicon dioxide serves as the waveguide cladding material, with a cladding refractive index of 1.45 at 1550 nm. A period of 0.32 µm with 50% periodicity is selected to design the Bragg wavelength, which is set at 1530 nm.

A resonance shift Δλ due to the change of refractive index Δn can be expressed by,

$$\frac{\Delta\lambda}{\lambda} = \frac{\Delta n}{n}$$

Previous studies have examined how strain, both in-plane and out-of-plane, impacts the light transmission or reflection from a nanostructured material deposited on a substrate [11][12]. They have also investigated how the bandgap of materials changes under strain to isolate the strain's effect on the optical properties of the device [13]. In this research, we employ finite element methods (FEM) to delve into the impact of strain on the refractive index of silicon. Specifically, we explore how the optical spectrum shifts when a specified force is applied perpendicular to the cantilever tip, either compressing it or extending it.

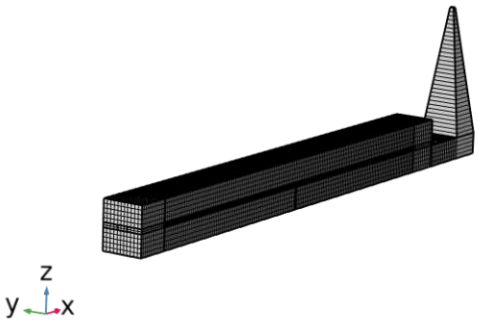


**Figure 2**. Mesh of the waveguide Bragg grating cantilever.

We conducted a numerical analysis of the geometry shown in Figure 1 using COMSOL Multiphysics Finite Element Modelling software. The software generated a user-controlled swept mesh, as depicted in Figure 2. To achieve a high-frequency response, we selected specific dimensions for the cantilever, and the substrate width was set to 2 µm.

For our mechanical study, we employed the Solid Mechanics Physics interface and assumed a Linear Elastic Material Model in a Frequency Domain study. The first half of the WBG, away from the tip side, was set as fixed, while a force of 1 µN was applied to the tip. The results of the stress simulation are illustrated in Figure 3(a) and (b).

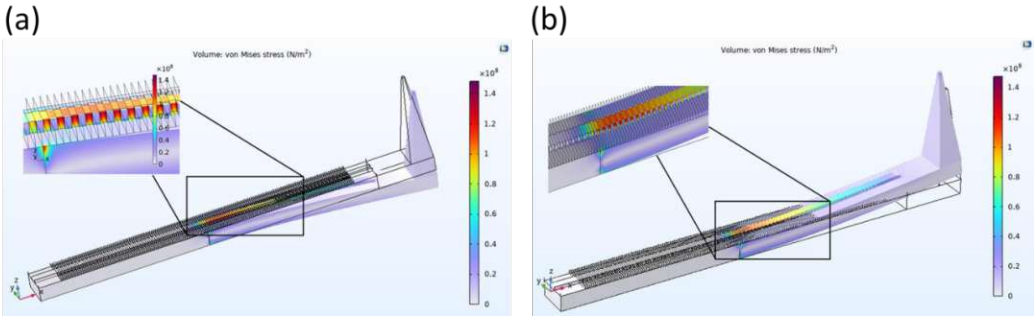


**Figure 3**. Stress simulation with $1\mu N$ force exerted on the cantilever tip (a) force is parallel to negative z direction (b) force is parallel to position z direction.

To study optical transmission, we employed the electromagnetic wave interface in frequency domain. We positioned an excitation source with a spatial distribution matching the fundamental waveguide mode on the left side of the waveguide. The reflected power was then observed at the left side of the waveguide. In order to obtain a reflection spectrum, we varied the wavelength of the excitation source as a parameter and conducted a parametric sweep across different wavelengths. To mitigate any reflections from the boundaries of the computational window, we applied first-order scattering boundary conditions.

## 3. Results and Discussions

In Figure 4, we present the reflectance spectrum of the WBG under steady conditions (dashed line) as a function of wavelength. The solid line represents the reflectance spectrum under the condition where a 100 µN force is applied parallel to the positivise z-direction on the cantilever tip, as shown in Figure 3(b). It's worth noting that when an external force is applied to the tip, there is a noticeable 1.6 nm red shift in the resonance. This shift is attributed to changes in the refractive index caused by the bending of the waveguide.

Additionally, we selected a specific wavelength, 1540 nm, which falls within the right side of the stop band. We conducted a parametric sweep for increasing forces at this wavelength. Figure 5 displays the reflected power as a function of the applied force to the tip, where the force is parallel to the negative z-direction, corresponding to the result in Figure 3(a). We observe that as the force increases, the reflected power decreases, indicating a blue shift in the resonance. Consequently, we can determine the direction of the applied force by monitoring the increase or decrease in reflected power at the specified wavelength or the red or blue shift in the resonance across the entire spectrum.

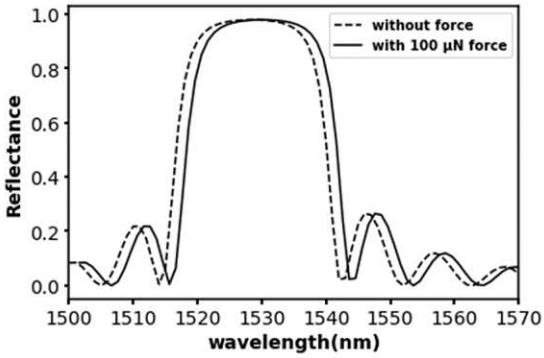


**Figure 4**. Reflectance spectra as functions of wavelength.

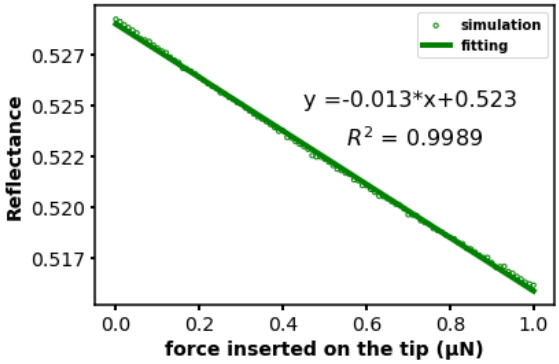


**Figure 5**. Reflected power as functions of force inserted to the cantilever tip at wavelength 1540 nm.

## 4. Conclusion

In this research paper, we designed and simulated a 3D Bragg grating-based optomechanical sensor that operates at room temperature using COMSOL Multiphysics software. This sensor is built upon a single-mode symmetric slab waveguide featuring planar Bragg gratings. It was designed with core dimensions in the sub-micron range, allowing for seamless integration into the evolving field of miniaturized photonic circuits.

To incorporate force sensitivity into the waveguide Bragg grating (WBG), we considered the fundamental change in refractive index induced by strain. We observed the strain's effects on the model in the form of shifts in the reflectance wavelength spectrum. During the simulation, we applied a series of forces ranging from 0 to 1 µN, and we observed a force sensitivity of approximately 16 m/N. Utilizing physics interfaces within the wave optics and structural mechanics module, we harnessed various features, including boundary mode analysis, frequency domain analysis, stationary study, and the ability to couple different simulation results.

To the best of our knowledge, this represents the first comprehensive 3D coupled finite element analysis aimed at understanding the mechanical stress-induced effects on electromagnetic wave

simulations. This study serves as a crucial reference point for guiding the design and experimentation of optomechanical sensors.

## 5. Acknowledgement

This work was funded with financial support from the European Union's Horizon 2020 research and innovation programme under the Marie Skłodowska-Curie project "OPTAPHI" (grant agreement No. 860808).

## References

[1] Heath, G.R., Kots, E., Robertson, J.L. et al. Localization atomic force microscopy. Nature 594, 385–390 (2021).

[2] Binnig, G., Quate, C. F. & Gerber, C. Atomic force microscope. Phys. Rev. Lett. 56, 930–933 (1986).

[3] Yuxiang Liu, Houxun Miao, Vladimir Aksyuk, and Kartik Srinivasan, "Wide cantilever stiffness range cavity optomechanical sensors for atomic force microscopy," Opt. Express 20, 18268-18280 (2012)

[4] Schwab, L., Allain, P.E., Mauran, N. et al. Very-high-frequency probes for atomic force microscopy with silicon optomechanics. Microsyst Nanoeng 8, 32 (2022).

[5] D. J. Perez-Morelo, M. Wang, V. Madhaven, M. Sathisivan, C. Tay and V. A. Aksyuk, "Integrated Photonic Optomechanical Atomic Force Microscopy Probes Batch Fabricated Using Deep UV Photolithography," in *Journal of Microelectromechanical Systems*.

[6] Murphy T., Hastings J. and Smith H. 2001 Fabrication and characterization of narrow-band Bragg-reflection filters in silicon-on-insulator ridge waveguides Journal of Lightwave Technology 19 12 1938–42

[7] G. Jiang, R. Chen, Q. Zhou, J. Yang, M. Wang and X. Jiang, "Slab-Modulated Sidewall Bragg Gratings in Silicon-on-Insulator Ridge Waveguides," in *IEEE Photonics Technology Letters*, vol. 23, no. 1, pp. 6-8, Jan.1, 2011, doi: 10.1109/LPT.2010.2089613.

[8] Xu Wang, Samantha Grist, Jonas Flueckiger, Nicolas A. F. Jaeger, and Lukas Chrostowski, "Silicon photonic slot waveguide Bragg gratings and resonators," Opt. Express 21, 19029-19039 (2013)

[9] K. Chiang, "Dual Effective-Index Method for the Analysis of Rectangular Waveguides," Applied Optics, vol. 25, pp. 2169–2174, 1986.

[10] D. Marcuse, "Cutoff condition of optical fibers," J. Opt. Soc. Am. 63, 1369-1371 (1973)

[11] H. Tran, W. Du, S.A. Ghetmiri, A. Mosleh, G. Sun, et al. Systematic study of GeSn absorption coefficient and refractive index for the device applications of Si-based optoelectronics, J. Appl. Phys., 119 (2016), pp. 103-106.

[12] Asma Darvishzadeh, Naif Alharbi, Amir Mosavi, Nima E. Gorji, Modeling the strain impact on refractive index and optical transmission rate, Physica B: Condensed Matter, 543 (2018), pp. 14-17.

[13] Cai J, Ishikawa Y, Wada K. Strain induced bandgap and refractive index variation of silicon. Opt Express. 2013 Mar 25;21(6):7162-70.

# 5. Conclusions and Outlook

This PhD thesis has offered new insights and developments in both the theoretical understanding and practical implementation of AFM-IR spectroscopy and optomechanical AFM sensing. By combining theoretical modeling, numerical simulations, and experimental validation, I have established new methodologies to improve spatial resolution in chemical imaging and enhance displacement and force sensitivity in AFM-based transducers.

**Point Spread Function Model for AFM-IR**

A central achievement of this work is the development of an analytical point spread function (PSF) model that quantitatively describes how sample geometry, thermal diffusion, absorber and matrix properties, and laser parameters influence AFM-IR spatial resolution and signal intensity. This model provides a theoretical framework for optimizing imaging conditions and offers new insights into resolution limitations. The PSF model was extensively validated through finite element method (FEM) simulations and experimental AFM-IR measurements, demonstrating strong agreement across a wide range of sample configurations. By bridging experimental observations with theoretical predictions, this study also enabled nanoscale investigations of interfacial thermal resistance between PMMA and PE, revealing its role in modifying heat transfer and signal formation in AFM-IR.

**Subsurface Chemical Imaging with AFM-IR**

Expanding the application of AFM-IR beyond surface characterization, this work systematically investigated the role of absorber size, depth, and topography in subsurface chemical imaging with tapping-mode AFM-IR. By fabricating well-controlled nanostructures, I established a direct correlation between feature size, AFM-IR signal intensity, and spatial resolution. Additionally, the study of sample structure provided new insights into heat conduction at the nanoscale, significantly impacting contrast and spatial resolution in heterogeneous samples. This work revealed how sample structure contributes to imaging broadening depending on whether excitation occurs in the covering or underlying layer. These findings enhance the capabilities of AFM-IR for depth-resolved chemical imaging, particularly in materials science and nanotechnology.

**Optomechanical AFM Probes with Ring Resonators**

To enhance force sensitivity in AFM, I I developed an optomechanical transducer design

based on a single-mode ring resonator. This design eliminates the instability issues associated with whispering gallery modes and enables robust, high-sensitivity displacement measurements. The transducer achieves a displacement sensitivity of $6.7 \times 10^{-16}\,\mathrm{m/Hz^{1/2}}$ and force detection down to $5.0 \times 10^{-14}\,\mathrm{N}$, with tunable mechanical resonance frequencies and stiffness for applications ranging from soft matter characterization to high-speed imaging. FEM simulations were used to validate the mechanical response and optical transduction efficiency, ensuring strong agreement between theoretical predictions and experimental results.

**Photonic Crystals-Based AFM Force Sensors**

Further expanding on optomechanical sensing, I integrated photonic crystal cavities with suspended cantilevers on $Si_3N_4$ platform, enabling high-Q optical resonances and strong optomechanical coupling. These novel architectures provide real-time, high-precision force and displacement measurements, with a tunable mechanical frequency range of 400 kHz to 75.12 MHz and adjustable spring constants from 0.3 N/m to 39 N/m. This sensor demonstrates the potential for achieving high frequency, high sensitivity, ultra-fast thermal dynamic measurements, and linear force or displacement detection. Such capabilities make it a promising tool for next-generation AFM applications, where rapid and precise nanoscale measurements are required.

**Outlook and Future Improvements**

While this work provides a foundation for further research, several challenges and opportunities remain. The PSF model proposed here offers a potential framework for analyzing spatial resolution in AFM-IR, but it requires additional experimental validation—particularly for samples with different interfacial thermal resistance. With further refinement, the model may help improve the interpretation of AFM-IR signals in soft matter, biological systems, and advanced nanocomposites, where interfacial thermal resistance can play a significant role.

This thesis also initiated preliminary work on a one-dimensional coupled photothermal and photoacoustic model for liquid environments. While initial results indicate the feasibility of simulating acoustic wave generation following pulsed IR absorption, the model is still in early stages and requires more extensive theoretical development and experimental testing. Its future expansion could eventually support the integration of photoacoustic contrast into AFM-based techniques, potentially enabling subsurface sensing and imaging in liquid-phase settings.

On the optomechanical side, improvements in nanofabrication and packaging techniques—such as achieving full cantilever release and implementing fiber-based optical coupling—will likely be important for integrating ring resonators and photonic crystal sensors

into practical AFM systems. Testing under more realistic conditions will help determine the robustness and applicability of these approaches for high-speed, high-sensitivity measurements.

Looking ahead, the methods and models developed in this thesis may serve as a useful basis for future investigations in nanoscale metrology, near-field optical imaging, and hybrid AFM modalities. Addressing the remaining challenges will be key to advancing the capabilities of AFM-IR and optomechanical AFM in both scientific and applied contexts.

# List of Figures

# List of Tables

# Bibliography


[1] A. Dazzi, F. Glotin, and R. Carminati, "Theory of infrared nanospectroscopy by photothermal induced resonance", en, *Journal of Applied Physics*, vol. 107, no. 12, p. 124 519, Jun. 2010, ISSN: 0021-8979, 1089-7550. DOI: 10.1063/1.3429214. [Online]. Available: https://pubs.aip.org/jap/article/107/12/124519/146522/Theory-of-infrared-nanospectroscopy-by (visited on 08/14/2024).

[2] A. Dazzi, "PhotoThermal Induced Resonance. Application to Infrared Spectromicroscopy", en, in *Thermal Nanosystems and Nanomaterials*, S. Volz, Ed., vol. 118, Series Title: Topics in Applied Physics, Berlin, Heidelberg: Springer Berlin Heidelberg, 2009, pp. 469–503, ISBN: 978-3-642-04257-7. DOI: 10.1007/978-3-642-04258-4_16. [Online]. Available: https://link.springer.com/10.1007/978-3-642-04258-4_16 (visited on 02/20/2025).

[3] A. N. Morozovska, E. A. Eliseev, N. Borodinov, O. S. Ovchinnikova, N. V. Morozovsky, and S. V. Kalinin, "Photothermoelastic contrast in nanoscale infrared spectroscopy", en, *Applied Physics Letters*, vol. 112, no. 3, p. 033 105, Jan. 2018, ISSN: 0003-6951, 1077-3118. DOI: 10.1063/1.4985584. [Online]. Available: https://pubs.aip.org/apl/article/112/3/033105/36029/Photothermoelastic-contrast-in-nanoscale-infrared (visited on 02/03/2025).

[4] J. J. Schwartz, G. Pavlidis, and A. Centrone, "Understanding Cantilever Transduction Efficiency and Spatial Resolution in Nanoscale Infrared Microscopy", en, *Analytical Chemistry*, acs.analchem.2c02612, Sep. 2022, ISSN: 0003-2700, 1520-6882. DOI: 10.1021/acs.analchem.2c02612. [Online]. Available: https://pubs.acs.org/doi/10.1021/acs.analchem.2c02612 (visited on 09/21/2022).

[5] B. Stuart, *Infrared spectroscopy: fundamentals and applications* (Analytical techniques in the sciences), eng. Chichester: J.Wiley & sons, 2004, ISBN: 978-0-470-85427-3.

[6] J. M. Chalmers and P. R. Griffiths, Eds., *Handbook of Vibrational Spectroscopy*, en, 1st ed. Wiley, Dec. 2001, ISBN: 978-0-471-98847-2. DOI: 10.1002/0470027320. [Online]. Available: https://onlinelibrary.wiley.com/doi/book/10.1002/0470027320 (visited on 04/01/2025).

[7] J. M. Thompson, *Infrared Spectroscopy*, en, 1st ed. Jenny Stanford Publishing, Jan. 2018, ISBN: 978-1-351-20603-7. DOI: 10.1201/9781351206037. [Online]. Available: https://www.taylorfrancis.com/books/9781351206020 (visited on 04/01/2025).

[8] T. Mayerhöfer, *Wave optics in infrared spectroscopy: theory, simulation, and modeling*, eng. Amsterdam London Cambridge, MA: Elsevier, 2024, ISBN: 978-0-443-22031-9.

[9] P. R. Griffiths and J. A. De Haseth, *Fourier transform infrared spectrometry* (Chemical analysis v. 171), 2nd ed. Hoboken, N.J: Wiley-Interscience, 2007, OCLC: 70265583, ISBN: 978-0-471-19404-0.

[10] Y. Roggo, P. Chalus, L. Maurer, C. Lema-Martinez, A. Edmond, and N. Jent, "A review of near infrared spectroscopy and chemometrics in pharmaceutical technologies", en, *Journal of Pharmaceutical and Biomedical Analysis*, vol. 44, no. 3, pp. 683–700, Jul. 2007, ISSN: 07317085. DOI: 10.1016/j.jpba.2007.03.023. [Online]. Available: https://linkinghub.elsevier.com/retrieve/pii/S0731708507001884 (visited on 01/10/2025).

[11] F. Rico, L. Gonzalez, I. Casuso, M. Puig-Vidal, and S. Scheuring, "High-Speed Force Spectroscopy Unfolds Titin at the Velocity of Molecular Dynamics Simulations", en, *Science*, vol. 342, no. 6159, pp. 741–743, Nov. 2013, ISSN: 0036-8075, 1095-9203. DOI: 10.1126/science.1239764. [Online]. Available: https://www.science.org/doi/10.1126/science.1239764 (visited on 10/07/2024).

[12] A. Dabrowska, S. Lindner, A. Schwaighofer, and B. Lendl, "Mid-IR dispersion spectroscopy – A new avenue for liquid phase analysis", en, *Spectrochimica Acta Part A: Molecular and Biomolecular Spectroscopy*, vol. 286, p. 122 014, Feb. 2023, ISSN: 13861425. DOI: 10.1016/j.saa.2022.122014. [Online]. Available: https://linkinghub.elsevier.com/retrieve/pii/S1386142522011623 (visited on 01/13/2025).

[13] T. G. Mayerhöfer, A. V. Pipa, and J. Popp, "Beer's Law-Why Integrated Absorbance Depends Linearly on Concentration", en, *ChemPhysChem*, vol. 20, no. 21, pp. 2748–2753, Nov. 2019, ISSN: 1439-4235, 1439-7641. DOI: 10.1002/cphc.201900787. [Online]. Available: https://chemistry-europe.onlinelibrary.wiley.com/doi/10.1002/cphc.201900787 (visited on 01/14/2025).

[14] A. Röseler, "IR spectroscopic ellipsometry: Instrumentation and results", en, *Thin Solid Films*, vol. 234, no. 1-2, pp. 307–313, Oct. 1993, ISSN: 00406090. DOI: 10.1016/0040-6090(93)90275-T. [Online]. Available: https://linkinghub.elsevier.com/retrieve/pii/004060909390275T (visited on 03/27/2025).

[15] K. Hinrichs, T. Shaykhutdinov, C. Kratz, and A. Furchner, "Brilliant mid-infrared ellipsometry and polarimetry of thin films: Toward laboratory applications with laser based techniques", en, *Journal of Vacuum Science & Technology B, Nanotechnology and Microelectronics: Materials, Processing, Measurement, and Phenomena*, vol. 37, no. 6, p. 060 801, Nov. 2019, ISSN: 2166-2746, 2166-2754. DOI: 10.1116/1.5122869. [Online]. Available: https://pubs.aip.org/jvb/article/37/6/060801/586414/Brilliant-mid-infrared-ellipsometry-and (visited on 03/27/2025).

[16] A. Furchner and K. Hinrichs, "Mid-infrared laser ellipsometry: A new era beyond FTIR", en, *Advanced Optical Technologies*, vol. 11, no. 3-4, pp. 55–56, Sep. 2022, ISSN: 2192-8576, 2192-8584. DOI: 10.1515/aot-2022-0013. [Online]. Available: https://www.frontiersin.org/articles/10.1515/aot-2022-0013 (visited on 03/27/2025).

[17] V. Gold, A. McNaught, and The International Union of Pure and Applied Chemistry (IUPAC), Eds., *The IUPAC Compendium of Chemical Terminology: The Gold Book*, en, 5th ed. Research Triangle Park, NC: International Union of Pure and Applied Chemistry (IUPAC), 2025. DOI: 10.1351/goldbook. [Online]. Available: https://goldbook.iupac.org/ (visited on 01/13/2025).

[18] A. Y. Tolbin, V. E. Pushkarev, L. G. Tomilova, and N. S. Zefirov, "Threshold concentration in the nonlinear absorbance law", en, *Physical Chemistry Chemical Physics*, vol. 19, no. 20, pp. 12 953–12 958, 2017, ISSN: 1463-9076, 1463-9084. DOI: 10.1039/C7CP01514C. [Online]. Available: https://xlink.rsc.org/?DOI=C7CP01514C (visited on 01/13/2025).

[19] M. Miljković, B. Bird, and M. Diem, "Line shape distortion effects in infrared spectroscopy", en, *The Analyst*, vol. 137, no. 17, p. 3954, 2012, ISSN: 0003-2654, 1364-5528. DOI: 10.1039/c2an35582e. [Online]. Available: https://xlink.rsc.org/?DOI=c2an35582e (visited on 03/27/2025).

[20] A. Dazzi, A. Deniset-Besseau, and P. Lasch, "Minimising contributions from scattering in infrared spectra by means of an integrating sphere", en, *The Analyst*, vol. 138, no. 14, p. 4191, 2013, ISSN: 0003-2654, 1364-5528. DOI: 10.1039/c3an00381g. [Online]. Available: https://xlink.rsc.org/?DOI=c3an00381g (visited on 03/27/2025).

[21] J. Mathurin, A. Deniset-Besseau, D. Bazin, E. Dartois, M. Wagner, and A. Dazzi, "Photothermal AFM-IR spectroscopy and imaging: Status, challenges, and trends", *Journal of Applied Physics*, vol. 131, no. 1, p. 010 901, Jan. 2022, ISSN: 0021-8979.

DOI: 10.1063/5.0063902. [Online]. Available: https://doi.org/10.1063/5.0063902 (visited on 03/01/2024).

[22] A. Dazzi and C. B. Prater, "AFM-IR: Technology and Applications in Nanoscale Infrared Spectroscopy and Chemical Imaging", en, *Chemical Reviews*, vol. 117, no. 7, pp. 5146–5173, Apr. 2017, ISSN: 0009-2665, 1520-6890. DOI: 10.1021/acs.chemrev.6b00448. [Online]. Available: https://pubs.acs.org/doi/10.1021/acs.chemrev.6b00448 (visited on 08/14/2024).

[23] J. J. Schwartz, D. S. Jakob, and A. Centrone, "A guide to nanoscale IR spectroscopy: Resonance enhanced transduction in contact and tapping mode AFM-IR", en, *Chemical Society Reviews*, vol. 51, no. 13, pp. 5248–5267, 2022, Publisher: Royal Society of Chemistry. DOI: 10.1039/D2CS00095D. [Online]. Available: https://pubs.rsc.org/en/content/articlelanding/2022/cs/d2cs00095d (visited on 07/12/2022).

[24] A. C. V. D. Dos Santos, N. Hondl, V. Ramos-Garcia, J. Kuligowski, B. Lendl, and G. Ramer, "AFM-IR for Nanoscale Chemical Characterization in Life Sciences: Recent Developments and Future Directions", en, *ACS Measurement Science Au*, vol. 3, no. 5, pp. 301–314, Oct. 2023, ISSN: 2694-250X, 2694-250X. DOI: 10.1021/acsmeasuresciau.3c00010. [Online]. Available: https://pubs.acs.org/doi/10.1021/acsmeasuresciau.3c00010 (visited on 03/21/2024).

[25] S. E. Bialkowski, N. G. C. Astrath, and M. A. Proskurnin, *Photothermal Spectroscopy Methods*, en, 1st ed. Wiley, Apr. 2019, ISBN: 978-1-119-27907-5. DOI: 10.1002/9781119279105. [Online]. Available: https://onlinelibrary.wiley.com/doi/book/10.1002/9781119279105 (visited on 01/14/2025).

[26] Z. A. Yasa, W. B. Jackson, and N. M. Amer, "Photothermal spectroscopy of scattering media", en, *Applied Optics*, vol. 21, no. 1, p. 21, Jan. 1982, ISSN: 0003-6935, 1539-4522. DOI: 10.1364/AO.21.000021. [Online]. Available: https://opg.optica.org/abstract.cfm?URI=ao-21-1-21 (visited on 03/27/2025).

[27] D. L. Mazzoni and C. C. Davis, "Trace detection of hydrazines by optical homodyne interferometry", en, *Applied Optics*, vol. 30, no. 7, p. 756, Mar. 1991, ISSN: 0003-6935, 1539-4522. DOI: 10.1364/AO.30.000756. [Online]. Available: https://opg.optica.org/abstract.cfm?URI=ao-30-7-756 (visited on 01/15/2025).

[28] A. Hugi, R. Maulini, and J. Faist, "External cavity quantum cascade laser", *Semiconductor Science and Technology*, vol. 25, no. 8, p. 083 001, Aug. 2010, ISSN: 0268-1242, 1361-6641. DOI: 10.1088/0268-1242/25/8/083001. [Online]. Available:

https://iopscience.iop.org/article/10.1088/0268-1242/25/8/083001 (visited on 01/20/2025).

[29] G. Ricchiuti, A. Dabrowska, D. Pinto, G. Ramer, and B. Lendl, "Dual-Beam Photothermal Spectroscopy Employing a Mach–Zehnder Interferometer and an External Cavity Quantum Cascade Laser for Detection of Water Traces in Organic Solvents", en, *Analytical Chemistry*, vol. 94, no. 47, pp. 16 353–16 360, Nov. 2022, ISSN: 0003-2700, 1520-6882. DOI: 10.1021/acs.analchem.2c03303. [Online]. Available: https://pubs.acs.org/doi/10.1021/acs.analchem.2c03303 (visited on 01/20/2025).

[30] G. Ricchiuti *et al.*, "Photothermal spectroscopy on-chip sensor for the measurement of a PMMA film using a silicon nitride micro-ring resonator and an external cavity quantum cascade laser", en, *Nanophotonics*, vol. 13, no. 13, pp. 2417–2427, May 2024, ISSN: 2192-8614. DOI: 10.1515/nanoph-2024-0033. [Online]. Available: https://www.degruyter.com/document/doi/10.1515/nanoph-2024-0033/html (visited on 01/20/2025).

[31] A. A. Sifat, J. Jahng, and E. O. Potma, "Photo-induced force microscopy (PiFM) – principles and implementations", en, *Chemical Society Reviews*, vol. 51, no. 11, pp. 4208–4222, 2022, ISSN: 0306-0012, 1460-4744. DOI: 10.1039/D2CS00052K. [Online]. Available: https://xlink.rsc.org/?DOI=D2CS00052K (visited on 01/15/2025).

[32] M. Hippler, C. Mohr, K. A. Keen, and E. D. McNaghten, "Cavity-enhanced resonant photoacoustic spectroscopy with optical feedback cw diode lasers: A novel technique for ultratrace gas analysis and high-resolution spectroscopy", en, *The Journal of Chemical Physics*, vol. 133, no. 4, p. 044 308, Jul. 2010, ISSN: 0021-9606, 1089-7690. DOI: 10.1063/1.3461061. [Online]. Available: https://pubs.aip.org/jcp/article/133/4/044308/190490/Cavity-enhanced-resonant-photoacoustic (visited on 01/17/2025).

[33] P. Hodgson *et al.*, "Application of pulsed laser photoacoustic sensors in monitoring oil contamination in water", en, *Sensors and Actuators B: Chemical*, vol. 29, no. 1-3, pp. 339–344, Oct. 1995, ISSN: 09254005. DOI: 10.1016/0925-4005(95)01704-6. [Online]. Available: https://linkinghub.elsevier.com/retrieve/pii/0925400595017046 (visited on 01/17/2025).

[34] M. Born and E. Wolf, *Principles of optics: electromagnetic theory of propagation, interference and diffraction of light*, eng, 6th ed. Oxford New York: Pergamon Press, 1980, ISBN: 978-0-08-026482-0.

[35] B. E. A. Saleh and M. C. Teich, *Fundamentals of Photonics*, en, 1st ed. Wiley, Aug. 1991, ISBN: 978-0-471-83965-1. DOI: 10.1002/0471213748. [Online]. Available: https://onlinelibrary.wiley.com/doi/book/10.1002/0471213748 (visited on 01/23/2025).

[36] L. M. Miller and R. J. Smith, "Synchrotrons versus globars, point-detectors versus focal plane arrays: Selecting the best source and detector for specific infrared microspectroscopy and imaging applications", en, *Vibrational Spectroscopy*, vol. 38, no. 1-2, pp. 237–240, Jul. 2005, ISSN: 09242031. DOI: 10.1016/j.vibspec.2005.03.010. [Online]. Available: https://linkinghub.elsevier.com/retrieve/pii/S0924203105000676 (visited on 01/21/2025).

[37] K. Kadela *et al.*, "High-resolution infrared imaging performance of new high numerical aperture Schwarzschild objectives", en, *Spectrochimica Acta Part A: Molecular and Biomolecular Spectroscopy*, p. 125 769, Jan. 2025, ISSN: 13861425. DOI: 10.1016/j.saa.2025.125769. [Online]. Available: https://linkinghub.elsevier.com/retrieve/pii/S1386142525000757 (visited on 01/23/2025).

[38] G. Ramer and B. Lendl, "Attenuated Total Reflection Fourier Transform Infrared Spectroscopy", in *Encyclopedia of Analytical Chemistry*, R.A. Meyers and R.A. Meyers, Chichester, UK: John Wiley & Sons, Ltd, Mar. 2013, ISBN: 978-0-470-02731-8. DOI: 10.1002/9780470027318.a9287. [Online]. Available: http://doi.wiley.com/10.1002/9780470027318.a9287.

[39] S. G. Kazarian and K. L. A. Chan, "Micro- and Macro-Attenuated Total Reflection Fourier Transform Infrared Spectroscopic Imaging: Plenary Lecture at the 5th International Conference on Advanced Vibrational Spectroscopy, 2009, Melbourne, Australia", en, *Applied Spectroscopy*, vol. 64, no. 5, 135A–152A, May 2010, ISSN: 0003-7028, 1943-3530. DOI: 10.1366/000370210791211673. [Online]. Available: https://journals.sagepub.com/doi/10.1366/000370210791211673 (visited on 01/23/2025).

[40] Y. Bai *et al.*, "Ultrafast chemical imaging by widefield photothermal sensing of infrared absorption", en, *Science Advances*, vol. 5, no. 7, eaav7127, Jul. 2019, ISSN: 2375-2548. DOI: 10.1126/sciadv.aav7127. [Online]. Available: https://www.science.org/doi/10.1126/sciadv.aav7127 (visited on 01/21/2025).

[41] A. Marchetti *et al.*, "Novel optical photothermal infrared (O-PTIR) spectroscopy for the noninvasive characterization of heritage glass-metal objects", en, *Science Advances*, vol. 8, no. 9, eabl6769, Mar. 2022, ISSN: 2375-2548. DOI: 10.1126/sciadv.

abl6769. [Online]. Available: https://www.science.org/doi/10.1126/sciadv.abl6769 (visited on 01/21/2025).

[42] C. B. Prater, M. Kansiz, and J.-X. Cheng, "A tutorial on optical photothermal infrared (O-PTIR) microscopy", en, *APL Photonics*, vol. 9, no. 9, p. 091 101, Sep. 2024, ISSN: 2378-0967. DOI: 10.1063/5.0219983. [Online]. Available: https://pubs.aip.org/app/article/9/9/091101/3312368/A-tutorial-on-optical-photothermal-infrared-O-PTIR (visited on 04/01/2025).

[43] G. Binnig, C. F. Quate, and C. Gerber, "Atomic Force Microscope", en, *Physical Review Letters*, vol. 56, no. 9, pp. 930–933, Mar. 1986, ISSN: 0031-9007. DOI: 10.1103/PhysRevLett.56.930. [Online]. Available: https://link.aps.org/doi/10.1103/PhysRevLett.56.930 (visited on 07/19/2024).

[44] S. Kawai *et al.*, "Van der Waals interactions and the limits of isolated atom models at interfaces", en, *Nature Communications*, vol. 7, no. 1, p. 11 559, May 2016, ISSN: 2041-1723. DOI: 10.1038/ncomms11559. [Online]. Available: https://www.nature.com/articles/ncomms11559 (visited on 12/10/2024).

[45] N. Zhou *et al.*, "P-GaSe/N-$MoS_2$ Vertical Heterostructures Synthesized by van der Waals Epitaxy for Photoresponse Modulation", en, *Small*, vol. 14, no. 7, p. 1 702 731, Feb. 2018, ISSN: 1613-6810, 1613-6829. DOI: 10.1002/smll.201702731. [Online]. Available: https://onlinelibrary.wiley.com/doi/10.1002/smll.201702731 (visited on 12/10/2024).

[46] A. Centrone, "Infrared Imaging and Spectroscopy Beyond the Diffraction Limit", en, *Annual Review of Analytical Chemistry*, vol. 8, no. 1, pp. 101–126, Jul. 2015, ISSN: 1936-1327, 1936-1335. DOI: 10.1146/annurev-anchem-071114-040435. [Online]. Available: https://www.annualreviews.org/doi/10.1146/annurev-anchem-071114-040435 (visited on 08/14/2024).

[47] L.-Z. Cheong, W. Zhao, S. Song, and C. Shen, "Lab on a tip: Applications of functional atomic force microscopy for the study of electrical properties in biology", en, *Acta Biomaterialia*, vol. 99, pp. 33–52, Nov. 2019, ISSN: 17427061. DOI: 10.1016/j.actbio.2019.08.023. [Online]. Available: https://linkinghub.elsevier.com/retrieve/pii/S1742706119305793 (visited on 12/10/2024).

[48] P. J. Eaton and P. West, *Atomic force microscopy*, eng. Oxford: Oxford university press, 2018, ISBN: 978-0-19-882628-6.

[49] K. Iwata *et al.*, "Chemical structure imaging of a single molecule by atomic force microscopy at room temperature", en, *Nature Communications*, vol. 6, no. 1, p. 7766,

Jul. 2015, ISSN: 2041-1723. DOI: 10.1038/ncomms8766. [Online]. Available: https://www.nature.com/articles/ncomms8766 (visited on 04/02/2025).

[50] F. S. Ruggeri, B. Mannini, R. Schmid, M. Vendruscolo, and T. P. J. Knowles, "Single molecule secondary structure determination of proteins through infrared absorption nanospectroscopy", en, *Nature Communications*, vol. 11, no. 1, p. 2945, Jun. 2020, ISSN: 2041-1723. DOI: 10.1038/s41467-020-16728-1. [Online]. Available: https://www.nature.com/articles/s41467-020-16728-1 (visited on 04/02/2025).

[51] N. Ishida, "Atomic force microscopy", en, in *Non-Destructive Material Characterization Methods*, Elsevier, 2024, pp. 89–125, ISBN: 978-0-323-91150-4. DOI: 10.1016/B978-0-323-91150-4.00011-2. [Online]. Available: https://linkinghub.elsevier.com/retrieve/pii/B9780323911504000112 (visited on 03/28/2025).

[52] C. Gerber and H. P. Lang, "How the doors to the nanoworld were opened", en, *Nature Nanotechnology*, vol. 1, no. 1, pp. 3–5, Oct. 2006, ISSN: 1748-3387, 1748-3395. DOI: 10.1038/nnano.2006.70. [Online]. Available: https://www.nature.com/articles/nnano.2006.70 (visited on 10/07/2024).

[53] W. Bao *et al.*, "Mapping Local Charge Recombination Heterogeneity by Multidimensional Nanospectroscopic Imaging", en, *Science*, vol. 338, no. 6112, pp. 1317–1321, Dec. 2012, ISSN: 0036-8075, 1095-9203. DOI: 10.1126/science.1227977. [Online]. Available: https://www.science.org/doi/10.1126/science.1227977 (visited on 10/07/2024).

[54] L. Baldassarre *et al.*, "Mapping the amide I absorption in single bacteria and mammalian cells with resonant infrared nanospectroscopy", *Nanotechnology*, vol. 27, no. 7, p. 075 101, Feb. 2016, ISSN: 0957-4484, 1361-6528. DOI: 10.1088/0957-4484/27/7/075101. [Online]. Available: https://iopscience.iop.org/article/10.1088/0957-4484/27/7/075101 (visited on 09/02/2024).

[55] Y. F. Dufrêne *et al.*, "Imaging modes of atomic force microscopy for application in molecular and cell biology", en, *Nature Nanotechnology*, vol. 12, no. 4, pp. 295–307, Apr. 2017, ISSN: 1748-3387, 1748-3395. DOI: 10.1038/nnano.2017.45. [Online]. Available: https://www.nature.com/articles/nnano.2017.45 (visited on 10/07/2024).

[56] A. Laraoui, H. Aycock-Rizzo, Y. Gao, X. Lu, E. Riedo, and C. A. Meriles, "Imaging thermal conductivity with nanoscale resolution using a scanning spin probe", en, *Nature Communications*, vol. 6, no. 1, p. 8954, Nov. 2015, ISSN: 2041-1723. DOI: 10.1038/ncomms9954. [Online]. Available: https://www.nature.com/articles/ncomms9954 (visited on 12/10/2024).

[57] S. Y. Leblebici *et al.*, "Facet-dependent photovoltaic efficiency variations in single grains of hybrid halide perovskite", en, *Nature Energy*, vol. 1, no. 8, p. 16 093, Jul. 2016, ISSN: 2058-7546. DOI: 10.1038/nenergy.2016.93. [Online]. Available: https://www.nature.com/articles/nenergy201693 (visited on 12/10/2024).

[58] F. Rico, L. Gonzalez, I. Casuso, M. Puig-Vidal, and S. Scheuring, "High-Speed Force Spectroscopy Unfolds Titin at the Velocity of Molecular Dynamics Simulations", en, *Science*, vol. 342, no. 6159, pp. 741–743, Nov. 2013, ISSN: 0036-8075, 1095-9203. DOI: 10.1126/science.1239764. [Online]. Available: https://www.science.org/doi/10.1126/science.1239764 (visited on 08/08/2024).

[59] T.-W. Lu and P.-T. Lee, "Ultra-high sensitivity optical stress sensor based on double-layered photonic crystal microcavity", en, *Optics Express*, vol. 17, no. 3, p. 1518, Feb. 2009, ISSN: 1094-4087. DOI: 10.1364/OE.17.001518. [Online]. Available: https://opg.optica.org/oe/abstract.cfm?uri=oe-17-3-1518 (visited on 10/23/2024).

[60] M. H. Korayem, S. Zafari, A. Amanati, M. Damircheli, and N. Ebrahimi, "Analysis and control of micro-cantilever in dynamic mode AFM", en, *The International Journal of Advanced Manufacturing Technology*, vol. 50, no. 9-12, pp. 979–990, Oct. 2010, ISSN: 0268-3768, 1433-3015. DOI: 10.1007/s00170-010-2588-4. [Online]. Available: http://link.springer.com/10.1007/s00170-010-2588-4 (visited on 01/23/2025).

[61] N. Hosseini, A. P. Nievergelt, J. D. Adams, V. T. Stavrov, and G. E. Fantner, "A monolithic MEMS position sensor for closed-loop high-speed atomic force microscopy", *Nanotechnology*, vol. 27, no. 13, p. 135 705, Apr. 2016, ISSN: 0957-4484, 1361-6528. DOI: 10.1088/0957-4484/27/13/135705. [Online]. Available: https://iopscience.iop.org/article/10.1088/0957-4484/27/13/135705 (visited on 01/23/2025).

[62] P. J. Eaton and P. West, *Atomic force microscopy*, en. Oxford ; New York: Oxford University Press, 2010, OCLC: ocn455831540, ISBN: 978-0-19-957045-4.

[63] G. Binnig, C. F. Quate, and C. Gerber, "Atomic Force Microscope", en, *Physical Review Letters*, vol. 56, no. 9, pp. 930–933, Mar. 1986, ISSN: 0031-9007. DOI: 10.1103/PhysRevLett.56.930. [Online]. Available: https://link.aps.org/doi/10.1103/PhysRevLett.56.930 (visited on 07/26/2024).

[64] H.-J. Butt, B. Cappella, and M. Kappl, "Force measurements with the atomic force microscope: Technique, interpretation and applications", en, *Surface Science Reports*, vol. 59, no. 1-6, pp. 1–152, Oct. 2005, ISSN: 01675729. DOI: 10.1016/j.

surfrep.2005.08.003. [Online]. Available: https://linkinghub.elsevier.com/retrieve/pii/S0167572905000488 (visited on 04/02/2025).

[65] R. García, "Dynamic atomic force microscopy methods", *Surface Science Reports*, vol. 47, no. 6-8, pp. 197–301, Sep. 2002, ISSN: 01675729. DOI: 10.1016/S0167-5729(02)00077-8. [Online]. Available: https://linkinghub.elsevier.com/retrieve/pii/S0167572902000778 (visited on 03/28/2025).

[66] I. Carlucho, M. De Paula, S. A. Villar, and G. G. Acosta, "Incremental Q -learning strategy for adaptive PID control of mobile robots", en, *Expert Systems with Applications*, vol. 80, pp. 183–199, Sep. 2017, ISSN: 09574174. DOI: 10.1016/j.eswa.2017.03.002. [Online]. Available: https://linkinghub.elsevier.com/retrieve/pii/S0957417417301513 (visited on 01/23/2025).

[67] H. Liu *et al.*, "Intelligent tuning method of PID parameters based on iterative learning control for atomic force microscopy", en, *Micron*, vol. 104, pp. 26–36, Jan. 2018, ISSN: 09684328. DOI: 10.1016/j.micron.2017.09.009. [Online]. Available: https://linkinghub.elsevier.com/retrieve/pii/S0968432817303074 (visited on 01/23/2025).

[68] D.-A. Mendels *et al.*, "Dynamic properties of AFM cantilevers and the calibration of their spring constants", *Journal of Micromechanics and Microengineering*, vol. 16, no. 8, pp. 1720–1733, Aug. 2006, ISSN: 0960-1317, 1361-6439. DOI: 10.1088/0960-1317/16/8/037. [Online]. Available: https://iopscience.iop.org/article/10.1088/0960-1317/16/8/037 (visited on 08/02/2024).

[69] U. Rabe, J. Turner, and W. Arnold, "Analysis of the high-frequency response of atomic force microscope cantilevers", en, *Applied Physics A*, vol. 66, no. 1, S277–S282, Mar. 1998, ISSN: 1432-0630. DOI: 10.1007/s003390051145. [Online]. Available: https://doi.org/10.1007/s003390051145 (visited on 05/15/2024).

[70] A. D. Polyanin and V. F. Zaitsev, *Handbook of Ordinary Differential Equations*, en, 0th ed. Chapman and Hall/CRC, Nov. 2017, ISBN: 978-1-4665-6940-9. DOI: 10.1201/9781315117638. [Online]. Available: https://www.taylorfrancis.com/books/9781466569409 (visited on 04/02/2025).

[71] M.-H. Bao, "Basic mechanics of beam and diaphragm structures", en, in *Handbook of Sensors and Actuators*, vol. 8, Elsevier, 2000, pp. 23–88, ISBN: 978-0-444-50558-3. DOI: 10.1016/S1386-2766(00)80016-X. [Online]. Available: https://linkinghub.elsevier.com/retrieve/pii/S138627660080016X (visited on 04/03/2025).

[72] Q. Yu, G. Qin, C. Darne, C. Cai, W. Wosik, and S.-S. Pei, "Fabrication of short and thin silicon cantilevers for AFM with SOI wafers", en, *Sensors and Actuators A: Physical*, vol. 126, no. 2, pp. 369–374, Feb. 2006, ISSN: 09244247. DOI: 10.1016/j.sna.2005.10.019. [Online]. Available: https://linkinghub.elsevier.com/retrieve/pii/S0924424705005911 (visited on 01/15/2025).

[73] M. B. Viani, T. E. Schäffer, A. Chand, M. Rief, H. E. Gaub, and P. K. Hansma, "Small cantilevers for force spectroscopy of single molecules", en, *Journal of Applied Physics*, vol. 86, no. 4, pp. 2258–2262, Aug. 1999, ISSN: 0021-8979, 1089-7550. DOI: 10.1063/1.371039. [Online]. Available: https://pubs.aip.org/jap/article/86/4/2258/487604/Small-cantilevers-for-force-spectroscopy-of-single (visited on 01/15/2025).

[74] A. V. Novak, V. R. Novak, A. A. Dedkova, and E. E. Gusev, "Dependence of Mechanical Stresses in Silicon Nitride Films on the Mode of Plasma-Enhanced Chemical Vapor Deposition", en, *Semiconductors*, vol. 52, no. 15, pp. 1953–1957, Dec. 2018, ISSN: 1063-7826, 1090-6479. DOI: 10.1134/S1063782618150095. [Online]. Available: http://link.springer.com/10.1134/S1063782618150095 (visited on 03/28/2025).

[75] I. Lampouras, M. Holz, S. Strehle, and J. Körner, "Precisely controlled batch-fabrication of highly sensitive co-resonant cantilever sensors from silicon-nitride", *Journal of Micromechanics and Microengineering*, vol. 34, no. 1, p. 015 005, Jan. 2024, ISSN: 0960-1317, 1361-6439. DOI: 10.1088/1361-6439/ad0d80. [Online]. Available: https://iopscience.iop.org/article/10.1088/1361-6439/ad0d80 (visited on 03/28/2025).

[76] K. I. Schiffmann, "Investigation of fabrication parameters for the electron-beam-induced deposition of contamination tips used in atomic force microscopy", *Nanotechnology*, vol. 4, no. 3, pp. 163–169, Jul. 1993, ISSN: 0957-4484, 1361-6528. DOI: 10.1088/0957-4484/4/3/006. [Online]. Available: https://iopscience.iop.org/article/10.1088/0957-4484/4/3/006 (visited on 01/15/2025).

[77] A. Folch, M. Wrighton, and M. Schmidt, "Microfabrication of oxidation-sharpened silicon tips on silicon nitride cantilevers for atomic force microscopy", *Journal of Microelectromechanical Systems*, vol. 6, no. 4, pp. 303–306, Dec. 1997, ISSN: 10577157. DOI: 10.1109/84.650126. [Online]. Available: http://ieeexplore.ieee.org/document/650126/ (visited on 01/15/2025).

[78] P. Systems, "AFM Probe Selection Guide", Park Systems, Brochure / Technical Guide (optional, in "Extra" field), 2019. [Online]. Available: https://www.

parksystems.com/images/media/brochures/probe/Park_AFM_ProbeGuide_190620E32AB.pdf (visited on 04/04/2025).

[79] B. Derjaguin, V. Muller, and Y. Toporov, "Effect of contact deformations on the adhesion of particles", en, *Journal of Colloid and Interface Science*, vol. 53, no. 2, pp. 314–326, Nov. 1975, ISSN: 00219797. DOI: 10.1016/0021-9797(75)90018-1. [Online]. Available: https://linkinghub.elsevier.com/retrieve/pii/0021979775900181 (visited on 01/24/2025).

[80] G. J. Verbiest, T. H. Oosterkamp, and M. J. Rost, "Cantilever dynamics in heterodyne force microscopy", *Ultramicroscopy*, vol. 135, pp. 113–120, Dec. 2013, ISSN: 0304-3991. DOI: 10.1016/j.ultramic.2013.07.008. [Online]. Available: https://www.sciencedirect.com/science/article/pii/S0304399113001940 (visited on 03/01/2024).

[81] Y. Seo and W. Jhe, "Atomic force microscopy and spectroscopy", *Reports on Progress in Physics*, vol. 71, no. 1, p. 016 101, Jan. 2008, ISSN: 0034-4885, 1361-6633. DOI: 10.1088/0034-4885/71/1/016101. [Online]. Available: https://iopscience.iop.org/article/10.1088/0034-4885/71/1/016101 (visited on 01/30/2025).

[82] M. D. A. Norman, S. A. Ferreira, G. M. Jowett, L. Bozec, and E. Gentleman, "Measuring the elastic modulus of soft culture surfaces and three-dimensional hydrogels using atomic force microscopy", en, *Nature Protocols*, vol. 16, no. 5, pp. 2418–2449, May 2021, ISSN: 1754-2189, 1750-2799. DOI: 10.1038/s41596-021-00495-4. [Online]. Available: https://www.nature.com/articles/s41596-021-00495-4 (visited on 12/16/2024).

[83] J. H. Cantrell and S. A. Cantrell, "Analytical model of the nonlinear dynamics of cantilever tip-sample surface interactions for various acoustic atomic force microscopies", en, *Physical Review B*, vol. 77, no. 16, p. 165 409, Apr. 2008, ISSN: 1098-0121, 1550-235X. DOI: 10.1103/PhysRevB.77.165409. [Online]. Available: https://link.aps.org/doi/10.1103/PhysRevB.77.165409 (visited on 01/30/2025).

[84] C. Möller, M. Allen, V. Elings, A. Engel, and D. J. Müller, "Tapping-Mode Atomic Force Microscopy Produces Faithful High-Resolution Images of Protein Surfaces", en, *Biophysical Journal*, vol. 77, no. 2, pp. 1150–1158, Aug. 1999, ISSN: 00063495. DOI: 10.1016/S0006-3495(99)76966-3. [Online]. Available: https://linkinghub.elsevier.com/retrieve/pii/S0006349599769663 (visited on 04/03/2025).

[85] D. H. Cho, S. Aguayo, and A. X. Cartagena-Rivera, "Atomic force microscopy-mediated mechanobiological profiling of complex human tissues", en, *Biomaterials*, vol. 303, p. 122 389, Dec. 2023, ISSN: 01429612. DOI: 10.1016/j.biomaterials.2023.122389. [Online]. Available: https://linkinghub.elsevier.com/retrieve/pii/S0142961223003976 (visited on 04/03/2025).

[86] P. Attard, "Measurement and interpretation of elastic and viscoelastic properties with the atomic force microscope", *Journal of Physics: Condensed Matter*, vol. 19, no. 47, p. 473 201, Nov. 2007, ISSN: 0953-8984, 1361-648X. DOI: 10.1088/0953-8984/19/47/473201. [Online]. Available: https://iopscience.iop.org/article/10.1088/0953-8984/19/47/473201 (visited on 04/03/2025).

[87] A. F. Payam, D. Martin-Jimenez, and R. Garcia, "Force reconstruction from tapping mode force microscopy experiments", *Nanotechnology*, vol. 26, no. 18, p. 185 706, May 2015, ISSN: 0957-4484, 1361-6528. DOI: 10.1088/0957-4484/26/18/185706. [Online]. Available: https://iopscience.iop.org/article/10.1088/0957-4484/26/18/185706 (visited on 04/03/2025).

[88] A. M. Katzenmeyer, G. Holland, J. Chae, A. Band, K. Kjoller, and A. Centrone, "Mid-infrared spectroscopy beyond the diffraction limit via direct measurement of the photothermal effect", en, *Nanoscale*, vol. 7, no. 42, pp. 17 637–17 641, 2015, ISSN: 2040-3364, 2040-3372. DOI: 10.1039/C5NR04854K. [Online]. Available: https://xlink.rsc.org/?DOI=C5NR04854K (visited on 08/14/2024).

[89] A. Dazzi, C. B. Prater, Q. Hu, D. B. Chase, J. F. Rabolt, and C. Marcott, "AFM–IR: Combining Atomic Force Microscopy and Infrared Spectroscopy for Nanoscale Chemical Characterization", en, *Applied Spectroscopy*, vol. 66, no. 12, pp. 1365–1384, Dec. 2012, ISSN: 0003-7028, 1943-3530. DOI: 10.1366/12-06804. [Online]. Available: http://journals.sagepub.com/doi/10.1366/12-06804 (visited on 09/20/2022).

[90] A. C. V. Dos Santos, B. Lendl, and G. Ramer, "Systematic analysis and nanoscale chemical imaging of polymers using photothermal-induced resonance (AFM-IR) infrared spectroscopy", en, *Polymer Testing*, vol. 106, p. 107 443, Feb. 2022, ISSN: 01429418. DOI: 10.1016/j.polymertesting.2021.107443. [Online]. Available: https://linkinghub.elsevier.com/retrieve/pii/S014294182100386X (visited on 01/30/2025).

[91] J. Chae *et al.*, "Nanophotonic Atomic Force Microscope Transducers Enable Chemical Composition and Thermal Conductivity Measurements at the Nanoscale", en, *Nano Letters*, vol. 17, no. 9, pp. 5587–5594, Sep. 2017, ISSN: 1530-6984, 1530-6992.

DOI: 10.1021/acs.nanolett.7b02404. [Online]. Available: https://pubs.acs.org/doi/10.1021/acs.nanolett.7b02404 (visited on 08/14/2024).

[92] G. Ramer, V. A. Aksyuk, and A. Centrone, "Quantitative Chemical Analysis at the Nanoscale Using the Photothermal Induced Resonance Technique", en, *Analytical Chemistry*, vol. 89, no. 24, pp. 13 524–13 531, Dec. 2017, ISSN: 0003-2700, 1520-6882. DOI: 10.1021/acs.analchem.7b03878. [Online]. Available: https://pubs.acs.org/doi/10.1021/acs.analchem.7b03878 (visited on 12/14/2021).

[93] A. Dazzi, R. Prazeres, F. Glotin, and J. M. Ortega, "Local infrared microspectroscopy with subwavelength spatial resolution with an atomic force microscope tip used as a photothermal sensor", en, *Optics Letters*, vol. 30, no. 18, p. 2388, Sep. 2005, ISSN: 0146-9592, 1539-4794. DOI: 10.1364/OL.30.002388. [Online]. Available: https://opg.optica.org/abstract.cfm?URI=ol-30-18-2388 (visited on 02/03/2025).

[94] D. Kurouski, A. Dazzi, R. Zenobi, and A. Centrone, "Infrared and Raman chemical imaging and spectroscopy at the nanoscale", en, *Chemical Society Reviews*, vol. 49, no. 11, pp. 3315–3347, 2020, ISSN: 0306-0012, 1460-4744. DOI: 10.1039/C8CS00916C. [Online]. Available: https://xlink.rsc.org/?DOI=C8CS00916C (visited on 02/03/2025).

[95] K. Wieland, G. Ramer, V. U. Weiss, G. Allmaier, B. Lendl, and A. Centrone, "Nanoscale chemical imaging of individual chemotherapeutic cytarabine-loaded liposomal nanocarriers", en, *Nano Research*, vol. 12, no. 1, pp. 197–203, Jan. 2019, ISSN: 1998-0124, 1998-0000. DOI: 10.1007/s12274-018-2202-x. [Online]. Available: http://link.springer.com/10.1007/s12274-018-2202-x (visited on 01/20/2025).

[96] A. C. V. D. Dos Santos, D. Tranchida, B. Lendl, and G. Ramer, "Nanoscale chemical characterization of a post-consumer recycled polyolefin blend using tapping mode AFM-IR", en, *The Analyst*, vol. 147, no. 16, pp. 3741–3747, 2022, ISSN: 0003-2654, 1364-5528. DOI: 10.1039/D2AN00823H. [Online]. Available: https://xlink.rsc.org/?DOI=D2AN00823H (visited on 01/30/2025).

[97] F. Tang, P. Bao, and Z. Su, "Analysis of Nanodomain Composition in High-Impact Polypropylene by Atomic Force Microscopy-Infrared", en, *Analytical Chemistry*, vol. 88, no. 9, pp. 4926–4930, May 2016, ISSN: 0003-2700, 1520-6882. DOI: 10.1021/acs.analchem.6b00798. [Online]. Available: https://pubs.acs.org/doi/10.1021/acs.analchem.6b00798 (visited on 11/27/2022).

[98] A. Dazzi, R. Prazeres, F. Glotin, J. Ortega, M. Al-Sawaftah, and M. De Frutos, "Chemical mapping of the distribution of viruses into infected bacteria with a photothermal method", en, *Ultramicroscopy*, vol. 108, no. 7, pp. 635–641, Jun. 2008, ISSN: 03043991. DOI: 10.1016/j.ultramic.2007.10.008. [Online]. Available: https://linkinghub.elsevier.com/retrieve/pii/S0304399107002288 (visited on 01/30/2025).

[99] Y. Yuan *et al.*, "Photovoltaic Switching Mechanism in Lateral Structure Hybrid Perovskite Solar Cells", en, *Advanced Energy Materials*, vol. 5, no. 15, p. 1 500 615, Aug. 2015, ISSN: 1614-6832, 1614-6840. DOI: 10.1002/aenm.201500615. [Online]. Available: https://onlinelibrary.wiley.com/doi/10.1002/aenm.201500615 (visited on 01/30/2025).

[100] J. Houel *et al.*, "Ultraweak-Absorption Microscopy of a Single Semiconductor Quantum Dot in the Midinfrared Range", en, *Physical Review Letters*, vol. 99, no. 21, p. 217 404, Nov. 2007, ISSN: 0031-9007, 1079-7114. DOI: 10.1103/PhysRevLett.99.217404. [Online]. Available: https://link.aps.org/doi/10.1103/PhysRevLett.99.217404 (visited on 11/27/2022).

[101] F. Lu and M. A. Belkin, "Infrared absorption nano-spectroscopy using sample photoexpansion induced by tunable quantum cascade lasers", en, *Optics Express*, vol. 19, no. 21, p. 19 942, Oct. 2011, ISSN: 1094-4087. DOI: 10.1364/OE.19.019942. [Online]. Available: https://opg.optica.org/oe/abstract.cfm?uri=oe-19-21-19942 (visited on 02/03/2025).

[102] M. Wang *et al.*, "High Throughput Nanoimaging of Thermal Conductivity and Interfacial Thermal Conductance", en, *Nano Letters*, vol. 22, no. 11, pp. 4325–4332, Jun. 2022, ISSN: 1530-6984, 1530-6992. DOI: 10.1021/acs.nanolett.2c00337. [Online]. Available: https://pubs.acs.org/doi/10.1021/acs.nanolett.2c00337 (visited on 08/14/2024).

[103] Y. Zhang, U. Yilmaz, G. V. B. Lukasievicz, L. O'Faolain, B. Lendl, and G. Ramer, "An analytical model of label-free nanoscale chemical imaging reveals avenues toward improved spatial resolution and sensitivity", en, *Proceedings of the National Academy of Sciences*, vol. 122, no. 4, e2403079122, Jan. 2025, ISSN: 0027-8424, 1091-6490. DOI: 10.1073/pnas.2403079122. [Online]. Available: https://pnas.org/doi/10.1073/pnas.2403079122 (visited on 01/27/2025).

[104] A. M. Katzenmeyer, V. Aksyuk, and A. Centrone, "Nanoscale Infrared Spectroscopy: Improving the Spectral Range of the Photothermal Induced Resonance Technique", en, *Analytical Chemistry*, vol. 85, no. 4, pp. 1972–1979, Feb. 2013,

ISSN: 0003-2700, 1520-6882. DOI: 10.1021/ac303620y. [Online]. Available: https://pubs.acs.org/doi/10.1021/ac303620y (visited on 04/04/2025).

[105] L. V. Brown *et al.*, "Nanoscale Mapping and Spectroscopy of Nonradiative Hyperbolic Modes in Hexagonal Boron Nitride Nanostructures", en, *Nano Letters*, vol. 18, no. 3, pp. 1628–1636, Mar. 2018, ISSN: 1530-6984, 1530-6992. DOI: 10.1021/acs.nanolett.7b04476. [Online]. Available: https://pubs.acs.org/doi/10.1021/acs.nanolett.7b04476 (visited on 04/04/2025).

[106] A. M. Katzenmeyer, G. Holland, K. Kjoller, and A. Centrone, "Absorption Spectroscopy and Imaging from the Visible through Mid-Infrared with 20 nm Resolution", en, *Analytical Chemistry*, vol. 87, no. 6, pp. 3154–3159, Mar. 2015, ISSN: 0003-2700, 1520-6882. DOI: 10.1021/ac504672t. [Online]. Available: https://pubs.acs.org/doi/10.1021/ac504672t (visited on 02/03/2025).

[107] J. Lübbe *et al.*, "Achieving high effective $Q$ -factors in ultra-high vacuum dynamic force microscopy", *Measurement Science and Technology*, vol. 21, no. 12, p. 125 501, Dec. 2010, ISSN: 0957-0233, 1361-6501. DOI: 10.1088/0957-0233/21/12/125501. [Online]. Available: https://iopscience.iop.org/article/10.1088/0957-0233/21/12/125501 (visited on 04/04/2025).

[108] J. Lübbe, M. Temmen, H. Schnieder, and M. Reichling, "Measurement and modelling of non-contact atomic force microscope cantilever properties from ultra-high vacuum to normal pressure conditions", *Measurement Science and Technology*, vol. 22, no. 5, p. 055 501, May 2011, ISSN: 0957-0233, 1361-6501. DOI: 10.1088/0957-0233/22/5/055501. [Online]. Available: https://iopscience.iop.org/article/10.1088/0957-0233/22/5/055501 (visited on 04/04/2025).

[109] C. T. Gibson, B. L. Weeks, J. R. I. Lee, C. Abell, and T. Rayment, "A nondestructive technique for determining the spring constant of atomic force microscope cantilevers", en, *Review of Scientific Instruments*, vol. 72, no. 5, pp. 2340–2343, May 2001, ISSN: 0034-6748, 1089-7623. DOI: 10.1063/1.1361080. [Online]. Available: https://pubs.aip.org/rsi/article/72/5/2340/350172/A-nondestructive-technique-for-determining-the (visited on 04/04/2025).

[110] G. Ramer, F. Reisenbauer, B. Steindl, W. Tomischko, and B. Lendl, "Implementation of Resonance Tracking for Assuring Reliability in Resonance Enhanced Photothermal Infrared Spectroscopy and Imaging", en, *Applied Spectroscopy*, vol. 71, no. 8, pp. 2013–2020, Aug. 2017, ISSN: 0003-7028, 1943-3530. DOI: 10.1177/0003702817695290. [Online]. Available: http://journals.sagepub.com/doi/10.1177/0003702817695290 (visited on 02/03/2025).

[111] M. Tuteja, M. Kang, C. Leal, and A. Centrone, "Nanoscale partitioning of paclitaxel in hybrid lipid–polymer membranes", en, *The Analyst*, vol. 143, no. 16, pp. 3808–3813, 2018, ISSN: 0003-2654, 1364-5528. DOI: 10.1039/C8AN00838H. [Online]. Available: https://xlink.rsc.org/?DOI=C8AN00838H (visited on 12/17/2024).

[112] X. Ma *et al.*, "Revealing the Distribution of Metal Carboxylates in Oil Paint from the Micro- to Nanoscale", en, *Angewandte Chemie International Edition*, vol. 58, no. 34, pp. 11 652–11 656, Aug. 2019, ISSN: 1433-7851, 1521-3773. DOI: 10.1002/anie.201903553. [Online]. Available: https://onlinelibrary.wiley.com/doi/10.1002/anie.201903553 (visited on 01/07/2025).

[113] G. Verbiest and M. Rost, "Beating beats mixing in heterodyne detection schemes", en, *Nature Communications*, vol. 6, no. 1, p. 6444, Mar. 2015, ISSN: 2041-1723. DOI: 10.1038/ncomms7444. [Online]. Available: https://www.nature.com/articles/ncomms7444 (visited on 02/05/2025).

[114] J. Mathurin *et al.*, "How to unravel the chemical structure and component localization of individual drug-loaded polymeric nanoparticles by using tapping AFM-IR", en, *The Analyst*, vol. 143, no. 24, pp. 5940–5949, 2018, ISSN: 0003-2654, 1364-5528. DOI: 10.1039/C8AN01239C. [Online]. Available: https://xlink.rsc.org/?DOI=C8AN01239C (visited on 03/28/2025).

[115] G. Ramer *et al.*, "High- $Q$ dark hyperbolic phonon-polaritons in hexagonal boron nitride nanostructures", en, *Nanophotonics*, vol. 9, no. 6, pp. 1457–1467, Jun. 2020, ISSN: 2192-8614, 2192-8606. DOI: 10.1515/nanoph-2020-0048. [Online]. Available: https://www.degruyter.com/document/doi/10.1515/nanoph-2020-0048/html (visited on 03/28/2025).

[116] T. Ando, N. Kodera, E. Takai, D. Maruyama, K. Saito, and A. Toda, "A high-speed atomic force microscope for studying biological macromolecules", en, *Proceedings of the National Academy of Sciences*, vol. 98, no. 22, pp. 12 468–12 472, Oct. 2001, ISSN: 0027-8424, 1091-6490. DOI: 10.1073/pnas.211400898. [Online]. Available: https://pnas.org/doi/full/10.1073/pnas.211400898 (visited on 02/25/2025).

[117] G. Meyer and N. M. Amer, "Novel optical approach to atomic force microscopy", en, *Applied Physics Letters*, vol. 53, no. 12, pp. 1045–1047, Sep. 1988, ISSN: 0003-6951, 1077-3118. DOI: 10.1063/1.100061. [Online]. Available: https://pubs.aip.org/apl/article/53/12/1045/54207/Novel-optical-approach-to-atomic-force-microscopy (visited on 10/23/2024).

[118] H. Sadeghian, R. Herfst, B. Dekker, J. Winters, T. Bijnagte, and R. Rijnbeek, "High-throughput atomic force microscopes operating in parallel", en, *Review of Scientific Instruments*, vol. 88, no. 3, p. 033 703, Mar. 2017, ISSN: 0034-6748, 1089-7623. DOI: 10.1063/1.4978285. [Online]. Available: https://pubs.aip.org/rsi/article/88/3/033703/1021074/High-throughput-atomic-force-microscopes-operating (visited on 07/29/2024).

[119] S.-H. " Lim, D. Raorane, S. Satyanarayana, and A. Majumdar, "Nano-chemo-mechanical sensor array platform for high-throughput chemical analysis", en, *Sensors and Actuators B: Chemical*, vol. 119, no. 2, pp. 466–474, Dec. 2006, ISSN: 09254005. DOI: 10.1016/j.snb.2006.01.032. [Online]. Available: https://linkinghub.elsevier.com/retrieve/pii/S0925400506000141 (visited on 10/23/2024).

[120] T. R. Albrecht, P. Grütter, D. Horne, and D. Rugar, "Frequency modulation detection using high- $Q$ cantilevers for enhanced force microscope sensitivity", en, *Journal of Applied Physics*, vol. 69, no. 2, pp. 668–673, Jan. 1991, ISSN: 0021-8979, 1089-7550. DOI: 10.1063/1.347347. [Online]. Available: https://pubs.aip.org/jap/article/69/2/668/19814/Frequency-modulation-detection-using-high-Q (visited on 02/25/2025).

[121] T. Kouh, D. Karabacak, D. H. Kim, and K. L. Ekinci, "Diffraction effects in optical interferometric displacement detection in nanoelectromechanical systems", en, *Applied Physics Letters*, vol. 86, no. 1, p. 013 106, Jan. 2005, ISSN: 0003-6951, 1077-3118. DOI: 10.1063/1.1843289. [Online]. Available: https://pubs.aip.org/apl/article/86/1/013106/568148/Diffraction-effects-in-optical-interferometric (visited on 07/29/2024).

[122] C. Braunsmann, J. Seifert, J. Rheinlaender, and T. E. Schäffer, "High-speed force mapping on living cells with a small cantilever atomic force microscope", en, *Review of Scientific Instruments*, vol. 85, no. 7, p. 073 703, Jul. 2014, ISSN: 0034-6748, 1089-7623. DOI: 10.1063/1.4885464. [Online]. Available: https://pubs.aip.org/rsi/article/85/7/073703/355839/High-speed-force-mapping-on-living-cells-with-a (visited on 02/25/2025).

[123] J. J. Schwartz, G. Pavlidis, and A. Centrone, "Understanding Cantilever Transduction Efficiency and Spatial Resolution in Nanoscale Infrared Microscopy", *Analytical Chemistry*, vol. 94, no. 38, pp. 13 126–13 135, Sep. 2022, Publisher: American Chemical Society, ISSN: 0003-2700. DOI: 10.1021/acs.analchem.2c02612. [On-

line]. Available: https://doi.org/10.1021/acs.analchem.2c02612 (visited on 01/28/2025).

[124] A. C. V. D. Dos Santos *et al.*, "Nanoscale Infrared Spectroscopy and Chemometrics Enable Detection of Intracellular Protein Distribution", en, *Analytical Chemistry*, vol. 92, no. 24, pp. 15 719–15 725, Dec. 2020, ISSN: 0003-2700, 1520-6882. DOI: 10.1021/acs.analchem.0c02228. [Online]. Available: https://pubs.acs.org/doi/10.1021/acs.analchem.0c02228 (visited on 01/30/2025).

[125] X. Ma, G. Pavlidis, E. Dillon, K. Kjoller, B. Berrie, and A. Centrone, "Nanoscale IR spectroscopy: From Principles to Nanoscale Imaging and Identification of Metal Soaps", en, *Microscopy and Microanalysis*, vol. 27, no. S1, pp. 2814–2815, Aug. 2021, ISSN: 1431-9276, 1435-8115. DOI: 10.1017/S1431927621009831. [Online]. Available: https://academic.oup.com/mam/article/27/S1/2814/6888511 (visited on 11/30/2023).

[126] S. Kenkel *et al.*, "Chemical imaging of cellular ultrastructure by null-deflection infrared spectroscopic measurements", *Proceedings of the National Academy of Sciences*, vol. 119, no. 47, e2210516119, Nov. 2022, Publisher: Proceedings of the National Academy of Sciences. DOI: 10.1073/pnas.2210516119. [Online]. Available: https://www.pnas.org/doi/10.1073/pnas.2210516119 (visited on 03/04/2024).

[127] M. Aspelmeyer, T. J. Kippenberg, and F. Marquardt, "Cavity optomechanics", en, *Reviews of Modern Physics*, vol. 86, no. 4, pp. 1391–1452, Dec. 2014, ISSN: 0034-6861, 1539-0756. DOI: 10.1103/RevModPhys.86.1391. [Online]. Available: https://link.aps.org/doi/10.1103/RevModPhys.86.1391 (visited on 07/29/2024).

[128] D. Van Thourhout and J. Roels, "Optomechanical device actuation through the optical gradient force", en, *Nature Photonics*, vol. 4, no. 4, pp. 211–217, Apr. 2010, ISSN: 1749-4885, 1749-4893. DOI: 10.1038/nphoton.2010.72. [Online]. Available: https://www.nature.com/articles/nphoton.2010.72 (visited on 10/23/2024).

[129] I. Favero and K. Karrai, "Optomechanics of deformable optical cavities", en, *Nature Photonics*, vol. 3, no. 4, pp. 201–205, Apr. 2009, ISSN: 1749-4885, 1749-4893. DOI: 10.1038/nphoton.2009.42. [Online]. Available: https://www.nature.com/articles/nphoton.2009.42 (visited on 07/29/2024).

[130] A. Clerk, "Facing Heisenberg at the nanoscale", en, *Nature Nanotechnology*, vol. 4, no. 12, pp. 796–798, Dec. 2009, ISSN: 1748-3387, 1748-3395. DOI: 10.1038/nnano.2009.368. [Online]. Available: https://www.nature.com/articles/nnano.2009.368 (visited on 07/29/2024).

[131] M. Eichenfield, R. Camacho, J. Chan, K. J. Vahala, and O. Painter, "A picogram- and nanometre-scale photonic-crystal optomechanical cavity", en, *Nature*, vol. 459, no. 7246, pp. 550–555, May 2009, ISSN: 0028-0836, 1476-4687. DOI: 10.1038/nature08061. [Online]. Available: https://www.nature.com/articles/nature08061 (visited on 07/29/2024).

[132] G. Anetsberger *et al.*, "Near-field cavity optomechanics with nanomechanical oscillators", en, *Nature Physics*, vol. 5, no. 12, pp. 909–914, Dec. 2009, ISSN: 1745-2473, 1745-2481. DOI: 10.1038/nphys1425. [Online]. Available: https://www.nature.com/articles/nphys1425 (visited on 10/23/2024).

[133] P. E. Allain *et al.*, "Optomechanical resonating probe for very high frequency sensing of atomic forces", en, *Nanoscale*, vol. 12, no. 5, pp. 2939–2945, 2020, ISSN: 2040-3364, 2040-3372. DOI: 10.1039/C9NR09690F. [Online]. Available: https://xlink.rsc.org/?DOI=C9NR09690F (visited on 10/07/2024).

[134] K. Srinivasan, H. Miao, M. T. Rakher, M. Davanço, and V. Aksyuk, "Optomechanical Transduction of an Integrated Silicon Cantilever Probe Using a Microdisk Resonator", en, *Nano Letters*, vol. 11, no. 2, pp. 791–797, Feb. 2011, ISSN: 1530-6984, 1530-6992. DOI: 10.1021/nl104018r. [Online]. Available: https://pubs.acs.org/doi/10.1021/nl104018r (visited on 12/10/2024).

[135] K. Cole, J. Beck, A. Haji-Sheikh, and B. Litkouhi, *Heat Conduction Using Greens Functions*, en, 0th ed. CRC Press, Jul. 2010, ISBN: 978-0-429-10918-8. DOI: 10.1201/9781439895214. [Online]. Available: https://www.taylorfrancis.com/books/9781439895214 (visited on 11/04/2022).

[136] S. E. Miller, "Coupled Wave Theory and Waveguide Applications", en, *Bell System Technical Journal*, vol. 33, no. 3, pp. 661–719, May 1954, ISSN: 00058580. DOI: 10.1002/j.1538-7305.1954.tb02359.x. [Online]. Available: https://ieeexplore.ieee.org/document/6772177 (visited on 02/07/2025).

[137] K. Okamoto, *Fundamentals of optical waveguides*, eng, Third edition. London San Diego, CA: Academic Press, 2022, ISBN: 978-0-12-815602-5.

[138] I. Chremmos, O. Schwelb, and N. Uzunoglu, Eds., *Photonic Microresonator Research and Applications* (Springer Series in Optical Sciences). Boston, MA: Springer US, 2010, vol. 156, ISBN: 978-1-4419-1743-0. DOI: 10.1007/978-1-4419-1744-7. [Online]. Available: http://link.springer.com/10.1007/978-1-4419-1744-7 (visited on 03/03/2025).

[139] Y. Kokubun, "High Index Contrast Optical Waveguides and Their Applications to Microring Filter Circuit and Wavelength Selective Switch", en, *IEICE Transactions on Electronics*, vol. E90-C, no. 5, pp. 1037–1045, May 2007, ISSN: 0916-8524, 1745-1353. DOI: 10.1093/ietele/e90-c.5.1037. [Online]. Available: http://search.ieice.org/bin/summary.php?id=e90-c_5_1037&category=C&year=2007&lang=E&abst= (visited on 03/03/2025).

[140] B. Liu, A. Shakouri, and J. E. Bowers, "Passive microring-resonator-coupled lasers", en, *Applied Physics Letters*, vol. 79, no. 22, pp. 3561–3563, Nov. 2001, ISSN: 0003-6951, 1077-3118. DOI: 10.1063/1.1420585. [Online]. Available: https://pubs.aip.org/apl/article/79/22/3561/516098/Passive-microring-resonator-coupled-lasers (visited on 03/03/2025).

[141] J. Poon, J. Scheuer, and A. Yariv, "Wavelength-Selective Reflector Based on a Circular Array of Coupled Microring Resonators", en, *IEEE Photonics Technology Letters*, vol. 16, no. 5, pp. 1331–1333, May 2004, ISSN: 1041-1135. DOI: 10.1109/LPT.2004.826152. [Online]. Available: http://ieeexplore.ieee.org/document/1291501/ (visited on 03/03/2025).

[142] A. Rosenthal and M. Horowitz, "Analysis and design of nonlinear fiber Bragg gratings and their application for optical compression of reflected pulses", en, *Optics Letters*, vol. 31, no. 9, p. 1334, May 2006, ISSN: 0146-9592, 1539-4794. DOI: 10.1364/OL.31.001334. [Online]. Available: https://opg.optica.org/abstract.cfm?URI=ol-31-9-1334 (visited on 03/03/2025).

[143] J. H. Marburger and F. S. Felber, "Theory of a lossless nonlinear Fabry-Perot interferometer", en, *Physical Review A*, vol. 17, no. 1, pp. 335–342, Jan. 1978, ISSN: 0556-2791. DOI: 10.1103/PhysRevA.17.335. [Online]. Available: https://link.aps.org/doi/10.1103/PhysRevA.17.335 (visited on 03/03/2025).

[144] Y. A. Vlasov, M. O'Boyle, H. F. Hamann, and S. J. McNab, "Active control of slow light on a chip with photonic crystal waveguides", en, *Nature*, vol. 438, no. 7064, pp. 65–69, Nov. 2005, ISSN: 0028-0836, 1476-4687. DOI: 10.1038/nature04210. [Online]. Available: https://www.nature.com/articles/nature04210 (visited on 03/03/2025).

[145] J. B. Khurgin, "Optical buffers based on slow light in electromagnetically induced transparent media and coupled resonator structures: Comparative analysis", en, *Journal of the Optical Society of America B*, vol. 22, no. 5, p. 1062, May 2005, ISSN: 0740-3224, 1520-8540. DOI: 10.1364/JOSAB.22.001062. [Online]. Available:

https://opg.optica.org/abstract.cfm?URI=josab-22-5-1062 (visited on 03/03/2025).

[146] B.-B. Li, L. Ou, Y. Lei, and Y.-C. Liu, "Cavity optomechanical sensing", en, *Nanophotonics*, vol. 10, no. 11, pp. 2799–2832, Aug. 2021, ISSN: 2192-8614. DOI: 10.1515/nanoph-2021-0256. [Online]. Available: https://www.degruyter.com/document/doi/10.1515/nanoph-2021-0256/html (visited on 03/03/2025).

[147] X. Sun, K. Y. Fong, C. Xiong, W. H. P. Pernice, and H. X. Tang, "GHz optomechanical resonators with high mechanical Q factor in air", en, *Optics Express*, vol. 19, no. 22, p. 22 316, Oct. 2011, ISSN: 1094-4087. DOI: 10.1364/OE.19.022316. [Online]. Available: https://opg.optica.org/oe/abstract.cfm?uri=oe-19-22-22316 (visited on 03/03/2025).

[148] M. He, S. Liao, L. Liu, and J. Dong, "Theoretical analysis for optomechanical all-optical transistor", en, *Frontiers of Optoelectronics*, vol. 9, no. 3, pp. 406–411, Sep. 2016, ISSN: 2095-2759, 2095-2767. DOI: 10.1007/s12200-016-0601-8. [Online]. Available: http://link.springer.com/10.1007/s12200-016-0601-8 (visited on 03/03/2025).

[149] I.-T. Chen, B. Li, S. Lee, S. Chakravarthi, K.-M. Fu, and M. Li, "Optomechanical ring resonator for efficient microwave-optical frequency conversion", en, *Nature Communications*, vol. 14, no. 1, p. 7594, Nov. 2023, ISSN: 2041-1723. DOI: 10.1038/s41467-023-43393-x. [Online]. Available: https://www.nature.com/articles/s41467-023-43393-x (visited on 03/03/2025).

[150] H. Li and M. Li, "Optomechanical photon shuttling between photonic cavities", en, *Nature Nanotechnology*, vol. 9, no. 11, pp. 913–919, Nov. 2014, ISSN: 1748-3387, 1748-3395. DOI: 10.1038/nnano.2014.200. [Online]. Available: https://www.nature.com/articles/nnano.2014.200 (visited on 10/23/2024).

[151] J. Gomis-Bresco *et al.*, "A one-dimensional optomechanical crystal with a complete phononic band gap", en, *Nature Communications*, vol. 5, no. 1, p. 4452, Jul. 2014, ISSN: 2041-1723. DOI: 10.1038/ncomms5452. [Online]. Available: https://www.nature.com/articles/ncomms5452 (visited on 07/29/2024).

[152] E. Luan, H. Yun, M. Ma, D. M. Ratner, K. C. Cheung, and L. Chrostowski, "Label-free biosensing with a multi-box sub-wavelength phase-shifted Bragg grating waveguide", en, *Biomedical Optics Express*, vol. 10, no. 9, p. 4825, Sep. 2019, ISSN: 2156-7085, 2156-7085. DOI: 10.1364/BOE.10.004825. [Online]. Available: https://opg.optica.org/abstract.cfm?URI=boe-10-9-4825 (visited on 07/29/2024).

[153] X. Sun, L. Zeng, Y. Hu, and J. Duan, "Fabrication and Sensing Application of Phase Shifted Bragg Grating Sensors", en, *Materials*, vol. 15, no. 10, p. 3720, May 2022, ISSN: 1996-1944. DOI: 10.3390/ma15103720. [Online]. Available: https://www.mdpi.com/1996-1944/15/10/3720 (visited on 08/02/2024).

[154] K. O. Hill, Y. Fujii, D. C. Johnson, and B. S. Kawasaki, "Photosensitivity in optical fiber waveguides: Application to reflection filter fabrication", en, *Applied Physics Letters*, vol. 32, no. 10, pp. 647–649, May 1978, ISSN: 0003-6951, 1077-3118. DOI: 10.1063/1.89881. [Online]. Available: https://pubs.aip.org/apl/article/32/10/647/1059743/Photosensitivity-in-optical-fiber-waveguides (visited on 07/29/2024).

[155] T. Yeo, Tong Sun, K. Grattan, D. Parry, R. Lade, and B. Powell, "Polymer-coated fiber Bragg grating for relative humidity sensing", *IEEE Sensors Journal*, vol. 5, no. 5, pp. 1082–1089, Oct. 2005, ISSN: 1530-437X. DOI: 10.1109/JSEN.2005.847935. [Online]. Available: http://ieeexplore.ieee.org/document/1504772/ (visited on 07/29/2024).

[156] A. Othonos and K. Kalli, *Fiber Bragg gratings: fundamentals and applications in telecommunications and sensing* (Artech House optoelectronics library), eng. Boston, Mass.: Artech House, 1999, ISBN: 978-0-89006-344-6.

[157] N. N. Klimov, S. Mittal, M. Berger, and Z. Ahmed, "On-chip silicon waveguide Bragg grating photonic temperature sensor", en, *Optics Letters*, vol. 40, no. 17, p. 3934, Sep. 2015, ISSN: 0146-9592, 1539-4794. DOI: 10.1364/OL.40.003934. [Online]. Available: https://opg.optica.org/abstract.cfm?URI=ol-40-17-3934 (visited on 08/02/2024).

[158] T. Murphy, J. Hastings, and H. Smith, "Fabrication and characterization of narrow-band Bragg-reflection filters in silicon-on-insulator ridge waveguides", *Journal of Lightwave Technology*, vol. 19, no. 12, pp. 1938–1942, Dec. 2001, ISSN: 07338724. DOI: 10.1109/50.971688. [Online]. Available: http://ieeexplore.ieee.org/document/971688/ (visited on 02/07/2025).

[159] G. Jiang, R. Chen, Q. Zhou, J. Yang, M. Wang, and X. Jiang, "Slab-Modulated Sidewall Bragg Gratings in Silicon-on-Insulator Ridge Waveguides", *IEEE Photonics Technology Letters*, p. 5 608 492, Jan. 2010, ISSN: 1041-1135, 1941-0174. DOI: 10.1109/LPT.2010.2089613. [Online]. Available: http://ieeexplore.ieee.org/document/5608492/ (visited on 02/07/2025).

[160] X. Wang, S. Grist, J. Flueckiger, N. A. F. Jaeger, and L. Chrostowski, "Silicon photonic slot waveguide Bragg gratings and resonators", en, *Optics Express*, vol. 21, no. 16, p. 19 029, Aug. 2013, ISSN: 1094-4087. DOI: 10.1364/OE.21.019029. [Online]. Available: https://opg.optica.org/oe/abstract.cfm?uri=oe-21-16-19029 (visited on 02/07/2025).

[161] M. Nejbauer, T. M. Kardaś, Y. Stepanenko, and C. Radzewicz, "Spectral compression of femtosecond pulses using chirped volume Bragg gratings", en, *Optics Letters*, vol. 41, no. 11, p. 2394, Jun. 2016, ISSN: 0146-9592, 1539-4794. DOI: 10.1364/OL.41.002394. [Online]. Available: https://opg.optica.org/abstract.cfm?URI=ol-41-11-2394 (visited on 02/07/2025).

[162] J. Želudevičius, R. Danilevičius, and K. Regelskis, "Optimization of pulse compression in a fiber chirped pulse amplification system by adjusting dispersion parameters of a temperature-tuned chirped fiber Bragg grating stretcher", en, *Journal of the Optical Society of America B*, vol. 32, no. 5, p. 812, May 2015, ISSN: 0740-3224, 1520-8540. DOI: 10.1364/JOSAB.32.000812. [Online]. Available: https://opg.optica.org/abstract.cfm?URI=josab-32-5-812 (visited on 02/07/2025).

[163] H. A. Haus, A. W. Snyder, and W. P. Huang, "Coupled-mode formulations", en, *Optics Letters*, vol. 14, no. 21, p. 1222, Nov. 1989, ISSN: 0146-9592, 1539-4794. DOI: 10.1364/OL.14.001222. [Online]. Available: https://opg.optica.org/abstract.cfm?URI=ol-14-21-1222 (visited on 02/07/2025).

[164] J. Čtyroký *et al.*, "Design of narrowband Bragg spectral filters in subwavelength grating metamaterial waveguides", en, *Optics Express*, vol. 26, no. 1, p. 179, Jan. 2018, ISSN: 1094-4087. DOI: 10.1364/OE.26.000179. [Online]. Available: https://opg.optica.org/abstract.cfm?URI=oe-26-1-179 (visited on 02/07/2025).

[165] F. Brückerhoff-Plückelmann *et al.*, "General design flow for waveguide Bragg gratings", en, *Nanophotonics*, Jan. 2025, ISSN: 2192-8606, 2192-8614. DOI: 10.1515/nanoph-2024-0498. [Online]. Available: https://www.degruyter.com/document/doi/10.1515/nanoph-2024-0498/html (visited on 02/07/2025).

[166] C. Kittel, *Introduction to solid state physics*, eng, 8. ed., [repr.] Hoboken, NJ: Wiley, ISBN: 978-0-471-41526-8.

[167] R. Kashyap, *Fiber Bragg gratings*, 2nd ed. Burlington, MA: Academic Press, 2010, OCLC: ocn233544011, ISBN: 978-0-12-372579-0.

[168] A. Yariv, P. Yeh, and A. Yariv, *Photonics: optical electronics in modern communications* (The Oxford series in electrical and computer engineering), 6th ed. New York: Oxford University Press, 2007, OCLC: ocm58648003, ISBN: 978-0-19-517946-0.

[169] C. Husko, A. Ducharme, N. M. Fahrenkopf, and J. R. Guest, "Phase-shifted Bragg gratings in a foundry silicon nitride platform", en, *OSA Continuum*, vol. 4, no. 3, p. 933, Mar. 2021, ISSN: 2578-7519. DOI: 10.1364/OSAC.413672. [Online]. Available: https://opg.optica.org/abstract.cfm?URI=osac-4-3-933 (visited on 02/12/2025).

[170] S. John, "Strong localization of photons in certain disordered dielectric superlattices", en, *Physical Review Letters*, vol. 58, no. 23, pp. 2486–2489, Jun. 1987, ISSN: 0031-9007. DOI: 10.1103/PhysRevLett.58.2486. [Online]. Available: https://link.aps.org/doi/10.1103/PhysRevLett.58.2486 (visited on 02/12/2025).

[171] Q. He, I. Zaquine, G. Roosen, and R. Frey, "Bragg diffraction in thin 2D refractive index modulated semiconductor samples", en, *Journal of the Optical Society of America B*, vol. 26, no. 3, p. 390, Mar. 2009, ISSN: 0740-3224, 1520-8540. DOI: 10.1364/JOSAB.26.000390. [Online]. Available: https://opg.optica.org/abstract.cfm?URI=josab-26-3-390 (visited on 04/11/2025).

[172] R. Gadhwal, P. Kaushik, and A. Devi, "A review on 1D photonic crystal based reflective optical limiters", en, *Critical Reviews in Solid State and Materials Sciences*, vol. 48, no. 1, pp. 93–111, Jan. 2023, ISSN: 1040-8436, 1547-6561. DOI: 10.1080/10408436.2022.2041394. [Online]. Available: https://www.tandfonline.com/doi/full/10.1080/10408436.2022.2041394 (visited on 02/12/2025).

[173] E. Kuramochi, H. Taniyama, T. Tanabe, K. Kawasaki, Y.-G. Roh, and M. Notomi, "Ultrahigh-Q one-dimensional photonic crystal nanocavities with modulated mode-gap barriers on SiO_2 claddings and on air claddings", en, *Optics Express*, vol. 18, no. 15, p. 15 859, Jul. 2010, ISSN: 1094-4087. DOI: 10.1364/OE.18.015859. [Online]. Available: https://opg.optica.org/oe/abstract.cfm?uri=oe-18-15-15859 (visited on 02/12/2025).

[174] P. T. Rakich *et al.*, "Achieving centimetre-scale supercollimation in a large-area two-dimensional photonic crystal", en, *Nature Materials*, vol. 5, no. 2, pp. 93–96, Feb. 2006, ISSN: 1476-1122, 1476-4660. DOI: 10.1038/nmat1568. [Online]. Available: https://www.nature.com/articles/nmat1568 (visited on 02/12/2025).

[175] F. Wen, S. David, X. Checoury, M. El Kurdi, and P. Boucaud, "Two-dimensional photonic crystals with large complete photonic band gaps in both TE and TM polarizations", en, *Optics Express*, vol. 16, no. 16, p. 12 278, Aug. 2008, ISSN: 1094-4087. DOI: 10.1364/OE.16.012278. [Online]. Available: https://opg.optica.org/oe/abstract.cfm?uri=oe-16-16-12278 (visited on 02/12/2025).

[176] R. K. Cersonsky, J. Antonaglia, B. D. Dice, and S. C. Glotzer, "The diversity of three-dimensional photonic crystals", en, *Nature Communications*, vol. 12, no. 1, p. 2543, May 2021, ISSN: 2041-1723. DOI: 10.1038/s41467-021-22809-6. [Online]. Available: https://www.nature.com/articles/s41467-021-22809-6 (visited on 02/12/2025).

[177] J. D. Joannopoulos, J. N. Winn, and S. G. Johnson, *Photonic Crystals: Molding the Flow of Light - Second Edition*, eng. Princeton, NJ: Princeton University Press, 2011, ISBN: 978-0-691-12456-8. DOI: 10.1515/9781400828241.

[178] Y. Akahane, T. Asano, B.-S. Song, and S. Noda, "High-Q photonic nanocavity in a two-dimensional photonic crystal", en, *Nature*, vol. 425, no. 6961, pp. 944–947, Oct. 2003, ISSN: 0028-0836, 1476-4687. DOI: 10.1038/nature02063. [Online]. Available: https://www.nature.com/articles/nature02063 (visited on 02/19/2025).

[179] M. Notomi, E. Kuramochi, and H. Taniyama, "Ultrahigh-Q Nanocavity with 1D Photonic Gap", en, *Optics Express*, vol. 16, no. 15, p. 11 095, Jul. 2008, ISSN: 1094-4087. DOI: 10.1364/OE.16.011095. [Online]. Available: https://opg.optica.org/abstract.cfm?URI=oe-16-15-11095 (visited on 02/19/2025).

[180] W. Bogaerts *et al.*, "Silicon microring resonators", en, *Laser & Photonics Reviews*, vol. 6, no. 1, pp. 47–73, Jan. 2012, ISSN: 1863-8880, 1863-8899. DOI: 10.1002/lpor.201100017. [Online]. Available: https://onlinelibrary.wiley.com/doi/10.1002/lpor.201100017 (visited on 04/06/2025).

[181] R. José Pérez Menéndez, "Fiber-Optic Ring Resonator Interferometer", en, in *Interferometry - Recent Developments and Contemporary Applications*, M. Bhowmick and B. Ullrich, Eds., IntechOpen, Aug. 2019, ISBN: 978-1-78985-926-3. DOI: 10.5772/intechopen.80569. [Online]. Available: https://www.intechopen.com/books/interferometry-recent-developments-and-contemporary-applications/fiber-optic-ring-resonator-interferometer (visited on 02/13/2025).

[182] *Integrated Ring Resonators* (Springer Series in Optical Sciences), en. Berlin, Heidelberg: Springer Berlin Heidelberg, 2007, vol. 127, ISBN: 978-3-540-68786-3. DOI: 10.1007/978-3-540-68788-7. [Online]. Available: http://link.springer.com/10.1007/978-3-540-68788-7 (visited on 02/14/2025).

[183] D. W. Hahn and M. N. Özişik, *Heat conduction*, eng, 3. ed. Hoboken, NJ: Wiley, 2012, ISBN: 978-0-470-90293-6.

[184] N. Noda, R. B. Hetnarski, and Y. Tanigawa, *Thermal stresses*, 2nd ed. New York: Taylor & Francis, 2003, ISBN: 978-1-56032-971-8.

[185] O. C. Zienkiewicz, R. L. Taylor, and J. Z. Zhu, *The finite element method: its basis and fundamentals*, eng, 7th edition. Amsterdam: Elsevier, Butterworth-Heinemann, 2013, ISBN: 978-1-85617-633-0.

[186] L. Faria and R. L. Moreira, "Infrared spectroscopic investigation of chain conformations and interactions in P(VDF-TrFE)/PMMA blends", en, *Journal of Polymer Science Part B: Polymer Physics*, vol. 38, no. 1, pp. 34–40, Jan. 2000, ISSN: 0887-6266, 1099-0488. DOI: 10.1002/(SICI)1099-0488(20000101)38:1<34::AID-POLB4>3.0.CO;2-R. [Online]. Available: https://onlinelibrary.wiley.com/doi/10.1002/(SICI)1099-0488(20000101)38:1%3C34::AID-POLB4%3E3.0.CO;2-R (visited on 03/03/2025).

[187] J. Wang, M. K. Lee, S.-M. Park, S. Hong, and N. Kim, "A study on the mechanical properties and deformation behavior of injection molded PMMA-TSP laminated composite", en, *Korea-Australia Rheology Journal*, vol. 24, no. 1, pp. 23–33, Mar. 2012, ISSN: 1226-119X, 2093-7660. DOI: 10.1007/s13367-012-0003-4. [Online]. Available: http://link.springer.com/10.1007/s13367-012-0003-4 (visited on 03/03/2025).

[188] H.-S. Yang, M. P. Wolcott, H.-S. Kim, and H.-J. Kim, "Thermal properties of lignocellulosic filler-thermoplastic polymer bio-composites", en, *Journal of Thermal Analysis and Calorimetry*, vol. 82, no. 1, pp. 157–160, Sep. 2005, ISSN: 1388-6150, 1572-8943. DOI: 10.1007/s10973-005-0857-5. [Online]. Available: http://link.springer.com/10.1007/s10973-005-0857-5 (visited on 03/03/2025).

[189] I. Henins, "Precision density measurement of silicon", en, *Journal of Research of the National Bureau of Standards Section A: Physics and Chemistry*, vol. 68A, no. 5, p. 529, Sep. 1964, ISSN: 0022-4332. DOI: 10.6028/jres.068A.050. [Online]. Available: https://nvlpubs.nist.gov/nistpubs/jres/68A/jresv68An5p529_A1b.pdf (visited on 03/03/2025).

[190] M. J. Assael, S. Botsios, K. Gialou, and I. N. Metaxa, "Thermal Conductivity of Polymethyl Methacrylate (PMMA) and Borosilicate Crown Glass BK7", en, *International Journal of Thermophysics*, vol. 26, no. 5, pp. 1595–1605, Sep. 2005, ISSN: 0195-928X, 1572-9567. DOI: 10.1007/s10765-005-8106-5. [Online]. Available: http://link.springer.com/10.1007/s10765-005-8106-5 (visited on 03/03/2025).

[191] R. Sheldon and S. K. Lane, "Thermal conductivities of polymers II—Polyethylene", en, *Polymer*, vol. 6, no. 4, pp. 205–212, Apr. 1965, ISSN: 00323861. DOI: 10.1016/

0032-3861(65)90042-X. [Online]. Available: https://linkinghub.elsevier.com/retrieve/pii/003238616590042X (visited on 03/03/2025).

[192] K. Kadoya, N. Matsunaga, and A. Nagashima, "Viscosity and Thermal Conductivity of Dry Air in the Gaseous Phase", en, *Journal of Physical and Chemical Reference Data*, vol. 14, no. 4, pp. 947–970, Oct. 1985, ISSN: 0047-2689, 1529-7845. DOI: 10.1063/1.555744. [Online]. Available: https://pubs.aip.org/jpr/article/14/4/947/241383/Viscosity-and-Thermal-Conductivity-of-Dry-Air-in (visited on 03/03/2025).

[193] U. Gaur, S.-f. Lau, B. B. Wunderlich, and B. Wunderlich, "Heat Capacity and Other Thermodynamic Properties of Linear Macromolecules VI. Acrylic Polymers", en, *Journal of Physical and Chemical Reference Data*, vol. 11, no. 4, pp. 1065–1089, Oct. 1982, ISSN: 0047-2689, 1529-7845. DOI: 10.1063/1.555671. [Online]. Available: https://pubs.aip.org/jpr/article/11/4/1065/241227/Heat-Capacity-and-Other-Thermodynamic-Properties (visited on 03/03/2025).

[194] J. L. Jordan *et al.*, "Elastic properties of polyethylene from high pressure sound speed measurements", en, *Polymer*, vol. 212, p. 123 164, Jan. 2021, ISSN: 00323861. DOI: 10.1016/j.polymer.2020.123164. [Online]. Available: https://linkinghub.elsevier.com/retrieve/pii/S0032386120309897 (visited on 03/03/2025).

[195] T. Nogueira, R. Botan, F. Wypych, and L. Lona, "Study of thermal and mechanical properties of PMMA/LDHs nanocomposites obtained by in situ bulk polymerization", en, *Composites Part A: Applied Science and Manufacturing*, vol. 42, no. 8, pp. 1025–1030, Aug. 2011, ISSN: 1359835X. DOI: 10.1016/j.compositesa.2011.04.006. [Online]. Available: https://linkinghub.elsevier.com/retrieve/pii/S1359835X11001126 (visited on 03/03/2025).

[196] B. Salameh, S. Yasin, D. A. Fara, and A. M. Zihlif, "Dependence of the Thermal Conductivity of PMMA, PS and PE on Temperature and Crystallinity", en, *Polymer Korea*, vol. 45, no. 2, pp. 281–285, Mar. 2021, ISSN: 0379-153X, 2234-8077. DOI: 10.7317/pk.2021.45.2.281. [Online]. Available: http://www.dbpia.co.kr/Journal/ArticleDetail/NODE10538083 (visited on 03/03/2025).

[197] K. Li, G. Xu, X. Huang, Z. Xie, and F. Gong, "Manufacturing of Micro-Lens Array Using Contactless Micro-Embossing with an EDM-Mold", en, *Applied Sciences*, vol. 9, no. 1, p. 85, Dec. 2018, ISSN: 2076-3417. DOI: 10.3390/app9010085. [Online]. Available: https://www.mdpi.com/2076-3417/9/1/85 (visited on 03/03/2025).

[198] M. A. Hopcroft, W. D. Nix, and T. W. Kenny, "What is the Young's Modulus of Silicon?", *Journal of Microelectromechanical Systems*, vol. 19, no. 2, pp. 229–238, Apr. 2010, ISSN: 1057-7157, 1941-0158. DOI: 10.1109/JMEMS.2009.2039697. [Online]. Available: http://ieeexplore.ieee.org/document/5430873/ (visited on 03/03/2025).

[199] H. Wu, S. Grabarnik, A. Emadi, G. De Graaf, and R. F. Wolffenbuttel, "Characterization of thermal cross-talk in a MEMS-based thermopile detector array", *Journal of Micromechanics and Microengineering*, vol. 19, no. 7, p. 074 022, Jul. 2009, ISSN: 0960-1317, 1361-6439. DOI: 10.1088/0960-1317/19/7/074022. [Online]. Available: https://iopscience.iop.org/article/10.1088/0960-1317/19/7/074022 (visited on 03/20/2025).

[200] I.-L. Ngo, S. Jeon, and C. Byon, "Thermal conductivity of transparent and flexible polymers containing fillers: A literature review", en, *International Journal of Heat and Mass Transfer*, vol. 98, pp. 219–226, Jul. 2016, ISSN: 00179310. DOI: 10.1016/j.ijheatmasstransfer.2016.02.082. [Online]. Available: https://linkinghub.elsevier.com/retrieve/pii/S0017931015304932 (visited on 03/20/2025).

[201] J. D. Achenbach, *Wave propagation in elastic solids* (North-Holland series in applied mathematics and mechanics v. 16), eng. Amsterdam New York: North-Holland Pub. Co. American Elsevier Pub. Co, 1973, ISBN: 978-0-7204-2367-9.

[202] F. Bai, R. Bertram, and B. R. Karamched, "A closed-loop multi-scale model for intrinsic frequency-dependent regulation of axonal growth", en, *Mathematical Biosciences*, vol. 344, p. 108 768, Feb. 2022, ISSN: 00255564. DOI: 10.1016/j.mbs.2021.108768. [Online]. Available: https://linkinghub.elsevier.com/retrieve/pii/S0025556421001632 (visited on 02/20/2025).

[203] S. Kenkel, S. Mittal, and R. Bhargava, "Closed-loop atomic force microscopy-infrared spectroscopic imaging for nanoscale molecular characterization", en, *Nature Communications*, vol. 11, no. 1, p. 3225, Jun. 2020, ISSN: 2041-1723. DOI: 10.1038/s41467-020-17043-5. [Online]. Available: https://www.nature.com/articles/s41467-020-17043-5 (visited on 02/20/2025).

[204] P. E. Hopkins, "Thermal Transport across Solid Interfaces with Nanoscale Imperfections: Effects of Roughness, Disorder, Dislocations, and Bonding on Thermal Boundary Conductance", en, *ISRN Mechanical Engineering*, vol. 2013, pp. 1–19, Jan. 2013, ISSN: 2090-5130. DOI: 10.1155/2013/682586. [Online]. Available: https://www.hindawi.com/journals/isrn/2013/682586/ (visited on 02/20/2025).

[205] J. Song and Y. Zhang, "Effect of an interface layer on thermal conductivity of polymer composites studied by the design of double-layered and triple-layered composites", en, *International Journal of Heat and Mass Transfer*, vol. 141, pp. 1049–1055, Oct. 2019, ISSN: 00179310. DOI: 10.1016/j.ijheatmasstransfer.2019.07.002. [Online]. Available: https://linkinghub.elsevier.com/retrieve/pii/S0017931019316394 (visited on 02/20/2025).

[206] S. Rizevsky, K. Zhaliazka, T. Dou, M. Matveyenka, and D. Kurouski, "Characterization of Substrates and Surface-Enhancement in Atomic Force Microscopy Infrared Analysis of Amyloid Aggregates", en, *The Journal of Physical Chemistry C*, vol. 126, no. 8, pp. 4157–4162, Mar. 2022, ISSN: 1932-7447, 1932-7455. DOI: 10.1021/acs.jpcc.1c09643. [Online]. Available: https://pubs.acs.org/doi/10.1021/acs.jpcc.1c09643 (visited on 02/20/2025).

[207] N. Prine, C. Cardinal, and X. Gu, "Understanding and controlling the depth sensitivity of scanning probe based infrared imaging and nanospectroscopy for buried polymeric structures", en, *Nanoscale*, vol. 15, no. 24, pp. 10 244–10 253, 2023, ISSN: 2040-3364, 2040-3372. DOI: 10.1039/D3NR01657A. [Online]. Available: http://xlink.rsc.org/?DOI=D3NR01657A (visited on 03/21/2024).

[208] A. Dazzi *et al.*, "Photothermal AFM-IR Depth Sensitivity: An Original Pathway to Tomographic Reconstruction", en, *Analytical Chemistry*, vol. 96, no. 45, pp. 17 931–17 940, Nov. 2024, ISSN: 0003-2700, 1520-6882. DOI: 10.1021/acs.analchem.4c01969. [Online]. Available: https://pubs.acs.org/doi/10.1021/acs.analchem.4c01969 (visited on 12/09/2024).

[209] D. S. Jakob, J. J. Schwartz, G. Pavlidis, K. E. Grutter, and A. Centrone, "Understanding AFM-IR Signal Dependence on Sample Thickness and Laser Excitation: Experimental and Theoretical Insights", en, *Analytical Chemistry*, vol. 96, no. 41, pp. 16 195–16 202, Oct. 2024, ISSN: 0003-2700, 1520-6882. DOI: 10.1021/acs.analchem.4c02834. [Online]. Available: https://pubs.acs.org/doi/10.1021/acs.analchem.4c02834 (visited on 12/09/2024).

[210] C. Shin *et al.*, "Fast, exact and non-destructive diagnoses of contact failures in nanoscale semiconductor device using conductive AFM", en, *Scientific Reports*, vol. 3, no. 1, p. 2088, Jun. 2013, ISSN: 2045-2322. DOI: 10.1038/srep02088. [Online]. Available: https://www.nature.com/articles/srep02088 (visited on 03/21/2024).

[211] Z. Cui *et al.*, "Seeing Down to the Bottom: Nondestructive Inspection of All-Polymer Solar Cells by Kelvin Probe Force Microscopy", en, *Advanced Materials Interfaces*, vol. 3, no. 18, p. 1 600 446, Sep. 2016, ISSN: 2196-7350, 2196-7350. DOI: 10.1002/

admi.201600446. [Online]. Available: https://onlinelibrary.wiley.com/doi/10.1002/admi.201600446 (visited on 04/05/2024).

[212] J. Xie, J. Yan, D. Zhu, and G. He, "Atomic-Level Insight into the Formation of Subsurface Dislocation Layer and Its Effect on Mechanical Properties During Ultrafast Laser Micro/Nano Fabrication", en, *Advanced Functional Materials*, vol. 32, no. 15, p. 2 108 802, Apr. 2022, ISSN: 1616-301X, 1616-3028. DOI: 10.1002/adfm.202108802. [Online]. Available: https://onlinelibrary.wiley.com/doi/10.1002/adfm.202108802 (visited on 12/17/2024).

[213] F. Mooshammer *et al.*, "Nanoscale Near-Field Tomography of Surface States on $(Bi_{0.5}\,Sb_{0.5})_2\,Te_3$", en, *Nano Letters*, vol. 18, no. 12, pp. 7515–7523, Dec. 2018, ISSN: 1530-6984, 1530-6992. DOI: 10.1021/acs.nanolett.8b03008. [Online]. Available: https://pubs.acs.org/doi/10.1021/acs.nanolett.8b03008 (visited on 01/30/2025).

[214] L. Mester, A. A. Govyadinov, S. Chen, M. Goikoetxea, and R. Hillenbrand, "Subsurface chemical nanoidentification by nano-FTIR spectroscopy", en, *Nature Communications*, vol. 11, no. 1, p. 3359, Jul. 2020, ISSN: 2041-1723. DOI: 10.1038/s41467-020-17034-6. [Online]. Available: https://www.nature.com/articles/s41467-020-17034-6 (visited on 01/30/2025).

[215] K. Ho, K. S. Kim, L. Gilburd, R. Mirzoyan, S. De Beer, and G. C. Walker, "Nanoscale Subsurface Morphologies in Block Copolymer Thin Films Revealed by Combined Near-Field Infrared Microscopy and Mechanical Mapping", en, *ACS Applied Polymer Materials*, vol. 1, no. 5, pp. 933–938, May 2019, ISSN: 2637-6105, 2637-6105. DOI: 10.1021/acsapm.9b00189. [Online]. Available: https://pubs.acs.org/doi/10.1021/acsapm.9b00189 (visited on 01/30/2025).

[216] Y. Liu, H. Miao, V. Aksyuk, and K. Srinivasan, "Wide cantilever stiffness range cavity optomechanical sensors for atomic force microscopy", en, *Optics Express*, vol. 20, no. 16, p. 18 268, Jul. 2012, ISSN: 1094-4087. DOI: 10.1364/OE.20.018268. [Online]. Available: https://opg.optica.org/oe/abstract.cfm?uri=oe-20-16-18268 (visited on 12/10/2024).

[217] A. Schliesser, O. Arcizet, R. Rivière, G. Anetsberger, and T. J. Kippenberg, "Resolved-sideband cooling and position measurement of a micromechanical oscillator close to the Heisenberg uncertainty limit", en, *Nature Physics*, vol. 5, no. 7, pp. 509–514, Jul. 2009, ISSN: 1745-2473, 1745-2481. DOI: 10.1038/nphys1304. [Online]. Available: https://www.nature.com/articles/nphys1304 (visited on 10/23/2024).

[218] L. Schwab *et al.*, "Very-high-frequency probes for atomic force microscopy with silicon optomechanics", en, *Microsystems & Nanoengineering*, vol. 8, no. 1, p. 32, Mar. 2022, ISSN: 2055-7434. DOI: 10.1038/s41378-022-00364-4. [Online]. Available: https://www.nature.com/articles/s41378-022-00364-4 (visited on 07/26/2024).

[219] F. Galeotti *et al.*, "On-chip waveguide-coupled opto-electro-mechanical system for nanoscale displacement sensing", en, *APL Photonics*, vol. 5, no. 2, p. 026 103, Feb. 2020, ISSN: 2378-0967. DOI: 10.1063/1.5131576. [Online]. Available: https://pubs.aip.org/app/article/5/2/026103/123200/On-chip-waveguide-coupled-opto-electro-mechanical (visited on 10/23/2024).

[220] B. Li, F.-L. Hsiao, and C. Lee, "Configuration analysis of sensing element for photonic crystal based NEMS cantilever using dual nano-ring resonator", en, *Sensors and Actuators A: Physical*, vol. 169, no. 2, pp. 352–361, Oct. 2011, ISSN: 09244247. DOI: 10.1016/j.sna.2011.03.020. [Online]. Available: https://linkinghub.elsevier.com/retrieve/pii/S092442471100149X (visited on 10/23/2024).

[221] C. Lee and J. Thillaigovindan, "Optical nanomechanical sensor using a silicon photonic crystal cantilever embedded with a nanocavity resonator", en, *Applied Optics*, vol. 48, no. 10, p. 1797, Apr. 2009, ISSN: 0003-6935, 1539-4522. DOI: 10.1364/AO.48.001797. [Online]. Available: https://opg.optica.org/abstract.cfm?URI=ao-48-10-1797 (visited on 10/23/2024).

[222] T. T. Mai, F.-L. Hsiao, C. Lee, W. Xiang, C.-C. Chen, and W. Choi, "Optimization and comparison of photonic crystal resonators for silicon microcantilever sensors", en, *Sensors and Actuators A: Physical*, vol. 165, no. 1, pp. 16–25, Jan. 2011, ISSN: 09244247. DOI: 10.1016/j.sna.2010.01.006. [Online]. Available: https://linkinghub.elsevier.com/retrieve/pii/S0924424710000075 (visited on 10/23/2024).

[223] Wenfeng Xiang and Chengkuo Lee, "Nanophotonics Sensor Based on Microcantilever for Chemical Analysis", *IEEE Journal of Selected Topics in Quantum Electronics*, vol. 15, no. 5, pp. 1323–1326, 2009, ISSN: 1077-260X, 1558-4542. DOI: 10.1109/JSTQE.2009.2016578. [Online]. Available: http://ieeexplore.ieee.org/document/4957056/ (visited on 12/10/2024).

[224] M. Eichenfield, R. Camacho, J. Chan, K. J. Vahala, and O. Painter, "A picogram- and nanometre-scale photonic-crystal optomechanical cavity", en, *Nature*, vol. 459, no. 7246, pp. 550–555, May 2009, ISSN: 0028-0836, 1476-4687. DOI: 10.1038/

nature08061. [Online]. Available: https://www.nature.com/articles/nature08061 (visited on 10/23/2024).

[225] J. Gomis-Bresco *et al.*, "A one-dimensional optomechanical crystal with a complete phononic band gap", en, *Nature Communications*, vol. 5, no. 1, p. 4452, Jul. 2014, ISSN: 2041-1723. DOI: 10.1038/ncomms5452. [Online]. Available: https://www.nature.com/articles/ncomms5452 (visited on 10/23/2024).

[226] A. Boisen, S. Dohn, S. S. Keller, S. Schmid, and M. Tenje, "Cantilever-like micromechanical sensors", *Reports on Progress in Physics*, vol. 74, no. 3, p. 036 101, Mar. 2011, ISSN: 0034-4885, 1361-6633. DOI: 10.1088/0034-4885/74/3/036101. [Online]. Available: https://iopscience.iop.org/article/10.1088/0034-4885/74/3/036101 (visited on 10/07/2024).

[227] I. Voiculescu and M. Zaghloul, Eds., *Nanocantilever Beams: Modeling, Fabrication, and Applications*, en, 0th ed. Jenny Stanford Publishing, Dec. 2015, ISBN: 978-0-429-09520-7. DOI: 10.1201/b19340. [Online]. Available: https://www.taylorfrancis.com/books/9789814613248 (visited on 07/29/2024).

[228] B. O. Alunda and Y. J. Lee, "Review: Cantilever-Based Sensors for High Speed Atomic Force Microscopy", en, *Sensors*, vol. 20, no. 17, p. 4784, Aug. 2020, ISSN: 1424-8220. DOI: 10.3390/s20174784. [Online]. Available: https://www.mdpi.com/1424-8220/20/17/4784 (visited on 10/07/2024).

[229] M. Alvarez and L. M. Lechuga, "Microcantilever-based platforms as biosensing tools", en, *The Analyst*, vol. 135, no. 5, p. 827, 2010, ISSN: 0003-2654, 1364-5528. DOI: 10.1039/b908503n. [Online]. Available: https://xlink.rsc.org/?DOI=b908503n (visited on 10/07/2024).

[230] C. Ziegler, "Cantilever-based biosensors", en, *Analytical and Bioanalytical Chemistry*, vol. 379, no. 7-8, Aug. 2004, ISSN: 1618-2642, 1618-2650. DOI: 10.1007/s00216-004-2694-y. [Online]. Available: http://link.springer.com/10.1007/s00216-004-2694-y (visited on 10/07/2024).

[231] K. Eom, H. S. Park, D. S. Yoon, and T. Kwon, "Nanomechanical resonators and their applications in biological/chemical detection: Nanomechanics principles", en, *Physics Reports*, vol. 503, no. 4-5, pp. 115–163, Jun. 2011, ISSN: 03701573. DOI: 10.1016/j.physrep.2011.03.002. [Online]. Available: https://linkinghub.elsevier.com/retrieve/pii/S0370157311000639 (visited on 10/07/2024).